

Bangor University

DOCTOR OF PHILOSOPHY

Laser control of the photoisomerisation of azo-compounds: a theoretical study

Hywel, Meilir

Award date:
2008

Awarding institution:
Bangor University

[Link to publication](#)

General rights

Copyright and moral rights for the publications made accessible in the public portal are retained by the authors and/or other copyright owners and it is a condition of accessing publications that users recognise and abide by the legal requirements associated with these rights.

- Users may download and print one copy of any publication from the public portal for the purpose of private study or research.
- You may not further distribute the material or use it for any profit-making activity or commercial gain
- You may freely distribute the URL identifying the publication in the public portal ?

Take down policy

If you believe that this document breaches copyright please contact us providing details, and we will remove access to the work immediately and investigate your claim.

Download date: 09. Apr. 2024

Laser Control of the Photoisomerisation of Azo-compounds: A Theoretical Study

A Thesis Submitted

By

MEILIR HYWEL B.Sc.

To the University of Wales in candidature for the degree of
Philosophiae Doctor

Department of Chemistry
University of Wales, Bangor
September 2008



Acknowledgements

First and foremost I would like to thank my supervisor Dr Keith Hughes for his patient guidance and encouragement over the years of my Ph.D. research. The endless discussions we've had on the physical concepts touched upon in this work have been both interesting and enlightening. I would also like to thank Richard Anderson, Stephen Parry, Andrew Davies and M. Hama-Ali Rasheed for their company at various times during my research, including helpful discussions on aspects of computational chemistry. I am also grateful to Dr John Macdonald for his enthusiastic introduction of the complex subject of quantum mechanics during my time as an undergraduate. Thanks also goes to the University of Wales for the funding over the years.

Buaswn hefyd yn hoffi diolch i Mam, Dad, Dyfrig, Iwan (ag Elen), FFflos, Nel, Twm, Bess, Yogi, Idwal a Brython am eu cymorth dros y blynyddoedd.

Abstract

The quantum control of the isomerisation of azomethane and a 10-membered dibenzoazo crown ether (referred to as O2N2) was studied for the inversion and torsional coordinates. Density functional theory was used to generate the ground (S_0) and first excited (S_1) electronic state potential energy functions required to simulate the wavepacket dynamics. Laser control pulses were generated manually by observation of the wavepacket dynamics, and these were subsequently refined by using optimal control theory.

For azomethane, greater isomerisation control is possible along the torsional isomerisation coordinate than along the inversion coordinate. Control along the inversion coordinate is hindered by the existence of a potential barrier on the S_1 potential energy function, and hence a complicated 4-pulse sequence is required to overcome it. Furthermore the control of azomethane isomerisation along both coordinates is limited by the small transition dipole moment coupling the S_0 and S_1 electronic states.

The topology of O2N2's S_1 potential energy surface favours the torsional *trans* \rightarrow *cis* isomerisation channel, where again an energy barrier is observed along the S_1 inversion pathway. However, a greater yield is observed along the inversion pathway utilising a 4-pulse sequence since the locality of the wavepacket is easier to maintain along this coordinate, as opposed to the periodic torsional coordinate.

Finally, in chapter 6, the effect of environmental dissipation on the laser control of a model isomerisation system is investigated using the Caldeira-Leggett quantum master equation in Wigner phase space. As expected, energy dissipation and decoherence have a negative effect on the amount of quantum control possible, and the effect increases with respect to the size of the friction coefficient η .

Contents

1	Introduction	4
2	Background Theory	12
2.1	Separation of Electronic and Nuclear Motion	12
2.2	The Time Dependent Wavepacket	14
2.3	Coupling of Electronic States via External Electromagnetic Field	17
2.4	Non-Adiabatic Transitions	22
3	Computational Molecular Dynamics	25
3.1	<i>Ab Initio</i> Calculations	26
3.1.1	Hartree-Fock theory	27
3.1.2	Configuration Interaction	30
3.1.3	Density Functional Theory	31
3.2	Wavepacket Dynamics	36
3.2.1	Defining the Initial Wavepacket	37
3.2.2	Wavepacket Propagation	42
3.3	Wavepacket Propagation on Two Coupled Electronic States .	45
3.3.1	Electronic State Population Transfer on a Model 2 State Harmonic Oscillator Example	45
4	Quantum Control of Molecular Dynamics	54
4.1	Laser Control of Wavepacket Dynamics	55
4.1.1	Tannor and Rice pump/dump Pulses	55
4.1.2	Optimal Control Theory	57
4.1.3	Laser Pulse Parameters	63

4.2	Photoisomerisation of Azomethane	63
4.2.1	Azomethane DFT Calculations Results	64
4.2.2	Control of Azomethane Isomerisation Along Torsional Coordinate	69
4.2.3	Control of Azomethane Isomerisation Along Inversion Coordinate	77
5	Optimal Control of an Ether Capped Azobenzene Molecule	87
5.1	Background	88
5.2	Photoisomerisation of the Azobenzene Derivative O2N2	93
5.2.1	O2N2 DFT Calculations Results	94
5.2.2	Control of O2N2 Isomerisation Along Inversion Coor- dinate	102
5.2.3	Control of O2N2 Isomerisation Along Torsional Coor- dinate	108
5.2.4	Control of O2N2 Isomerisation: <i>cis</i> \rightarrow <i>trans</i>	112
5.2.5	Effect of transition dipole moment and orientation . . .	116
5.3	Summary and Discussion of Chapter	123
5.3.1	Mechanism of Isomerisation of O2N2	123
5.3.2	Limitations and Further Work	126
6	Optimal Control of Dissipative Quantum Phase Space Dy- namics	133
6.1	Introduction	133
6.1.1	The Density Operator	135
6.1.2	Wigner Phase Space Distribution	137
6.2	Dissipative Dynamics	142
6.2.1	The Caldeira-Leggett Quantum Master Equation . . .	143
6.2.2	Optimal Control Theory for Wigner Phase Space Dy- namics	149
6.3	Optimal Control of a Model Isomerisation System with Dissi- pation in Phase Space	154
6.3.1	Control in Non-dissipative Phase Space	156

6.3.2	Effect of C-L Dissipation on Control	161
6.3.3	Momentum Specific Target States	162
6.4	Further Work	167
A	Split-Operator Numerical Method on Two electronic states	171
B	Determination of Reduced Moment of Inertia	175
C	Derivation of the Wigner-Moyal equation	177
C.1	One Electronic State	177
C.2	Two Electronic State	181
D	Derivation of the Caldeira-Leggett equation	189
D.1	Contour integration of C_R and C_I	202
D.1.1	C_I	202
D.1.2	C_R	204
D.2	Plemelj Identity	206
D.3	Hamilton commutator	207

Chapter 1

Introduction

Azobenzene derivatives have long been used as dyes due to their strong absorption of electromagnetic radiation in the visible region of the spectrum, resulting in their vivid colouration ranging characteristically from red, orange to yellow. Some, e.g. methyl orange, have also been utilised as acid/base indicators due to their propensity to change colour under different pH conditions.

Another characteristic of azobenzene and its derivatives is their ability to undergo *trans* \leftrightarrow *cis* photoisomerisation [1, 2] when illuminated with UV/visible light of the correct wavelength. Due to their ability to isomerise quickly (picosecond timescale), and that their separate conformers are stable and spectroscopically distinguishable, azobenzene and its derivatives have been identified as having potential applications in optical data storage, data processing, biochemical activity, and as optical switches in molecular machines and nano devices (see ref. [3] and references therein). Understandably, the mechanism of the photoisomerisation of azobenzene has been extensively studied and debated in the literature in recent years [3, 4, 5, 6, 7, 8, 9]. The main point of discussion is whether the preferred path of isomerisation occurs via torsion or inversion around the central azo component of the molecule Fig. 1.1.

A particular subgroup of azobenzene derivatives are characterised by their apparent resistance towards the torsional photoisomerisation mechanism, the

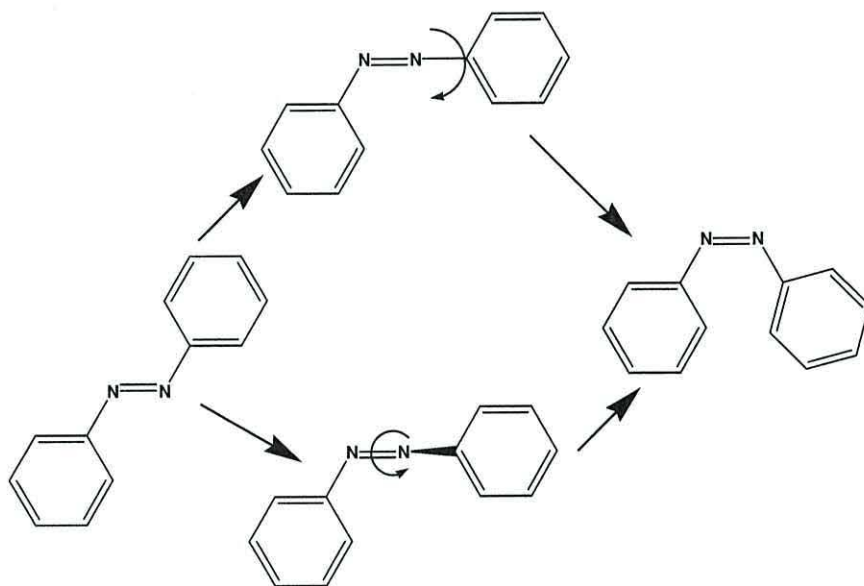


Figure 1.1: Schematic diagram of the two likeliest routes of azobenzene photoisomerisation, inversion (top) and torsion (bottom) around the $N=N$ bond.

so called rotation-restricted azobenzenes. Fig. 1.2 illustrates molecules which may be regarded as rotation-restricted, where the torsion isomerisation mechanism was believed to be hindered by the fact that the phenyl rings are connected [10, 12]. The azobenzene derivative which provides the focus of this work is a 10-membered dibenzoazo crownether [13], depicted in Fig. 1.2 B for $n=1$, where the phenyl rings are connected by an ether linkage. The motivation for the investigation into the photoisomerisation of this particular molecule is its relatively small size, hence the prospect of less computationally demanding theoretical calculations, and the relative thermal stability of its *cis* conformer [13], which is a crucial attribute for an isomerising molecular switch.

Throughout this thesis, the 10-membered dibenzoazo crownether will be

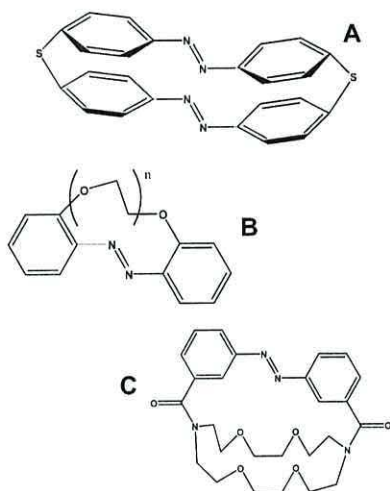


Figure 1.2: A: an azobenzenophane molecule [10]. B: Series of azocrownethers, O₂N₂ when $n=1$ [11] C: Azocrownether of ref. [12] where the torsional photoisomerisation pathway was believed to be sterically hindered

referred to by the abbreviation **O₂N₂**, which is a reference to the number of Oxygen and Nitrogen atoms present in the 10-membered ring formed by the ether linkage. A primary objective of this thesis is to gain insight into the mechanism of photoisomerisation of O₂N₂ by exploring the relevant sections of its ground and first excited electronic state potential energy surfaces (PES). Recent theoretical investigations into other rotation-restricted azobenzenes have raised doubts about the extent of this torsional restriction [14, 15].

Laser Control of Chemical Reactions

Since the advent of the laser in the 1950s, chemists have pondered about the viability of their use for controlling chemical reactions. Initial attempts at realising product selectivity in a photoinduced chemical reaction centred around the capability of generating light fields of very high intensity and small spectral bandwidth [16], and hence the possibility of exciting a particular

bond in a molecule discriminately leading to selective dissociation. This approach had limited success since the rate of intramolecular energy transfer is almost always considerably greater than the rate of dissociation.

The development of ultrafast laser pulses (of less than picosecond duration) in the 1980s led to the possibility of influencing the dynamics of a molecule in ‘real time’, since successive applications of laser pulses could be achieved on a similar time scale of a molecular vibration. Tannor and Rice [17, 18] illustrated the possibility of controlling the location of a time dependent wavepacket on a ground state PES, via mediation of an excited state PES, and hence potentially controlling the geometry of a molecule. A natural extension to the Tannor/Rice control scheme is *optimal control theory* (OCT) [19, 20, 21], where the laser pulses are refined by an optimisation algorithm to increase the yield of this control. OCT has been applied to find optimal shapes of pulses for a wide range of quantum mechanical systems [16]. Its application range from small molecular systems, such as control over the photo-fragmentation of a diatomic [22], to considerably more complex molecular systems, such as the selective preparation of enantiomers [23], and the control of the cyclohexadiene \leftrightarrow hexatriene photoreaction [26].

Laser Control of Azo-compounds

Recent theoretical and experimental investigations into the photoisomerisation of azobenzene suggest that the torsional mechanism is favoured [3, 24, 25]. In particular, it is generally accepted that a conical intersection exists at a C-N-N-C dihedral angle of 90° between the ground electronic state S_0 and the first excited electronic state S_1 . The conical intersection provides a funnel for radiationless transition between the electronic states, and, due to its location, a ratio of *cis/trans* product is observed. Control of a reaction in the vicinity of a conical intersection is limited by the unpredictable nature of the ratio of products they yield. The decision to investigate the dynamics of O₂N₂ photoisomerisation was strongly motivated by the possibility that the torsional mechanism was blocked (hence avoiding the conical intersection), leading to the possibility of greater control along the inversion isomerisation

coordinate.

Structure of Thesis

Chapter 2 provides a discussion of the general background theory relevant to this thesis. In Chapter 3, the details of the computational methods utilised in this thesis are presented, including details of electronic structure theory and the evolution of time dependent wavepackets on a two electronic state system.

In Chapter 4, details of the aforementioned Tannor/Rice control scheme and OCT are presented. Density functional theory (DFT) is used to generate potential energy functions along the torsion and inversion isomerisation coordinates of azomethane, and the Tannor/Rice control scheme and OCT are implemented on this system in the wavepacket framework discussed in Chapter 3. Azomethane undergoes similar photoisomerisation to azobenzene and its derivatives when in a condensed phase [27], and since it is a considerably less complex system, the computational effort required for such an investigation is dramatically reduced. Calculations on azomethane were carried out to demonstrate the computational methods used in this thesis, and to help predict the feasibility of a similar investigation on the larger O₂N₂ system.

Chapters 2-4 serves to assemble the necessary quantum methodologies required for the application of quantum control and OCT on the photoisomerisation dynamics of O₂N₂ in Chapter 5. The DFT potential energy functions along the photoisomerisation coordinates of O₂N₂ are presented in Chapter 5, followed by a discussion of the most likely route of isomerisation and comparison with experimental data. Again, OCT is applied in the wavepacket formalism of quantum mechanics to find the pulses which maximise the yield of the photoisomerisation, followed by a discussion of the experimental relevance of the generated pulses and avenues for further research.

Finally, Chapter 6 investigates the effects of environmental dissipation on the possible control of isomerisation type model systems. In this work,

Caldeira-Leggett [28] dissipation is implemented on these systems in Wigner phase space, hence a novel optimal control formalism is presented for systems in Wigner phase space.

Bibliography

- [1] G. Zimmerman, L.-Y. Chow, U.-J. Paik, *J. Am. Chem. Soc.*, (1958), **80**, 3528.
- [2] P. Bortolus, S. Monti, *J. Phys. Chem.*, (1979), **83**, 648.
- [3] E. W.-G. Diau, *J. Phys. Chem. A*, (2004), **108**, 950.
- [4] T. Fujino, T. Tahara, *J. Chem. Phys.*, (2000), **104**, 4203.
- [5] T. Fujino, S. Y. Arzhantsev, T. Tahara, *J. Phys. Chem.*, (2001), **105**, 8123.
- [6] P. Cattaneo, M. Persico, *Phys. Chem. Chem. Phys.*, (1999), **1**, 4739.
- [7] Y.-C. Lu, C.-W. Chang, E. W.-G. Diau, *J. Chin. Chem. Soc.*, (2002), **49**, 693.
- [8] C.-W. Chang, Y.-C. Lu, T.-T. Wang, E. W.-G. Diau, *J. Am. Chem. Soc.*, (2004), **126**, 10109.
- [9] C. Ciminelli, G. Granucci, M. Persico, *Chem.-Eur. J.*, (2004), **10**, 2327.
- [10] H. Rau, E. Lüeddecke, *J. Am. Chem. Soc.*, (1982), **104**, 1616.
- [11] K. Janus, J. Sworakowski, *J. Phys. Chem. B*, (2005), **109**, 93.
- [12] H. Rau, *Journal of Photochemistry*, (1984), **26**, 221.
- [13] K. Janus, J. Sworakowski, E. Luboch, *Chem. Phys.*, (2002), **285**, 47.
- [14] C. Ciminelli, G. Granucci, M. Persico, *J. Chem. Phys.*, (2005), **123**, 174317.
- [15] C. Nonnenburg, H. Gaub, I. Frank, *Chem. Phys. Chem.*, (2006), **7**, 1455.
- [16] S. A. Rice, M. Zhao, *Optimal Control of Molecular Dynamics*, Wiley, (2000).

- [17] D. J. Tannor and S. A. Rice, *J. Chem. Phys.*, (1985), **83**, 5013.
- [18] D. J. Tannor, R. Kosloff and S. A. Rice, *J. Chem. Phys.*, (1986), **85**, 5805.
- [19] S. Shi, A. Woody, H. Rabitz, *J. Chem. Phys.*, (1988), **88**, 6870.
- [20] R. Kosloff, S. A. Rice, P. Gaspard, S. Tersigni, D. J. Tannor, *Chem. Phys.*, (1989), **139**, 201.
- [21] S. Shi and H. Rabitz, *Comp. Phys. Commun.*, (1991), **63**, 71.
- [22] B. Amstrup, R.J. Carlson, A. Matro, S. A. Rice, *J. Phys. Chem.*, (1991), **95**, 8019.
- [23] D Kröner, *Theory of Selective Preparation of Enantiomers*, Ph.D Thesis, Freie Universität Berlin, (2003)
- [24] T. Ishikawa, T. Noro, T. Shoda, *J. Chem. Phys.*, (2001), **115**, 7503.
- [25] C.-W. Chang, Y.-C. Lu, T.-T. Wang, E. W.-G. Diau, *J. Am. Chem. Soc.*, (2004), **126**, 10109.
- [26] D. Geppert, R. de Vivie-Riedle, *Chem. Phys. Lett.*, (2005), **404**, 289.
- [27] E. W.-G. Diau, A. H. Zewail, *Chem. Phys. Chem.*, (2003), **4**, 445.
- [28] A. O. Caldeira, A. J. Leggett, *Phys. Rev. Lett.*, (1981), **46**, 211.

Chapter 2

Background Theory

2.1 Separation of Electronic and Nuclear Motion

The energy of a general molecular system is characterised by the full molecular Hamiltonian

$$H = \sum_i -\frac{\hbar^2 P_{e,i}^2}{2m} + \sum_{j>i} \frac{e^2}{|r_i - r_j|} + \sum_i -\frac{\hbar^2 P_{N,i}^2}{2M_i} + \sum_{j>i} \frac{Z_i Z_j e^2}{|R_i - R_j|} - \sum_i j \frac{Z_j e^2}{|r_i - R_j|} \quad (2.1)$$

or in shorthand form

$$\hat{H}(r, R) = T_e(r) + V_{ee}(r) + T_n(R) + V_{nn}(R) + V_{en}(r, R) \quad (2.2)$$

where the terms T_n and T_e represent the kinetic energy of the nuclei and electrons respectively, and V_{nn} , V_{ee} , and V_{en} represent the potential energy arising from nuclei-nuclei repulsion, electron-electron repulsion, and nuclei-electron attraction respectively. The terms R and r represent nuclear and electronic coordinates respectively. Eq. (2.2) contains the term $V_{en}(r, R)$ which couples the motion of the electrons to the motion of the nuclei, hence the molecular wavefunction, $\Psi(r, R)$, is prevented from being written as a

simple product of nuclear and electronic terms

$$\Psi(r, R) = \Phi(R)\phi(r) \quad (2.3)$$

where $\Phi(R)$ and $\phi(r)$ represents the nuclear and electronic wavefunctions respectively.

For an instantaneous nuclear configuration R the nuclear-nuclear repulsion term $V_{nn}(R)$ in Eq. (2.2) is constant, and the nuclear kinetic energy term $T_n(R) = 0$, hence the *Electronic* Time Independent Schrödinger Equation (TISE) is given by

$$\begin{aligned} H_e \phi_i(r; R) &= \epsilon_i(R) \phi_i(r; R) \\ [T_e(r) + V_{ee}(r) + V_{en}(r; R)] \phi_i(r; R) &= \epsilon_i(R) \phi_i(r; R) \end{aligned} \quad (2.4)$$

where $\phi_i(r, R)$ and $\epsilon_i(R)$ are the *adiabatic* electronic eigenfunctions and eigenenergies for the set of fixed nuclear coordinates R respectively. The adiabatic electronic eigenfunctions form a complete orthonormal set, hence the total wavefunction may be expanded in this eigenbasis

$$\Psi(r, R) = \sum_i \Phi_i(R) \phi_i(r; R) \quad (2.5)$$

where the expansion coefficients $\Phi_i(R)$ are the nuclear wavefunctions in the adiabatic representation.

Inserting Eq. (2.5) into the full TISE, multiplying from the left by a particular electronic wavefunction ϕ_j , and then integrating over the electronic coordinates gives

$$[T_n(R) + \epsilon_j(R)] \Phi_j(R) + \sum_i \Lambda_{ji} \Phi_i(R) = E \Phi_j(R) \quad (2.6)$$

where E is the total energy and $\Lambda_{ji}(R)$ is the non-adiabatic coupling matrix that involves derivatives of Φ with respect to R . The matrix elements of Λ are non-trivial to compute, however, in the adiabatic approximation the off-diagonal elements $j \neq i$ are discarded. The justification for this ap-

proximation is based on the fact that the nuclear mass is much greater than the electron mass, therefore the nuclei move much slower than the electrons. Consequently the nuclear motions are small and therefore the derivatives with respect to R are also small. Within the adiabatic approximation the nuclear TISE has the form

$$[T_n + \epsilon_j(R) + \Lambda_{jj}(R)] \Phi_j(R) = E \Phi_j(R). \quad (2.7)$$

A further simplification can be made by implementing the Born-Oppenheimer approximation where Λ_{jj} are also discarded by the justification that the small massed electrons adjust instantaneously to any motion of the nuclei and

$$[T_n + \epsilon_j(R)] \Phi_j(R) = E \Phi_j(R) \quad (2.8)$$

where $\epsilon_j(R)$ is the potential energy of the molecule for the nuclear coordinates R . By solving the electronic TISE for a range of values of R , an effective potential energy function $V(R)$ under which the nuclei move can be generated.

2.2 The Time Dependent Wavepacket

When the potential energy function V has been determined along a particular displacement coordinate q (e.g. bond length, normal mode of vibration), the nuclear Time *Dependent* Schrödinger Equation (TDSE) may be written in one dimension as

$$i\hbar \frac{\partial}{\partial t} \Psi(q, t) = [T_n(q) + V(q)] \Psi(q, t) \quad (2.9)$$

where $\Psi(q, t)$ is the wavefunction describing the motion along the nuclear coordinate q . The square of the wavefunction, $|\Psi(q, t)|^2$, represents the time dependent probability distribution of finding the molecule at a particular nuclear coordinate q .

While the nuclear eigenfunctions $\Phi(q)$ yielded by Eq. (2.8) are also particular solutions of the TDSE, their probability density distributions do not

vary with time, hence there is still effectively no discernable motion. However, any linear combination of a particular solution of the TDSE is also a particular solution of the TDSE. Therefore, $\Psi(q, t)$ may be expanded in the eigenbasis of the TISE Hamiltonian

$$\Psi(q, t) = \sum_{n=0}^{\infty} c_n \Phi_n(q) e^{-\frac{i}{\hbar} E_n t} \quad (2.10)$$

where Φ_n and E_n are the n 'th eigenfunction and eigenenergy of the system Hamiltonian, and c_n is the n 'th complex valued expansion coefficient given by the overlap integral

$$c_n = \int \Phi_n(q) \Psi(q, t_0) dq. \quad (2.11)$$

It can be shown that such a superposition of eigenstates has a time dependent probability density distribution, $|\Psi(q, t)|^2$, by considering the simple superposition of 2 eigenstates

$$\Psi(q, t) = c_1 \Phi_1(q) e^{-\frac{i}{\hbar} E_1 t} + c_2 \Phi_2(q) e^{-\frac{i}{\hbar} E_2 t} \quad (2.12)$$

which has the probability density distribution

$$\begin{aligned} |\Psi(q, t)|^2 &= |c_1|^2 \left(\Phi_1(q) e^{-\frac{i}{\hbar} E_1 t} \right)^* \Phi_1(q) e^{-\frac{i}{\hbar} E_1 t} + \\ &\quad |c_2|^2 \left(\Phi_2(q) e^{-\frac{i}{\hbar} E_2 t} \right)^* \Phi_2(q) e^{-\frac{i}{\hbar} E_2 t} + \\ &\quad 2\Re\{c_1^* c_2 \Phi_1^*(q) \Phi_2(q) e^{-i \frac{(E_2 - E_1)t}{\hbar}}\} \\ &= |c_1|^2 |\Phi_1(q)|^2 + |c_2|^2 |\Phi_2(q)|^2 + \\ &\quad 2\Re\{c_1^* c_2 \Phi_1^*(q) \Phi_2(q) e^{-i \frac{(E_2 - E_1)t}{\hbar}}\} \end{aligned} \quad (2.13)$$

where the symbol \Re refers to the real part and A^* is the complex conjugate of A . The third term in Eq. (2.13), which arises from the interference between the different eigenstates, is the only term which depends on time.

Fig. 2.2 illustrates the first 5 eigenstates of a harmonic oscillator potential. It is also illustrated how a superposition of such eigenstates may, via

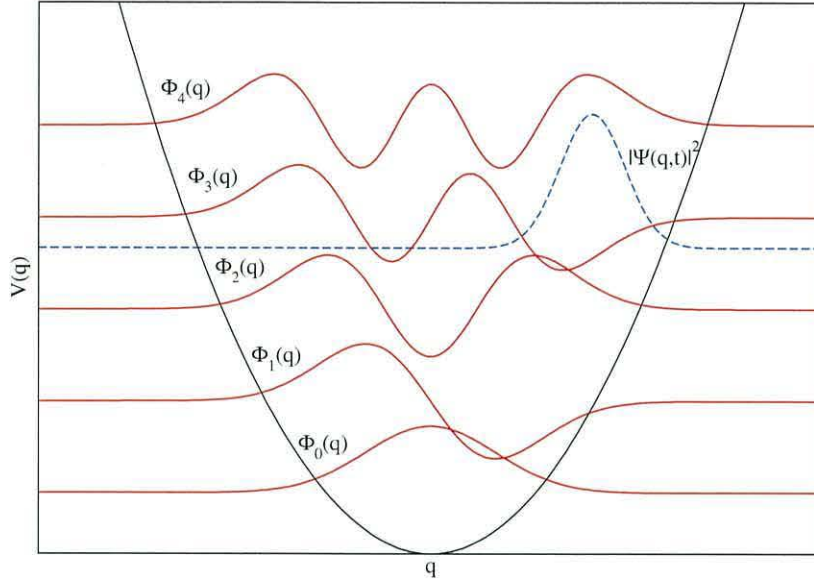


Figure 2.1: Illustration of the 5 lowest energy eigenstates (red) of a harmonic oscillator potential function, together with the probability density distribution of a localised wavepacket (blue) generated by their superposition.

an appropriate choice of expansion coefficients c_n , generate a localised time dependent wavepacket $\Psi(q, t)$. The more localised a wavepacket, the less uncertainty there is in the location of the particle it represents. This is a manifestation of the Heisenberg uncertainty principle

$$\Delta p \Delta x \geq \frac{\hbar}{2} \quad (2.14)$$

where the standard deviation of the momentum p of the particle multiplied by the standard deviation of its location is never less than $\frac{\hbar}{2}$. Since the generation of a localised wavepacket requires contributions from a large number of eigenstates, the decrease in uncertainty of location is coupled with an increase in uncertainty of the momentum and energy of the system.

The time dependent wavepacket (or state function) $\Psi(q, t)$ provides a complete description of the state of an individual system in terms of the specific internal coordinate q . This inherently statistical description relates

to the probabilities of all outcomes of all conceivable measurements that can be performed on the system [1]. Each experimental observable of the system is associated with a Hermitian operator \hat{A} [2], and the expectation value of an experimental observable for a normalised wavefunction¹ is given by

$$\langle A \rangle = \int_{-\infty}^{\infty} \Psi^*(q, t) \hat{A} \Psi(q, t) dq = \left\langle \Psi(q, t) \left| \hat{A} \right| \Psi(q, t) \right\rangle \quad (2.15)$$

where Dirac notation has been introduced². The Hermitian operator associated with the energy of a system is of course the Hamiltonian operator, hence the expectation value of the total energy of a wavepacket, at a particular time t , is given by

$$\langle E_T \rangle = \left\langle \Psi(q, t) \left| \hat{H} \right| \Psi(q, t) \right\rangle. \quad (2.16)$$

For a system which may be described by an adequate approximation of its Hamiltonian Eq. (2.1), the time dependent wavepacket model provides an intuitive picture of molecular motion. In contrast to the time independent picture, the model of a localised wavepacket propagating on a potential energy surface resembles the dynamics of the intuitive classical picture of a particle over small time scales, while still encompassing strictly quantum mechanical phenomena, such as tunnelling through a potential barrier [3].

2.3 Coupling of Electronic States via External Electromagnetic Field

Photochemical reactions, such as photoisomerisations, involve multiple electronic states, hence the time dependent Schrödinger equation for a manifold

¹often in the literature, the terms *wavefunction* and *wavepacket* are interchangeable.

²in simplified terms the Dirac Bra-Ket notation is a shorthand for representing the inner product of wavefunctions. The wavefunction ψ is represented by the ket vector $|\psi\rangle$ and its complex conjugate by $\langle\psi|$. Combining the two produces the BraKet $\langle\psi|\psi\rangle = \int \psi^* \psi$ which, when applied to large expressions, is convenient compared to expressing the cumbersome integrals.

of j electronic states may be written in matrix form

$$i\hbar \frac{\partial}{\partial t} \begin{bmatrix} \Psi_1(t) \\ \Psi_2(t) \\ \vdots \\ \Psi_j(t) \end{bmatrix} = \begin{bmatrix} T_1 + V_1 & V_{12} & \cdots & V_{nj} \\ V_{21} & T_2 + V_2 & \cdots & V_{nj} \\ \vdots & \vdots & \ddots & \vdots \\ V_{j1} & V_{j2} & \cdots & T_j + V_j \end{bmatrix} \begin{bmatrix} \Psi_1(t) \\ \Psi_2(t) \\ \vdots \\ \Psi_j(t) \end{bmatrix} \quad (2.17)$$

where T_j is the nuclear kinetic energy operator acting on the portion of the wavepacket occupying electronic state j , and V_j is the adiabatic potential energy function of electronic state j . The off diagonal elements V_{jk} represent the coupling between electronic states j and k - essentially they govern the transfer of population between the electronic states j and k .

Atomic and molecular systems absorb and emit electromagnetic radiation in discrete packets of energy corresponding to the difference in energy between different states of the system. As well as electronic states, a molecular system consists also of vibrational and rotational states, and hence a vast combination of transitions are possible for polyatomic molecules.

The interaction between electromagnetic radiation and molecules generally occurs between the electric field component of the radiation and the electric dipole moment of the molecule which is given by

$$\mu = \sum_i q_i r_i \quad (2.18)$$

where q_i and r_i are the charge and position vector of the i 'th particle in the molecule. The intensity of a transition is proportional to the square of the transition dipole moment R which, for a vibronic³ transition, is given by [4]

$$R_{ev} = \langle \psi'_{ev} | \mu | \psi''_{ev} \rangle \quad (2.19)$$

where ψ'_{ev} and ψ''_{ev} are the higher and lower energy vibronic states involved in the transition. If the nuclei are regarded as stationary compared to the fast moving electrons (Born-Oppenheimer approximation), then the vibronic

³*vibronic* transitions refer to electronic transitions accompanied by a vibrational transition

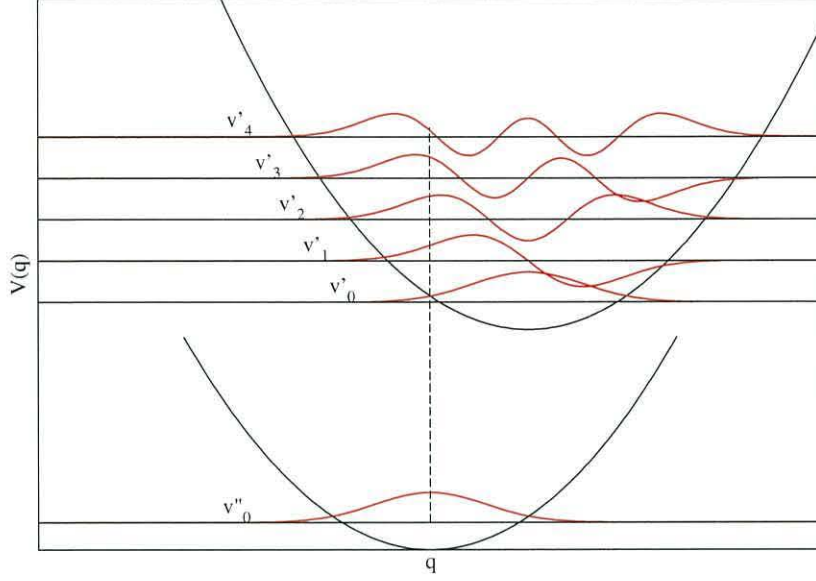


Figure 2.2: Ground and first excited electronic states of a model system where both states have harmonic potentials. The dashed line indicates the position at which we should look for maximum overlap between v''_0 and v'_1

state ψ_{ev} may be factorised into $\psi_e\psi_v$. The vibronic transition dipole moment may now be expressed as

$$R_{ev} = R_e \langle \psi'_v | \psi''_v \rangle \quad (2.20)$$

where

$$R_e = \langle \psi'_e | \mu | \psi''_e \rangle. \quad (2.21)$$

The overlap integral $\langle \psi'_v | \psi''_v \rangle$ is a measure of the degree of overlap between vibrational wavefunctions. Its square is known as the Franck-Condon factor, and is useful in determining the relative intensities of vibronic transitions. Fig. 2.2 illustrates the ground and first excited state of a model system consisting of harmonic potentials. The electrons are assumed to adjust instantaneously during the transition, while the nuclei remain at the nuclear coordinate q at the instant of the transition, hence Franck-Condon transitions are also referred to as vertical transitions. For the model system depicted in Fig. 2.2 the vibronic transition with the largest Franck-Condon factor is the

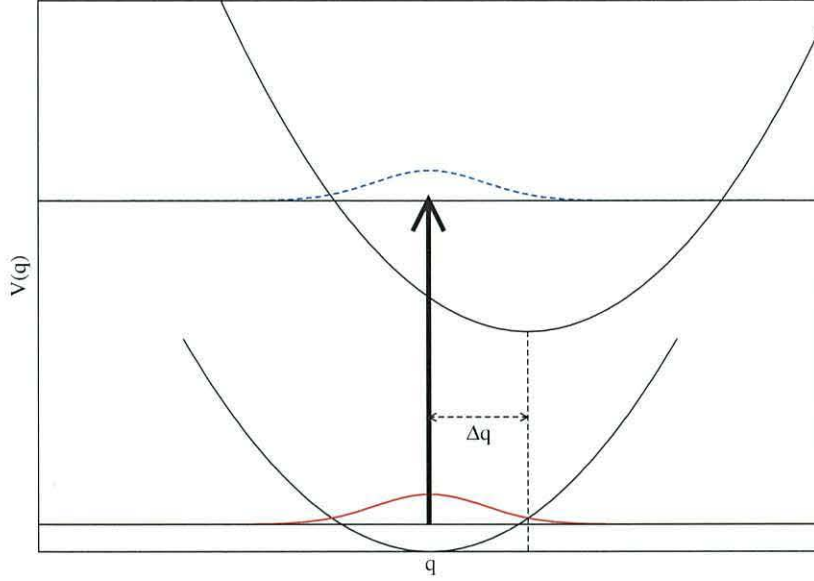


Figure 2.3: vertical transition of a vibrational eigenstate of the ground electronic state to produce a superposition of eigenstates on the excited electronic state i.e. a time dependent wavepacket.

$v_0'' \rightarrow v_2'$ transition.

Fig. 2.2 represents the Franck-Condon (F-C) principle within the time independent picture. When the Hamiltonian for a molecular system is accurately approximated, then it's possible to envision how the F-C principle may be utilised to predict the vibrational structure of electronic spectra.

Vertical transitions are also applicable in the time dependent wavepacket model. Fig. 2.3 illustrates a F-C transition from the ground vibrational state of the ground electronic state into the first excited electronic state. In this instance, the nuclear wavefunction maintains its ground state form in the excited state, again due to the instantaneousness of electronic transitions compared to nuclear motion. The wavefunction is now a superposition of the vibrational eigenstates of the excited electronic state

$$\Psi(t) = \sum_{n=0}^{\infty} c_n \psi_n^{v'} e^{-\frac{i}{\hbar} E_n t} \quad (2.22)$$

where the complex expansion coefficients are determined by the vibrational overlap integral $c_n = \langle \psi'_{nv} | \psi''_v \rangle$.

Another result of a vertical transition is the dependency of the energy of the excited wavepacket on the displacement Δq of the excited state minimum compared to the ground state minimum. For large Δq , the superposition wavepacket will comprise of more significant contributions from higher energy eigenfunctions than for systems with small Δq . As such, high energy wavepackets are often referred to as ‘vibrationally hot’ wavepackets.

The coupling of electronic states by electromagnetic radiation may be included in the TDSE

$$i\hbar \frac{\partial}{\partial t} \begin{bmatrix} \Psi_i(t) \\ \Psi_j(t) \end{bmatrix} = \begin{bmatrix} T_i + V_i & \mu_{ij}\epsilon(t) \\ \mu_{ji}\epsilon(t) & T_j + V_j \end{bmatrix} \begin{bmatrix} \Psi_i(t) \\ \Psi_j(t) \end{bmatrix} \quad (2.23)$$

where μ_{ij} is the electronic transition dipole moment between the states i and j , and $\epsilon(t)$ is the electric field component of the electromagnetic radiation interacting with the molecule. For simplicity, the matrix Hamiltonian has been truncated to include only two electronic states, and the coupling terms V_{ij} have been neglected by the assumption that the states are energetically well separated.

To generate a localised wavepacket on an excited electronic state (Fig. 2.3), the complete transition must be accomplished in an ultrashort time scale. Components of the wavepacket will start to evolve on the excited state surface instantly after transition, hence the longer the duration of the transition the more de-localised the wavepacket will become. Localisation is achieved by the application of ultrashort femtosecond laser pulses, which have a lifetime an order of magnitude less than the vibrational period of a typical molecular mode.

2.4 Non-Adiabatic Transitions

The non-adiabatic coupling matrix Λ_{ji} introduced in Eq. (2.6) initiates transitions between electronic states, the origin of these transitions lie in the coupling between the nuclear and electronic motions (often called *vibronic coupling* in the literature.). By definition, these transitions are unaccounted for within the adiabatic approximation.

For electronic states which are widely separated in energy, the adiabatic and Born-Oppenheimer approximations are assumed to hold. These approximations are justified since the matrix elements $\Lambda_{j\neq i}$ only become non-negligible when the electronic states are close in energy [6]. When electronic states are close in energy, radiationless transitions can occur as a result of this vibronic coupling, i.e. electronic transitions occur without absorbing/emitting electromagnetic radiation (this purely internal occurrence is often referred to as *internal conversion* in the literature.). Close lying electronic states are a regular occurrence in polyatomic molecules with a large number of degrees of freedom.

A particularly efficient pathway for non-adiabatic radiationless transitions occurs at conical intersections between electronic potential energy surfaces (PESs). Conical intersections are degenerate points on separate adiabatic electronic PESs, they are characterised by a single degenerate point where the local topology of the surfaces may be described by a cone. Conical intersections (also known as photochemical funnels) provide an ultrafast pathway for interstate crossing on the femtosecond timescale, and have been shown to play a crucial role in the photochemistry of many polyatomic molecules including azobenzene [5]. For a more detailed account of conical intersections, and their inclusion in dynamical calculations, the reader is referred to Refs. [6, 7].

The external laser control of the dynamics through a conical intersection is limited. This limitation arises from the fact that external *active* control (Chapter 4.1.2) is lost whenever an electronic transition occurs via an internal mechanism. While it is possible to manipulate the product ratios which occur after passage through a conical intersection to some degree [8], the influence of

the external electromagnetic field is lost *during* the non-adiabatic transition [9]. In this work non-adiabatic effects are ignored. However, as discussed in Chapter 5.3, the influence of a conical intersection is scope for further work.

Bibliography

- [1] P. R. Holland, *The Quantum Theory of Motion, An Account of the de Broglie-Bohm Causal Interpretation of Quantum Mechanics*, Cambridge University Press, (1993).
- [2] D. J. Tannor, *Introduction to Quantum Mechanics, A Time-Dependent Perspective*, University Science Books, (2007).
- [3] K. H. Hughes, J. N. Macdonald, *Phys. Chem. Chem. Phys.*, (2000), **2**, 4267.
- [4] J. M. Hollas, *Modern Spectroscopy*, second edition, Wiley, (1995).
- [5] E. W.-G. Diau, *J. Phys. Chem. A*, (2004), **108**, 950.
- [6] G. A. Worth, L. S. Cederbaum, *Annu. Rev. Phys. Chem.*, (2004), **55**, 127.
- [7] D. R. Yarkony, *Acc. Chem. Res.*, (1998), **31**, 511.
- [8] H. Tamura, S. Nanbu, T. Ishida, H. Nakamura, *J. Chem. Phys.*, (2006), **125**, 034307.
- [9] D. Geppert, R. de Vivie-Riedle, *Chem. Phys. Lett.*, (2005), **404**, 289.

Chapter 3

Computational Molecular Dynamics

Chapter 2 introduced the Born-Oppenheimer approximation as a means of separating the nuclear and electronic motions of a molecule, and thus splitting the molecular Schrödinger equation into more manageable parts. By first solving the *electronic* time independent Schrödinger equation (TISE), Eq. (3.1), for different conformations along a rotational/vibrational mode, or an intrinsic reaction coordinate, a potential energy function, $(V_{nn}(R)+\epsilon_i(R))$, for that particular motion is produced. Subsequent calculation of the *nuclear* time independent Schrödinger equation, Eq. (3.2), yields the nuclear eigenfunctions $\Phi_{ik}(R)$ and eigenenergies E_{ik} for the system, which are then used as the basis for a time dependent picture of the system, characterised by the time *dependent* Schrödinger equation (TDSE) Eq. (3.3).

$$[T_e(r) + V_{ee}(r) + V_{en}(r, R)]\phi_i(r, R) = \epsilon_i(R)\phi_i(r, R) \quad (3.1)$$

$$[T_n(R) + V_{nn}(R) + \epsilon_i(R)]\Phi_{ik}(R) = E_{ik}\Phi_{ik}(R) \quad (3.2)$$

$$i\hbar\frac{\partial\Psi}{\partial t} = \hat{H}\Psi \quad (3.3)$$

In the present chapter, details of the computational programs used throughout the thesis are presented. Section 3.1 outlines the *ab initio* methodology behind calculating the relevant potential energy functions. Section 3.2 gives details of the Fourier Grid Hamiltonian Method (FGH) used to solve the *nuclear* time independent Schrödinger equation, and outlines the computational details of the wavepacket methodology described in Chapter 2.2. Finally, Section 3.3 demonstrates the wavepacket methodology on a model two electronic state system consisting of 2 harmonic oscillator potentials.

3.1 *Ab Initio* Calculations

Although the Born-Oppenheimer approximation allows a separation of the electronic motion from the nuclear motion, solving the electronic Schrödinger equation is still a formidable task without the implementation of further approximations. The field of electronic structure theory is an immense area of research, and great inroads have been made into developing accurate and/or rapid computational approaches for solving the electronic TISE. There are two main classes of electronic structure methods:

- 1) Semi-empirical methods utilise observed experimental parameters to simplify the computation, where an approximate form of the Schrödinger equation is then solved. Different semi-empirical methods are characterised by which experimental parameters are used.

- 2) *Ab initio* methods rely on the first principles of quantum mechanics, as well as a limited number of physical constants i.e. Planck's constant, the speed of light, and the mass and charges of electrons and nuclei. Different *ab initio* methods are characterised by their different set of approximations.

Electronic structure packages such as *Gaussian* [1] have proved an invaluable tool to the computational chemist in recent decades. The *Gaussian* suite of programs is based on Hartree-Fock theory.

3.1.1 Hartree-Fock theory

The 1st approximation of Hartree-Fock theory is to decompose the electronic molecular wavefunction Ψ into a combination of orthonormal molecular orbitals ϕ_1, ϕ_2, \dots . A simple way of combining these molecular orbitals would be to form their Hartree product

$$\Psi(r) = \phi_1(r_1)\phi_2(r_2)\dots\phi_n(r_n) \quad (3.4)$$

However, such a wavefunction is inconsistent with the antisymmetry requirement of fermions such as electrons. Furthermore, the intrinsic angular momentum of the electron has not been taken into account, as such the hartree product is combined with a spin function ($\alpha(i)$ for spin $+\frac{1}{2}$, and $\beta(i)$ for spin $-\frac{1}{2}$) e.g. $\phi_1(r_1)\alpha(1)$.

Using this notation, the total electronic wavefunction $\Psi(r)$ can be represented in terms of a *Slater determinant*, where $\frac{n}{2}$ molecular orbitals are defined for a system of n electrons

$$\Psi(r) = (n!)^{-\frac{1}{2}} \begin{vmatrix} \phi_1(r_1)\alpha(1) & \phi_1(r_1)\beta(1) & \cdots & \phi_{\frac{n}{2}}(r_1)\beta(1) \\ \phi_1(r_2)\alpha(2) & \phi_1(r_2)\beta(2) & \cdots & \phi_{\frac{n}{2}}(r_2)\beta(2) \\ \vdots & \vdots & \vdots & \vdots \\ \phi_1(r_n)\alpha(n) & \phi_1(r_n)\beta(n) & \cdots & \phi_{\frac{n}{2}}(r_n)\beta(n) \end{vmatrix} \quad (3.5)$$

where each row represents all the possible assignments of electron n to all orbital-spin combinations. Interchanging any two rows of the determinant changes the sign of $\Psi(r)$, hence the antisymmetry of fermions is accounted for. Another convenient feature of the Slater determinant is that the Pauli Exclusion Principle is automatically encapsulated, if two electrons with the same spin occupy the same spatial orbital, then the wavefunction Eq. (3.5) vanishes.

Basis Sets

The spatial part of the spin-orbitals, $\phi_i(r_i)$, are unknown in practice, hence the 2nd approximation of Hartree-Fock theory is to define ϕ_i as a linear

combination of 1-electron basis functions χ_μ

$$\phi_i = \sum_{\mu=1}^N c_{\mu i} \chi_\mu \quad (3.6)$$

where $c_{\mu i}$ are the molecular orbital expansion coefficients, χ_μ is an arbitrary basis function and ϕ_i an arbitrary molecular orbital.

The *Gaussian* electronic structure programs uses Gaussian type orbitals (gto) as basis functions

$$g(\alpha, r) = cx^n y^m z^l e^{-\alpha r^2} \quad (3.7)$$

where c is a normalisation constant and α is the radial extent of the Gaussian type orbital g . In its basic form each *primitive* Gaussian g may be considered as an approximation for an atomic orbital e.g. for s and p_y atomic orbitals

$$g_s(\alpha, r) = \left(\frac{2\alpha}{\pi}\right)^{\frac{3}{4}} e^{-\alpha r^2} \quad (3.8)$$

$$g_{p_y}(\alpha, r) = \left(\frac{128\alpha^5}{\pi^3}\right)^{\frac{1}{4}} y e^{-\alpha r^2} \quad (3.9)$$

However, linear combinations of these Gaussian functions are used to produce the actual basis functions of the calculation, and these are expressed as

$$\chi_\mu = \sum_p d_{\mu p} g_p \quad (3.10)$$

where $d_{\mu p}$ are fixed constants within a given basis set, and χ_μ are called contracted Gaussians. Hence the expansion for an approximate molecular orbital is given by

$$\phi_i = \sum_{\mu} c_{\mu i} \chi_\mu = \sum_{\mu} c_{\mu i} \left(\sum_p d_{\mu p} g_p \right) \quad (3.11)$$

Obviously, the larger the number of primitive Gaussians per contraction, as well as the actual number of contractions, the more accurate the calculation.

However, the calculations get computationally more expensive with increasing number of Gaussians, hence compromises must be made in the quest for accuracy and efficiency.

Roothan-Hall Equations

To calculate the molecular orbitals ϕ_i , the challenge within H-F theory is to find the molecular orbital expansion coefficients $c_{\mu i}$. The variational principle states that for the ground state of any antisymmetric normalised function of the electronic coordinates Ξ , the expectation value for the energy corresponding to Ξ will always be greater than the the energy for the molecular system

$$E(\Xi) > E(\Psi); \Xi \neq \Psi \quad (3.12)$$

An iterative procedure may be utilised which minimises $E(\Xi)$ up to a certain specified criterion, which in turn yields a function of electronic coordinates Ξ as close as possible to the exact wavefunction Ψ .

The *Roothan-Hall* equations [2] may be represented in matrix form as

$$FC = SC\epsilon \quad (3.13)$$

where ϵ is a diagonal matrix of orbital energies, each of its elements, ϵ_i , corresponds to the one-electron orbital energy of molecular orbital ϕ_i . The matrix C contains the coefficients $c_{\mu i}$ of the basis functions χ_μ .

S is the overlap matrix containing the elements

$$S_{ij} = \langle \phi_i(r) | \phi_j(r) \rangle \quad (3.14)$$

and finally, F is the Fock matrix which contains the elements

$$F_{ij} = \langle \phi_i(r) | \hat{F}(r) | \phi_j(r) \rangle \quad (3.15)$$

The term $\hat{F}(r)$ is the Fock operator, which is analogous to the Hamiltonian

operator in the Schrödinger equation and has the form

$$\hat{F}(r) = \hat{h}(r_i) + \hat{V}^{HF} = \hat{h}(r_i) + \sum_{j=1}^{N_{el}} (2\hat{J}_j(r_i) - \hat{K}_j(r_i)) \quad (3.16)$$

where $\hat{h}(r_i)$ is the single particle operator

$$\hat{h}(r_i) = \frac{P_i^2}{2m_e} - \sum_{n=1}^{N_{nuc}} \frac{Z_n e}{(r_i - R_n)} \quad (3.17)$$

which describes the effect of the field of the nuclear configuration R on a single electron. \hat{V}^{HF} is called the Hartree-Fock potential and consists of the coulomb operator \hat{J}_j and the exchange operator \hat{K}_j . \hat{V}^{HF} describes the interaction of the electron with all the other electrons.

Since the elements of the Fock matrix F depend on the coefficients $c_{\mu i}$ contained in the matrix C , Eq. (3.13) must be solved iteratively. An initial guess of C^0 is required which is used to calculate the first Fock matrix F^0 . The eigenvalue problem is then solved via the diagonalisation of F^0 .

As a solution of the diagonalisation, a new coefficient matrix C^1 is obtained, which in turn is used to construct a new Fock matrix F^1 . This procedure is then repeated until a convergence criterion is reached.

The coefficients $c_{\mu i}$ of Eq. (3.11) provide, for the given basis set, the optimal spin-orbitals $\phi_i(r_i)\alpha/\beta(i)$, and their corresponding eigenenergies $\epsilon(i)$. The Slater determinant Eq. (3.5) is then constructed using the spin-orbitals from which the total electronic energy, E_{el} , may be obtained via the expectation value of the total electronic operator \hat{H}_{el} .

3.1.2 Configuration Interaction

While Hartree-Fock theory includes the major correlation effects between pairs of electrons of the same spin, termed the *exchange correlation*, the motions of electrons of opposite spin remain uncorrelated. As a result, the electrons are further apart than predicted by Hartree-Fock theory.

Any electronic structure method which attempts to deal with this inadequacy is called an *electron correlation* method. There are numerous ways of incorporating electron correlation into the calculation, for example Møller Plesset perturbation theory [3] and configuration interaction ¹.

The N_{el} electron system within the configuration interaction method is made up of a linear combination of N_{el} particle wavefunctions i.e. Slater determinants

$$\Psi = b_0\psi_0 + \sum_{n>0} b_n\psi_n \quad (3.18)$$

where ψ_0 is the Hartree-Fock Slater determinant, and $\psi_{n>0}$ are the Slater determinants for different electronic configurations e.g. the electronic configuration of a single electron excitation, where a single virtual orbital replaces an occupied orbital in the determinant. The superposition coefficients b_n are derived variationally.

If all possible electronic configurations are taken into account, then a full Configuration Interaction is reached, which (when an infinite basis set is considered) approaches the exact solution for the non-relativistic time independent Schrödinger equation within the Born-Oppenheimer approximation. However, such a calculation is computationally un-feasible for all but the smallest systems, hence the CI is usually truncated after a few determinants.

An alternative to the truncated CI method is the Complete Active Space Self Consistent Field (CASSCF) approach. Here, the so-called *active space* is treated with a full CI, whereas the rest of the molecule is left in a fixed configuration. CASSCF has been used extensively in a number of studies, and is widely used in the treatment of excited states [4, 5, 6]. However CASSCF requires a suitable choice of active space, and therefore this approach requires an experienced computational chemist.

3.1.3 Density Functional Theory

Another electronic structure method which takes account of electron correlation is Density Functional Theory (DFT), although it invokes a different

¹both are referred to as post Hartree-Fock methods

approach to the methods based on Hartree-Fock theory discussed previously.

Hohenberg and Kohn discovered that there is enough information in the charge density, $\rho(r)$, of a molecule to calculate molecular energies [2]. It is stated in the first Hohenberg-Kohn (H-K) theorem that the complete molecular potential V is a functional of the charge density $\rho(r)$, since the molecular potential is embedded in the molecular Hamiltonian \hat{H} , the full many particle ground state Ψ_g of the molecule is also a functional of $\rho(r)$. Even though the H-K theorem demonstrated the existence of an unique functional which determines the ground state energy and density exactly, it does not provide a form for this functional.

Therefore the goal of DFT calculations is to minimise the charge density functional

$$E_{el}(\rho_{el}) = \langle \Psi_{el}(\rho_{el}) | \hat{H} | \Psi_{el}(\rho_{el}) \rangle \quad (3.19)$$

which depends on the electron density, which is a sum of non-interacting single electron functions

$$\rho_{el}(r) = \sum_i^{N_{el}} |\psi_i(r)|^2 \quad (3.20)$$

where $\psi_i(r)$ is the spatial part of a single electron function. Analogous to the H-F equations Section 3.1.1, a series of single particle equations, called the Kohn-Sham equations, are solved iteratively. The main difference is that the H-F potential \hat{V}^{HF} , in Eq. (3.16), is replaced by the potential

$$\hat{V}^{KS}(r) = \int \frac{\rho(r')}{|r - r'|} dr' + \hat{V}_{xc} \quad (3.21)$$

where the first term accounts for the coulomb electron-electron interaction and \hat{V}_{xc} is the potential due to the non-classical exchange correlation energy E_{xc} ,

$$\hat{V}_{xc} = \frac{\delta E_{xc}}{\delta \rho} \quad (3.22)$$

these equations may easily be extended to unrestricted calculations, i.e. $\rho_\alpha \neq \rho_\beta$ where α and β denote spin up and spin down respectively. Such

calculations require two Kohn-Sham potentials \hat{V}_σ^{KS} , one for each spin σ , with \hat{V}_σ^{XC} the functional derivative of E_{XC} with respect to the spin density ρ_σ .

The total DFT electronic energy is a sum of energy functionals

$$E_{DFT} = E_T(\rho) + E_V(\rho) + E_J(\rho) + E_{xc}(\rho) \quad (3.23)$$

where E_T is the kinetic energy of the non-interacting electrons, E_V is the energy resulting from the electron-nuclei interactions, and E_J results from electron-electron repulsion.

In the variational computation of E_{DFT} a trial charge density ρ is used to obtain an initial ground state energy E_{DFT}^0 , which serves as an upper limit for the exact ground state energy which would be provided if the exact functional was used,

$$E_{DFT} \geq E_{EXACT} \quad (3.24)$$

Crucially the accuracy of the DFT method depends on the quality of the functionals used for the exchange correlation energy E_{xc} .

Usually, the exchange correlation functional is partitioned into two parts

$$E_{xc}(\rho) = E_x(\rho) + E_c(\rho) \quad (3.25)$$

where $E_x(\rho)$ and $E_c(\rho)$ are called the *exchange* and *correlation* functionals respectively. Physically, they correspond to the same-spin and mixed-spin interactions of electrons respectively ².

The simplest approximation of the *exchange* functional is the Local Density Approximation (LDA)

$$E_x^{LDA} = -\frac{3}{2} \left(\frac{3}{4\pi} \right)^{1/3} \int \rho^{4/3} d^3r \quad (3.26)$$

where ρ is a function of r . In this form, the functional reproduces the exchange energy of a *uniform electron gas*.

²it is the latter which is not treated by H-F theory

Obviously, an atomic/molecular density is not uniform, even on a local scale, hence an improvement on the basic LDA model can be made with the addition of a non-uniform *gradient correction* term [7]

$$E_x = E_x^{LDA} - b \sum_{\sigma} \int \rho_{\sigma}^{4/3} \frac{x_{\sigma}^2}{(1 + 6bx_{\sigma} \sinh^{-1} x_{\sigma})} d^3r \quad (3.27)$$

where x_{σ} is a non-uniformity parameter defined by

$$x_{\sigma} = \frac{|\nabla \rho_{\sigma}|}{\rho_{\sigma}^{4/3}} \quad (3.28)$$

and b is a constant with value 0.0042 a.u., determined by a fit to exact H-F exchange energies of the noble gases He to Rn.

H-F theory also includes an electron exchange term as part of its formulation, hence a further improvement on the LDA exchange functional with gradient correction has been achieved with its inclusion in the formulation [8]

$$E_{hybrid}^x = a_{HF} E_{HF}^x + a_{DFT} E_{DFT}^x \quad (3.29)$$

forming a H-F DFT *hybrid* functional, where the a 's determine the amount each constituent functional contributes to the complete functional.

Similarly, the *correlation* functionals, E^c , may be approximated by a combination of local and gradient corrected functionals, and hence the complete *exchange-correlation* functional may have the form

$$E_{B3LYP}^{xc} = E_{LDA}^x + a_0(E_{HF}^x - E_{LDA}^x) + a_x \Delta E_{B88}^x + E_{VWN3}^c + a_c(E_{LYP}^c - E_{VWN3}^c) \quad (3.30)$$

here E_{VWN3}^c is a local *correlation* functional with E_{LYP}^c [9] as its gradient correction. E_{B88}^x is the gradient correction for the *exchange* functional and E_{HF}^x is the Hartree-Fock electron exchange term. a_0 , a_x , and a_c are semi-empirical parameters which were determined by Becke [8] via an appropriate fit to experimental data.

For a more detailed discussion on exchange-correlation functionals consult [2, 7, 8] and references therein.

TD-DFT

For the calculation of electronic excited states, Time Dependent-Density Functional Theory (TD-DFT) is applied [11, 10]. TD-DFT is a time dependent extension to the Hohenberg-Kohn-Sham DFT outlined above, where a system initially in its ground stationary state is subject to a time dependent perturbation $v(r, t)$. The system is now subject to the time dependent Kohn-Sham equation [10]

$$\left[-\frac{1}{2}\nabla^2 + v(r, t) + \int \frac{\rho(r', t)}{|\rho - \rho'|} + \hat{V}_{xc}(r, t) \right] \Psi_j(r, t) = i \frac{\partial}{\partial t} \Psi_j(r, t) \quad (3.31)$$

where the time dependent charge density is again given by the sum of the orbital densities

$$\rho(r, t) = \sum_i^{N_{el}} |\psi_i(r)|^2 \quad (3.32)$$

The adiabatic approximation is applied to allow the use of the same exchange-correlation potential as in the time-independent theory

$$\hat{V}_{xc}(r, t) \simeq \frac{\delta E_{xc}}{\delta \rho^t(r)} \quad (3.33)$$

except that it is calculated with respect to the charge density at time t , $\rho^t(r)$.

From the response of the charge density to the time dependent electric field (perturbation), the response of the dipole moment may also be determined. This response is described by the dynamic polarisability $\alpha(\omega)$, from which the excitation energies ω_i may be determined via the sum-over-states relation

$$\alpha(\omega) = \sum_i \frac{f_i}{\omega_i^2 - \omega^2} \quad (3.34)$$

f_i are the residues which determine the corresponding oscillator strengths.

3.2 Wavepacket Dynamics

The time dependent wavepacket $\Psi(t)$ was introduced in Chapter 2.2 as a quantum dynamical model suitable to describe the nuclear motion of a molecule. The wavepacket may be constructed as a linear combination of the eigenfunctions of the system

$$\Psi(t) = \sum_{n=0}^{\infty} c_n \psi_n e^{-\frac{i}{\hbar} E_n t} \quad (3.35)$$

where the time dependency is governed by the oscillating complex exponential. If the solution of the nuclear time independent Schrödinger (TISE) equation is known

$$H\psi_n = E_n\psi_n \quad (3.36)$$

the dynamics of the wavepacket is straight forward. However, solving the TISE is often computationally demanding, and often requires the computation of complicated integrals.

An alternative method of wavepacket propagation is via a grid-based representation. In a grid based approach the continuous wavepacket is represented in terms of a set of time evolving complex amplitudes at a set of discrete grid points

$$\Psi(x) = \sum_{n=1}^N b_n \phi_n(x_i) \quad i = 1, \dots, N \quad (3.37)$$

where the basis functions $\phi_n(x_i)$ may be interpreted as a set of i delta functions located at the discrete grid points x_i , and b_n are the basis functions' complex amplitudes.

Numerous numerical methods exist to propagate grid based wavepackets. A similar strategy to Eq. (3.35) may be employed if the operation of $H\Psi$ on a grid of points x_i is first evaluated. The approximate grid based eigenfunctions and eigenenergies determined in this way may then be used to propagate the wavepacket, however the computationally demanding task of diagonalisation of the H matrix persists.

Alternatively, the time dependent Schrödinger equation Eq. (3.3) may be rearranged and integrated to yield

$$\Psi(t) = e^{-\frac{H}{\hbar}t}\Psi(0) \quad (3.38)$$

where the wavepacket at time t may be determined from the initial wavepacket $\Psi(0)$ through the application of the evolution operator $e^{-\frac{H}{\hbar}t}$. In the following sections the numerical methods used in this work to evaluate the initial wavepacket $\Psi(0)$, and the action of the evolution operator upon it, are outlined.

3.2.1 Defining the Initial Wavepacket

In the numerical evaluation of Eq. (3.38), the first task is to assign an initial form for the wavepacket $\Psi(0)$. Primarily in this thesis, ground state potentials of the type illustrated in Fig. 3.1 are investigated, where each minimum of the asymmetric double well corresponds to a different geometrical isomer. The initial wavepacket for an isomerisation simulation should therefore be localised in a particular well.

Ground state potentials involving the inversion or torsion around a double bond are typified by a high and wide energy barrier between its minima, and hence the overlap between eigenstates of different wells are negligible to non-existent. A suitable initial $\Psi(t)$ may therefore be the lowest vibrational eigenfunction in a particular well, that is obtained by solving the TISE Eq. (3.36). The TISE is usually solved by setting up the Hamiltonian matrix H_{ij} which has the elements

$$H_{ij} = \langle \phi_i | \hat{T} | \phi_j \rangle + \langle \phi_i | \hat{V} | \phi_j \rangle \quad (3.39)$$

where \hat{T} and \hat{V} are the kinetic and potential energy operators respectively, and $\phi_{i/j}$ compose an orthonormal set of basis functions. The eigenfunctions ψ_n and eigenenergies E_n of the system are then determined by diagonalising the matrix H_{ij} to determine the coefficients of the basis functions. Various numerical methods exist to set up H_{ij} [12, 13, 14], each one is defined by the

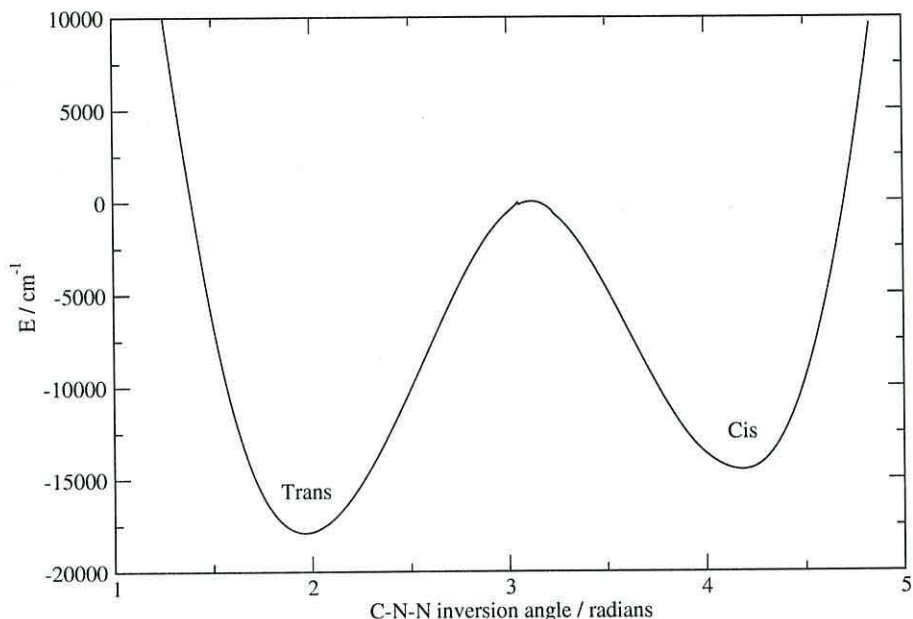


Figure 3.1: Ground electronic state potential of the trans-cis isomerisation of azomethane via inversion of N-N-C bond.

type of basis ϕ_n used and the way the operators \hat{T} and \hat{V} are implemented. The method adopted in this work is the Fourier grid Hamiltonian (FGH) method [15], which conveniently evaluates the eigenfunctions on a discrete set of points ready for inclusion in the following wavepacket calculations.

Fourier Grid Hamiltonian

The operators \hat{T} and \hat{V} have different characteristics, whereas the action of \hat{V} may be easily be implemented by a simple multiplication in coordinate space, the action of \hat{T} involves derivatives with respect to the coordinate space and may be tedious to calculate. The action of \hat{T} may be easier to implement in a different representation, and in the FGH method [15] this is achieved in a momentum space representation.

Two basis sets are therefore required to represent the Hamiltonian on a subspace of the Hilbert space. The principle representation is the coordinate representation

$$\hat{x} |x\rangle = x |x\rangle \quad (3.40)$$

where $\hat{\mathbf{x}}$ is the position operator and $|x\rangle$ are its eigenvectors. The second basis set representation comprises of

$$\hat{\mathbf{p}}|k\rangle = k\hbar|k\rangle \quad (3.41)$$

where $\hat{\mathbf{p}}$ is the momentum operator and $|k\rangle$ its eigenvectors. Both representations satisfy the completeness relations of an orthonormal basis set

$$\langle x|x'\rangle = \delta(x - x') \quad (3.42)$$

$$\hat{\mathbf{I}}_x = \int_{-\infty}^{\infty} dx |x\rangle \langle x| \quad (3.43)$$

and

$$\langle k|k'\rangle = \delta(k - k') \quad (3.44)$$

$$\hat{\mathbf{I}}_k = \int_{-\infty}^{\infty} dk |k\rangle \langle k|. \quad (3.45)$$

The basis vectors of both representations are related by

$$\langle k|x\rangle = \frac{1}{\sqrt{2\pi}} e^{-ikx}. \quad (3.46)$$

In coordinate space the Hamiltonian matrix elements may be written as

$$\langle x|\hat{\mathbf{H}}|x'\rangle = \langle x|\hat{\mathbf{T}}|x'\rangle + V(x)\delta(x - x') \quad (3.47)$$

where the second term arises from the diagonal nature of the potential operator in coordinate space. By inserting the identity relation, Eq. (3.45), to the right of the kinetic operator in Eq. (3.47), and subsequent use of Eq. (3.46) yields

$$\langle x|\hat{\mathbf{H}}|x'\rangle = \frac{1}{2\pi} \int_{-\infty}^{\infty} e^{ik(x-x')} T_k dk + V(x)\delta(x - x') \quad (3.48)$$

where $T_k = \frac{\hbar^2 k^2}{2m}$.

Numerically, the matrix elements of Eq. (3.48) are calculated on a discretised grid, hence the continuous function x is replaced by an array of N

evenly spaced grid points

$$x_i = i\Delta x \quad i = 1, \dots, N \quad (3.49)$$

where Δx is the grid spacing. The new discrete basis satisfies the orthonormal relations

$$\Delta x \langle x_i | x_j \rangle = \delta_{ij} \quad (3.50)$$

$$\hat{\mathbf{I}} = \sum_{i=1}^N |x_i\rangle \Delta x \langle x_i|. \quad (3.51)$$

The grid length, $L = N\Delta x$, in coordinate space determines the grid spacing in momentum space. L is also the longest wavelength in the momentum representation of the same subspace

$$\Delta k = 2\pi/L.$$

By taking the central value of the momentum grid space to be zero, the momentum grid then spans the values $-\frac{N-1}{2}\Delta k \rightarrow \frac{N-1}{2}\Delta k$ for an odd value of N . The Hamiltonian matrix elements Eq. (3.48) may now be re-written in the discrete representation after some manipulation to yield

$$H_{ij} = \frac{1}{\Delta x} \left(\sum_{l=-(N-1)/2}^{(N-1)/2} \frac{e^{il\Delta 2\pi(i-j)/N}}{N} * T_l + V(x_i)\delta_{ij} \right) \quad (3.52)$$

where

$$T_l = \frac{\hbar^2}{2m} \times (l\Delta k)^2. \quad (3.53)$$

An arbitrary wavefunction $|\phi\rangle$ may be expressed as a linear combination of the grid points

$$|\phi\rangle = \sum_{i=1}^N |x_i\rangle \Delta x \phi_i \quad (3.54)$$

where ϕ_i is the value of the wavefunction at the grid point x_i , and the ex-

pectation value of its energy given by

$$\langle E \rangle = \frac{\langle \phi | \hat{\mathbf{H}} | \phi \rangle}{\langle \phi | \phi \rangle} = \frac{\sum_{ij} \phi_i^* \Delta x H_{ij} \Delta x \phi_j}{\Delta x \sum_i |\phi_i|^2}. \quad (3.55)$$

The secular determinant may now be set up and the diagonalisation of the Hermitian matrix yields the eigenfunctions ψ_n and eigenvalues E_n of the Hamiltonian within the subspace of the discrete Hilbert space.

The FGH method is known as a pseudo-spectral method³ [12]. Generally, a pseudo-spectral representation allows for easier computation of the matrix elements H_{ij} , at a cost of the requirement of a larger matrix for diagonalisation to achieve comparable accuracy. A pseudo-spectral representation which significantly reduces the number of required grid points is a Discrete Variable Representation (DVR) [16]. In a DVR, the N grid points are the roots of an N 'th order orthogonal polynomial $P_N(x)$ which make up the equivalent spectral basis functions $\phi_n(x) = w(x)P_n(x)$ where $w(x)$ are appropriate weight functions. Utilising the unitary transform which exists between the spectral and pseudo-spectral representations of the DVR, an efficient algorithm may be deduced where the kinetic energy operator is implemented in the more convenient spectral basis, and the potential operator is evaluated in the grid basis $V(x_i)\delta_{ij}$. Of course the evaluation of the nuclear TISE is an area of considerable research, and numerous methods exist to yield the eigenfunctions/values of a Hamiltonian, which include approaches which do not require the diagonalisation of a Hamiltonian matrix such as the Dynamic Fourier Method (DFM) [17]. In the DFM, an initial wavefunction is propagated in imaginary time, where it is allowed to relax to the lowest eigenstate of the Hamiltonian. DFM is related to the FGH method by their implementation of the kinetic energy operator in momentum space.

³where 'spectral' refers to the representation of the reduced Hilbert space \mathcal{H}_N on a conventional basis set of N orthogonal functions, and 'pseudo-spectral' refers to the representation of \mathcal{H}_N on a set of N basis functions localised around particular coordinates x_i .

3.2.2 Wavepacket Propagation

With the initial wavepacket $\Psi(0)$ defined, a suitable time integrator is needed to observe the time dependent dynamics of the molecule

$$\Psi(t) = e^{-i\frac{\hat{H}}{\hbar}t}\Psi(0). \quad (3.56)$$

Various approaches exist for the implementation of the exponential propagator. As with the time independent problem, it is desirable to implement the kinetic energy operator \hat{T} and potential energy operator \hat{V} separately. However they are entangled through the exponential, and since these operators do not commute the separation

$$e^{-i\frac{\hat{H}}{\hbar}t} \neq e^{-i\frac{\hat{T}}{\hbar}t}e^{-i\frac{\hat{V}}{\hbar}t} \quad (3.57)$$

is invalid, with a significant error term. Some approaches expand the exponential operator as a polynomial $e^{-i\frac{\hat{H}}{\hbar}t} \approx \sum_{n=1}^N c_n P_n(\hat{H})$, one example of this approach is the Chebyshev method [19] where the exponential is expanded as a Chebyshev polynomial. In such an approach, the wavepacket for any later time t may be evaluated from the initial wavepacket $\Psi(0)$ with just a single application of the propagator. Alternative approaches to evaluate the action of the evolution operator may involve the approximation

$$e^{-i\frac{\hat{H}}{\hbar}t_f} \approx \sum_{n=1}^N e^{-i\frac{\hat{H}}{\hbar}\Delta t} \quad t_f = N\Delta t \quad (3.58)$$

where the long time propagator is approximated by successive applications of a short time propagator. One advantage of such an approach is the ease of incorporating explicit time dependence to the Hamiltonian, such as the time dependent coupling between electronic states via an external electromagnetic field. This is, of course, with the assumption that Δt is sufficiently small that each small time propagator may be considered, individually, time independent.

Split-Operator Method

Although a number of methods exist for solving the TDSE, the approach adopted in this work was the Split-Operator Method (SOM) [21, 22]. It has been widely used in a number of studies [23, 24, 25], is efficient [27], and the SOM can also readily be extended to incorporate a second electronic state coupled to the first [23, 27].

While the separation of operators Eq. (3.57) involves errors arising from the non-commutation of operators, they may be minimised by adopting a symmetric separation

$$e^{-i\hat{H}\Delta t} = e^{-i(\hat{T}+\hat{V})\Delta t} = e^{-i\Delta t\hat{T}/2}e^{-i\Delta t\hat{V}}e^{-i\Delta t\hat{T}/2} + O(\Delta t)^3 \quad (3.59)$$

which is the central theme of the split-operator method. The last term in the separation is the error term which is proportional to Δt^3 , hence for very short time steps the numerical error is minimal, and has been shown, for sufficiently small time steps, to be numerically equivalent to methods implementing the long time propagator [25].

As discussed for the pseudo-spectral methods in the previous section, the wavepacket in the SOM is represented on a discretised grid in coordinate space x_i , which allows for the implementation of $e^{-i\hat{V}t/\hbar}$ as a simple multiplication in coordinate space. Again, the kinetic energy operator is non-trivial to apply in coordinate space, and therefore an equivalent representation of the wavepacket in momentum space is sought.

The wavepacket $\Psi(x)$ is converted to its momentum representation by a discrete fast Fourier transform (FFT)

$$\Psi_k = \frac{1}{N\sqrt{2\pi}} \sum_{j=1}^N \Psi(x_j) e^{-ikx_j/L} \quad (3.60)$$

where N is the number of grid points and L is the length of the grid. The inverse fast Fourier transform (FFT⁻¹) is implemented to transform the

wavepacket back to coordinate space

$$\Psi_x = \frac{1}{\sqrt{2\pi}} \sum_{i=-N/2-1}^{N/2} \Psi(k_i) e^{ik_i x/L}. \quad (3.61)$$

Since the FFT algorithm allows for a quick and efficient transformation from one representation to the other, a logical algorithm may be deduced to implement the short time propagator of Eq. (3.59), as seen in Fig. 3.2.

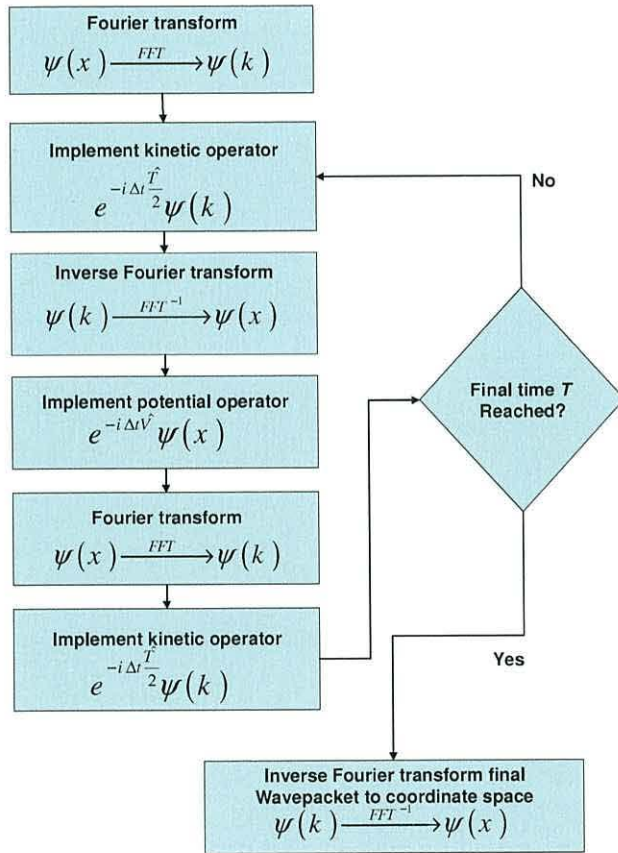


Figure 3.2: Split operator method algorithm.

3.3 Wavepacket Propagation on Two Coupled Electronic States

As detailed in Appendix A, the SOM can be extended to simulate the dynamics of 2 coupled electronic states, where the time dependent Schrödinger equation takes the form

$$i\hbar \frac{\partial}{\partial t} \begin{bmatrix} \Psi_g(t) \\ \Psi_e(t) \end{bmatrix} = \begin{bmatrix} T_g + V_g & V_{ge} \\ V_{eg} & T_e + V_e \end{bmatrix} \begin{bmatrix} \Psi_g(t) \\ \Psi_e(t) \end{bmatrix} \quad (3.62)$$

where the subscripts g and e refer to the ground and excited electronic states respectively, and V_{ge} represents the coupling between the electronic states. As stated in Chapter 2.4, it is assumed in this work that the vibronic coupling between electronic states is zero, and hence V_{ge} represents the action of the electromagnetic field alone

$$V_{ge} = \mu_{ge}\epsilon(t) \quad (3.63)$$

where μ is the transition electric dipole moment⁴ between the ground and excited electronic states, and $\epsilon(t)$ is the time dependent electromagnetic field.

3.3.1 Electronic State Population Transfer on a Model 2 State Harmonic Oscillator Example

To demonstrate the transfer of wavepacket density between different electronic states under the influence of an external electromagnetic field, the Split-Operator numerical method is applied to a model two electronic state system, consisting of two identical harmonic oscillator potentials separated by an energy E , Fig. 3.3.

Each harmonic oscillator has a force constant $k = 0.005$ a.u., and they are separated by an arbitrary energy $E = 0.04556$ hartree. The system is assigned a reduced mass of $M_\mu = 20000$ a.u. and the transition dipole moment is given a constant value of $\mu = 1$ a.u.. The initial wavepacket, $\Psi(0)$, is

⁴ μ is generally coordinate dependent, however the Condon approximation is assumed where $\mu = \text{const.}$

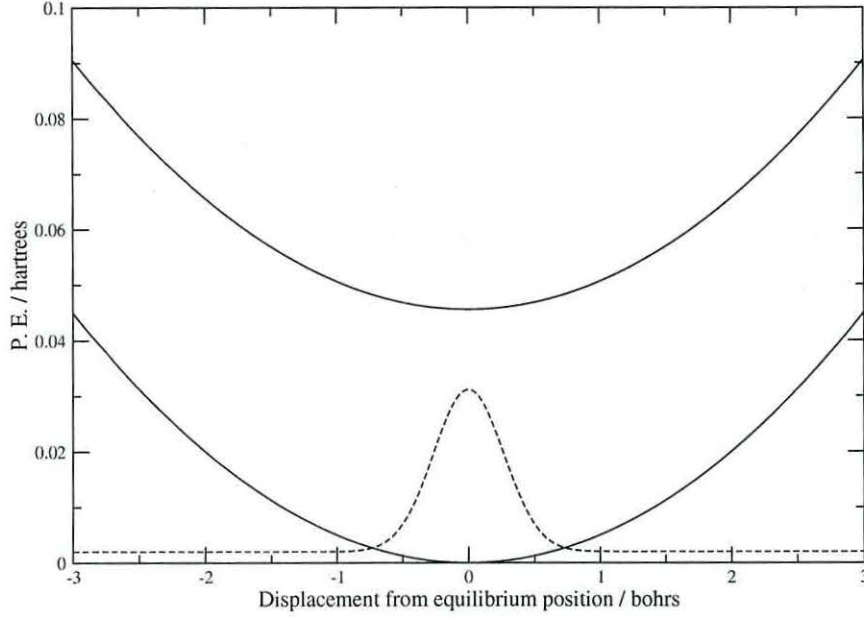


Figure 3.3: Illustration of the model system described in the text. The full lines represent harmonic oscillator potential energy functions, and the broken line represents the lowest energy eigenstate of the ground electronic state (not to scale)

the ground vibrational eigenfunction of the lowest energy harmonic oscillator potential. Consequently, since both potentials are identical except for a separation of E , when wavepacket density is transferred between the states the wavepacket will maintain the profile of the ground state eigenfunction when occupying either potential.

As a simple illustration, the model system will be subject to a continuous wave electromagnetic field $\epsilon(t) = A \cos(\omega t)$, where A is the wave's amplitude and ω its carrier frequency. Fig. 3.4 depicts the results of a series of calculations where ω is varied incrementally between 0.005 hartree and 0.1 hartree, and the resulting maximum amount of wavepacket density transferred to the excited electronic state in each case.

Fig. 3.4 demonstrates that the maximum amount of wavepacket transfer occurs when ω is equal to the energy gap E between the ground vibrational state of both potentials, and this amount falls dramatically as the carrier frequency deviates from E , in complete agreement with the expected Lorentzian

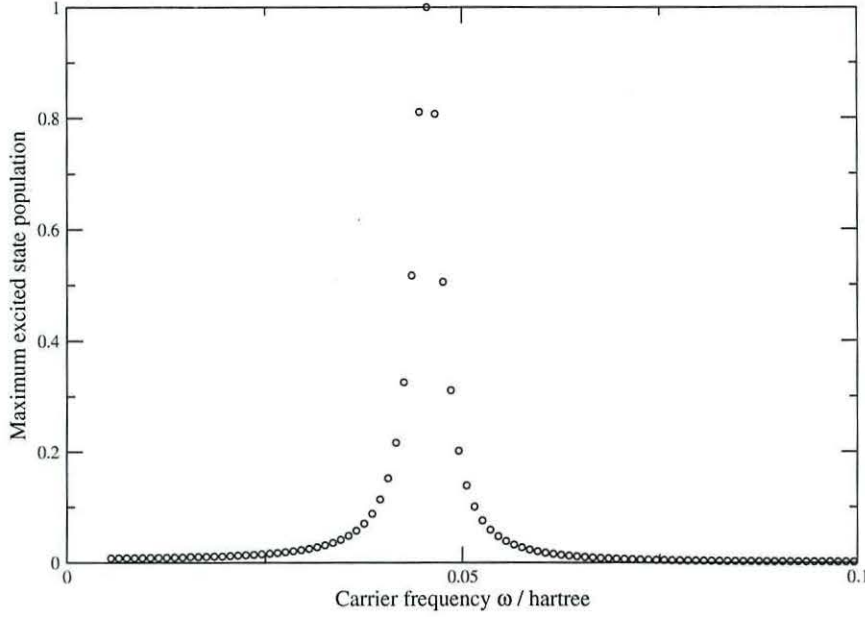


Figure 3.4: Plot of maximum wavepacket transfer against carrier frequency ω . The amplitude remains constant for each calculation, $A = 0.002$ a.u.

distribution [26].

Rabi Frequency

The time dependent populations of the 2 electronic states are depicted in Fig. 3.5 for the system under the influence of a continuous wave with parameters of on resonant frequency $\omega = 0.04556$ a.u. and amplitude $A = 0.002$ a.u. (in black).

The transfer of probability density between the states is complete, and they oscillate according to the relation

$$P_k(t) = \frac{|A\mu_{kl}|^2}{|A\mu_{kl}|^2 + \hbar^2 (\omega_{kl} - \omega)^2} \sin^2 \Omega_R t \quad (3.64)$$

where P_k is the probability amplitude located in state k , ω_{kl} and ω are the resonant frequency of the transition and carrier frequency of the continuous wave respectively. Ω_R is called the Rabi frequency [12] and is the frequency

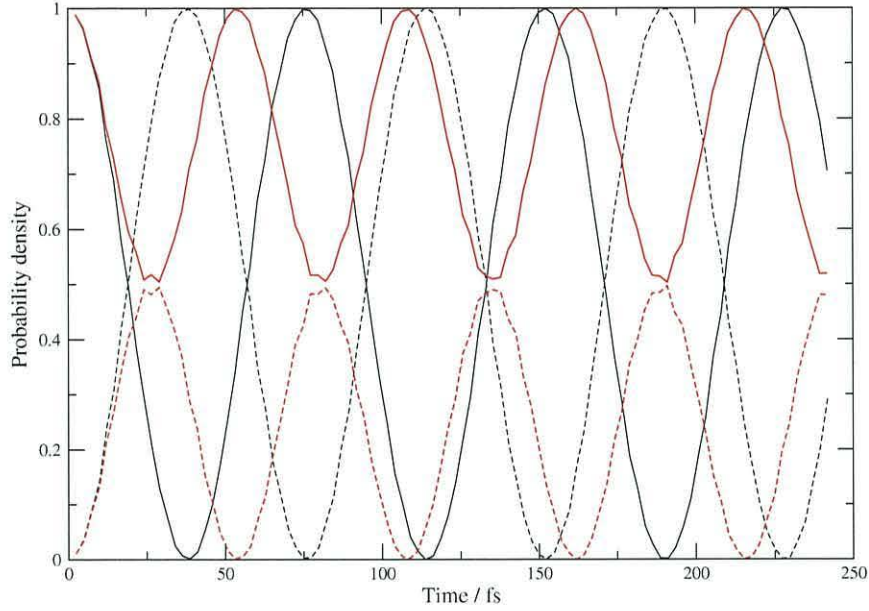


Figure 3.5: Black: ground (full line) and excited (dashed) electronic state population variation under the influence of a continuous wave with parameters $A = 0.002\text{a.u.}$ and $\omega = 0.04556\text{a.u.}$. Red: ground (full line) and excited (dashed) electronic state population variation with off-resonance continuous wave parameters of $A = 0.002\text{a.u.}$ and $\omega = 0.04356\text{a.u.}$.

of oscillation of the probability amplitude given by

$$\Omega_R = \frac{1}{2\hbar} [|A\mu_{kl}|^2 + \hbar^2 (\omega_{kl} - \omega)^2]^{\frac{1}{2}}, \quad (3.65)$$

where it may be deduced that an off resonance carrier frequency yields a larger Rabi frequency as depicted by the red curves in Fig. 3.5, while increasing the amplitude of the continuous wave also increases the frequency of these oscillations, (see Fig. 3.6). Rabi-oscillations may be interpreted in terms of the periodic shift between stimulated absorption and stimulated emission, i.e. as the population of the excited state increases during a cycle the process of stimulated emission becomes more dominant, and vice versa.

Since these oscillations have a regular period, it may be reasoned that population inversion occurs every time a particular amount of radiation has been absorbed. In terms of the *Area Theorem* [28], population inversion is

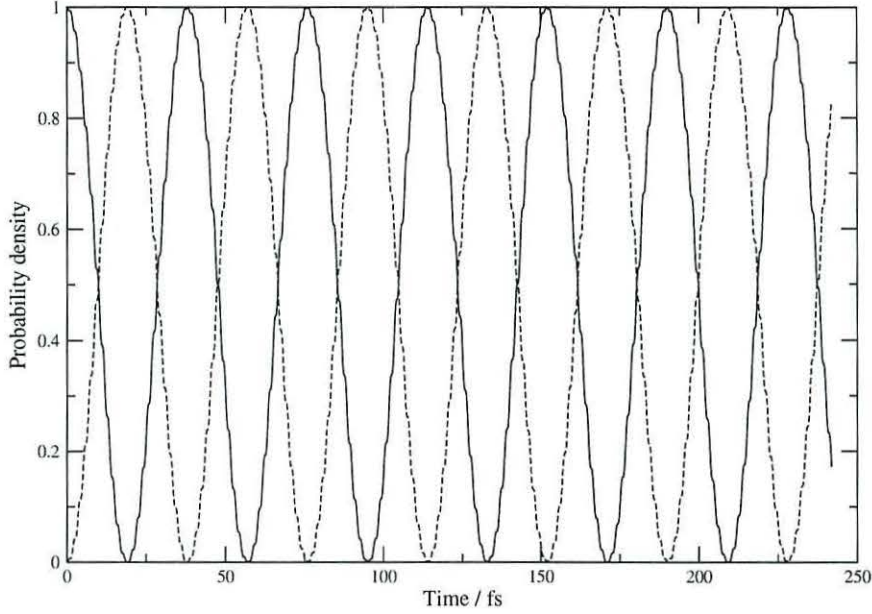


Figure 3.6: Ground (full line) and excited (dashed) electronic state population variation under the influence of a continuous wave with parameters $A = 0.004\text{a.u.}$ and $\omega = 0.04556\text{a.u.}$

achieved when the area under a pulse envelope, $\int_{t_0}^{t_\infty} AS(t)dt$, multiplied by the transition dipole moment μ and divided by \hbar , is equal to an odd integer multiple of π .

$$A_\pi = \frac{\mu}{\hbar} \int_{t_0}^{t_\infty} AS(t)dt = (2N + 1)\pi \quad (3.66)$$

where N is a positive integer.

Π -pulse

In the following example the electric field is damped by a Gaussian

$$S(t) = e^{-\gamma(t-t_0)^2} \quad (3.67)$$

where γ determines the pulse width and t_0 is the position of the pulse maximum. A single pulse with area A_π may be achieved by varying the amplitude (maximum) A and width γ of the pulse appropriately.

Fig. 3.7 illustrates the effect of three different π type pulses on the ground

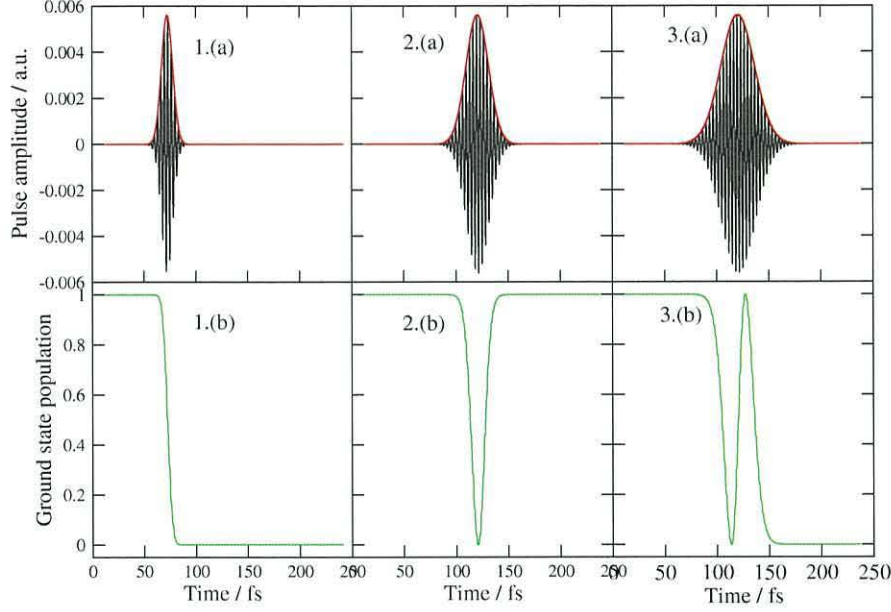


Figure 3.7: Top: Gaussian type pulses (black) and their envelopes (red). Bottom: Corresponding ground electronic state populations (green). Pulse Parameters (in atomic units): 1. $A = 0.005605$, $\omega = 0.04556$, $\gamma = 1 \times 10^{-5}$. 2. $A = 0.005605$, $\omega = 0.04556$, $\gamma = 2.5 \times 10^{-6}$. 3. $A = 0.005605$, $\omega = 0.04556$, $\gamma = 1.111 \times 10^{-6}$

state population of the harmonic oscillator system. Frames 1, 2, and 3 represent pulses with A_π values of 1π , 2π and 3π respectively. It is clear that population inversion occurs every π cycle of pulse that is absorbed by the system, however subtle differences appear when π pulses are applied to systems where the electronic state potentials are not identical, this will become apparent in Chapter 4.

Bibliography

- [1] Gaussian 03, Revision B.04, M. J. Frisch, G. W. Trucks, H. B. Schlegel, G. E. Scuseria, M. A. Robb, J. R. Cheeseman, J. A. Montgomery, Jr., T. Vreven, K. N. Kudin, J. C. Burant, J. M. Millam, S. S. Iyengar, J. Tomasi, V. Barone, B. Mennucci, M. Cossi, G. Scalmani, N. Rega, G. A. Petersson, H. Nakatsuji, M. Hada, M. Ehara, K. Toyota, R. Fukuda, J. Hasegawa, M. Ishida, T. Nakajima, Y. Honda, O. Kitao, H. Nakai, M. Klene, X. Li, J. E. Knox, H. P. Hratchian, J. B. Cross, V. Bakken, C. Adamo, J. Jaramillo, R. Gomperts, R. E. Stratmann, O. Yazyev, A. J. Austin, R. Cammi, C. Pomelli, J. W. Ochterski, P. Y. Ayala, K. Morokuma, G. A. Voth, P. Salvador, J. J. Dannenberg, V. G. Zakrzewski, S. Dapprich, A. D. Daniels, M. C. Strain, O. Farkas, D. K. Malick, A. D. Rabuck, K. Raghavachari, J. B. Foresman, J. V. Ortiz, Q. Cui, A. G. Baboul, S. Clifford, J. Cioslowski, B. B. Stefanov, G. Liu, A. Liashenko, P. Piskorz, I. Komaromi, R. L. Martin, D. J. Fox, T. Keith, M. A. Al-Laham, C. Y. Peng, A. Nanayakkara, M. Challacombe, P. M. W. Gill, B. Johnson, W. Chen, M. W. Wong, C. Gonzalez, and J. A. Pople, Gaussian, Inc., Pittsburgh PA, (2003).
- [2] J. B. Foresman, A. Frisch, *Exploring Chemistry with Electronic Structure Methods*, Gaussian, Inc, (1993).
- [3] W. J. Hehre, L. Radom, P. V. R. Schleyer and J. A. Pople, *Ab Initio Molecular Orbital Theory*, Wiley-Interscience, New York, (1986).
- [4] E. W.-G. Diau, *J. Phys. Chem. A*, (2004), **108**, 950.
- [5] T. Ishikawa, T. Noro, T. Shoda, *J. Chem. Phys.*, (2001), **115**, 7503.
- [6] P. Cattaneo, M. Persico, *Theor. Chem. Acc.*, (1999), **103**, 390.

- [7] A. D. Becke, *J. Chem. Phys.*, (1992), **96**, 2155.
- [8] A. D. Becke, *J. Chem. Phys.*, (1993), **98**, 5648.
- [9] C. T. Lee, W. T. Yang, R. G. Parr, *Phys. Rev. B*, (1988), **37**, 785.
- [10] M. E. Casida, C. Jamorski, K. C. Casida, D. R. Salahub, *J. Chem. Phys.*, (1998), **108**, 4439.
- [11] C. Jamorski, M. E. Casida, D. R. Salahub, *J. Chem. Phys.*, (1996), **104**, 5134.
- [12] D. J. Tannor, *Introduction to Quantum Mechanics: a Time-Dependent Perspective*, University Science Books, (2007).
- [13] W. Yang, A. C. Peet, *Chem. Phys. Lett.*, (1988), **153**, 98.
- [14] V. Szalay, L. Nemes, *Chem. Phys. Lett.*, (1994), **231**, 225.
- [15] C. C. Marston, G. G. Balint-Kurti, *J. Chem. Phys.*, (1989), **91**, 3571.
- [16] J. C. Light, I. P. Hamilton, J. V. Lill, *J. Chem. Phys.*, (1985), **82**, 1400.
- [17] R. Kosloff, H. Tal-Ezer, *Chem. Phys. Lett.*, (1986), **127**, 223.
- [18] C. Cohen-Tannoudji, *Quantum Mechanics*, wiley, (1977).
- [19] H. Tal-Ezer and R. Kosloff, *J. Chem. Phys.*, (1984), **81**, 3967.
- [20] R. Kosloff, *J. Phys. Chem.*, (1998), **92**, 2087.
- [21] M.D. Feit, J.A. Fleck Jr., *J. Chem. Phys.*, (1983), **78**, 301.
- [22] M.D. Feit, J.A. Fleck Jr., *J. Chem. Phys.*, (1984), **80**, 2578.
- [23] J. Broeckhove, B. Feyen, L. Lathouwers, F. Aricks and P. Van Leuven, *Chem. Phys. Lett.*, (1990), **174**, 504.
- [24] X. Ma, D. J. Curry, and D. K. Hoffman, *Chem. Phys. Lett.*, (1993), **208**, 207.
- [25] M. Braun, C. Meier, V. Engel, *Comp. Phys. Comm.*, (1996), **93**, 152.

- [26] J. M. Hollas, *Modern Spectroscopy*, second edition, Wiley, (1995).
- [27] S. A. Rice, M. Zhao. *Optimal Control of Molecular Dynamics*, Wiley, (2000).
- [28] D. Kröner, *Theory of Selective Preparation of Enantiomers*, Ph.D Thesis, Freie Universität Berlin, (2003).

Chapter 4

Quantum Control of Molecular Dynamics

One of the main goals of a chemist is to control the outcome of a chemical reaction. A synthetic chemist will utilise various reagents, catalysts and physical conditions to maximise the product yield. Theoretically, reagents and catalysts alter the landscape of the potential energy surface (PES) of the reactants by increasing the energy barriers along the pathways towards unwanted by-products, and/or decreasing the energy barriers along the pathway towards the desired product/s. Of course, the choice of reagent/catalyst is usually made by intuition and trial and error rather than from a time consuming rigorous theoretical approach. Often, the temperature which the reaction takes place is crucial towards controlling the ratio of products to unwanted by-products. Theoretically, the temperature controls the energy of the system (or wavepacket for an individual molecule), which in turn governs which barriers of the PES it is able to overcome. Of course, the action of temperature is indiscriminate, and the control is superficial since the products are still governed by the landscape of the PES.

While laser technology was developed during the middle of the 20th century, there was optimism that it could be used to excite particular modes of a molecule discriminately leading to selective bond breaking, and thus a more ‘active’ contribution towards the control of the reaction. However, it was

soon discovered that intramolecular energy re-distribution (IVR) occurred at a greater rate than bond dissociation, rendering the initial concept futile. A huge step towards the reality of laser control of chemical reactions was realised with the development of ultrafast laser pulses in the femtosecond time regime in the 1980's. The timescale of these pulses are smaller than the period of oscillation of molecular vibrations, leading to the possibility of bypassing the problem of inconvenient IVR.

In the present chapter, the Tannor-Rice [1, 2] concept of pump and dump laser pulses is introduced, whereby a wavepacket's location on the ground state potential energy surface is manipulated by consecutive population transfer between electronic states. Optimal Control Theory is then outlined which serves as a refinement on the limitations on the basic Tannor-Rice pump/dump theory. Finally, these concepts are demonstrated on the isomerisation of azomethane, which also serves as a precursor for the applicability of such a technique on the photoisomerisation of the larger azobenzene type molecules.

4.1 Laser Control of Wavepacket Dynamics

4.1.1 Tannor and Rice pump/dump Pulses

Chapter 3.3.1 demonstrated the transfer of wavepacket density between electronic states through the application of laser pulses. Such a transition is referred to as a vertical transition, where the electron transfer is effectively instantaneous compared to the response of the nuclei to the transition i.e. the wavepacket will occupy the same nuclear coordinates on the excited state as it did on the ground state at the instant of excitation. This type of transition is referred to as a Franck-Condon vertical transition, and arises from the fact that the mass of a nucleus is very large relative to the mass of an electron.

Tannor, Kosloff and Rice [1, 2] suggested that such vertical transitions may be exploited to utilise an excited electronic state to manipulate the position of the wavepacket on the ground state. The position of the wavepacket

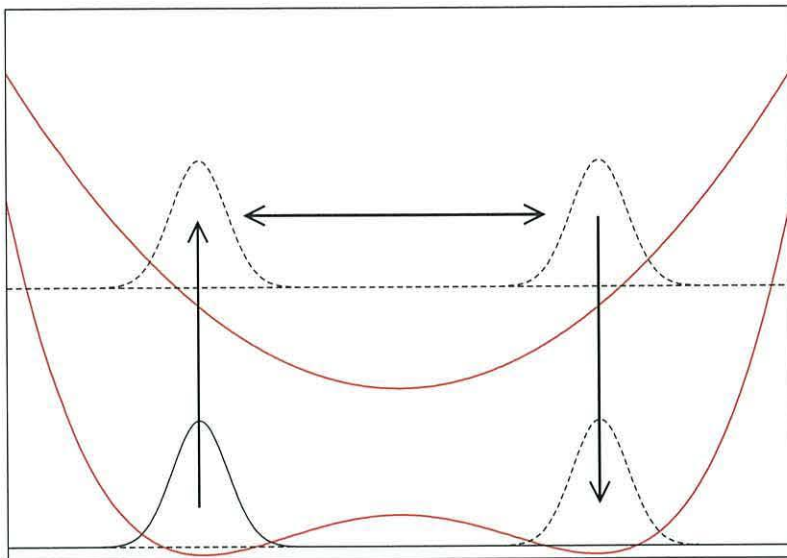


Figure 4.1: Graphic illustration of the Tannor-Rice model. A wavepacket located in a particular well on the ground electronic state PES is moved to another via mediation of the 1st excited electronic state.

on a potential surface corresponds to the nuclear coordinates of the molecule it represents, hence if the position of the wavepacket on a PES can be manipulated then the geometry of the molecule can be controlled, and thus possibly control a reaction such as a change of conformation or a dissociation.

This control of geometry would be accomplished by the application of pump and dump pulses. A first ultrashort laser pulse would vertically transfer the wavepacket from a certain conformation on the ground state, to the same conformation on the excited state. However, in the excited electronic state, the wavepacket will be subject to a different potential surface, and will begin to propagate on this surface. A second ultrashort laser pulse will then be applied to the system when the wavepacket in the excited electronic state occupies a region above the ground state which corresponds to a different conformation. This second pulse will instigate a vertical transition back down to the ground state, effectively ‘dumping’ the wavepacket into its new conformation. This process is illustrated by Fig. 4.1.

Tannor, Kosloff and Rice have shown [1, 2], for some particular forms of the potential energy surface of the first excited state, that windows in

separation time between the two pulses do exist where one set of products is predominant over the other. Indeed, there are some experimental examples in the literature whereby the separation times of appropriate pump/dump pulses alone have led to selectivity in the product of a reaction [3, 4].

4.1.2 Optimal Control Theory

While it has been shown that selectivity is possible for certain reactions using the Tannor-Rice pump/dump scheme, there are obvious limitations. Tannor, Kosloff and Rice demonstrated [2], using various harmonic oscillator examples, that the excited state PES requires specific characteristics to achieve the goal of a localised wavepacket over the product coordinates. They found that, for most circumstances, either the wavepacket never reaches the desired coordinates in significant proportions, or that the wavepacket spreads (de-localises) over a large region of coordinates, effectively destroying the selectivity of the process. These limitations arise from the fact that the Tannor/Rice scheme demonstrates *passive* control as opposed to *active* control. After the application of the pump pulse, the wavepacket propagation is solely determined by the excited state Hamiltonian, as opposed to the outside influence of the experimentalist who guides the pulses, i.e. we are entirely dependent on the form of the excited state PES to deliver the wavepacket localised over the coordinates of the product on the ground state.

Rabitz and co-workers [7] recognised that the problem of generating a pulse sequence to create a wavepacket on a specific region of the PES is an inverse problem¹. Since the initial wavepacket and the target wavepacket is known, only the form of the electric field $\epsilon(t)$ is unknown, and that an iterative procedure based on optimal control (utilised in other theoretical fields prior) may be practical in finding an optimal $\epsilon(t)$. Optimal control theory (OCT) [7, 8, 9, 10, 11] is a variational iterative procedure where an initial guess field $\epsilon^0(t)$ is gradually improved over several cycles.

The aim of optimal control algorithms is to maximise the objective func-

¹also independently recognised by Kosloff, Rice *et al* [8]

tional J

$$J = \langle \Psi(t_f) | P | \Psi(t_f) \rangle \quad (4.1)$$

where $\Psi(t_f)$ is the wavepacket at the time after the pulse sequence is complete, and P is the projection operator which chooses the final location of the wavepacket, i.e. the target state. The maximum value of J corresponds to a perfect overlap between the target target state and the wavepacket at a defined final time t_f . Since $|\Psi(t_f)\rangle$ is a function of the electric field, J is maximised through the variation of the functional form of the pulse $\epsilon(t)$, i.e. $\delta J / \delta \epsilon(t) = 0$

The objective functional may be converted to a constrained functional \bar{J} by applying a constraint on the total energy of the pulse

$$E = \int_{t_0}^{t_f} |\epsilon(t)|^2 dt \quad (4.2)$$

where E is the maximum total energy of the pulse. The constraint Eq. (4.2) has the welcome effect of removing the possibility of unrealistically large amplitude laser pulses, which in practice would ionise the molecule rather than control the reaction. When the above constraint is considered together with the constraints on the Time Dependent Schrödinger Equation, the modified objective functional becomes

$$\bar{J} = \langle \Psi(t_f) | P | \Psi(t_f) \rangle + 2\Re \int_{t_0}^{t_f} dt \left\langle \chi(t) \left| i\hbar \frac{\partial}{\partial t} - \hat{H} \right| \Psi \right\rangle - \lambda \left(\int_{t_0}^{t_f} |\epsilon(t)|^2 dt - E \right) \quad (4.3)$$

where λ is a positive real number serving as the penalty factor on the energy of the laser pulse, and χ is a boundary condition of the time dependent Schrödinger equation given by

$$|\chi(t_f)\rangle = P |\Psi(t_f)\rangle. \quad (4.4)$$

The new goal of optimal control is therefore to maximise the modified objective functional, $\delta \bar{J} = 0$, with respect to variation of all the parameters in

Eq. (4.3) via the equations:

$$i\hbar \frac{\partial}{\partial t} \chi(x, t) = \hat{H} \chi(x, t) \quad (4.5)$$

subject to the boundary condition of Eq. (4.4),

$$i\hbar \frac{\partial}{\partial t} \Psi(x, t) = \hat{H} \Psi(x, t) \quad (4.6)$$

subject to the boundary condition $\Psi(x, 0)$, and finally the laser pulse shape is given by

$$\epsilon(t) = \frac{i}{\lambda} [\langle \chi_e(t) | \mu_{eg} | \Psi_g(t) \rangle - \langle \Psi_e(t) | \mu_{eg} | \chi_g(t) \rangle] = \lambda^{-1} O(t) \quad (4.7)$$

where $O(t)$ is known as the overlap function. The Lagrange multiplier λ is evaluated from the constant energy constraint Eq. (4.2)

$$\lambda = \pm \sqrt{\frac{1}{E} \int_{t_0}^{t_F} dt |O(t)|^2}. \quad (4.8)$$

Since Eq. (4.7) is implicit with respect to the electric field², an iterative procedure is required to find the optimal pulse shape such as the one presented in Fig. 4.2.

The iterative procedure is terminated after a specified convergence criterion is met, usually this is determined when a specific amount of $|\Psi(t_f)\rangle$ has reached the target area of the potential energy surface. The procedure described in Fig. 4.2 may be stabilised if a conjugate gradient line search is introduced [9]. The new field $\epsilon^k(t)$ (for the k 'th iteration) is determined discretely for each time step i (where $t = i\Delta t$) from the field of the previous iteration

$$\epsilon^k(i\Delta t) = \epsilon^{k-1} + \gamma \text{grad} \quad (4.9)$$

where grad is the gradient of the field at time $i\Delta t$, specified by Eq. (4.7), and γ is a multiplicative factor maximised by the appropriate line search³.

²since $|\Psi(t)\rangle$ and $|\chi(t)\rangle$ are dependent on $\epsilon(t)$.

³details on possible line search procedures may be found in [11]

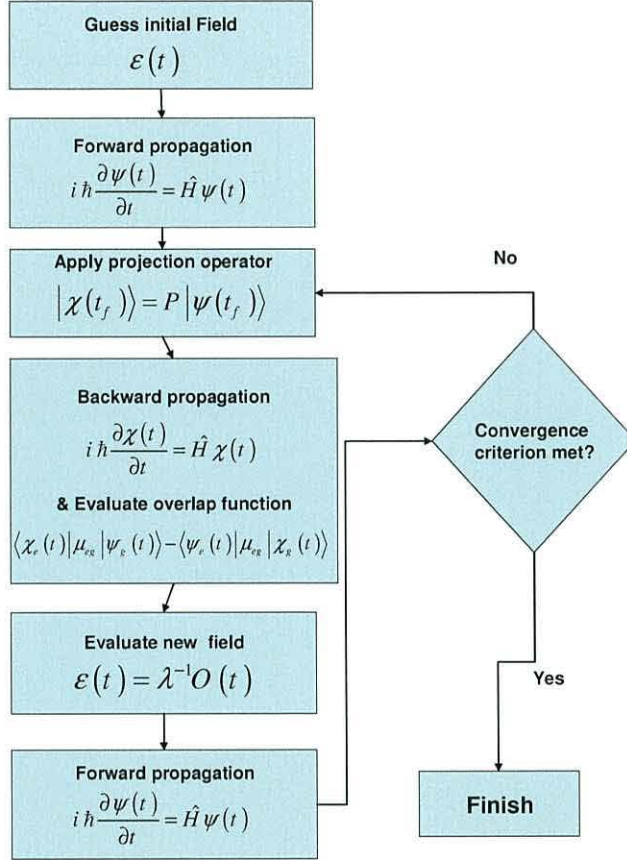


Figure 4.2: Delayed feedback optimal control algorithm [8]

The conjugate gradient method makes small incremental changes to the electric field at each iteration, consequently this approach can be time consuming, especially when a good initial guess is unavailable. The Krotov method [9, 10, 11] is an alternative approach where large changes are made to the electric field at each iteration, resulting in a fast convergence regardless of the quality of the initial guess field.

Krotov method

In the Krotov method the constrained objective functional, Eq. (4.3), is partitioned into time dependent and time independent segments to be maximised separately

$$\bar{J} = G + \int_0^T R(t) dt \quad (4.10)$$

where

$$G = \langle \Psi(t_f) | P | \Psi(t_f) \rangle - (\langle \chi(t) | \Psi(t) \rangle + \text{c.c.}) \Big|_0^{t_f} \quad (4.11)$$

and

$$R(t) = \lambda \epsilon^2(t) + \left(\langle \dot{\chi}(t) | \Psi(t) \rangle + \left\langle \chi(t) \left| \frac{\hat{\mathbf{H}}(\epsilon(t))}{i\hbar} \right| \Psi(t) \right\rangle + \text{c.c.} \right) \quad (4.12)$$

where the dot refers to a time derivative and c.c is the complex conjugate. We now consider the variation of G and R independently [10]

$$\begin{aligned} \Delta G &= G(\Psi(t_f) + \Delta \Psi(t_f)) - G(\Psi(t_f)) \\ &= \langle \Delta \Psi(t_f) | P | \Delta \Psi(t_f) \rangle \geq 0 \end{aligned} \quad (4.13)$$

if $|\chi(t_f)\rangle = P |\Psi(t_f)\rangle$, and

$$\Delta R(t) = -\lambda(\Delta \epsilon)^2 - 2\lambda\epsilon\Delta\epsilon + \frac{2}{\hbar}\Delta\epsilon\Im(\langle \chi(t) | \mu | \Psi(t) + \Delta \Psi(t) \rangle) \quad (4.14)$$

if $|\chi\rangle$ satisfies the TDSE, and where \Im corresponds to the imaginary part. $\Delta R(t)$ takes a maximum positive value when

$$\Delta \epsilon^{k+1}(t) = \Im \left(\left\langle \chi(t) \left| \frac{\mu}{\lambda \hbar} \right| \Psi(t) + \Delta \Psi(t) \right\rangle \right) - \epsilon^k(t). \quad (4.15)$$

The procedure for finding the optimal field via the Krotov methodology is presented in Fig. 4.3. In the step designated by (A), the value of $\epsilon^{k+1}(t=0)$ is calculated from the overlap of $|\chi(t=0)\rangle$ and $|\Psi(t=0)\rangle$, then $\epsilon^{k+1}(t=0)$ is used to propagate $|\Psi(t=0)\rangle$ to $|\Psi(t=1 \times \Delta t)\rangle$ and is repeated for $i = 1, \dots, N$, which serves as a means of immediate feedback in contrast to the delayed feedback of the conjugate gradient method outlined in the previous

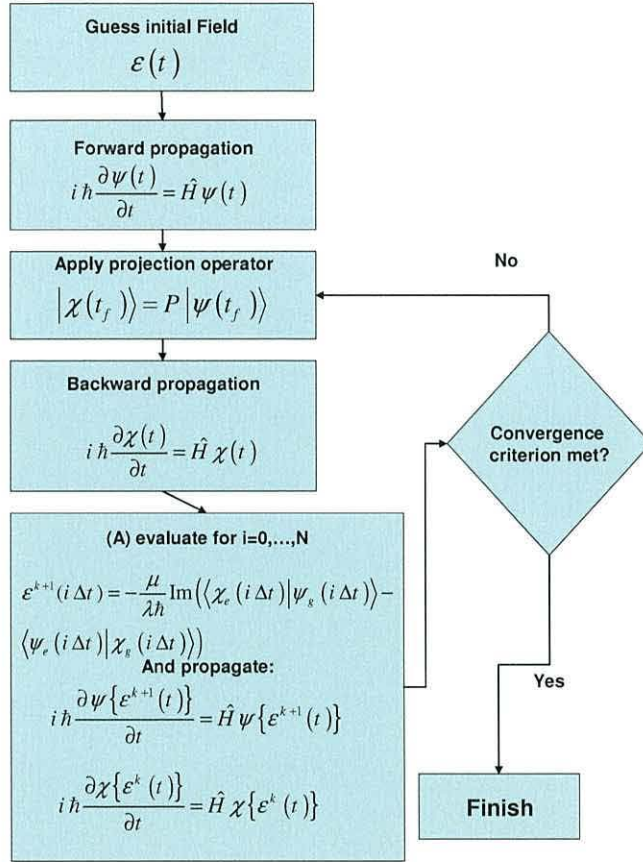


Figure 4.3: Optimal control algorithm for the Krotov method [9]. ‘k’ represents a particular iteration/cycle of the algorithm i.e. ϵ^{k+1} refers to the electric field evaluated in the present cycle and ϵ^k refers to the electric field evaluated in the previous cycle.

section. This results in a more efficient procedure as it allows for greater strides in the improvement of the electric field per iteration.

4.1.3 Laser Pulse Parameters

Throughout this work, Gaussian shaped pulses have been utilised for the initial guess field for each control scheme

$$\epsilon(t) = \sum_n A_n e^{-\gamma_n(t-t_n)^2} \cos(\omega_n t) \quad (4.16)$$

where A_n , γ_n , t_n and ω_n correspond to the amplitude, shape factor, centre time, and carrier frequency respectively of the n 'th Gaussian pulse in the sequence. The shape factor γ is proportional to the inverse squared of the pulse duration

$$\gamma \propto \frac{1}{t_{dur}^2}. \quad (4.17)$$

The pulse amplitude is related to the pulse intensity I via [5]

$$I = \frac{1}{2\mu_0\epsilon_0} A^2 \quad (4.18)$$

where μ_0 and ϵ_0 are the vacuum permeability and vacuum permittivity respectively. I and A have the units of Watt/cm² and Volt/cm respectively. Very high intensity laser pulses have the undesired effect of multi-photon excitation, which leads to the ionisation of molecules rather than transitions between the relevant electronic states. In this work, a limit of 20 TW/cm² is assigned to the electric field intensity [6], which translates to a pulse amplitude of 1.23×10^8 V/cm - or 0.02388 in a.u..

4.2 Photoisomerisation of Azomethane

Similar to its larger aromatic relatives, azomethane undergoes interesting photochemistry [12]. In the gas phase, azomethane undergoes fragmentation following $n\text{-}\pi^*$ excitation, however when in solution azomethane undergoes isomerisation following a similar excitation due to the *caging* effect of the solvent molecules [13]. It is the latter phenomenon which is of interest in this work.

There are striking similarities between the PESs of azomethane [12] and azobenzene [14, 15, 16] in the regions where isomerisation occurs. In particular, the most recent high level *ab initio* calculations tend to favour a rotation mechanism of photoisomerisation as opposed to inversion for both species. While an energy barrier exists on the S_1 state along the inversion coordinate, the torsional coordinate is essentially barrierless and also approaches the S_0 state in energy with a C-N-N-C dihedral angle of 90° , suggesting the existence of a relaxation channel at this geometry which would facilitate isomerisation.

In this work, DFT calculations were carried out to generate 1D potential energy functions (PEF), along the inversion and torsional coordinates of azomethane isomerisation, for their use in wavepacket calculations, and subsequent control of the wavepacket via femtosecond laser pulses. The small size of the azomethane molecule (relative to the size of the azobenzene derivative O2N2) allows for a much less computationally expensive investigation into the isomerisation mechanisms, and still (due to apparent similarities between the mechanisms in the literature) may have qualitative relevance for the larger molecule.

4.2.1 Azomethane DFT Calculations Results

All the electronic structure calculations in this chapter were carried out using the B3LYP hybrid functionals combined with the 6-31G* basis set. The first set of calculations run were geometry optimisations at minima and transition states along the isomerisation coordinates on the electronic ground (S_0) state (see Fig. 4.4). The *trans* and *cis* (minima) geometries were allowed to optimise without geometrical constraints, whereas the rotamer (rotation transition state) was constrained with a $\angle\text{CNNC}$ dihedral angle of 90° , and the invertomer (inversion transition state) was constrained with one $\angle\text{NNC}$ angle at 179.9° , and the $\angle\text{CNNC}$ dihedral angle set at 180° .

Table 4.1 compares the results of these calculations with results from CASSCF calculations [12], and experimental results from electron diffraction [18] and microwave spectroscopy [19] found in the literature. DFT compares favourably to the more computationally expensive CASSCF method, whereas

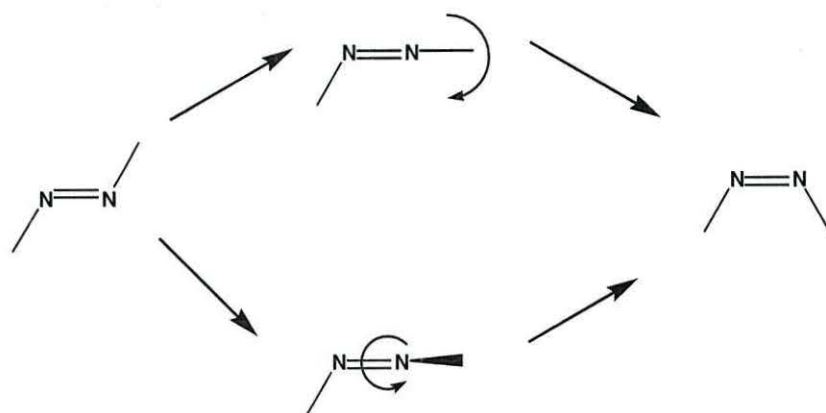


Figure 4.4: Schematic diagram of the two likeliest routes of azomethane photoisomerisation, inversion (top) and torsion (bottom) around the N=N bond.

DFT seems to underestimate the N=N bond length, the C-N bond lengths are closer to the experimental values than the CASSCF values, as well as the *cis* \angle CNN bond angle. The TD-DFT excitation energy value of 3.50 eV for *trans* azomethane also compares well with the experimental $S_0 \rightarrow S_1$ optical absorption value of 3.64 eV [20].

While DFT has been shown to produce results seemingly as accurate as the more rigorous CASSCF *ab initio* method, one major disadvantage is in the treatment of molecules in the excited electronic state. Time Dependent-Density Functional Theory (TD-DFT), Chapter 3.1.3, allows for the calculation of single point excitation energies to higher electronic states, however the option to optimise the molecule's geometry in these excited states is unavailable, unlike CASSCF. Since the Tannor/Rice control scheme relies on

Table 4.1: Comparison of DFT optimised structural parameters with results from the literature. CASSCF were taken from ref. [12], Exp(a) are results derived from electron diffraction [18], and Exp(b) are results derived from a microwave spectrum of *cis*-azomethane [19]. Bond lengths in Å, Bond angles in degrees and ΔE in kcal/mol. ΔE is the difference in energy of the structure compared to *trans*-azomethane. *two values for each R_{CN} and $\angle NNC$ due to the lack of symmetry in the invertomer species.

Molecule Geometry	Method	R_{NN}	R_{CN}	$\angle NNC$	$\angle CNNC$	ΔE
<i>trans</i> -	DFT	1.2439	1.4677	112.5	180.0	0.0
	CASSCF	1.2552	1.4669	112.4	180.0	0.0
	Exp(a)	1.2537	1.4742	111.9	180.0	
<i>cis</i> -	DFT	1.2430	1.4834	120.0	0.0	9.6
	CASSCF	1.2568	1.4632	124.3	0.0	11.0
	Exp(b)	1.2541	1.4801	119.3	0.0	
rotamer	DFT	1.2727	1.4571	115.5	90.0	67.7
	CASSCF	1.2970	1.4722	122.9	90.0	69.7
invertomer	DFT	1.2279	1.5151	115.2	180.0	51.0
			1.3935*	179.9*		
	CASSCF	1.2462	1.4801	115.2	180.0	55.3
			1.4108*	180.0*		

wavepacket propagation on the excited electronic state as much as on the ground state, this option would be beneficial since a more accurate minimum energy pathway could be found on the excited state potential energy surface.

To generate the relevant potential energy functions, geometry optimisation calculations were performed along the coordinates of interest (using the B3LYP hybrid functional combined with 6-31G* basis set). For the torsional coordinate, the $\angle CNNC$ dihedral angle was held constant for each calculation at intervals of 10° between the *cis* conformation at 0° and *trans* conformation at 180° . For the inversion coordinate, one $\angle CNN$ bond angle was held constant for each 10° interval between *trans*- 72° angle, sweeping through to *cis*- 82° angle. To generate the first excited electronic state, S_1 , potential energy functions (PEF), a TD-DFT single point excitation was carried out

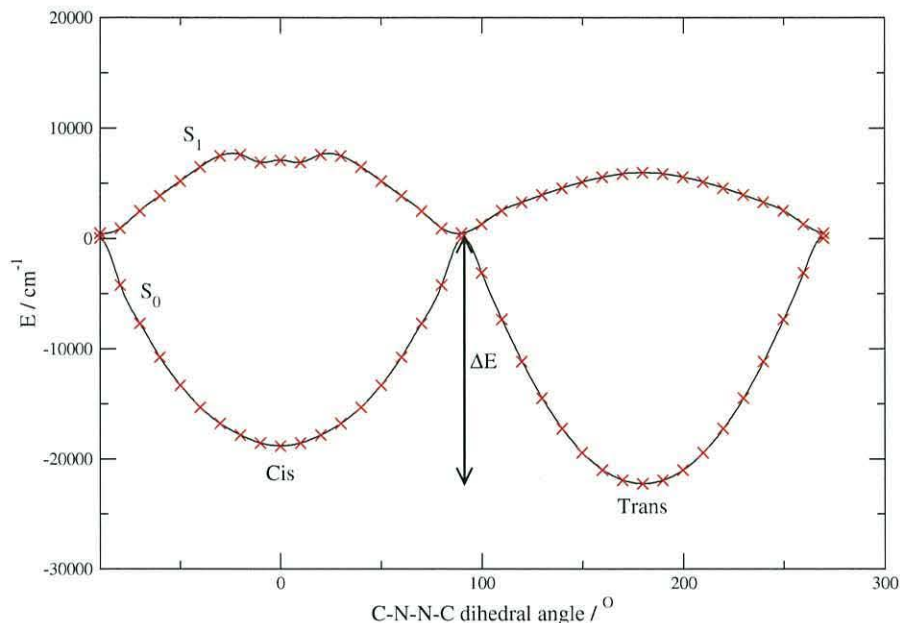


Figure 4.5: Ground S_0 and first excited S_1 electronic state potential energy functions along the torsional isomerisation coordinate. Crosses: energy relative to S_0 transition state of each individual DFT B3LYP/6-31G* calculation. Full line: cubic spline interpolation of the DFT points.

on each optimised geometry along both isomerisation coordinates.

Fig. 4.5 illustrates the S_0 and S_1 potentials along the torsional isomerisation coordinate⁴. The ground electronic state consists of a periodic asymmetric double well potential with a torsional barrier height of $\Delta E = 22,300 \text{ cm}^{-1}$, compared to the *trans* minimum, at 90° $\angle \text{CNNC}$ dihedral angle, which is typical of a torsional barrier about a double bond [21]. The *cis* minimum is measured at $3,420 \text{ cm}^{-1}$ higher than the *trans* minimum. These DFT results are comparable to the CASSCF results of $24,380 \text{ cm}^{-1}$ and $3,850 \text{ cm}^{-1}$, for the torsional barrier and *cis* minimum respectively [12]. The excited electronic state S_1 PEF has no barrier along the torsional isomerisation coordinate and reaches a minimum at $\angle \text{CNNC} \approx 90^\circ$ which is 420 cm^{-1} above S_0 , which resembles an avoided crossing at this geometry and infers the possible presence of a conical intersection nearby. The S_1 state PEF,

⁴A cubic spline interpolation algorithm was used to generate 512 interpolation points necessary for the subsequent quantum dynamical calculations.

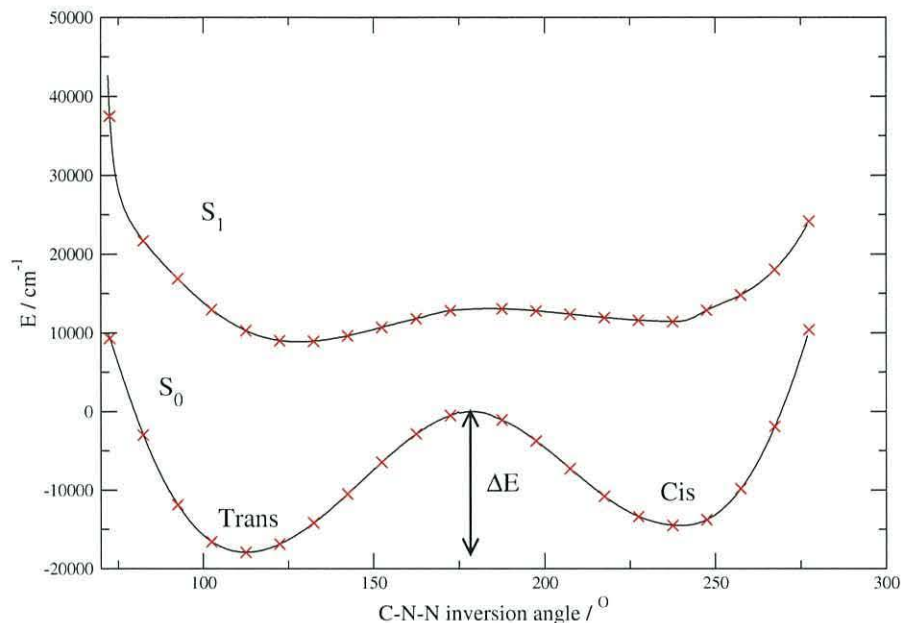


Figure 4.6: Ground S_0 and first excited S_1 electronic state potential energy functions along the inversion isomerisation coordinate. Crosses: energy relative to S_0 transition state of each individual DFT B3LYP/6-31G* calculation. Full line: least squares interpolation of the DFT points.

conversely to the S_0 state, increases in energy when C-N-N-C approaches planarity, reaching a local maximum at the *trans* geometry and an ambiguous discontinuity at the *cis* geometry.

Fig. 4.6 illustrates the S_0 and S_1 PEFs along the in plane inversion isomerisation coordinate. The ground electronic state consists of an asymmetric double well potential with minima at the *cis* and *trans* geometries, and a maximum located at the semi-linear geometry $\angle CNN = 180^\circ$. The maximum is found at an energy of $\Delta E = 17,900 \text{ cm}^{-1}$ above the *trans* minimum, which is approximately $4,500 \text{ cm}^{-1}$ less than the ground state torsional energy barrier in agreement with the CASSCF results [12]. The excited electronic state along the inversion coordinate also yields an asymmetric double well potential with a barrier to isomerisation of $2,740 \text{ cm}^{-1}$ higher in energy than the *trans* S_1 geometry. Even though this barrier is considerably lower than the ground state barrier, it still presents a significant obstacle for a low energy wavepacket to cross. This fact, together with the unlikely conditions neces-

sary to tunnel through an asymmetric barrier being met [22], suggests that a rather more complicated sequence of pulses will be required to isomerise azomethane via the inversion coordinate than a simple two pulse pump-dump sequence.

The DFT potential energy functions presented here are in agreement with the recent general consensus of the literature that the photoisomerisation of azo-compounds (azobenzene derivatives, and azomethane in solution) occurs predominantly via torsion about the N=N bond [12, 13, 14, 15, 16], as evidenced by the barrierless S_1 PEF. In the following sections, wavepacket calculations, together with optimal control theory, will be utilised to find efficient pulse sequences for photoisomerisation along both torsion and inversion isomerisation mechanisms. While it is unlikely that the isomerisation occurs via the inversion mechanism, the benefits of implementing wavepacket calculations along this coordinate lie in the anticipation of the possible hindrance of the torsional coordinate of the azobenzene derivative O2N2. Suitable pulse sequences derived here may, therefore, have future applications for molecular systems containing isomerisation coordinates characterised by asymmetric PEFs on both ground and first excited electronic states.

4.2.2 Control of Azomethane Isomerisation Along Torsional Coordinate

As depicted in Fig. 4.5 the barrier to isomerisation through rotation on the ground electronic state S_0 is very large $\approx 20,000 \text{ cm}^{-1}$. However, isomerisation on the first excited electronic state S_1 is essentially barrierless, facilitating a possible route from *trans* to *cis*-azomethane. For these simulations, constant values of $\mu = 0.0823 \text{ a.u.}$ and $M_\mu = 161,000 \text{ a.u.}$ were used for the transition dipole moment and reduced moment of inertia (reduced mass) respectively⁵. All calculations were carried out with 512 grid points and a time step $\Delta t = 1 \text{ a.u.}$.

⁵ μ is taken as the average along the torsional isomerisation coordinate taken from the TD-DFT calculations of this work. For these calculations, the Condon approximation of $\mu = \text{constant}$ is assumed for simplification purposes. The method of evaluating the reduced moment of inertia is presented in Appendix B

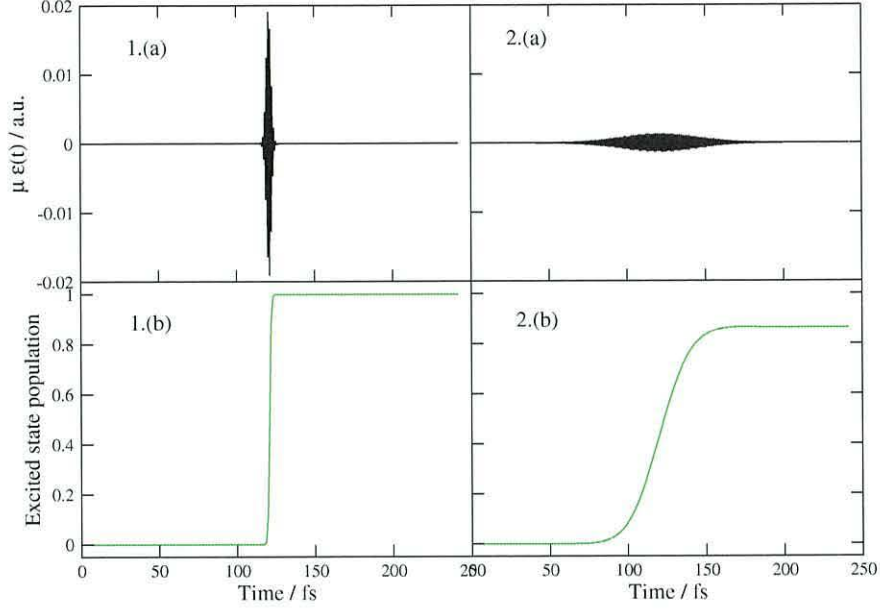


Figure 4.7: Femtosecond pulses, (a), and the corresponding S_1 population variation with time (b). Pulse Parameters: 1. $A = 0.236$ a.u., $\gamma = 1.2 \times 10^{-4}$ a.u. 2. $A = 0.0152$ a.u., $\gamma = 5 \times 10^{-7}$ a.u..

It was shown in Chapter 3.3.1 that population inversion is achieved through the application of π -pulses. The area of a Gaussian pulse envelope

$$S(t) = Ae^{-\gamma(t-t_0)^2} \quad (4.19)$$

is determined by its maximum amplitude A and its width γ , hence π -pulses of different durations may be generated. Fig. 4.7 illustrates the effect of two π -pulses, of different duration (≈ 8 fs for windows 1.(a)/(b), and ≈ 160 fs for windows 2.(a)/(b)), on the excited state population of azomethane. Fig. 4.8 shows $|\Psi(t)|^2$ at the instant the pulses in Fig. 4.7 are turned off, it is clearly seen that the wavepacket under the influence of the shorter pulse is far more localised, leading to a greater possibility of control.

On the evidence of Figures 4.7 and 4.8 it would seem that generating π -pulses of infinitesimal duration would accomplish the best control. However, a compromise must be reached as practical constraints on femtosecond pulse generation [5], and the effect of field intensity on the system [6], must be

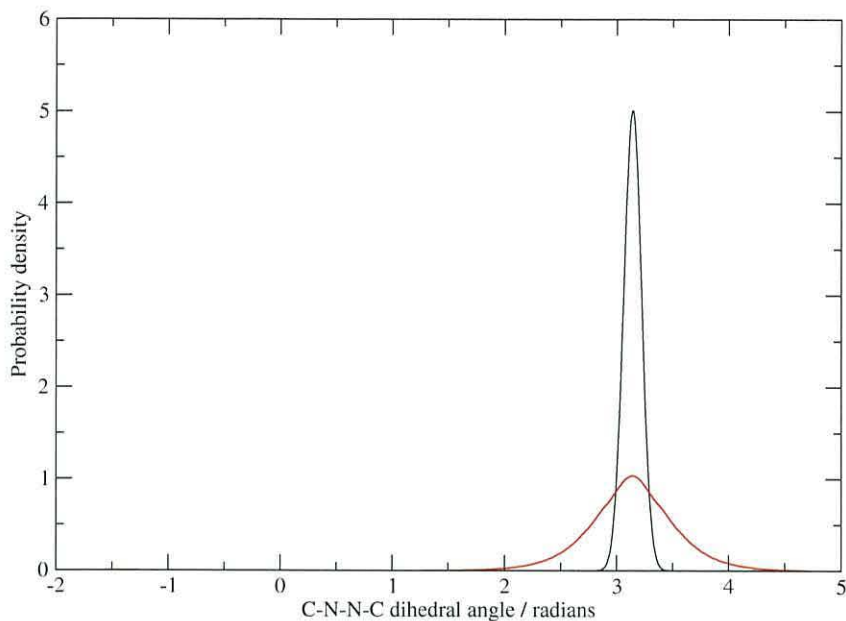


Figure 4.8: Wavepacket snapshots on the torsional S_1 state after population inversion following the application of an 8 fs π -pulse (black) and an 160 fs π -pulse (red)

taken into consideration. Due to azomethane's relatively small $S_0 \rightarrow S_1$ transition dipole moment (TDM), taken as 0.209 D, a large area for the pulse envelope ($\int S(t)dt$) is required to achieve the conditions of an on-resonant π -pulse Eq. (3.66). Taking the value of 20 TW/cm² as an upper limit for the maximum field intensity limits the choice of π -pulse to the example of longer duration.

Utilising the parameters of the longer (160 fs) pump pulse, the wavepacket was then allowed to propagate on the S_1 PEF. By direct observation of the wavepacket dynamics the timing of the dump pulse, as well as its carrier frequency ω , can be determined fairly accurately. Fig. 4.9 illustrates four wavepacket snapshots at different times during the pump - dump cycle, the 1st snapshot depicts the wavepacket in its initial *trans* ground state, the 2nd, 3rd and 4th snapshots shows the wavepacket distribution immediately after the pump pulse, immediately before the dump pulse and immediately after the dump pulse respectively.

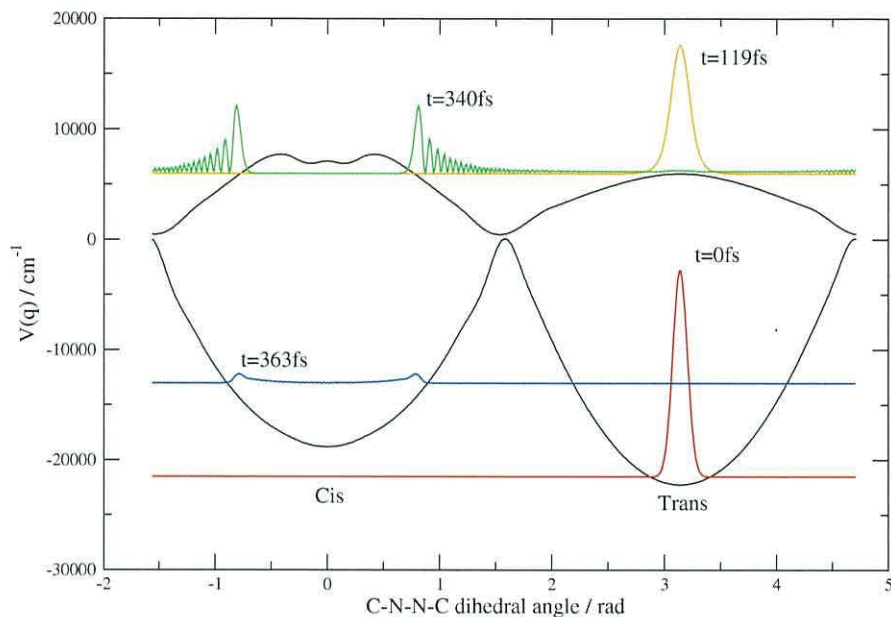


Figure 4.9: Wavepacket snapshots at various times during the pump dump cycle illustrated in Fig. 4.10.

While the pump pulse successfully transfers a fraction of 0.92 of the wavepacket density to the S_1 electronic state, the nature of the S_1 PEF results in some delocalisation and fragmentation of the wavepacket inhibiting the possibility of complete control of the isomerisation. Despite the delocalisation, at the time of the application of the dump pulse almost all the wavepacket is located above the *cis* well, however, the landscape of the S_1 PEF prevents the wavepacket from occupying the coordinates directly above the minimum of the *cis* well of the S_0 PEF. Consequently, the wavepacket must be ‘dumped’ on to a steep section of the S_0 PEF (as illustrated in Fig. 4.11) where the difference in energy between S_0 and S_1 ranges between approximately 10000 cm^{-1} and 15000 cm^{-1} , which in turn depletes the effectiveness of the dump pulse. The final population of azomethane in the *cis* S_0 state is 0.17.

It may be envisaged for such a situation (dumping on to a steep section of a PEF) that perhaps a pulse with a time dependent carrier frequency $\omega(t)$ may be beneficial. By scanning a range of frequencies, such pulses have

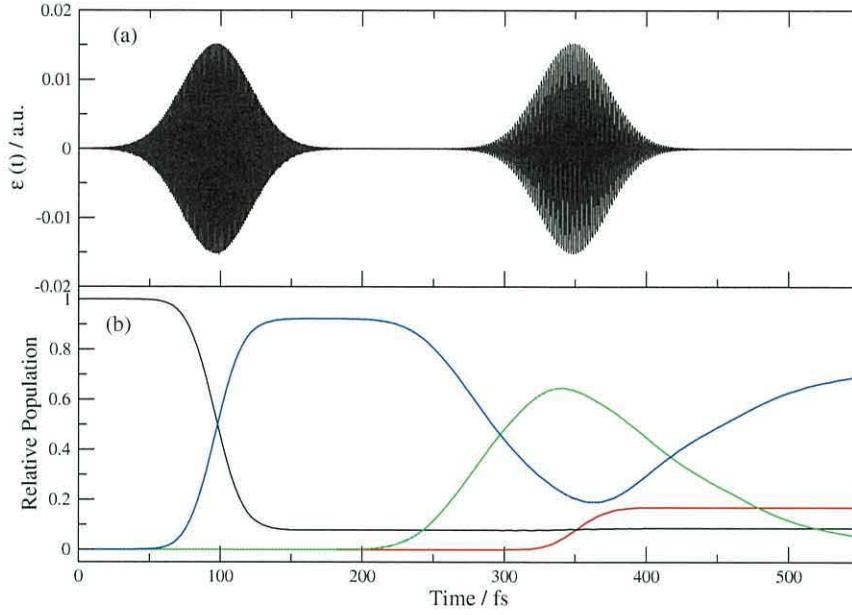


Figure 4.10: (a). Pump pulse parameters $A_1 = 0.0152$ a.u., $\gamma_1 = 5 \times 10^{-7}$ a.u., $\omega_1 = 0.1285$ a.u. dump pulse parameters the same with $\omega_2 = 0.0900$ a.u.. (b). corresponding time dependent populations black= $trans-S_0$, red= $cis-S_0$ blue= $trans-S_1$, green= $cis-S_1$.

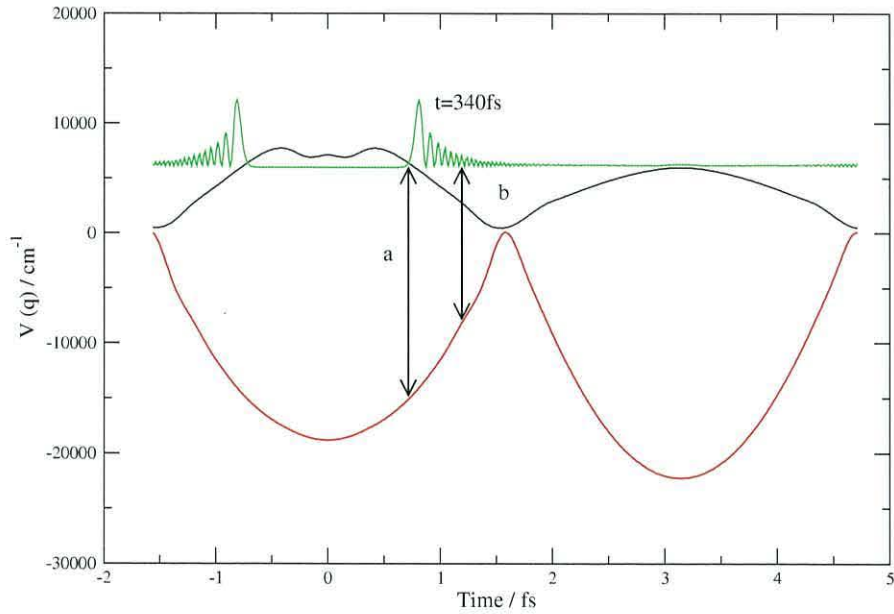


Figure 4.11: Wavepacket snapshot at time of dump pulse. 'a' and 'b' illustrates the range of ω required to dump various parts of the wavepacket.

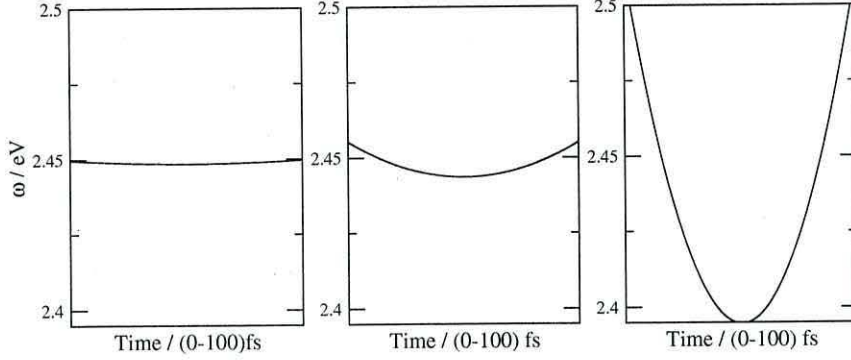


Figure 4.12: The variation of pulse carrier frequency ω with time for three different dump pulses of the type represented by Fig. 4.10. Chirp sweep rates: left panel - $\alpha_\omega = 1 \times 10^{-11}$, middle panel - $\alpha_\omega = 1 \times 10^{-10}$, right panel - $\alpha_\omega = 1 \times 10^{-9}$.

been shown to increase the efficiency of population transfer by matching the resonance frequency of different sections of the wavepacket, they are typically termed frequency chirped pulses [6]. The carrier frequency of quadratically chirped pulses varies according to

$$\omega(t) = \alpha_\omega(t - t_c)^2 + \beta_\omega \quad (4.20)$$

where α_ω , β_ω and t_c are the frequency sweep rate, minimum frequency and centre time of the pulse respectively. The simulation represented by figures 4.9 and 4.10 was repeated three times with varying frequency sweep rate for the now quadratically chirped dump pulse.

The central frequency of each simulation remains resonant with the energy gap between S_0 and S_1 coincident with the location of the wavepacket's centre while being dumped, 2.449 eV (0.09 a.u.). Contrary to expectations, quadratically chirped pulses proved ineffective in increasing the yield of *cis*-azomethane. Fig. 4.12 depicts the variation of ω with time for the three different dump pulses simulated, where yields of 0.149, 0.127 and 0.044 of *cis*-azomethane were recorded for the pulses with frequency sweep rates of $\alpha_\omega = 1 \times 10^{-11}$, $\alpha_\omega = 1 \times 10^{-10}$ and $\alpha_\omega = 1 \times 10^{-9}$ respectively. A possible explanation for the ineffectiveness of quadratically chirped pulses for this example may arise from the small μ_{01} (effectively diluting the magnitude of

the coupling to each frequency value swept), together with the possibility that the section of PEF on the S_0 state proves to be too steep, negating any positive effect the quadratic chirping may have on the result.

Optimal control

The Krotov approach of optimal control theory, Section 4.1.2, was implemented on the system to find a pulse shape which could substantially increase the yield produced by the pulse sequence depicted in Fig. 4.10, which was used as an initial guess, $\epsilon^{k=0}(t)$, for the procedure. At each iteration, k , the new electric field was calculated from

$$\epsilon^k(t) = -S(t) \frac{\mu}{\lambda \hbar} \Im (\langle \chi_e(t) | \psi_g(t) \rangle - \langle \psi_e(t) | \chi_g(t) \rangle) \quad (4.21)$$

where λ is a scalar quantity utilised as a penalty function on the energy of the optimised pulse, which can prevent the generation of optimised fields with unrealistically large amplitudes⁶. In addition to λ , a further constraint on the nature of the optimised field was imposed to ensure a smooth transition ‘on’ and ‘off’ of the electric field, achieved by the application of a shape function [23]

$$S(t) = \sin^2 \left(\pi \frac{t}{t_f} \right) \quad (4.22)$$

where t_f is the final time of the propagation. The target state was taken as

$$|\chi(t_f)\rangle = P |\psi(t_f)\rangle \quad (4.23)$$

where P projects the wavefunction at final time t_f on to the *cis* configuration of the ground electronic state. The value of λ needs to be chosen with caution, too small a penalty quickly leads to nonsensical pulses whereas too large a penalty leads to a diminishing yield at each iteration.

Fig. 4.13 illustrates the results of an optimisation procedure where the penalty was taken as $\lambda = 64.5$, all attempts with a larger penalty failed to

⁶Often, when left to its own devices, the OCT procedure quickly converges with large amplitude fields since they are most effective in population transfer

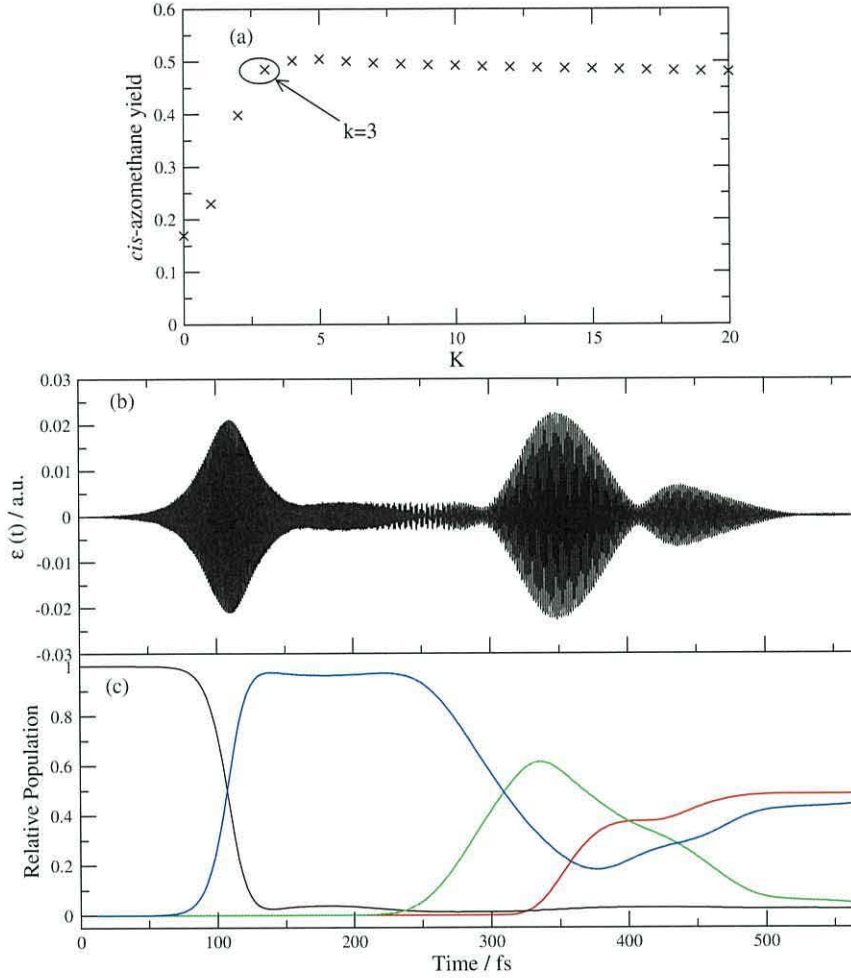


Figure 4.13: (a). Plot of *cis*-azomethane yield against *k*. (b). The optimised field after 3 iterations and (c) the corresponding time dependent populations black=*trans*-*S*₀, red=*cis*-*S*₀, blue=*trans*-*S*₁, green=*cis*-*S*₁.

lead to a better yield than the initial guess. The procedure was allowed to run for 20 iterations which converged at a maximum yield of 0.51 *cis*-azomethane after *k*=5, however all optimised fields generated after *k*=3 had sections with intensities above the chosen threshold of 20 TW/cm². The optimised field of the 3rd iteration increases the yield of the initial guess from 0.17 to 0.485, while maintaining the basic pump-dump structure of the initial guess.

Comparison of Figures 4.10 (a)/(b) and 4.13 (b)/(c) reveals that the increase of yield is the product of a more efficient pump pulse (transferring

almost all population to the S_1 state), together with a wider dump pulse which is more gradual than the initial guess. It is apparent that this increase in population transfer efficiency is largely a result of pulses with increased amplitude, and that merely changes in pulse shape are ineffective in substantially increasing the yield, hence it may be interpreted that the biggest limiting factor for control in this particular system is the small transition dipole moment between S_0 and S_1 .

4.2.3 Control of Azomethane Isomerisation Along Inversion Coordinate

The same strategy was utilised to search for a pulse sequence which would deliver a significant proportion of the wavepacket to the *cis* conformer via the inversion S_0 and S_1 PEF's (Fig. 4.6). For these simulations, values of $\mu = 0.0799$ a.u. and $M_\mu = 186,000$ a.u. were used for the transition dipole moment and reduced moment of inertia respectively. All calculations were carried out with 512 grid points and a time step $\Delta t = 1$ a.u..

Fig. 4.14 depicts wavepacket snapshots on the S_1 PEF after initial excitation by the π -pulse described in Fig. 4.15 (a). After the initial excitation the wavepacket propagates away from the Franck-Condon region towards the *cis* well where it encounters an energy barrier corresponding to the C-N-N linear geometry. It is apparent from Fig. 4.14 that the wavepacket has insufficient energy to overcome this barrier and therefore it is trapped in the *trans* conformation. The time dependent populations depicted by Fig. 4.15 (b) confirms that at no time does the wavepacket reach a *cis* geometry throughout the entire propagation. A simple pump-dump scheme is therefore unsuitable for a system with an excited state PEF of this nature.

By examining Fig. 4.14 in detail, it may be envisaged that a sequence of pulses exists which could produce a wavepacket on the S_1 inversion surface with sufficient energy to overcome the C-N-N linear barrier. The wavepacket reaches the first turning point at around 189 fs of the simulation, and is dominantly localised above an incline on the S_0 surface. A dump pulse at this point will produce a vibrationally 'hot' wavepacket (Chapter 2.3) which

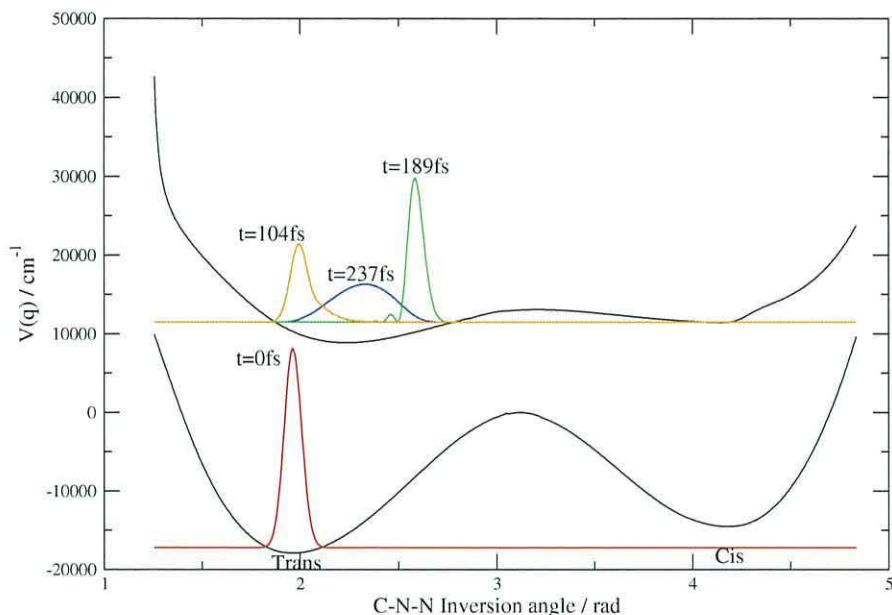


Figure 4.14: Wavepacket snapshots at various times before and after excitation to the S_1 state via the pump pulse illustrated in Fig. 4.15.

has a greater amplitude of oscillation in the S_0 *trans* well. A subsequent pump pulse when the wavepacket reaches the opposite turning point in the S_0 state will produce a vibrationally ‘hot’ wavepacket on the S_1 surface with sufficient energy to overcome the linear C-N-N barrier. Fig. 4.16 illustrates this strategy of a four pulse sequence. In this figure vertical arrows represent transitions as a result of interaction with a laser pulse, and the horizontal arrows represent the ‘direction’ of the wavepacket motion.

Fig. 4.17 depicts wavepacket snapshots at various times during a calculation where the wavepacket is subject to the pulse sequence illustrated in Fig. 4.18 (a). Again, as was the case for the torsional isomerisation coordinate, the small μ_{01} limits the choice of pulse to the longer variety, making the possibility of keeping the wavepacket significantly localised during the entire simulation unlikely, as well as compromising the effectiveness of the transfer of population density during each pulse application (see Fig. 4.18 (b)).

Following the initial pump pulse, the wavepacket at $t = 150$ fs (depicted by green in Fig. 4.17 (b)) is seen to be significantly de-localised in comparison

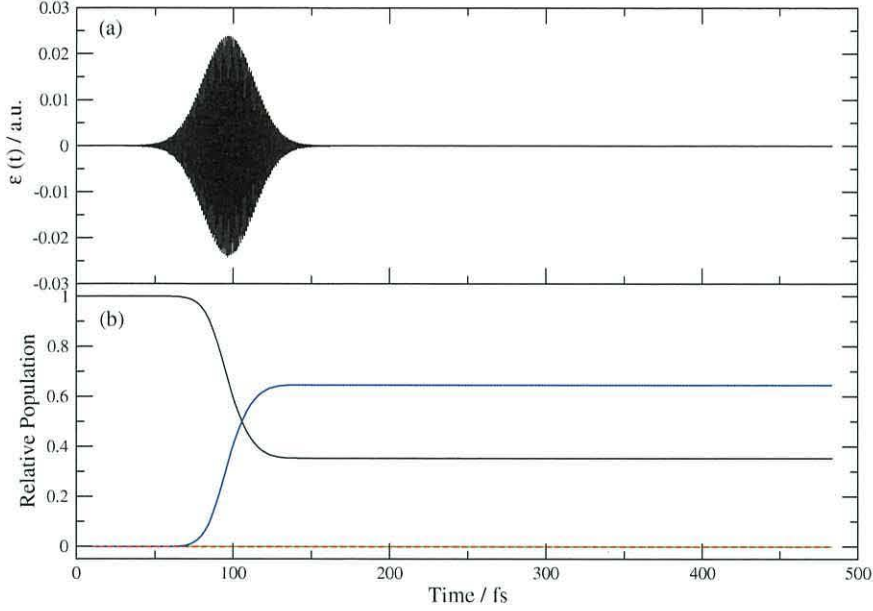


Figure 4.15: (a). Pump pulse parameters $A_1 = 0.02388$ a.u., $\gamma_1 = 1.1 \times 10^{-6}$ a.u., $\omega_1 = 0.1283$ a.u.. (b) corresponding time dependent populations black=*trans*- S_0 , red=*cis*- S_0 , blue=*trans*- S_1 , green=*cis*- S_1 .

Table 4.2: Pulse parameters for the pulse sequence illustrated in Fig. 4.18 (a)

Pulse n	t_n / fs	ω_n / a.u.	γ_n / a.u.
1 (pump)	97	0.12830	1.1×10^{-6}
2 (dump)	189	0.08376	1.1×10^{-6}
3 (pump)	249	0.12595	1.1×10^{-6}
4 (dump)	363	0.11838	1.1×10^{-6}

to its profile at $t=0$ fs. The initial pump pulse transfers ≈ 0.65 of the population to the S_1 state, while the second pulse transfers ≈ 0.3 of this population back down to the S_0 state, effectively eliminating 70 % of the wavepacket from the control sequence after only two pulses. Denoted by (a) in Fig. 4.17 are the portions of the wavepacket which were left unexcited by the initial pulse, (b) denotes the portion of the wavepacket excited by the third pulse back to S_1 which will have sufficient energy to overcome the energy barrier at $\angle C-N-N = \text{linear}$. Component (c) points towards the portion of the wavepacket which remained in the S_1 state following the initial 2 pulses,

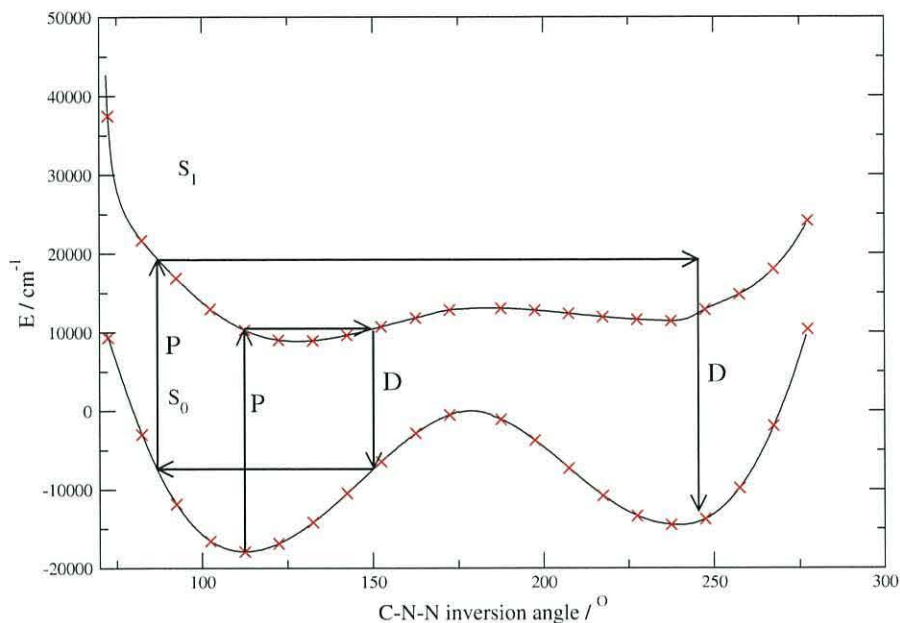


Figure 4.16: Schematic demonstrating the possible motion of a wavepacket under the 4 pulse sequence described in the text. Pump and dump transitions are labelled ‘P’ and ‘D’ respectively.

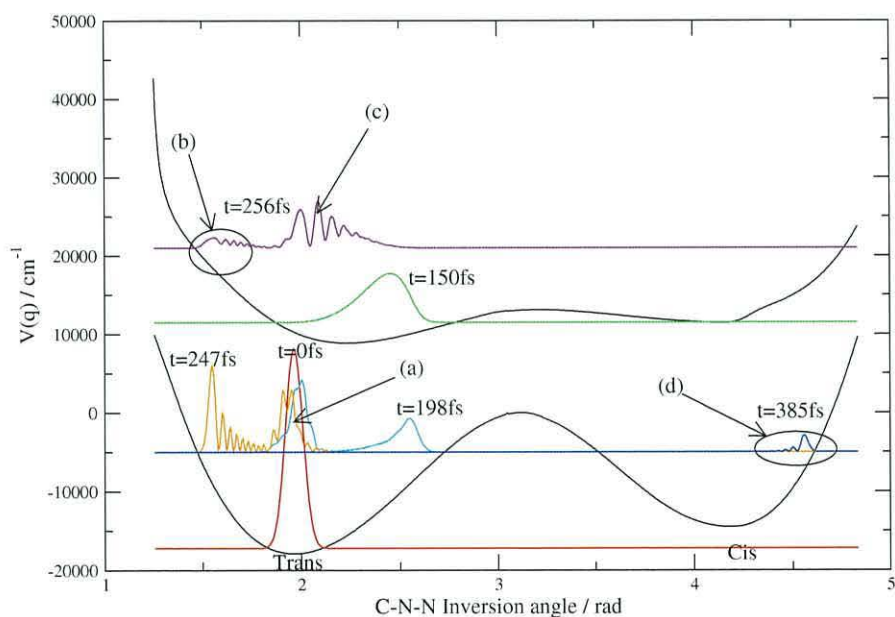


Figure 4.17: Wavepacket snapshots at various times before and after excitation to the S_1 state via the pulse sequence illustrated in Fig. 4.18 (b).

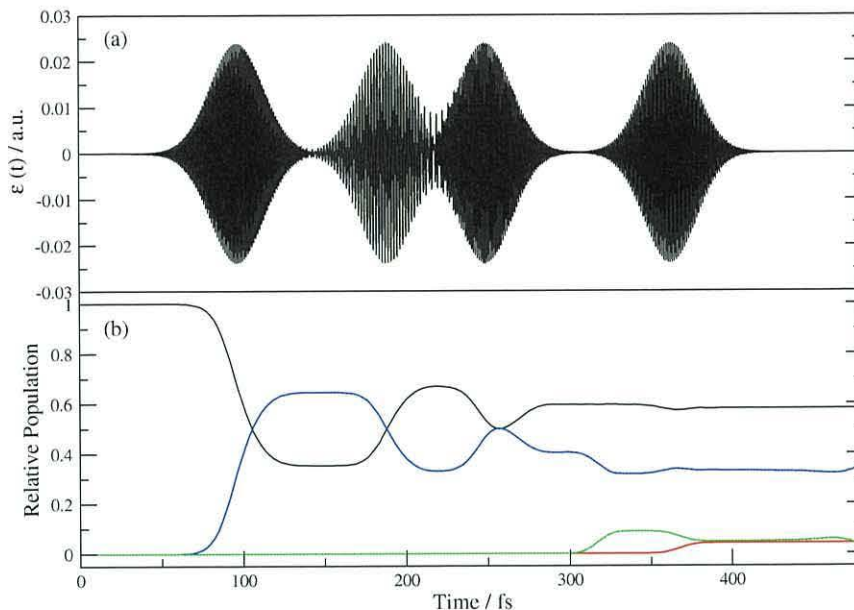


Figure 4.18: (a) 4 Pulse sequence pump-dump-pump-dump - pulse parameters in Table 4.2. (b). corresponding time dependent populations black= $trans$ - S_0 , red= cis - S_0 , blue= $trans$ - S_1 , green= cis - S_1 .

which remain oscillating within the S_1 *trans* well. The tiny portion of the wavepacket denoted by (d) eventually reaches the target *cis* configuration in the S_0 state.

Fig. 4.18 (b) illustrates the time dependent populations of the *trans* and *cis* conformers in the S_1 and S_0 electronic states with respect to $\epsilon(t)$. After ≈ 340 fs, 0.089 of the total population occupies the S_1 state in the *cis* configuration, 0.042 of this is transferred by the final pulse signifying the very small yield of *cis*-azomethane (depicted in red) produced by this particular pulse sequence.

Optimal control

Again, the Krotov approach of optimal control theory was implemented with the pulse sequence depicted by Fig. 4.18 (a) as an initial guess. Since the initial guess field is already at the maximum threshold of field intensity, all attempts to increase the yield of *cis*-azomethane using OCT proved futile

without surpassing the set amplitude limit. The small transition dipole moment μ_{01} coupled with a significant energy barrier to overcome on the S_1 state proved to be insurmountable obstacles for pulse shaping alone to overcome.

Fig. 4.19 depicts the results of an OCT procedure implemented on this system, however the value μ_{01} has been increased to a value of 1 a.u. to illustrate that the main limiting factor to control is indeed the small dipole interaction. As an initial guess for the procedure, the pulse sequence depicted by Fig. 4.18 (a) was modified by decreasing the peak amplitude of each pulse to 0.00191 a.u. which, coupled with a value of $\mu_{01} = 1$ a.u., yields the same time dependent populations as depicted by Fig. 4.18 (b).

To preserve the nature of the four pulse sequence (and hence maintain a recognisable mechanism⁷) an alternative version of Eq. (4.21) was used to calculate the new field at each iteration whereby the overlap integral acts as a refinement on the field of the previous iteration, rather than a replacement [24]

$$\epsilon^k(t) = \epsilon^{k-1}(t) - S(t) \frac{\mu}{\lambda \hbar} \Im (\langle \chi_e(t) | \psi_g(t) \rangle - \langle \psi_e(t) | \chi_g(t) \rangle). \quad (4.24)$$

A large penalty of $\lambda = 20$ was imposed on the refinement at each step and the calculation allowed to proceed for 20 iterations.

Fig. 4.19 (a) reveals that the procedure is successful in reaching a yield of 0.9 of *cis*-azomethane in only 5 iterations, and continues to improve on this value at each step reaching 0.98 after 20 iterations, proving that the small transition dipole moment was the main limiting factor in previous attempts. Although the optimal pulse seems rather complex, the four pulse pump-dump-pump-dump mechanism has been maintained as depicted by the time dependent populations in Fig. 4.19 (c). The first 2 population inversions between the S_0 and S_1 states work to produce a wavepacket in the *trans* configuration (depicted by black and blue) with sufficient momentum to overcome the energy barrier on the S_1 state to reach the *cis* configuration

⁷often the Optimal Control procedure will converge with an optimal pulse which yields a large percentage of product, however the resulting wavepacket motion may be rather complicated. An optimal field with a discernable mechanism has the benefit of further possible refinement via manual intuition.

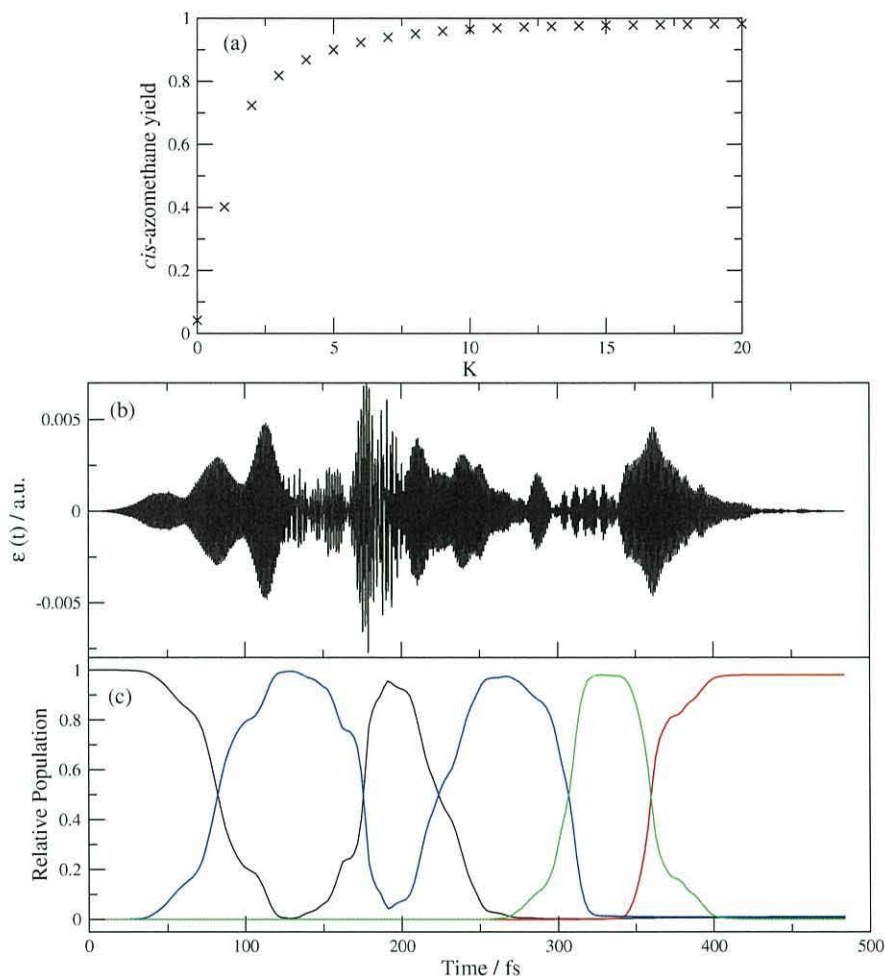


Figure 4.19: (a) Plot of *cis*-azomethane yield against k . (b). The optimised field after 20 iterations and the corresponding time dependent populations (c) black=*trans*- S_0 , red=*cis*- S_0 , blue=*trans*- S_1 , green=*cis*- S_1 .

(depicted by green and red).

The pulse sequences calculated in this chapter and Chapter 5 have varying degrees of success in terms of yield. When the conditions are favourable (large transition dipole moment, favourable PEF topology), isomerisation yields above 90 % are observed. The applicability of theoretically derived pulses on the actual (experimental) system clearly depends on how accurately

the model system describes the real system, i.e. the number and severity of the approximations and assumptions made to generate the model (discussed further in Chapter 5.3). However, what the theoretical investigations do provide are the main obstacles provided by the system's PES, and strategies on how they may be overcome. The results of a theoretical investigation therefore provide an invaluable starting point for the experimental investigation [25], where the effectiveness of the control field may be refined by techniques such as *feedback influenced control* and *adaptive learning control* (see chapter 7 of ref. [11] and references therein.).

Bibliography

- [1] D. J. Tannor and S. A. Rice, *J. Chem. Phys.*, (1985), **83**, 5013.
- [2] D. J. Tannor, R. Kosloff and S. A. Rice, *J. Chem. Phys.*, (1986), **85**, 5805.
- [3] T. Baumert, M. Grosser, R. Thalweiser, G. Gerber, *Phys. Rev. Lett.*, (1991), **67**, 3753.
- [4] E. D. Potter, J. L. Herek, S. Pederson, Q. Liu, A. H. Zewail, *Nature*, (1992), **355**, 66.
- [5] C. Rullière, *Femtosecond Laser Pulses: Principles and Experiments*, second edition, Springer, (2005).
- [6] H. Tamura, S. Nanbu, T. Ishida, H. Nakamura, *J. Chem. Phys.*, (2006), **125**, 034307.
- [7] A. P. Peirce, M. A. Dahleb, H. Rabitz, *Phys. Rev. A*, (1988), **37**, 4950.
- [8] R. Kosloff, S. A. Rice, P. Gaspard, S. Tersigni, D. J. Tannor, *Chem. Phys.*, (1989), **139**, 201.
- [9] J. Somló, V. A. Kazakov, D. J. Tannor, *Chem. Phys.*, (1993), **172**, 85.
- [10] I. R. Sola, J. Santamaria, D. J. Tannor, *J. Phys. Chem. A*, (1998), **102**, 4301.
- [11] S. A. Rice, M. Zhao, *Optimal Control of Molecular Dynamics*, Wiley, (2000).
- [12] P. Cattaneo, M. Persico, *Theor. Chem. Acc.*, (1999), **103**, 390.
- [13] P. Cattaneo, G. Granucci, M. Persico, *J. Chem. Phys. A*, (1999), **103**, 3364.
- [14] P. Cattaneo, M. Persico, *Phys. Chem. Chem. Phys.*, (1999), **1**, 4739.

- [15] T. Ishikawa, T. Noro, T. Shoda, *J. Chem. Phys.*, (2001), **115**, 7503.
- [16] E. W.-G. Diau, *J. Phys. Chem. A*, (2004), **108**, 950.
- [17] J. B. Foresman, A. Frisch, *Exploring Chemistry with Electronic Structure Methods*, Gaussian, Inc, (1993).
- [18] C. H. Chang, R. F. Porter, S. H. Bauer, *J. Am. Chem. Soc.*, (1970), **92**, 5313.
- [19] J. F. Stevens, R. F. Curl, P. S. Engel, *J. Phys. Chem.*, (1979), **83**, 1432.
- [20] O. A. Mosher, M. S. Foster, W. M. Flicker, A. Kuppermann, J. L. Beauchamp, *Chem. Phys. Lett.*, (1974), **29**, 236.
- [21] J. M. Hollas, *Modern Spectroscopy*, second edition, Wiley, (1995).
- [22] K. H. Hughes, J. N. Macdonald, *Chem. Phys. Phys. Chem.*, (2000), **2**, 4267.
- [23] J. Manz, K. Sundermann, R. de Vivie-Riedle, *Chem. Phys. Lett.*, (1998), **290**, 415.
- [24] J. P. Palao, R. Kosloff, *Phys. Rev. Lett.*, (2002), **89**, 188301-1.
- [25] H. Rabitz, W. Zhu, *Acc. Chem. Res.*, (2000), **33**, 572.

Chapter 5

Optimal Control of an Ether Capped Azobenzene Molecule

Over the last 30 years, there has been a vast amount of experimental and theoretical study on azobenzene and its derivatives [1, 3, 4, 5, 7, 10]. The motivation for these studies is the potential applications in optical data storage and processing, as well as molecular switches in biomolecules and nano-devices. It is the characteristic photoisomerisation that these molecules undergo when illuminated with UV/vis radiation which has identified them as possible candidates for the aforementioned tasks.

These characteristics were briefly discussed in Chapter 1, where the molecule abbreviated as O2N2 was introduced (structure B in Fig. 5.2). In the present chapter, a more detailed background of the possible mechanisms of photoisomerisation is presented via review of the literature in Section 5.1. Section 5.2.1 presents the results of DFT calculations carried out to generate relevant potential energy functions along the possible photoisomerisation coordinates of O2N2. The remainder of the chapter presents wavepacket calculations (Chapter 3) to observe the dynamics of the isomerisations on the calculated PEF's. Section 5.2.2 and Section 5.2.3 presents the results of wavepacket propagation calculations on the inversion PEF and torsional PEF respectively. These results include pump-dump strategies to increase isomerisation yield, followed by further refinement by the application of OCT. The

effect of a coordinate dependent dipole moment ' $\mu(q)$ ' on the effectiveness of OCT is discussed in Section 5.2.5, and finally, a summary and discussion of this chapter is presented in Section 5.3 including proposed further work on the subject.

5.1 Background

The UV visible spectrum of azobenzene, in solution, has two major absorption bands corresponding to $S_0 \rightarrow S_1$ and $S_0 \rightarrow S_2$ electronic transitions. The $S_0 \rightarrow S_1$ transition has been assigned to a symmetry forbidden $n \rightarrow \pi^*$ transition, of maximum intensity at $\approx 440\text{nm}$, whereas the $S_0 \rightarrow S_2$ transition has been assigned to a symmetry allowed $\pi \rightarrow \pi^*$ transition at $\approx 320\text{nm}$ [1]. Under both excitation wavelengths, *trans*-azobenzene undergoes photoisomerisation into its *cis* conformer.

The goal of most investigations into the azobenzene molecule (and its derivatives) is to find the actual mechanism by which the photoisomerisation occurs, by searching for either experimental [1, 4, 5, 6, 9, 12, 13, 14] or theoretical [3, 7, 10, 15, 16] evidence. Fig. 5.1 illustrates the two mechanisms which have been widely debated in the literature over the years, namely the *inversion* and *torsional* mechanisms.

Trans \rightarrow *cis* quantum yields of 0.11 and 0.24 were observed for the $S_0 \rightarrow S_2$ and $S_0 \rightarrow S_1$ excitations respectively [2]. These results implied that a different isomerisation mechanism existed for each excitation. Early *ab initio* calculations [3] supported this suggestion, where the inversion mechanism was purported to take place on the S_1 PEF, and a torsional mechanism on the S_2 PEF.

Similar experimental investigations on the so called rotation-restricted (r-r) azobenzenes (Chapter 1) seemed to provide further support for these findings. For the r-r azobenzenophane molecule [4] (see structure A of Fig. 5.2), the quantum yields for $S_0 \rightarrow S_2$ and $S_0 \rightarrow S_1$ excitations were found to be the same, implying that the same inversion mechanism occurred regardless of the excitation wavelength. The same result was observed for azobenzene confined inside a cyclo-dextrin cavity [5], where the 'cramped' environment is believed

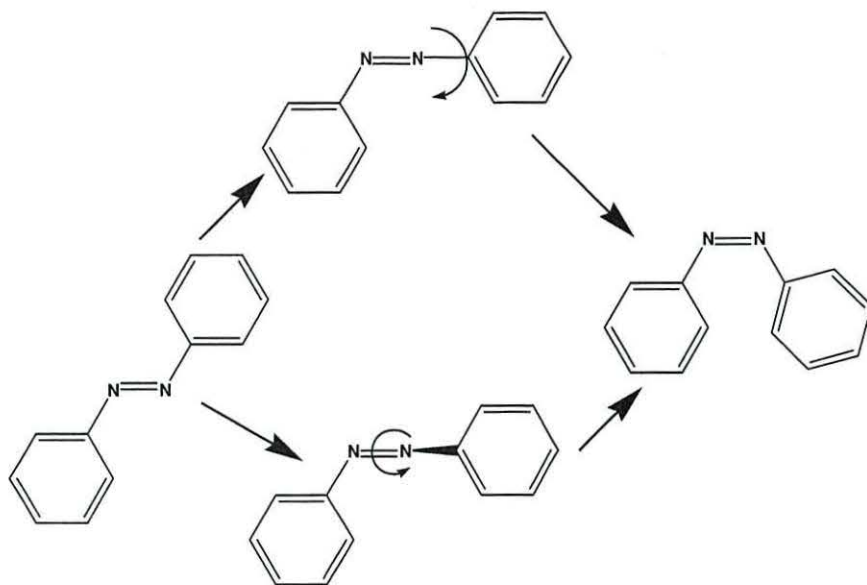


Figure 5.1: Schematic diagram of the two likeliest routes of azobenzene photoisomerisation, inversion of one CNN bond (top), and torsion around the N=N bond (bottom).

to also inhibit the torsional mechanism. The discrepancy in quantum yield for unrestricted azobenzene could therefore be explained by deducing that the alternative torsional route for isomerisation is accessible when excited to the S_2 electronic state, which would concur with the early *ab initio* results of ref. [3].

Fujino *et al* [6] conducted a femtosecond time-resolved fluorescence study of *trans*-azobenzene. Their findings included the lifetimes of *trans*-azobenzene in each excited electronic state, which were found to be ≈ 110 fs for an S_2 ($\pi \rightarrow \pi^*$) transition, and ≈ 500 fs for an S_1 ($n \rightarrow \pi^*$) transition. It was inferred from the fluorescence data that azobenzene in the S_2 state relaxes to the S_1 state first, before subsequent relaxation to the ground state in the

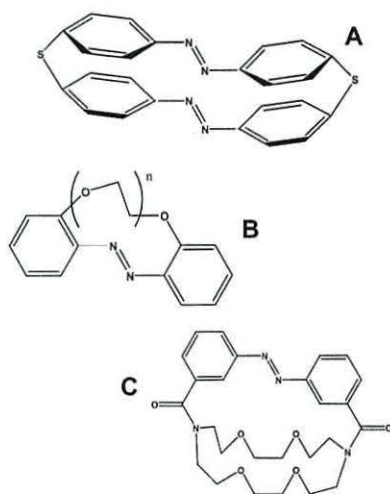


Figure 5.2: A: An azobenzenophane molecule [4]. B: Series of azocrownethers, O2N2 when $n=1$ [13] C: Azocrownether of ref. [19] where the torsional photoisomerisation pathway was believed to be sterically hindered.

same time scale as for a molecule which was initially excited to S_1 . The quantum yield of the initial $S_2 \rightarrow S_1$ relaxation was found to be almost unity, and, coupled with their observation that the *trans* \rightarrow *cis* isomerisation had not occurred before this relaxation, it was deduced that the photoisomerisation occurs exclusively on the S_1 electronic state, regardless of the initial excitation wavelength.

Since these observations appear to contradict the fact that there is a difference in isomerisation quantum yield depending on the initial excitation wavelength, it was suggested that another $S_1 \rightarrow S_0$ relaxation channel is accessible for a ‘vibrationally hot’ S_1 species resulting from a previous $S_2 \rightarrow S_1$ relaxation. This newly accessible pathway would relax to the *trans* form of azobenzene, hence accounting for the smaller quantum yield observed for an initial excitation to the S_2 state.

The picture presented by ref [6] is consistent with the evidence so far. However, recent *ab initio* results by Persico *et al* [7] and Ishikawa *et al* [8]

have countered the evidence which suggests that azobenzene photoisomerisation only occurs via inversion. Utilising high level CASSCF calculations, details of azobenzene’s PES along both isomerisation pathways were revealed. Both groups discovered that there is a considerable barrier on the S_1 PES along its inversion coordinate, whereas the torsional coordinate was found to be essentially barrierless. Furthermore, Ishikawa *et al* discovered a conical intersection located at $\approx 90^\circ$ along the torsional coordinate, providing a possible relaxation channel between S_1 and S_0 .

Together with the results of a femtosecond fluorescent anisotropy study by Diau *et al* [9], and subsequent *ab initio* calculations by the same authors [10], the torsional mechanism for isomerisation has gathered momentum recently. Using a semiclassical surface hopping approach, Ciminelli *et al* [11] demonstrated the possibility that azobenzenophanes (Fig. 5.2 A) may not be rotation restricted after all, hence opening up possible different interpretations of the evidence available so far.

Along with the postulated *torsion* and *inversion* mechanisms, another possible route of relaxation from S_0 to S_1 has been given some credibility recently. By scanning the S_1 PES using *ab initio* CASSCF methodology, Diau [10] discovered another possible conical intersection (CI) connecting the S_1 and S_0 surfaces along the *concerted inversion* coordinate Fig. 5.3. This particular CI is higher in energy than the CI associated with the torsional pathway, hence it could only be accessed by ‘vibrationally hot’ molecules, such as the molecules originally excited to the S_2 state. Since it appears that the concerted inversion pathway favours returning to the original *trans* conformer rather than isomerise, this newly discovered channel may be consistent with the quantum yield observations of Zimmerman *et al* [2], as well as the ‘vibrationally hot’ alternative relaxation channel postulated by Fujino *et al* [6].

Fig. 5.4 illustrates an excitation/relaxation diagram which summarises the conclusions of refs. [6, 10]. Following excitation to the S_1 electronic state, the molecule’s geometry relaxes along the torsional coordinate approaching a S_1/S_0 conical intersection (CI) at $\angle\text{C-N-N-C } 90^\circ$, which subsequently ‘fun-

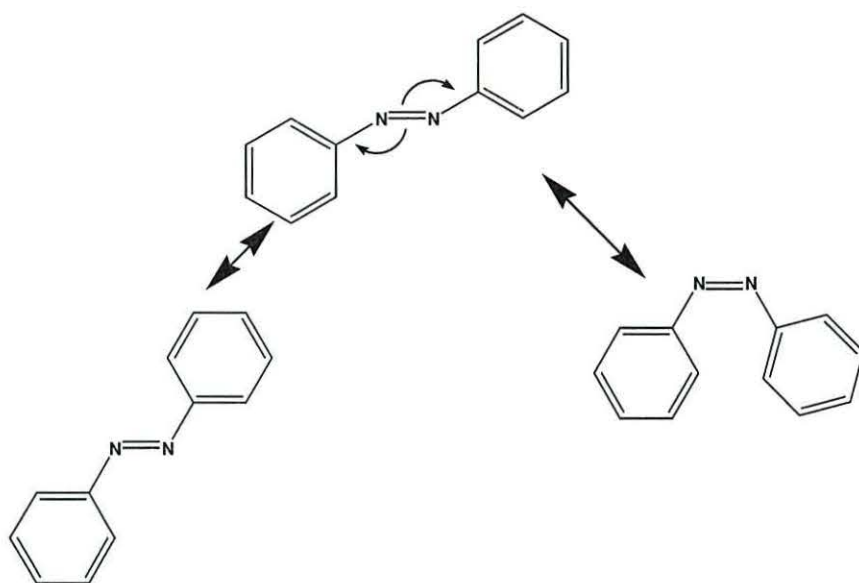


Figure 5.3: Schematic diagram of the concerted inversion pathway to photoisomerisation of azobenzene [10]

nels' the molecule back to the S_0 state with a quantum yield of 0.24 *cis*-azobenzene. Excitation to the S_2 state is quickly followed by relaxation to the S_1 state via a S_2/S_1 CI near the Franck-Condon geometry, generating a 'vibrationally hot' molecule with sufficient energy to access a S_1/S_0 CI along the concerted inversion pathway. This final CI is inaccessible following $S_0 \rightarrow S_1$ excitation of *trans*-azobenzene, which accounts for the different *cis/trans* product ratio depending on the initial excitation.

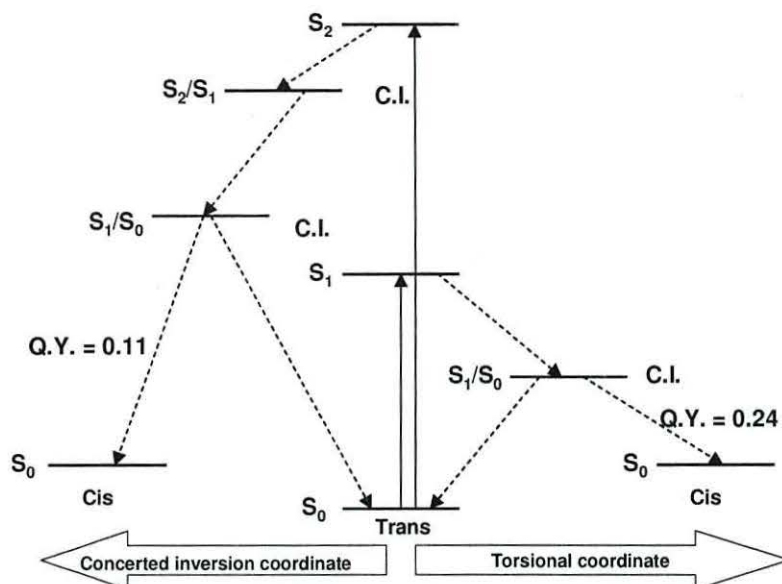


Figure 5.4: Qualitative excitation/relaxation diagram of the possible mechanisms of photoisomerisation of azobenzene described in the text.

5.2 Photoisomerisation of the Azobenzene Derivative O2N2

The motivation behind the choice of the molecule O2N2 (Fig. 5.2 B) for this study is its suitability for future applications in the optical data storage industry, in particular, due to the thermal stability of its *cis* conformer and good reversibility of the photoisomerisation compared to other azobenzene derivatives [12, 13]¹. In addition, the ether group linking the two benzene rings imposes constraints on the possible conformations of the molecules, which may obstruct the torsional and/or concerted inversion photoisomerisation pathways. If these pathways are indeed restricted, then the dimensionality of the isomerisation will be reduced to the inversion coordinate alone, leading to the possibility of a more straight forward dynamical investigation.

¹O2N2 is also the smallest azobenzene derivative containing an ether linkage [13], which is advantageous when considering computational demands.

Table 5.1: Selected bond lengths (Å) and angles (degrees) of the DFT/B3LYP/6-31G* optimised geometries of the *trans* and *cis* conformers of the molecule O2N2. *Comparison with X-ray data taken from ref. [18], numbered atoms taken from Fig. 5.5.

Atoms	<i>trans</i> -DFT	<i>trans</i> -X-ray*	<i>cis</i> -DFT	<i>cis</i> -X-ray*
Bond lengths:				
N(2)-N(1)	1.260	1.234	1.253	1.251
N(1)-C(3)	1.385	1.397	1.454	1.441
C(9)-N(2)	1.421	1.431	1.431	1.446
Angles:				
C(9)-N(2)-N(1)	121.49	118.9	124.32	120.3
N(2)-N(1)-C(3)	108.38	110.3	118.51	119.9
Dihedral Angle:				
C(9)-N(2)-N(1)-C(3)	173.48	174.62	-9.21	-7.7
C(4)-C(3)-N(1)-N(2)	163.52	175.4	116.54	116.2
C(14)-C(9)-N(2)-N(1)	31.69	28.1	-54.11	-67.3

5.2.1 O2N2 DFT Calculations Results

In this work, the hybrid functional B3LYP (Chapter 3.1.3) was used for all the DFT and TD-DFT calculations. To find the optimised geometry of *trans*-O2N2, a series of optimisation calculations were run with increasingly more demanding basis sets², leading to the structure in Fig. 5.5 with the 6-31G* basis set (a clearer 3 dimensional structure is depicted in Fig. 5.6). Table 5.1 compares some selected bond lengths and angles of this structural optimisation with X-ray data from the literature [18].

Table 5.1 reveals that the DFT calculations are in good agreement with the experimental values. In particular, structural characteristics unique to the 10-membered azocrownether³ have been captured, such as the discrep-

²An initial optimisation calculation was carried out with the basis set STO-3G. The resulting geometry then used as the initial guess for an optimisation calculation at the 4-31G level, and the procedure repeated for the 6-31G* basis set. Such an approach is often more efficient than a single calculation with the most demanding basis set when the initial guess is believed to be far away from the optimal geometry

³as compared to the family of azocrown ethers differentiated by the size of the central

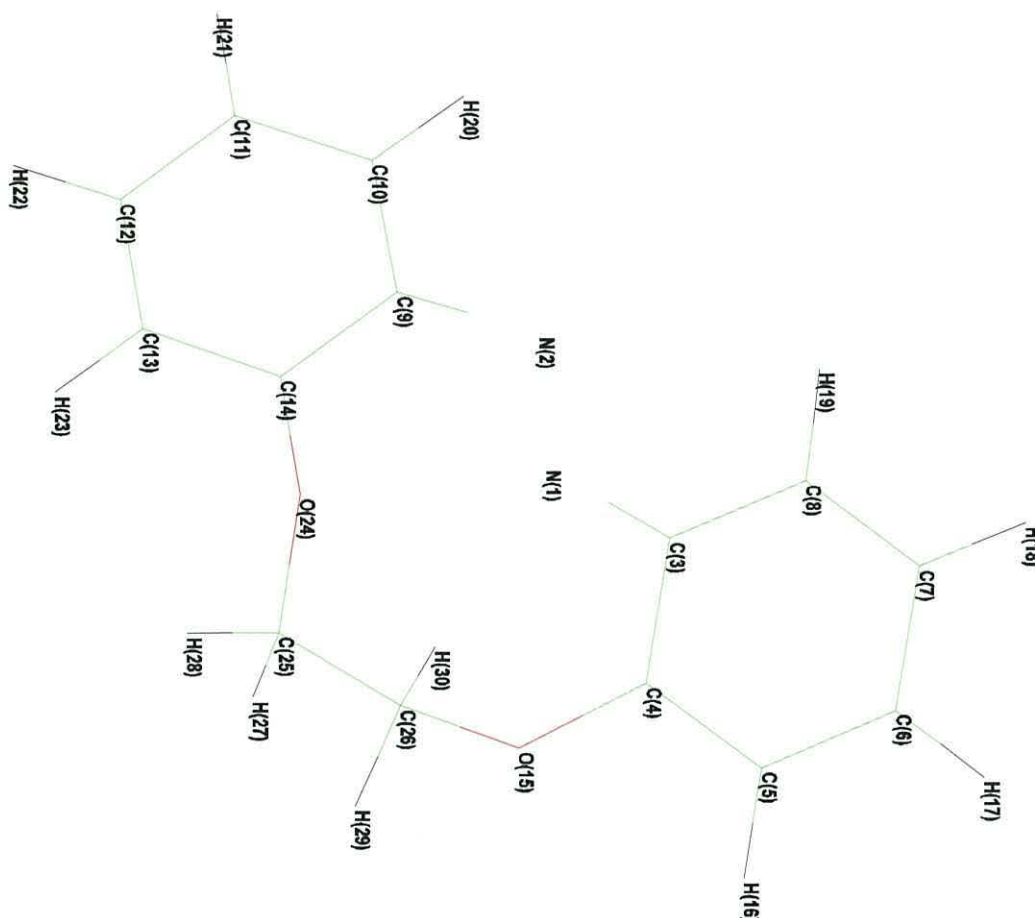


Figure 5.5: DFT optimised geometry of O2N2 with 6-31G* basis set.

ancy in the two $\angle\text{NNC}$ bond angles of the *trans* isomer arising from the strain caused by the relatively small ether linkage. The torsion angles around the C(3)-N(1) and C(9)-N(2) bonds are 163.52° and 31.69° respectively, indicating a different degree of π -conjugation of the azo-group with each benzene ring. Whereas the *trans* isomer is roughly planar in structure, the 10-membered macro-cycle of the *cis* isomer adopts a boat structure, see Fig. 5.6, again in agreement with the experimental data. The *cis* isomer of O2N2 is stable in comparison with its larger derivatives, and forms the most abundant oxygen containing macro-cycle [12, 13, 22, 23].

dant isomer in solution [18], it may be inferred that this relative stability arises from the large strain imposed on the *trans* conformer by the short ether linkage.

To generate the relevant potential energy functions, geometry optimisation calculations were performed along the coordinates of interest (using the B3LYP hybrid functional combined with 6-31G* basis set). For the inversion isomerisation coordinate, one $\angle\text{CNN}$ bond angle was held constant for each 10° interval between *trans* 81.49° angle, sweeping through to *cis* 98.51° angle. The PEF of the 1st excited state (S_1) was evaluated using TD-DFT single point excitation at each optimised geometry along the isomerisation coordinate. The S_0 and S_1 PEFs along the rotation isomerisation coordinates were evaluated in a similar manner, however this time the $\angle\text{CNNC}$ dihedral angle was held constant for each geometry optimisation and varied from the *trans* dihedral angle 180° to the *cis* dihedral angle 0° .

Fig. 5.6 illustrates the DFT S_0 and S_1 PEFs along the inversion coordinate. The ground state consists of an asymmetric double well with a large barrier to inversion of $12,000\text{ cm}^{-1}$ at $\angle\text{CNN} = 180^\circ$, analogous to the inversion potential of azomethane illustrated in Fig. 4.6 and the CASSCF inversion potentials of azobenzene[8, 10]. The S_1 PEF along the inversion coordinate is also an asymmetric double well with an energy barrier at $\angle\text{CNN} = 180^\circ$ of $\approx 4,000\text{ cm}^{-1}$ above the minimum in the S_1 *trans* well. As expected, there are many similarities with the inversion PEFs of azomethane, especially in the nature of the S_1 state where a four pulse control sequence (Chapter 4.2.3) may be required to maximise control of the isomerisation along the inversion coordinate.

In light of the recent computational investigations of refs. [11, 19] (where the torsional photoisomerisation pathway of azobenzenophane and a crown ether capped azobenzene were found to be feasible), the torsional isomerisation pathway of O2N2 was also investigated by variation of the $\angle\text{CNNC}$ dihedral angle. The results depicted in Fig. 5.7, which illustrates the S_0 and S_1 potentials along the torsional isomerisation coordinate of O2N2 together with the molecular geometries at relevant points along the S_0 PEF, shows

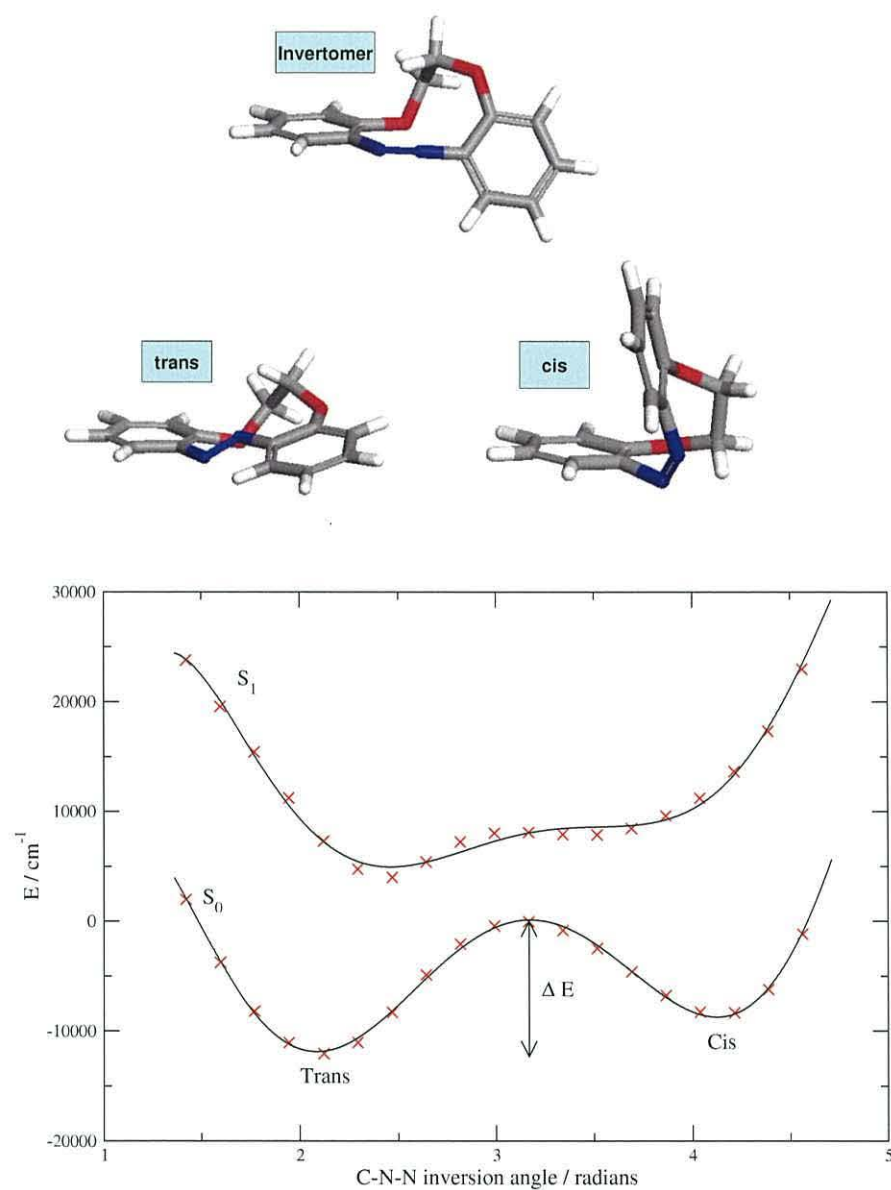


Figure 5.6: Ground S_0 and first excited S_1 electronic state potential energy functions along the inversion isomerisation coordinate. Crosses: energy relative to S_0 transition state of each individual DFT B3LYP/6-31G* calculation. Full line: polynomial series line of best fit of the DFT points. Top: optimised ground state geometries at the *trans* and *cis* minima, together with the invertomer transition state.

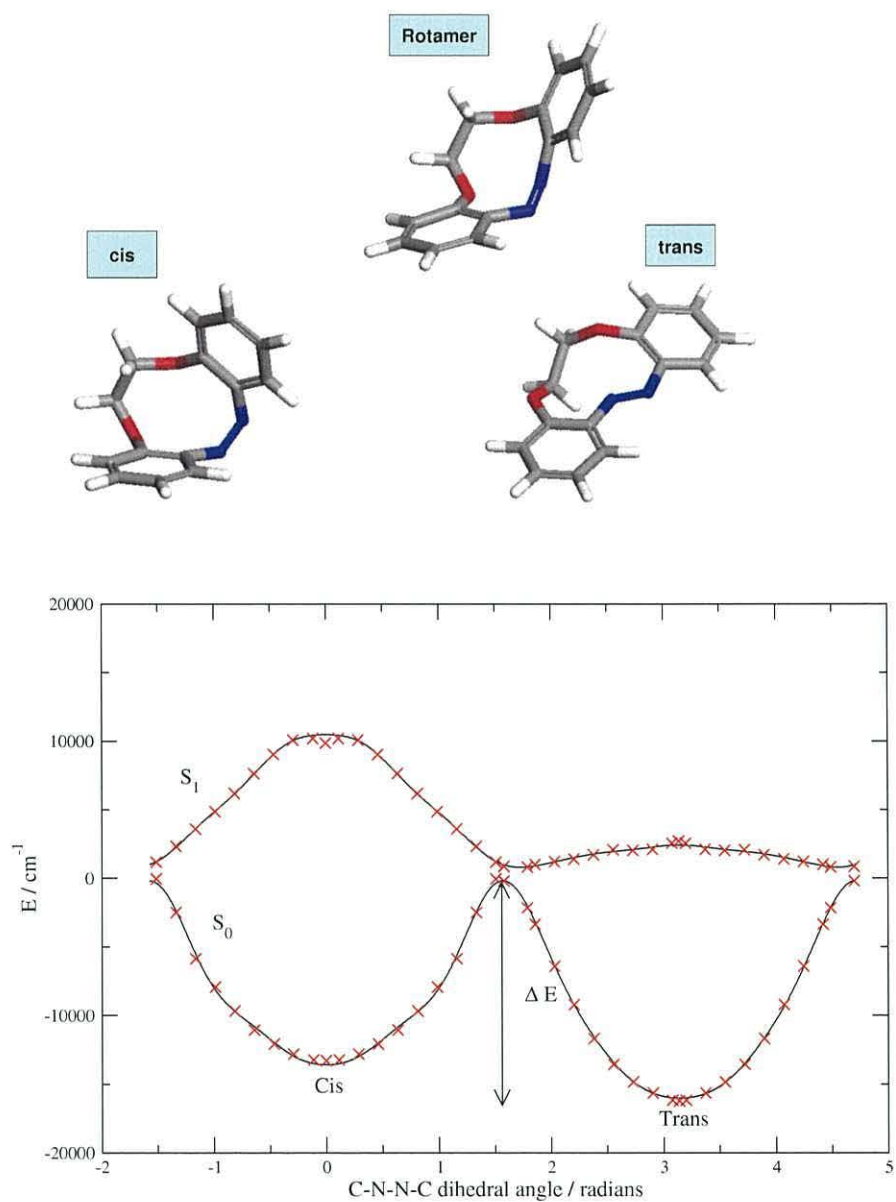


Figure 5.7: Ground S_0 and first excited S_1 electronic state potential energy functions along the torsional isomerisation coordinate. Crosses: energy relative to S_0 transition state of each individual DFT B3LYP/6-31G* calculation. Full line: Fourier series line of best fit of the DFT points. Top: optimised ground state geometries at the *trans* and *cis* minima, together with the rotamer transition state.

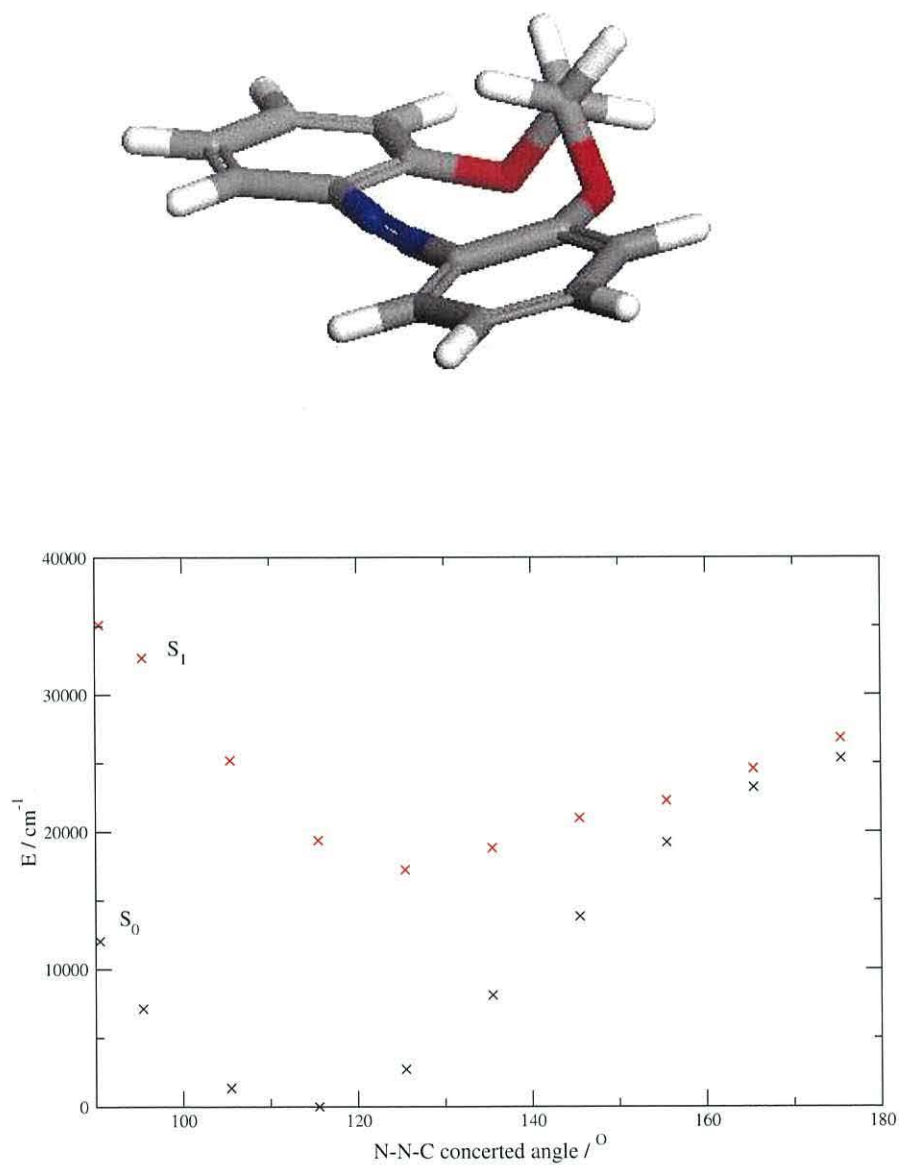


Figure 5.8: Ground S_0 and first excited S_1 electronic state potential energy functions along the concerted inversion coordinate. Crosses: energy relative to S_0 minimum of each individual DFT B3LYP/6-31G* calculation of the S_0 (black) and S_1 (red) states. Top: optimised S_0 geometry of O2N2 with each $\angle\text{NNC}$ held constant at 175.4877° .

that this pathway to isomerisation of O2N2 is likely unrestricted by the ether linkage. The ground electronic state S_0 consists of a periodic asymmetric double well potential with a torsional barrier height of $\Delta E = 16,078 \text{ cm}^{-1}$ above the *trans* minimum, at 90° $\angle\text{CNNC}$ dihedral angle, which is typical of a torsional barrier about a double bond [20]. The excited electronic state S_1 PEF is barrierless along the *trans-cis* torsional isomerisation coordinate and reaches a minimum at $\angle\text{CNNC} \approx 90^\circ$ which is $1,060 \text{ cm}^{-1}$ above S_0 . This feature rather resembles an avoided crossing and infers to the possible presence of a conical intersection nearby. The S_1 state PEF increases in energy when C-N-N-C approaches planarity, reaching a local maximum at the *trans* geometry and an ambiguous discontinuity at the *cis* geometry which is considerably higher in energy than the former. These results are similar to those of azomethane (Chapter 4.2.1) and azobenzene [10] where the torsional S_1 PEF were also found to be barrierless, and the steeper S_1 path for the torsion of *cis*-O2N2 compared to *trans*-O2N2 is also consistent with the shorter photoisomerisation time of *cis*-azobenzene [21].

Prompted by the *ab initio* work of Diau [10] on azobenzene, the concerted inversion pathway of O2N2 was also probed with DFT calculations. Again, the 6-31G* basis set was utilised and geometry optimisation calculations run where each $\angle\text{NNC}$ was held constant simultaneously, and repeated every 10° between 95.49° and 175.49° . Fig. 5.8 illustrates the PEF along the concerted inversion coordinate towards linearity of the C-N-N-C group. Similar to the corresponding investigations on azobenzene, the S_0 and S_1 states approach each other as the concerted $\angle\text{NNC}$ increases where the presence of a nearby conical intersection is a possibility⁴. Along the concerted minimum energy pathway azobenzene maintains a planar structure, however the ether linkage on the benzene rings of O2N2 imposes a constraint on its structure. Table 5.2 lists the variation of the $\angle\text{CNNC}$ dihedral angle with each optimised structure on the S_0 state along the concerted pathway. As the concerted $\angle\text{NNC}$ increases, the molecule is distorted further away from the planar *trans* dihedral angle of $\angle\text{CNNC}=180^\circ$. The ether linkage cannot be ‘stretched’ any further above $\angle\text{NNC}=165^\circ$ leading to an optimised structure

⁴for azobenzene a conical intersection is present at concerted $\angle\text{NNC}=157^\circ$ [10]

Table 5.2: Variation of C-N-N-C dihedral angle along concerted inversion coordinate of O2N2.

$\angle\text{NNC}$	$\angle\text{CNNC}$
115.49	-163.53
125.49	-161.96
135.49	-158.17
145.49	-154.53
155.49	-146.59
165.49	-122.70
175.49	5.01

with a *cis* conformation when $\angle\text{NNC}=175^\circ$.

Table 5.3 summarises the relative energies of the relevant conformations of O2N2 in kcal/mol. The relative energy of the concerted $\angle\text{NNC}=165^\circ$ geometry on the S_1 state is considerably higher than for the *trans* geometry, indicating that the concerted pathway is irrelevant upon $S_0 \rightarrow S_1$ excitation. The transition state (TS) along the torsional coordinate (rotamer) was found to be lower in energy than the TS along the inversion coordinate (invertomer) on the S_1 electronic state, leading to the conclusion that the photoisomerisation of O2N2 occurs predominantly via the torsional coordinate, in agreement with the recent theoretical data supporting the torsional mechanism of the parent azobenzene molecule [8, 10]. In contrast, on the ground electronic state the invertomer TS is lower in energy, leading to the conclusion that the thermal *cis* \rightarrow *trans* isomerisation occurs via the inversion mechanism, again in agreement with the theoretical studies on the parent azobenzene molecule [7]. Furthermore, the difference in energy between the invertomer TS and the *cis* minimum is calculated as 26.4 kcal/mol, in satisfactory agreement with the kinetically derived activation energy of 28.2 kcal/mol for the thermal reaction [12]⁵.

The UV/vis spectrum of *trans*-O2N2 [13] consists of two broad bands, the first intense peak with a range of $\approx 280\text{-}380$ nm has been assigned to the $S_2(\pi \rightarrow \pi^*)$ transition, and the second (less intense) band has been assigned

⁵where a range of 19.0 to 28.5 kcal/mol was calculated for the activation energies of the ether linked family of azobenzene derivatives

Table 5.3: Summary table of the relative energies of the most relevant O2N2 conformations in kcal/mol, where the *trans* minimum serves as an arbitrary zero point. *minimum along torsional coordinate with $\angle\text{CNNC}$ held constant; # $\angle\text{NNC}$ held constant along inversion coordinate.

Geometry	$\angle\text{NNC}$	$\angle\text{CNNC}$	$\Delta E (S_0)$	$\Delta E (S_1)$	$S_0 \rightarrow S_1$ (nm)
trans-	121.49	-173.45	0.00	55.38	516
	108.38				
*trans-	122.36	180.00	0.34	54.61	527
	108.45				
cis-	124.32	-9.21	10.67	73.54	455
	#118.51				
*cis-	122.30	0.00	7.98	75.05	426
	121.32				
invertomer-	#178.51	-31.86	34.38	57.64	1229
	119.15				
rotamer-	123.46	90.55	46.31	49.34	9436
	122.38				
165concerted	165.49	-122.70	70.39	74.35	7220
	165.49				
175concerted	175.49	5.01	76.44	80.74	6649
	175.49				

to the $S_1(n \rightarrow \pi^*)$ transition $\approx 440\text{-}540$ nm. While the calculated DFT S_1 transition lies within this range, the quality of this value, and the subsequent *cis*-O2N2 value, is inconclusive. The UV/vis spectrum of *cis*-O2N2 have bands in the same area, however they are blue shifted compared to the *trans* isomer, and the $S_2(\pi \rightarrow \pi^*)$ has a much diminished relative intensity, which serves as a means of observing the extent of the photoisomerisation reaction against time.

5.2.2 Control of O2N2 Isomerisation Along Inversion Coordinate

An average value of $\mu = 0.4759$ a.u. was extracted from the DFT calculations for the transition dipole moment between the S_0 and S_1 electronic states, and a value of $M_\mu = 4,805,000$ a.u. assigned for the reduced mo-

Table 5.4: Polynomial coefficients for the ground S_0 and first excited S_1 PEFs along the inversion coordinate. i.e. $y = \sum_n A_n x^n$

n	A_n S_0 -state	A_n S_1 -state
0	-575270.618791580	-750077.525814772
1	1601183.38929005	1908336.60339661
2	-1679472.05979195	-1828844.41598225
3	858242.143171120	874381.357294035
4	-228791.940138745	-223092.633472967
5	30519.4424923003	29047.3450827777
6	-1605.18669616180	-1514.82113570580

ment of inertia⁶. In Chapter 4.2.3 it was shown how a low value for μ can severely limit the possibility of control, however the value for this system is significantly greater than that for azomethane and hence a greater control of the wavepacket dynamics may be expected. All calculations were carried out with a time step $\Delta t = 1$ a.u., and the ground vibrational state of the S_0 *trans* well was taken as the initial wavepacket $\Psi(0)$. Due to the large size of the system a minimum of 2048 grid points were required for the dynamical calculations. The interpolation schemes utilised in Chapter 4 proved ineffective in generating such a large amount of points, hence a polynomial trend line of the type

$$y = \sum_n A_n x^n \quad (5.1)$$

was used to describe the S_0 and S_1 PEFs with the coefficients ' A_n ' listed in Table 5.4.

Qualitatively, the S_0 and S_1 PEFs along the inversion isomerisation coordinate are very similar to those of azomethane, the *trans* \rightarrow *cis* pathway is still impeded on the S_1 PEF by a significant barrier at $\angle \text{NNC} = 180^\circ$, while the reverse process is less obstructed. Perhaps the most significant difference is in the location of the *trans* and *cis* minima on the excited state, where they are shifted further towards the linear $\angle \text{NNC} = 180^\circ$ geometry (compare Figures 4.6 and 5.6). A Franck-Condon vertical transition will therefore pro-

⁶for details see Appendix B

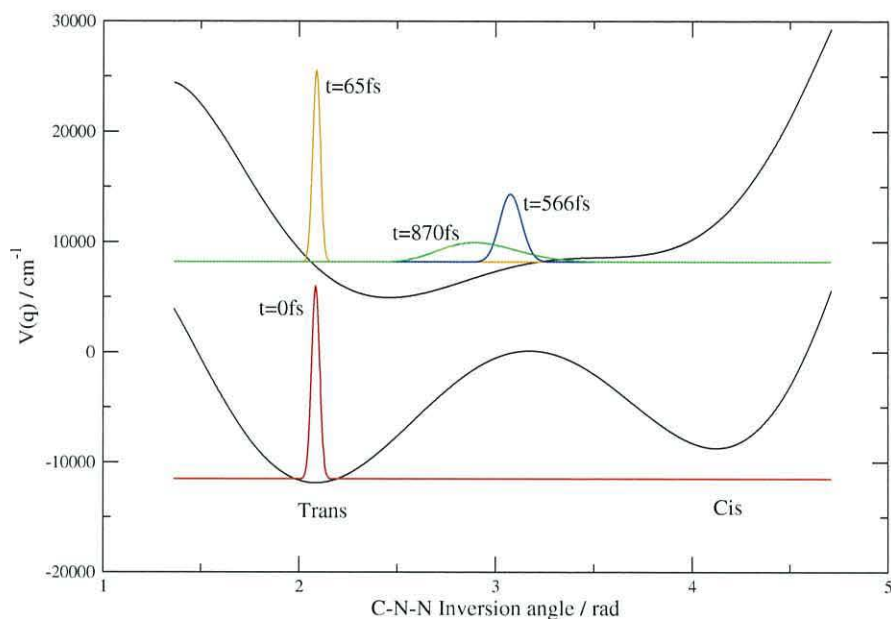


Figure 5.9: Wavepacket snapshots at various times before and after excitation to the S_1 state via the pump pulse illustrated in Fig. 5.11.

duce a vibrationally hot wavepacket on the S_1 state which may have sufficient energy to overcome the barrier to inversion.

Fig. 5.9 illustrates wavepacket snapshots on the S_1 state following a vertical excitation from the S_0 state by the 1st π -pulse in the sequence depicted in Fig. 5.11. Despite the displaced minimum of the S_1 state, the wavepacket still has insufficient energy to overcome the energy barrier in significant proportions, hence a multi-pulse strategy as described in Chapter 4.2.3 must be implemented again to maximise the yield of the photoisomerisation.

Fig. 5.10 depicts wavepacket snapshots during a calculation where the system is subject to the pulse sequence illustrated in Fig. 5.11. By direct observation of the wavepacket dynamics the appropriate centre time t_n , and carrier frequency ω_n , for the final three pulses were chosen to complete the pulse sequence. In contrast to azomethane, shorter pulse durations could be utilised, which helped maintain the locality of the majority of the wavepacket and consequently more control could be achieved with an eventual yield of 0.85 *cis*-O2N2.

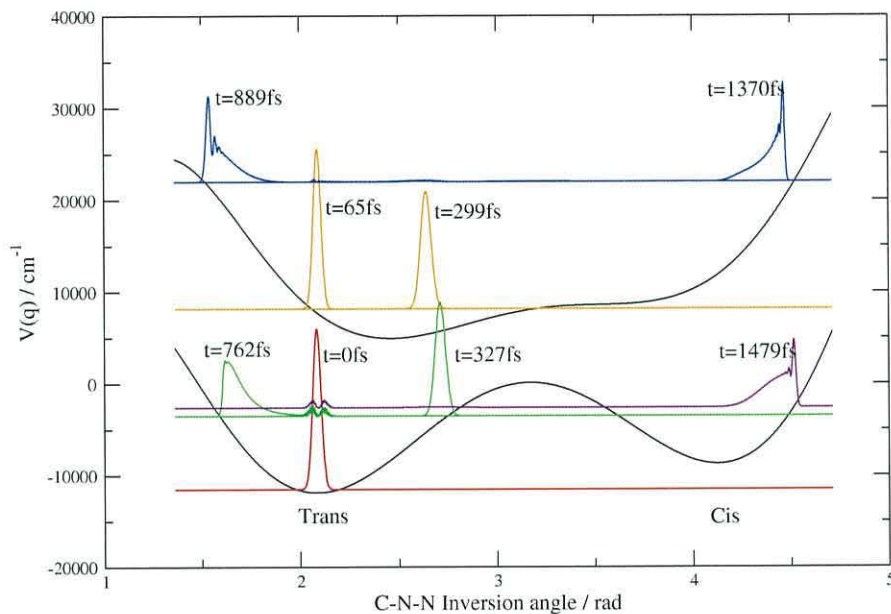


Figure 5.10: Wavepacket snapshots at various times before and after excitation to the S_1 state via the pulse sequence illustrated in Fig. 5.11.

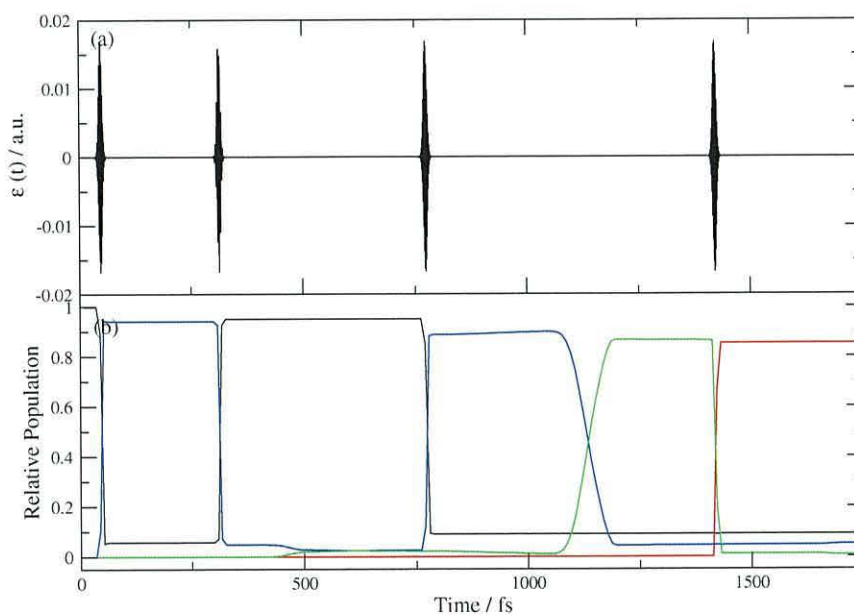


Figure 5.11: (a): 4 Pulse sequence pump-dump-pump-dump. Pulse parameters in Table 5.5 (b): corresponding time dependent populations black= $trans-S_0$, red= $cis-S_0$, blue= $trans-S_1$, green= $cis-S_1$.

Table 5.5: Pulse parameters for the pulse sequence illustrated in Fig. 5.11

Pulse n	t_n / fs	ω_n / a.u.	γ_n / a.u.	A_n / a.u.
1 (pump)	48	0.08960	2.056×10^{-5}	0.01689
2 (dump)	313	0.04626	2.056×10^{-5}	0.01689
3 (pump)	774	0.10842	2.056×10^{-5}	0.01689
4 (dump)	1422	0.11067	2.056×10^{-5}	0.01689

Window (b) of Fig. 5.11 is an excellent illustration of the intended result of the 4 pulse sequence. The initial pulse excites 0.94 of the wavepacket to the S_1 state and the second pulse dumps the majority of this wavepacket density at the turning point of the *trans* well generating a vibrationally hot wavepacket on the ground state. A third pulse re-excites the wavepacket at the opposite extremity of the S_0 *trans* well generating a wavepacket on the S_1 surface with sufficient momentum to overcome the inversion barrier at $\angle\text{NNC} = 180^\circ$. The final pulse dumps the wavepacket in the *cis* well with a yield of 0.85. Note that the most inefficient pulse in terms of wavepacket transfer is the initial pulse, each subsequent electronic state transfer occurs at a turning point of an oscillation where the wavepacket is more localised leading to a more successful transfer of probability density.

Optimal Control

The Krotov approach of OCT (Chapter 4.1.2) was implemented to increase the yield of the photoisomerisation, where the field depicted in Fig. 5.11 was the initial guess $\epsilon^0(t)$. To maintain the 4 pulse profile of the initial guess throughout the optimisation procedure, the overlap integral was used as a refinement on the field of the previous iteration, rather than a replacement

$$\epsilon^k(t) = \epsilon^{k-1}(t) - S(t) \frac{\mu}{\lambda \hbar} \Im(\langle \chi_e(t) | \psi_g(t) \rangle - \langle \psi_e(t) | \chi_g(t) \rangle). \quad (5.2)$$

where $S(t) = \sin^2\left(\pi \frac{t}{t_f}\right)$ is a shape function which ensures the smooth ‘on’ and ‘off’ transition of the electric field, and a large penalty factor $\lambda = 40$ was utilised to ensure small variations at each iteration k . As was the case

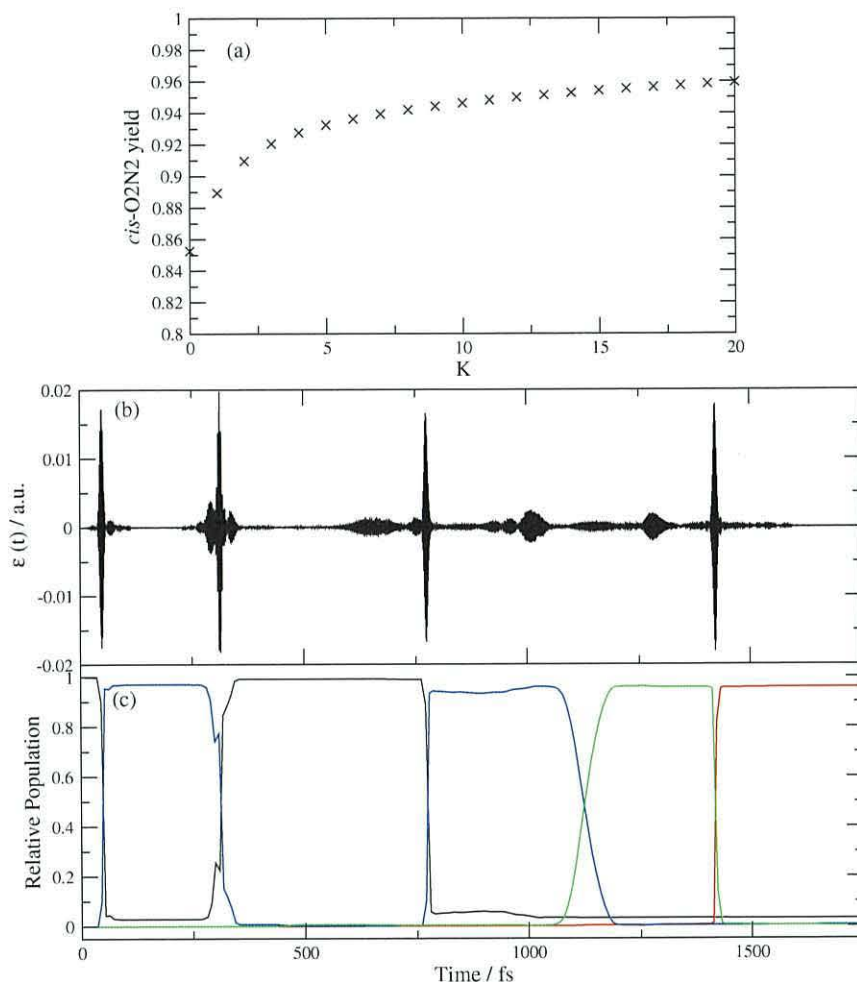


Figure 5.12: (a): Plot of *cis*-O₂N₂ yield against *k*. (b): The optimised field after 40 iterations and (c): the corresponding time dependent populations black=*trans*-*S*₀, red=*cis*-*S*₀, blue=*trans*-*S*₁, green=*cis*-*S*₁.

for azomethane, the *cis* well of the ground state was used as the target state $|\chi(t_f)\rangle = P|\psi(t_f)\rangle$.

Fig. 5.12 illustrates the progress of the procedure at each iteration '*k*'. After 20 iterations, the electric field generated successfully transfers 0.96 of the wavepacket density in the *S*₀ *cis* well without reaching a plateau, leading to possible refinement with further iterations. As expected, the optimised field has maintained the four pulse profile of the initial guess, and the time dependent relative populations confirm that the mechanism of isomerisation

is largely unchanged from that of the initial guess. It is clear, however, that each population inversion is increased in efficiency with additional electric field amplitude in-between the main 4-pulse framework making a significant contribution to the improvement in yield.

5.2.3 Control of O2N2 Isomerisation Along Torsional Coordinate

Along the $\angle\text{C-N-N-C}$ torsional coordinate (Fig. 5.7) the S_1 PEF is barrierless similar to the azomethane molecule, hence a similar pulse strategy may be utilised. An average value of $\mu = 0.4496$ a.u. was extracted from the TD-DFT calculations for the transition dipole moment between the electronic states of interest, and a value of $M_\mu = 3,500,000$ a.u. assigned for the reduced moment of inertia. All calculations were carried out with a time step of $\Delta t = 1$ a.u., and the ground vibrational state of the S_0 *trans* well was taken as the initial wavepacket $\Psi(0)$. Due to the large size of the system a minimum of 2048 grid points were required for the dynamical calculations. The interpolation schemes utilised in Chapter 4 proved ineffective in generating such a large amount of points, hence a Fourier series trend line of the type

$$y = \sum_n A_n \cos(nx) \quad (5.3)$$

was used to describe the S_0 and S_1 PEFs with the coefficients ' A_n ' listed in Table 5.6.

Fig. 5.13 illustrates instantaneous wavepacket snapshots at various times during a quantum dynamical calculation where the system is under the influence of the pulse sequence depicted in Fig. 5.14 (a). The initial pulse transfers nearly all the wavepacket density to the S_1 electronic state, which subsequently remains localised while propagating away from the Franck-Condon region eventually crossing into the *cis* conformation after $\approx 1,500$ fs (see relative time dependent populations in Fig. 5.14 (b)). The wavepacket is dumped into the S_0 *cis* well by the second laser pulse with an overall yield of 0.26, where the main limiting factor may be attributed to the inefficiency of the

Table 5.6: Fourier series coefficients for the ground S_0 and first excited S_1 PEFs along the torsional coordinate. i.e. $y = \sum_n A_n \cos(nx)$

n	A_n S_0 -state	A_n S_1 -state
0	-9236.58004588964	3968.20183867105
1	1113.59759214316	3771.23399728101
2	-6653.12835089107	2610.79258167755
3	332.850907966519	337.124379738442
4	1535.45361969678	-160.546501868345
5	-204.549344497146	38.6385740784863
6	-653.156945321873	108.474161729076
7	-71.3423317843183	-65.9249615854695
8	203.760127455666	-81.6161914217347
9	41.7339919125297	-54.3677495754957

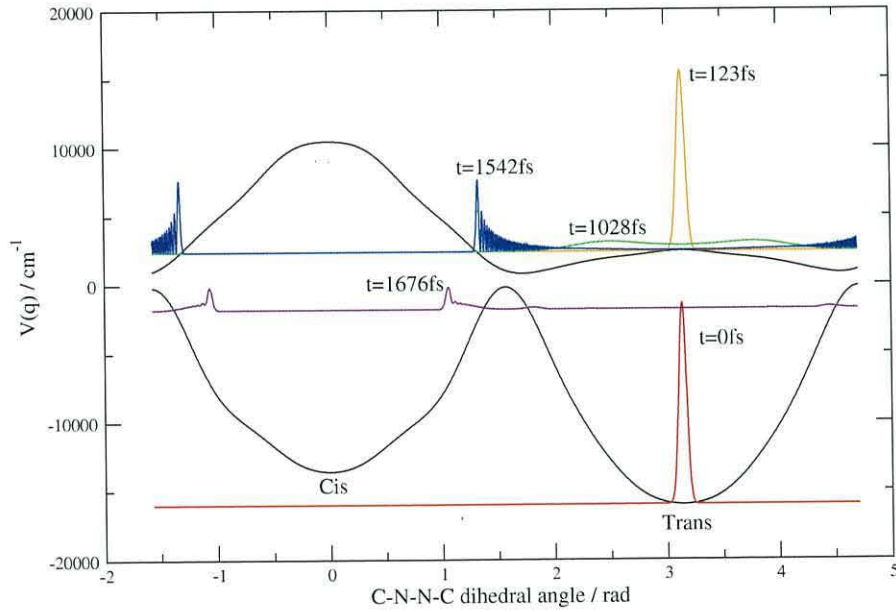


Figure 5.13: Wavepacket snapshots at various times before and after excitation to the S_1 state via the pulse sequence illustrated in Fig. 5.14 (a).

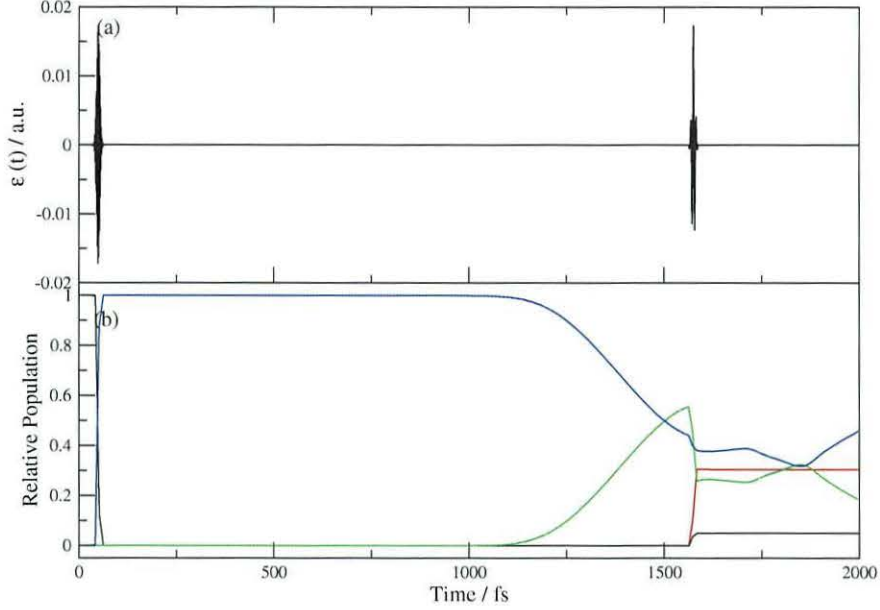


Figure 5.14: (a): pump pulse parameters $A_1 = 0.01737$ a.u., $\gamma_1 = 1.945 \times 10^{-5}$ a.u., $\omega_1 = 0.08399$ a.u. dump pulse parameters the same with $\omega_2 = 0.02172$ a.u. (b): corresponding time dependent populations black= $trans$ - S_0 , red= cis - S_0 , blue= $trans$ - S_1 , green= cis - S_1 .

second pulse due to the requirement of dumping onto a steep section of the S_0 PEF.

Optimal Control

The Krotov approach of OCT was again implemented to increase the yield of the photoisomerisation. A two Gaussian pulse sequence⁷ similar to the one depicted in Fig. 5.14 was used as the initial guess $\epsilon^0(t)$, however the pulses were condensed in amplitude to allow a greater ‘leeway’ for the optimal control algorithm and prevent the outcome from exceeding the previously decided maximum pulse amplitude of 0.0236 a.u., which corresponds to a pulse intensity of 20 TW/cm². The S_0 *cis* well was used as the target state, $|\chi(T)\rangle = P|\psi(T)\rangle$, for the procedure.

Again, the relation in Eq. (5.2) was used for the new electric field at

⁷each with width $\gamma_n = 9.45 \times 10^{-6}$ a.u. and maximum field amplitude $A_n = 0.01212$ a.u.

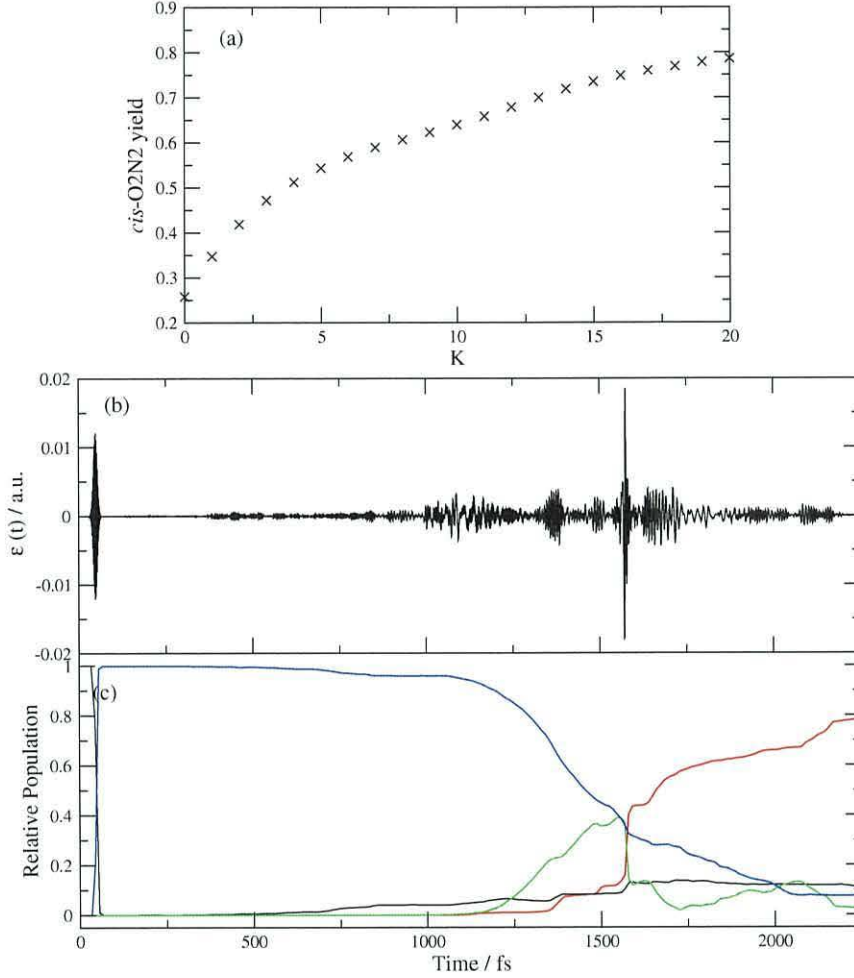


Figure 5.15: (a): Plot of *cis*-O₂N₂ yield against *k*. (b): The optimised field after 20 iterations and (c): the corresponding time dependent populations black=*trans*-S₀, red=*cis*-S₀, blue=*trans*-S₁, green=*cis*-S₁.

each iteration, where a large penalty $\lambda = 62.5$ was used and the process allowed to proceed for 20 iterations. Fig. 5.15 (a) depicts the progress of the procedure at each iteration, where the yield of the isomerisation eventually reaches a value of 0.79 when $k = 20$. The gradient of the progress line at $k = 20$ suggests further refinement of the optimised pulse may be achieved via additional iterations of the optimal control algorithm. Fig. 5.15 (b) is an illustration of the optimised pulse, where it is evident that the two pulse pump-dump mechanism has been maintained, and the main contribution to

the increase in yield is by the increased effectiveness of the dump pulse. Comparing the optimised pump pulse (which is largely unchanged, and has a similar profile to the second pulse of the initial guess $\epsilon^0(t)$) with the dump pulse, it is evident that the dump pulse has increased significantly both in width and maximum amplitude, and significant product is produced by the low amplitude section of the pulse between 1,600 fs and 2,200 fs.

Observing the corresponding time dependent populations (Fig. 5.15 (c)) reveals which sections of the optimised pulse (which has some amplitude throughout) are effective in wavepacket density transfer. While it is apparent that the smaller frequency (ω) second pulse of the optimised field begins at ≈ 400 fs, actual transfer from the S_1 *cis* well to the S_0 *cis* well (represented by ‘green’ and ‘red’ in Fig. 5.15 (c) respectively) does not occur until $\approx 1,200$ fs, consequently large parts of the optimised field are redundant. A final ‘blip’ of small amplitude electric field centred at $\approx 2,150$ fs transfers the final 12% of the wavepacket density into the S_0 *cis* well, demonstrating that while large portions of the optimised field may have little contribution to the reaction, other inconspicuous sections may have a more significant effect. It may therefore be envisaged that manual analysis of the optimal control field, in conjunction with the relative time dependent populations, may lead to the generation of a new control field with a less complex profile, and as such more attainable experimentally.

5.2.4 Control of O2N2 Isomerisation: *cis* \rightarrow *trans*

So far, only the *trans* \rightarrow *cis* isomerisation has been discussed. Table 5.3 compares the relative energies of the key structures on the PES of the O2N2 molecule. The relative energy of the *cis* structure on the S_1 surface is considerably higher than the transition states along both the inversion and torsional isomerisation coordinates, hence it seems a two pulse sequence will be sufficient for control along either coordinate.

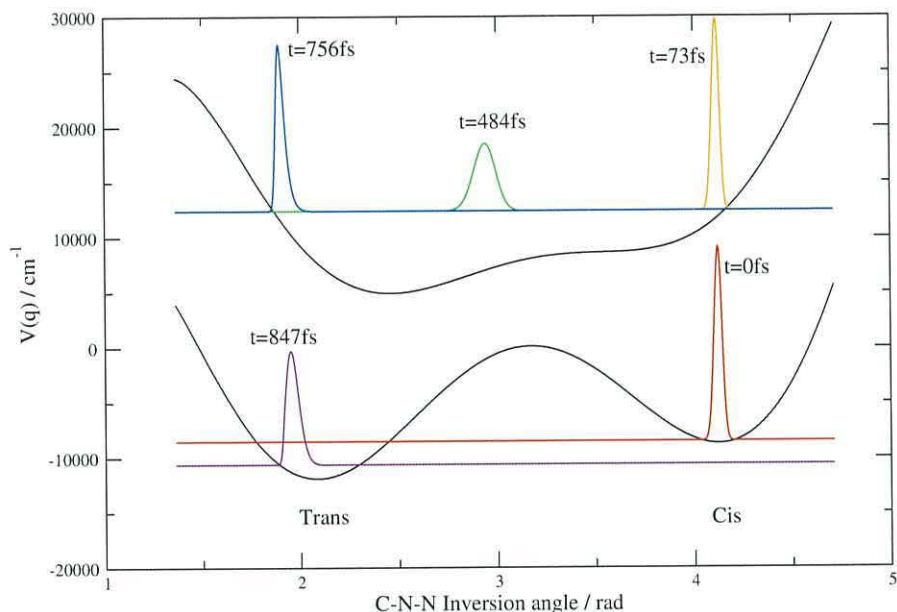


Figure 5.16: *cis* \rightarrow *trans* isomerisation wavepacket snapshots, along inversion coordinate, at various times before and after excitation to the S_1 state via the pulse sequence illustrated in the top panel of Fig. 5.17.

C-N-N Inversion Coordinate

Examination of the S_0 and S_1 PEF's along the inversion coordinate (Fig. 5.6) confirms that a wavepacket in the S_0 *cis* well excited vertically to the S_1 state will have an un-obstructed route towards the desired *trans* conformation. The same computational parameters of section 5.2.2 were used for these dynamical calculations, except the ground vibrational state of the S_0 *cis* well was taken as the initial wavepacket $\Psi(0)$.

Fig. 5.16 illustrates the time evolution of the wavepacket under the influence of the two pulse sequence depicted by window 1.(a) of Fig. 5.17. The initial pump pulse transfers 0.95 of the wavepacket density to the S_1 state, generating a localised wavepacket on the excited state potential function. Propagating away from the Franck-Condon region, the wavepacket demonstrates typical oscillatory behaviour within an enclosed well by expanding at the centre of the well and contracting at the turning points. The timing of the dump pulse was therefore aimed to coincide with the wavepacket

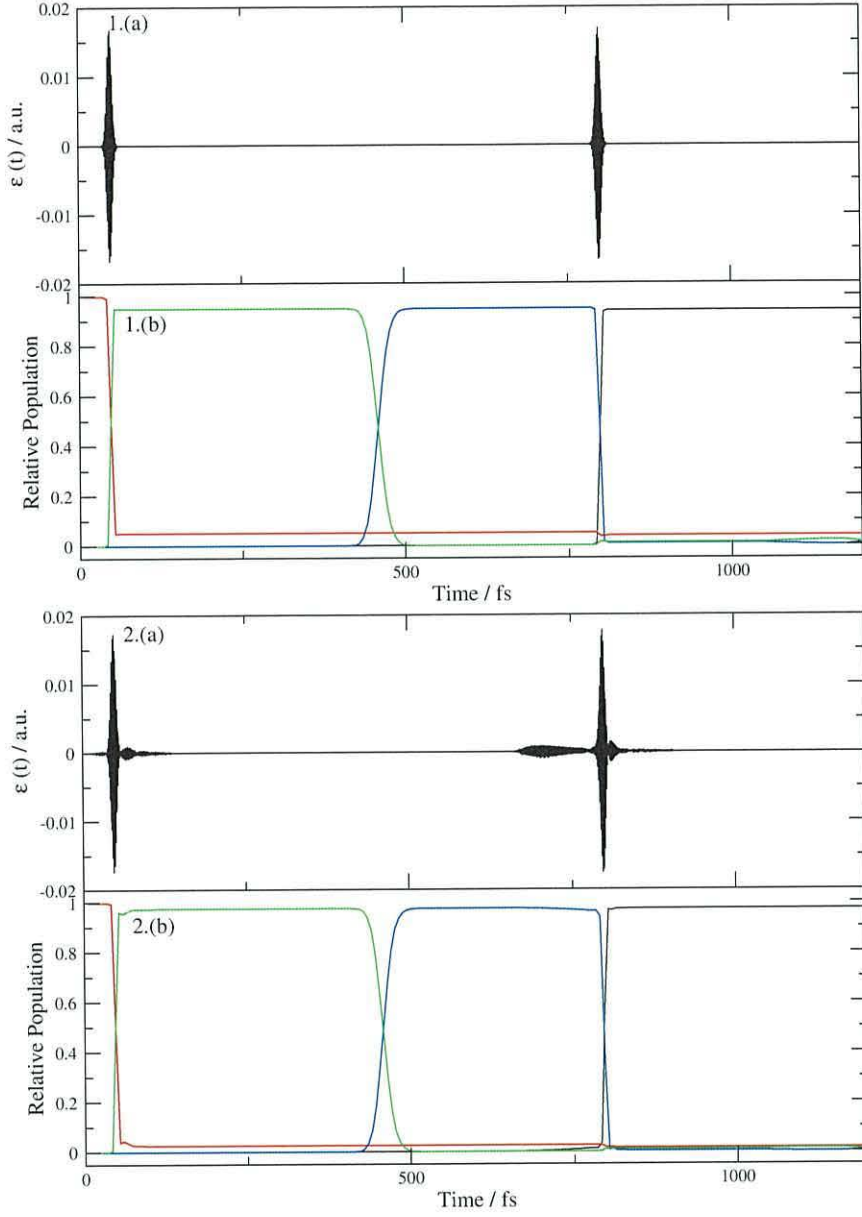


Figure 5.17: 1.(a): The initial guess field for *cis* \rightarrow *trans* isomerisation along the inversion coordinate. Parameters - $\gamma_1 = 2.056 \times 10^{-5}$ a.u., $A_1 = 0.01689$ a.u., $\omega_1 = 0.09330$ a.u., $\omega_2 = 0.10127$ a.u. and the corresponding time dependent populations (1.(b)). 2.(a): The optimised field after 20 iterations and the corresponding time dependent populations (2.(b)) black=*trans*- S_0 , red=*cis*- S_0 , blue=*trans*- S_1 , green=*cis*- S_1 .

localised at the turning point above the *trans* well (798 fs), and hence 0.94 of the total population is successfully dumped into the product well of the ground state.

Employing this pulse sequence as an initial guess $\epsilon^0(t)$, an optimal control procedure was implemented. Again, the relation of Eq. (5.2) was used to produce the improved field at each iteration, implemented with a penalty factor of $\lambda = 62.5$, and the S_0 *trans* well used as the target state $|\chi(t_f)\rangle = P|\psi(t_f)\rangle$. After 20 iterations the electric field (Fig. 5.17 - 2.(a)) was generated which increased the product yield of *trans*-O2N2 to 0.98. It is apparent from the corresponding time dependent populations (Fig. 5.17 - 2.(b)) that the increase in yield is mainly a consequence of the additional field amplitude arising immediately after the initial pump pulse, and the portion directly preceding the main dump pulse.

C-N-N-C Torsion coordinate

Examination of the S_0 and S_1 PEF's along the torsional coordinate (Fig. 5.7) verifies that a wavepacket in the S_0 *cis* well excited vertically to the S_1 state will have an un-obstructed route towards the desired *trans* conformation. The same computational parameters of section 5.2.3 were used for these dynamical calculations, except the ground vibrational state of the S_0 *cis* well was taken as the initial wavepacket $\Psi(0)$.

Fig. 5.18 illustrates the time evolution of the wavepacket under the influence of the two pulse sequence depicted by window 1.(a) of Fig. 5.19. The first pulse is successful in transferring 0.9998 of the wavepacket density to the S_1 state, generating an initially localised wavepacket at $\angle\text{CNNC} = 0$ radians. Since the wavepacket is higher in energy than the highest point of the S_1 PEF it is partially composed of the highly delocalised free-rotor eigenstates. This results in the rapid delocalisation of the wavepacket as it propagates away from the Franck-Condon region ($t = 677$ fs and 1177 fs in Fig. 5.18) limiting the amount of control possible via a simple two pulse scheme. The timing of the dump pulse was chosen to coincide with the wavepacket's maximum located at $\angle\text{CNNC} = 3.14$ radians at $1,202$ fs. Due to the highly delocalised

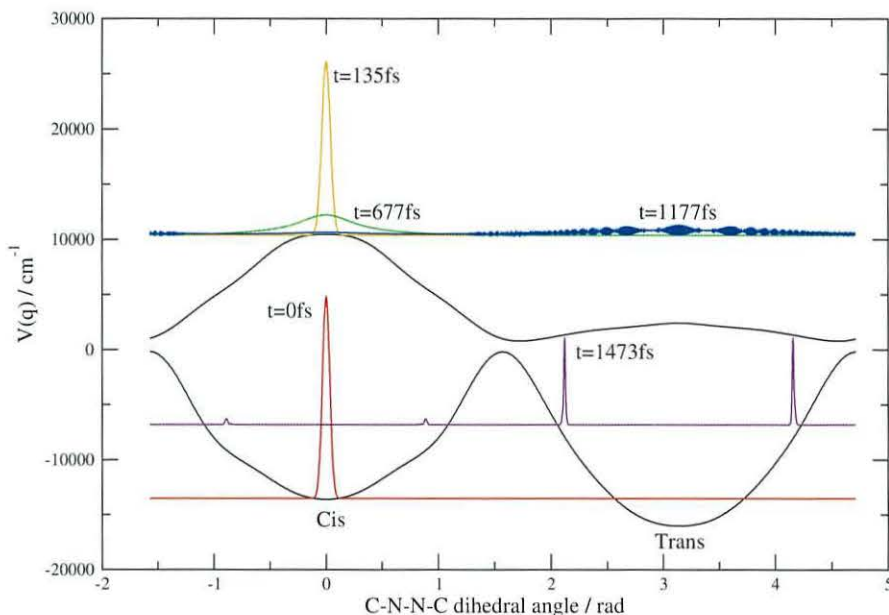


Figure 5.18: *cis* \rightarrow *trans* isomerisation wavepacket snapshots, along torsional coordinate, at various times before and after excitation to the S_1 state via the pulse sequence illustrated in the top panel of Fig. 5.19.

nature of the wavepacket a low yield of 0.22 *trans*-O₂N₂ is observed.

This pulse sequence (Fig. 5.19 - 1.(a)) was utilized as an initial guess field, $\epsilon^0(t)$, for a subsequent optimal control calculation. The relation of Eq. (5.2) was used to produce the improved field at each iteration, implemented with a penalty factor of $\lambda = 62.5$, and the S_0 *trans* well used as the target state $|\chi(t_f)\rangle = P|\psi(t_f)\rangle$. After 40 iterations the electric field (Fig. 5.19 - 2.(a)) was generated which increased the product yield of *trans*-O₂N₂ to 0.843. It is evident that the highly succesful pump pulse remains unchanged by the optimal control procedure, while the dump pulse is elongated to span over 800 fs due to the delocalised nature of the wavepacket on the S_1 PEF.

5.2.5 Effect of transition dipole moment and orientation

The interaction of an electromagnetic field with a molecule occurs predominantly between the electric field component of the radiation with the electric

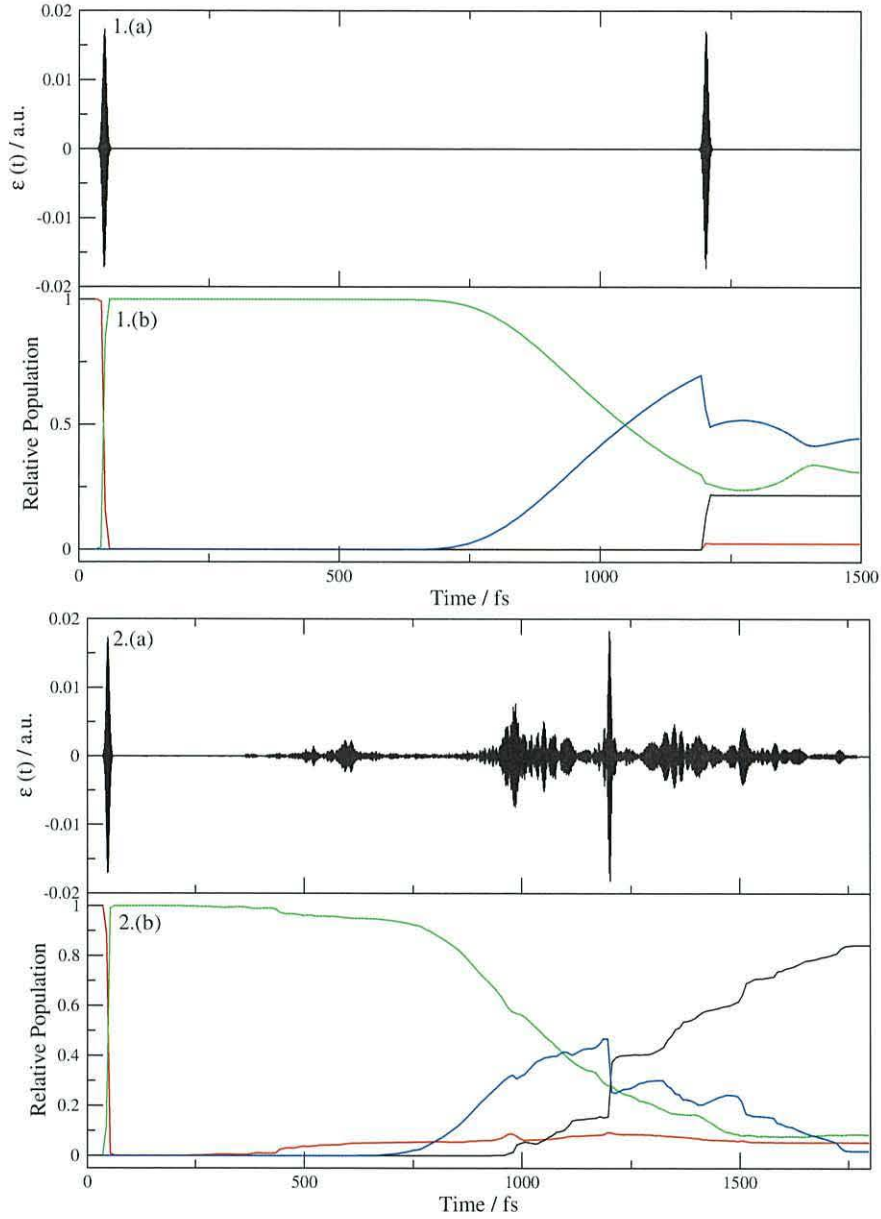


Figure 5.19: 1.(a): The initial guess field for *cis* \rightarrow *trans* isomerisation along the torsional coordinate. Parameters - $\gamma_1 = 1.945 \times 10^{-5}$ a.u., $A_1 = 0.01737$ a.u. $\omega_1 = 0.10964$ a.u., $\omega_2 = 0.08399$ a.u. and the corresponding time dependent populations (1.(b)). 2.(a): The optimised field after 40 iterations and the corresponding time dependent populations (2.(b)) black=*trans*- S_0 , red=*cis*- S_0 , blue=*trans*- S_1 , green=*cis*- S_1 .

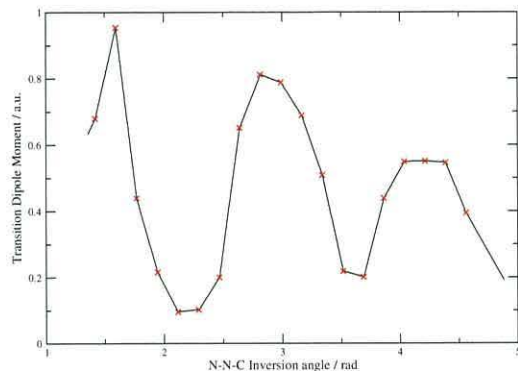


Figure 5.20: Variation of $S_0 \rightarrow S_1$ transition dipole moment (in a.u.) along the N-N-C inversion coordinate of O2N2. Crosses: TD-DFT values; Black: linear interpolation to produce the 2048 values required for the dynamical calculations.

dipole moment of the molecule (Chapter 2.3)

$$\vec{\mu} = \sum_i q_i \vec{r}_i. \quad (5.4)$$

The relative intensity of each vibronic transition is proportional to the square of the transition dipole moment (TDM) R for that particular transition

$$R_{ev} = \langle \psi'_{ev} | \mu | \psi''_{ev} \rangle. \quad (5.5)$$

So far, the electric field/dipole interaction has been treated in a simple manner, where the TDM has been treated as a constant along each isomerisation coordinate. However since the electric dipole moment⁸ $\vec{\mu}$ is a vector, in reality such a treatment is inadequate. During a torsional or large amplitude inversion motion it is clear, as the relative positions of the atoms change, that the direction and/or magnitude of the vector quantity $\vec{\mu}$ also varies, hence a coordinate dependent dipole moment $\mu(q)$ is necessary for a more complete treatment.

Not only is the field/molecule interaction dependent on the absolute magnitude of $\vec{\mu}$, but also on its relative orientation with respect to the incoming

⁸the character μ has been used interchangeably so far when describing the electric dipole moment *and* the TDM, in this section it will refer only to the former, and the character R for the latter.

electric field $\epsilon(t)$. Accordingly, an alternative parameter may be defined, μ_{eff} , which quantifies the magnitude of the component of the electric dipole *aligned* with the incoming electric field. Since the magnitude of μ_{eff} varies with the molecule's translational/rotational motion as well as its internal motion, it appears that its calculation is a formidable task. Certainly for a molecule in the gas phase not only does the randomness of the initial orientation of the molecule pose a difficult problem, the translational/rotational motion of the molecule varies the orientation *while* the interaction takes place. Computing μ_{eff} is greatly simplified when a molecule of fixed orientation is considered since its variation is solely dependent on the internal coordinate q , which is the case when a solid state system is considered⁹.

Fig. 5.20 illustrates the variation of the magnitude of the $S_0 \rightarrow S_1$ TDM with respect to the N-N-C inversion angle of O2N2 taken from the TD-DFT calculations of Section 5.2.1. While this relation for $R(q)$ does not take into account the relative orientation of the electric dipole and electric field, the purpose of this section is to illustrate the effect of a coordinate dependent TDM on the nature of the control pulses, and what potential obstacles may arise.

As an example, the system corresponding to *cis* \rightarrow *trans* isomerisation along the \angle NNC inversion coordinate was used, with the parameters described in Section 5.2.4. Fig. 5.21 compares the effect of an identical two pulse sequence on the system where a constant value for the TDM was considered for one example, and the coordinate dependent $R(q)$ depicted in Fig. 5.20 was used for the second example. Pulse parameters $\gamma_n = 7.93 \times 10^{-6}$ a.u. and $A_n = 0.01049$ a.u. were chosen to satisfy the π -pulse criteria for a constant TDM value of $R = 0.4759$ a.u.

$$A_\pi = \frac{R}{\hbar} \int_{t_0}^{t_\infty} A_n S(t) dt = \pi. \quad (5.6)$$

Of course, for the coordinate dependent ($R(q)$) case, the above equation is

⁹particularly appropriate in the case of azobenzene derivatives due to their proposed uses in optical data storage and nano devices.

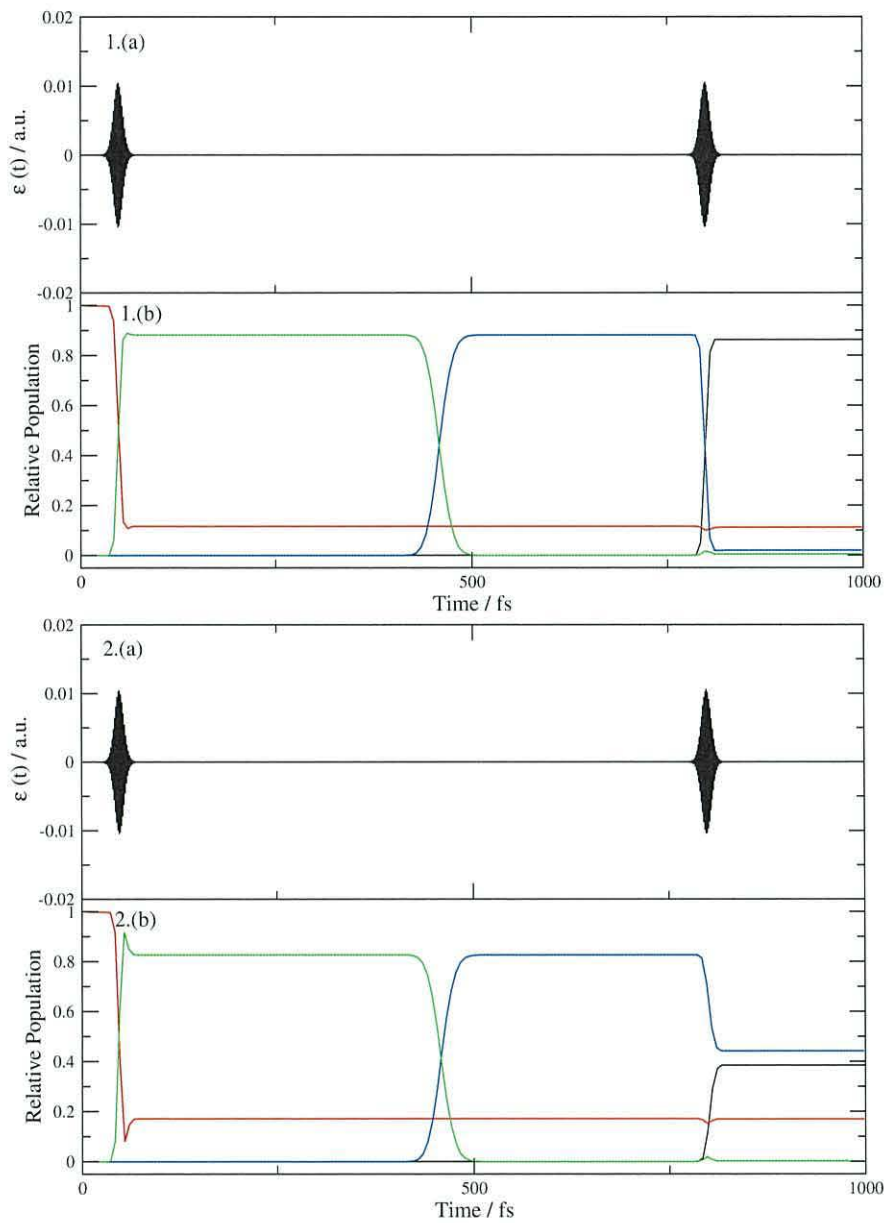


Figure 5.21: A two pulse sequence (a) and corresponding time dependent populations (b) for the *cis* \rightarrow *trans* isomerisation via \angle NNC inversion:- black=*trans*- S_0 , red=*cis*- S_0 , blue=*trans*- S_1 , green=*cis*- S_1 . 1. Constant transition dipole moment; 2. coordinate dependent TDM, $R(q)$, as depicted by Fig. 5.20.

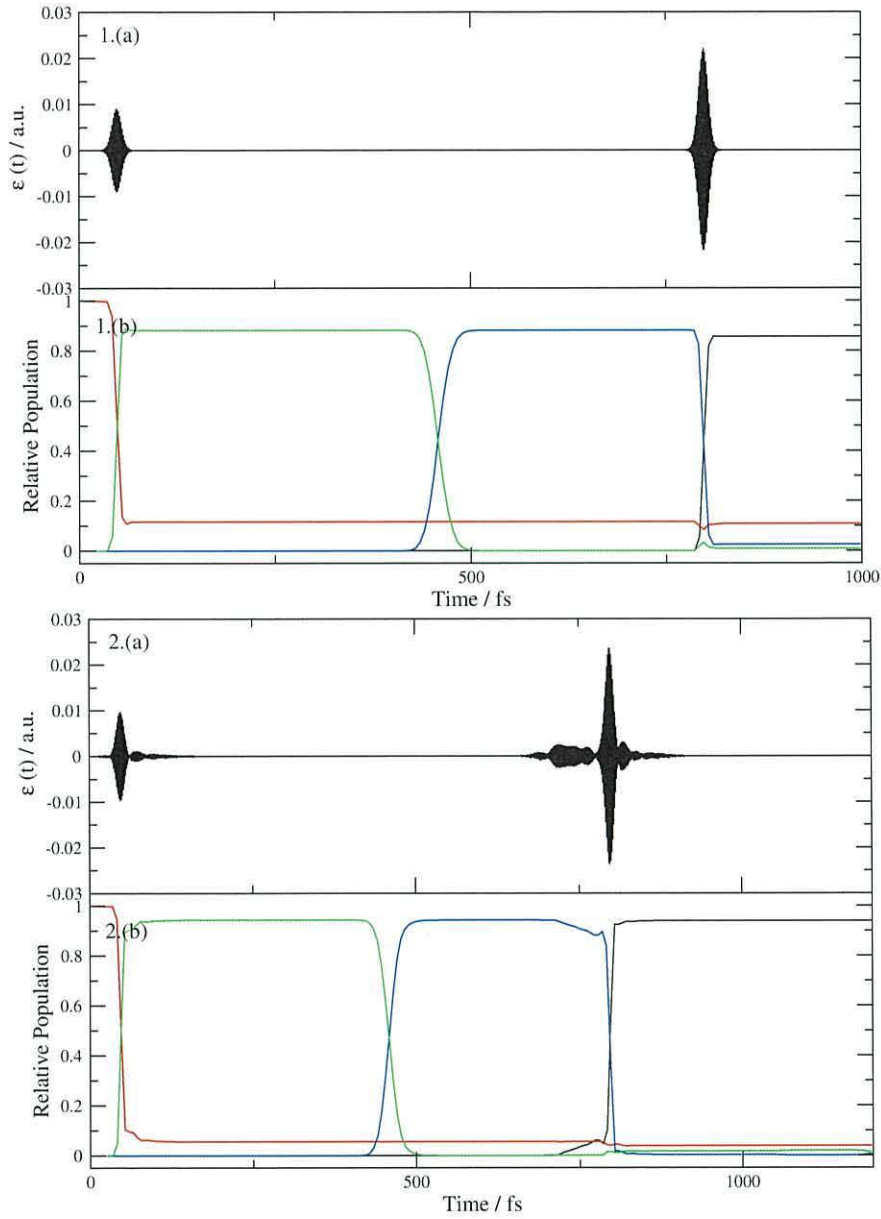


Figure 5.22: 1. The initial guess field (a) for *cis* \rightarrow *trans* isomerisation along the inversion coordinate and the corresponding time dependent populations (b), for the system with a coordinate dependent transition dipole moment (Compare with the coordinate independent scenario in Fig. 5.17). 2. (a) The optimised field after 20 iterations and the corresponding time dependent populations (b) black=*trans*- S_0 , red=*cis*- S_0 , blue=*trans*- S_1 , green=*cis*- S_1 .

not satisfied, hence the difference in the time dependent populations yielded in each case. The TDM of the molecule in the *cis* configuration ($\angle\text{NNC} \approx 4.2$ rad) is considerably higher than for the *trans* configuration ($\angle\text{NNC} \approx 2.1$ rad), therefore ' A_π ' for the pump pulse exceeds π and returns some of the excited population immediately back down to the S_0 state (depicted in green in Fig. 5.21 - 2.(b)). Conversely for the dump pulse $A_\pi < \pi$, consequently less than half of the excited wavepacket probability density is returned to the S_0 state.

While $R(q)$ will often have large variations along q , coupled with a complicated form, a simple relation can be employed to retrieve the yields exhibited by the case where $R = \text{const}$

$$R(q)A_n = \text{constant}. \quad (5.7)$$

By direct observation of the dynamics, the wavepacket's location (q) when an ultrafast laser pulse is applied can be determined, and hence A_n for this pulse can be adjusted manually via the relation in Eq. (5.7). Fig. 5.22 - 1.(a)/(b) illustrates the results of a calculation where the relevant A_n of each pulse have been adjusted in such a manner. A yield of 0.856 *trans*-O2N2 is produced, which is comparable to the yield of 0.862 produced by the $R(q) = \text{const}$ case. Using this manually modified pulse sequence as an initial guess, an optimal control procedure was implemented on the $R(q)$ system, with $\lambda = 40$, and the results for the 20th iteration presented in Fig. 5.22 - 2.(a)/(b). Reaching a yield of 0.95 *trans*-O2N2, it is apparent that a coordinate dependent TDM provides little restrictions on the effectiveness of the optimal control algorithm.

The results presented by Figures 5.21 and 5.22 show that laser control (computationally) of a molecular system when a coordinate dependent TDM is considered can yield results comparable to a system when the coordinate dependence is ignored. For a control scheme where the wavepacket's locality can be maintained, a rather crude relation (Eq. (5.7)) may be implemented with satisfactory results. Calculating the actual TDM from μ_{eff} , however, presents a tedious task, even for a molecule in a fixed orientation. In par-

ticular, determining the best orientation for the system may not be straight forward since a compromise must be found along the entire coordinate, i.e. for one value of q , μ_{eff} may be at a maximum, however for a different q the electric dipole moment $\vec{\mu}$ may be perpendicular to the incoming electric field, rendering $\mu_{eff} = 0$.

5.3 Summary and Discussion of Chapter

5.3.1 Mechanism of Isomerisation of O2N2

The precise nature of the photoisomerisation of azobenzene (and its derivatives) is an area of ongoing research. A vast amount of experimental and theoretical data have been reported [1]-[16][19, 21, 24], and various attempts have been made to rationalise these with the observed quantum yields for the reaction. For azobenzene, the isomerisation quantum yield is wavelength dependent with values of 0.24 and 0.11 reported for the visible $S_1(n \rightarrow \pi^*)$ and UV $S_2(\pi \rightarrow \pi^*)$ bands respectively [2]. A femtosecond time-resolved fluorescence study of *trans*-azobenzene (ref. [6]) determined that the isomerisation takes place exclusively on the S_1 state regardless of the initial excitation as a result of the short lifetime of the S_2 species. Recent *ab initio* [8, 10] and semi-empirical [15] investigations of the azobenzene's S_1 PES have revealed that the torsional mechanism is the most energetically favourable route for isomerisation. The discovery of a conical intersection (CI) along the concerted inversion coordinate [10] accounted for the different quantum yields observed for each excitation, as this internal conversion pathway to the S_0 state is only accessible following S_2 excitation.

Azobenzene derivatives where the phenyl rings are connected by a crownether or benzeneophane type structure Fig. 5.2 were long thought to be structurally restricted along the torsional isomerisation coordinate [4, 24]. During *inversion* about one N-N-C angle (Fig. 5.1), the rings of azobenzene remain in plane and hence the carbon atoms of each phenyl ring which were on the same side in the *trans* conformation, remain on the same side following the isomerisation. During the *torsional* isomerisation process, the phenyl

rings rotate with respect to each other and hence carbon atoms which were adjacent prior to isomerisation are on opposite sides of the molecule thereafter, hence this mechanism was believed to be restricted in species where the phenyl rings were connected. Recent theoretical investigations [11, 19], however, have determined that the torsional isomerisation pathway for these species are not only feasible, but also energetically favourable in comparison with the inversion pathway.

The DFT calculations of the present work (section 5.2.1) lead to the conclusion that the molecule O₂N₂ may also undergo photoisomerisation along the torsional coordinate on the S_1 electronic PES. The distance between the carbon atoms numbered C(14) and C(4) (see Fig. 5.5) is constrained by the ether linkage, and, in turn, the torsion about each C-N bond must vary during the torsional isomerisation to accommodate this. Fig. 5.23 illustrates the variation of the corresponding C(14)-C(9)-N(2)-N(1) and C(4)-C(3)-N(1)-N(2) dihedral angles with respect to the C-N-N-C torsional coordinate. During the *trans* \rightarrow *cis* isomerisation, the relative positions of the phenyl rings gradually change from slightly off-planar when in the *trans* conformation, to values of $\angle\text{CCNN} \approx 90^\circ$ where the rings face each other in the *cis* conformation.

The concerted inversion pathway is presumed to be available for a vibrationally hot wavepacket in the S_1 state of azobenzene, accounting for the disparity in quantum yield between S_1 and S_2 excitation¹⁰. For rotation-restricted azobenzene derivatives, the same quantum yields are observed for both S_1 and S_2 excitation [4, 24], initially explained by the absence of the torsional pathway. Recent theoretical investigations of the same molecules [11, 19] have revealed the feasibility of the torsional pathway, and the quantum yields are therefore explained by the restriction of the concerted inversion pathway.

The molecule O₂N₂ may also logically be classed with the constrained azobenzenes, however to the knowledge of the author no quantum yield data are currently available in the literature, hence the role of the concerted inver-

¹⁰where the quantum yields are determined by the probability of the wavepacket reaching a particular CI

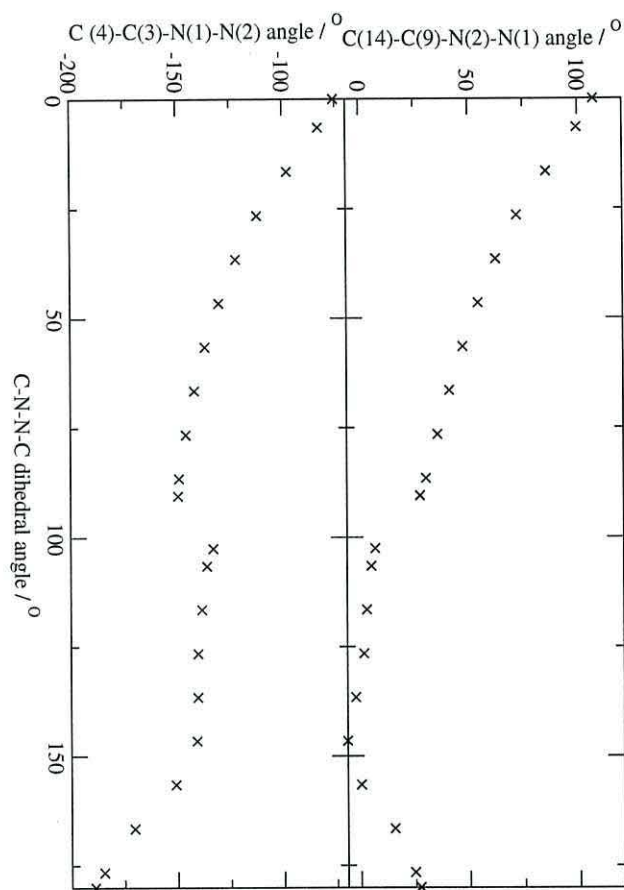


Figure 5.23: Variation of C-C-N-N angles with respect to torsional isomerisation of O2N2. Atom labels taken from Fig. 5.5.

sion pathway during photoisomerisation is still very speculative. According to the present DFT calculations (Section 5.2.1), motion along the concerted inversion pathway appears unlikely due to the strained conditions. The asymmetry of the two C-N-N angles enforced by the ether linkage also suggests that such a motion is unlikely.

5.3.2 Limitations and Further Work

Electronic structure potential energy functions

The choice of Density Functional Theory as the electronic structure method to investigate the PES of O₂N₂ was governed by a combination of the relatively large size of the molecule and limited available computer resources. In comparison to post Hartree-Fock (H-F) methods which also include the effects of electron correlation (e.g. Møller Plesset perturbation, CASSCF), DFT is computationally less expensive and therefore suitable for application of moderate to large organic molecules [25]. DFT, when coupled with the B3-LYP hybrid functional, has been widely utilised in the literature in the investigation of moderate/large molecules, successfully reproducing ground state potential barriers to large amplitude inversions and torsions in comparison to post H-F methods [26], and generating optimised structures in good agreement with X-ray data. TD-DFT has also been shown to reliably reproduce experimental vibrational spectra [28, 29].

In the present work, the DFT optimised ground state structures of *trans* and *cis* O₂N₂ are in good agreement with the X-ray experimental structures [18], and the ground state inversion barrier for the thermal *cis* → *trans* isomerisation is in good agreement with the experimental kinetic data [12]. The DFT PEFs along the isomerisation coordinates of O₂N₂ share similar characteristics with those calculated for azobenzene and its derivatives [10, 11] via different electronic structure methods. However, perhaps the most significant limitation of DFT in comparison to CASSCF (Chapter 3.1.2) is its inability to optimise electronic structures in the excited electronic states. TD-DFT calculates the excitation energy from the optimised ground state geometries, and while the main characteristic features of the excited state PEF are still observed, it would be preferable to find the minimum energy pathways on the excited states considering it is here that the isomerisation takes place.

Control of O2N2 photoisomerisation

The isomerisation of azobenzene and its derivatives involve large amplitude internal motions of the molecule which may be assumed to be sufficiently low in energy to be treated separately from the high energy small amplitude modes of the molecule [30]. Even when the large amplitude motions are treated in isolation, for systems such as azobenzene computing the dynamics is still a formidable task since it contains at least 5 internal coordinates which can undergo such motions (the CNNC and CCNN dihedral angles and NNC inversion angles) [15]. The primary motivation for the choice of the molecule O2N2 was therefore to reduce the number of internal large amplitude motions through the constraint of the ether linkage, effectively reducing the size of the dynamical problem. With the knowledge that the S_1 photoisomerisation of azobenzene occurs through a conical intersection along the torsional coordinate, and that this coordinate may be restricted by linking the phenyl rings, a secondary motivation was the possibility of conducting the dynamical equations without having to incorporate the complicated non-adiabatic couplings associated with close lying electronic states. In addition, the presence of conical intersections limits the amount of control possible as they are difficult to avoid and their product branching ratios are difficult to manipulate [31].

Section 5.2.2 presented the results of 1D quantum dynamical simulations along the inversion isomerisation coordinate of O2N2, where a near maximum yield of 0.97 isomerisation was achieved with the application of a 4 pulse sequence refined with OCT. Even when an energy barrier is present on the excited electronic state, significant control is possible as long as there is a strong interaction between the external electric field and the molecule's dipole moment (compare with azomethane in Chapter 4). Of course, with the newly discovered feasibility of the torsional pathway, the pulse sequences illustrated in this chapter are unlikely to yield such results in practise. The simplicity of the model system also serves to reduce the viability of the calculated pulses in practise, for example only two electronic states were considered (the calculated pulses are ultrashort in duration, and hence will exhibit

a large bandwidth capable of exciting multiple electronic states simultaneously - diminishing the effectiveness of the pulses), and the calculations were assumed for an isolated system (open systems are considered in the next chapter). In comparison to smaller systems such as azomethane, the longer timescale for the isomerisation will result in more significant contributions from Intramolecular Vibrational Energy Re-distribution (IVR) [33], which has also been neglected in the present work.

The PEF along the torsional coordinate of O₂N₂ has a very small gradient between the *trans* configuration and the rotamer configuration, consequently the wavepacket on the S_1 state takes $\approx 1,500$ fs to reach this transition state (see Fig. 5.14). Along the inversion coordinate, the wavepacket takes ≈ 313 fs to reach the first turning point of the *trans* well in the S_1 state (see Fig. 5.11), hence the second pulse along the inversion coordinate occurs before a significant progression of the wavepacket along the torsional coordinate. This suggests that, if the model is extended to a two dimensional system constructed from both coordinates, a 4 pulse sequence may exist for the isomerisation which avoids the unpredictable branching ratio of a conical intersection. A natural extension of the work presented in this chapter would therefore be an extensive investigation of the 2D PES of the S_0 and S_1 electronic states, followed by 2D dynamical calculations to search for appropriate pulse sequences. 2D quantum mechanical calculations have been applied to the photo-switching of cyclohexadiene [31, 32], where non-adiabatic coupling terms were used to characterise the relevant conical intersections of the system. In ref. [31] phase sensitive optimal control theory was used to generate wavepackets on the excited electronic states with pre defined momenta to manipulate which conical intersections are accessed, while ref. [32] used ultrashort quadratically chirped pulses to produce tightly localised wavepackets with favourable momenta which altered the branching ratio of particular conical intersections.

An alternative avenue of investigation would be to search for occurrences where either the torsional or inversion isomerisation coordinate of an azobenzene containing molecule is blocked. This may be the case when the azo-

molecule is confined to a small space such as a cyclo-dextrin cavity [5], or when present as a switch in a nano device. If such an occurrence exists, the sole large amplitude motion may be treated as a single dimension, while the rest of the molecular modes and surrounding environment may be treated as a dissipative extension acting on this 1D system. Regardless of whether such a system exists, the fact that the main practical uses of azobenzene and its derivatives occur when the molecule is in a condensed phase requires the inclusion of environmental effects.

Bibliography

- [1] P. Bortolus, S. Monti, *J. Phys. Chem.*, (1979), **83**, 648.
- [2] G. Zimmerman, L.-Y. Chow, U.-J. Paik, *J. Am. Chem. Soc.*, (1958), **80**, 3528.
- [3] S. Monti, G. Orlandi, P. Palmieri, *Chem. Phys.*, (1982), **71**, 87.
- [4] H. Rau, E. Lüeddecke, *J. Am. Chem. Soc.*, (1982), **104**, 1616.
- [5] P. Bortolus, S. Monti, *J. Phys. Chem.*, (1987), **91**, 5046.
- [6] T. Fujino, S. Y. Arzhantsev, T. Tahara, *J. Phys. Chem. A*, (2001), **105**, 8123.
- [7] P. Cattaneo, M. Persico, *Phys. Chem. Chem. Phys.*, (1999), **1**, 4739.
- [8] T. Ishikawa, T. Noro, T. Shoda, *J. Chem. Phys.*, (2001), **115**, 7503.
- [9] C.-W. Chang, Y.-C. Lu, T.-T. Wang, E. W.-G. Diau, *J. Am. Chem. Soc.*, (2004), **126**, 10109.
- [10] E. W.-G. Diau, *J. Phys. Chem. A*, (2004), **108**, 950.
- [11] C. Ciminelli, G. Granucci, M. Persico, *J. Chem. Phys.*, (2005), **123**, 174317.
- [12] K. Janus, J. Sworakowski, E. Luboch, *Chem. Phys.*, (2002), **285**, 47.
- [13] K. Janus, J. Sworakowski, *J. Phys. Chem. B*, (2005), **109**, 93.
- [14] Y.-C. Lu, E. W.-G. Diau, H. Rau, *J. Phys. Chem. A*, (2005), **109**, 2090.
- [15] C. Ciminelli, G. Granucci, M. Persico, *Chem. Eur. J.*, (2004), **10**, 2327.
- [16] G. Granucci, M. Persico, *Theor. Chem. Acc.*, (2007), **117**, 1131.

- [17] Gaussian 03, Revision B.04, M. J. Frisch, G. W. Trucks, H. B. Schlegel, G. E. Scuseria, M. A. Robb, J. R. Cheeseman, J. A. Montgomery, Jr., T. Vreven, K. N. Kudin, J. C. Burant, J. M. Millam, S. S. Iyengar, J. Tomasi, V. Barone, B. Mennucci, M. Cossi, G. Scalmani, N. Rega, G. A. Petersson, H. Nakatsuji, M. Hada, M. Ehara, K. Toyota, R. Fukuda, J. Hasegawa, M. Ishida, T. Nakajima, Y. Honda, O. Kitao, H. Nakai, M. Klene, X. Li, J. E. Knox, H. P. Hratchian, J. B. Cross, V. Bakken, C. Adamo, J. Jaramillo, R. Gomperts, R. E. Stratmann, O. Yazyev, A. J. Austin, R. Cammi, C. Pomelli, J. W. Ochterski, P. Y. Ayala, K. Morokuma, G. A. Voth, P. Salvador, J. J. Dannenberg, V. G. Zakrzewski, S. Dapprich, A. D. Daniels, M. C. Strain, O. Farkas, D. K. Malick, A. D. Rabuck, K. Raghavachari, J. B. Foresman, J. V. Ortiz, Q. Cui, A. G. Baboul, S. Clifford, J. Cioslowski, B. B. Stefanov, G. Liu, A. Liashenko, P. Piskorz, I. Komaromi, R. L. Martin, D. J. Fox, T. Keith, M. A. Al-Laham, C. Y. Peng, A. Nanayakkara, M. Challacombe, P. M. W. Gill, B. Johnson, W. Chen, M. W. Wong, C. Gonzalez, and J. A. Pople, Gaussian, Inc., Pittsburgh PA, 2003.
- [18] E. Luboch, E. Wagner-Wysiecka, V. Ch. Kravtsov and V. Kessler, *Polish. J. Chem.*, (2003), **77**, 189.
- [19] C. Nonnenburg, H. Gaub, I. Frank, *Chem. Phys. Chem.*, (2006), **7**, 1455.
- [20] J. M. Hollas, *Modern Spectroscopy*, second edition, Wiley, (1995).
- [21] H. Satzger, S. Spörlein, C. Root *et al*, *Chem. Phys. Lett.*, (2003), **372**, 216.
- [22] E. Luboch, J. F. Biernat, V. Ch. Kravtsov, Yu. A. Simonov, *J. of Inc. Phen. and Macro. Chem.*, (1998), **31**, 109.
- [23] A. M. Skwierawska, J. F. Biernat, V. Ch. Kravtsov, *Tetrahedron*, (2006), **62**, 149.
- [24] H. Rau, *J. Photochem.*, (1984), **26**, 221.
- [25] J. B. Foresman, A. Frisch, *Exploring Chemistry With Electronic Structure Methods*, Gaussian, Inc. Pittsburgh, PA, (1996).
- [26] L. Wang, X. Wang, *J. Mol. Str.-The.*, (2007), **806**, 179.

- [27] P. C. Chen, Y.C. Chieh, *J. Mol. Str.-The.*, (2003), **624**, 191.
- [28] C. H. Choi, M. Kertesz, *J. Phys. Chem. A*, (1997), **101**, 3823.
- [29] D. Guillaumont, S. Nakamura, *Dyes and Pigm.*, (2000), **46**, 85.
- [30] D. G. Lister, J, N, Macdonald, N. L. Owen, *Internal Rotation and Inversion, An Introduction to Large Amplitude Motions in Molecules*, Academic press, (1978).
- [31] D. Geppert, R. de Vivie-Riedle, *Chem. Phys. Lett.*, (2005), **404**, 289.
- [32] H. Tamura, S. Nanbu, T. Ishida, H. Nakamura, *J. Chem. Phys.*, (2006), **125**, 034307.
- [33] G. S. Evans, *The Development of a Quantum Mechanical Description of Intramolecular Energy Transfer*, Ph.D Thesis, University of Wales Bangor, (2005).

Chapter 6

Optimal Control of Dissipative Quantum Phase Space Dynamics

6.1 Introduction

In the preceding chapters attention was focused on chemical processes that involved a single degree of freedom. Although many processes may justifiably be described in isolation from its surroundings, for most processes of chemical interest the interaction cannot be ignored. In certain cases the interaction with the other degrees of freedom (DoF) is so important that the dynamics of the other modes must be treated explicitly in a multi-dimensional calculation. However, in many cases the influence of the surrounding (environment) DoF is less dramatic and may be treated as a perturbation upon the dynamics of the modes of interest. Different DoF of a single molecule are known to interact in the form of intramolecular vibrational energy redistribution (IVR) [1], and the interactions of the surrounding molecules can only justifiably be neglected when the molecule is present in the medium of a low pressure gas. Theoretical methods which incorporate the influence of the environment are sought after in many fields of research including NMR, solid-state physics, quantum optics and condensed phase chemical physics (see refs. [2, 3] and

references therein).

It is possible to reduce the magnitude of the problem by treating the small relevant sub-system rigorously, while limiting the treatment of the environment DoF as a thermal bath of oscillators. In this work, the term **total system** will refer to the complete ensemble of DoF under study, the term **system** will refer to the small number of DoF whose dynamics we are explicitly interested in, and **environment** will refer to the remaining DoF whose dynamics we are not particularly interested in, only their effect on the **system**.

The theory of systems which are coupled to their environment is referred to as the theory of open quantum systems [4]. Interaction with an environment usually affects the system dynamics in the form of energy relaxation, and a loss of quantum interference - a process known as decoherence. The Hamiltonian for an open quantum system generally has the form

$$\hat{H}_T = \hat{H}_S + \hat{H}_E + \hat{H}_{SE} \quad (6.1)$$

where \hat{H}_T is the total Hamiltonian, \hat{H}_S is the Hamiltonian governing the dynamics of the **system**, \hat{H}_E is the Hamiltonian governing the dynamics of the **environment** and \hat{H}_{SE} is the Hamiltonian which describes the interaction between the two sub-systems.

Recently, environmental effects have been incorporated in the field of laser control. In particular, environmental dissipative effects have been applied to the area of laser cooling [5, 6, 7], where the environment consists of the vacuum modes of the electromagnetic field, and the source of dissipation is spontaneous emission. For laser cooling, the dissipative effects of the environment provides a welcome assistance for the control procedure, rather than just a necessary extension for a more complete description of the total system. Environmental effects have also been included for the laser control of tunnelling in a symmetric double well potential [8]. In addition, environmental effects have been included for the optimal control of time dependent wavepackets [9] and exact solutions have been formulated for control in a model two state Brownian oscillator system [10].

In this chapter a brief outline of the theory of open quantum systems will be presented, beginning with the introduction of the density operator and the phase space Wigner distribution function. Particular attention is given to the Caldeira-Leggett approach which is applied to the Wigner phase space description of the dynamics. A primary aim of the calculations presented in this chapter is to observe the consequences environmental effects (relaxation/decoherence) have on the potential for laser control of a photoisomerisation type system. A novel approach of Optimal Control Theory in Wigner phase space is presented, since no derivation of an optimal control scheme has been developed or published in the literature, a detailed derivation is provided in Section 6.2.2.

The new optimal control scheme is implemented on the photoisomerisation dynamics of a model system, characterised by an asymmetric ground electronic state potential and a harmonic excited electronic state potential and subject to Caldeira-Leggett type dissipation. While the application of OCT to dissipative systems has already been established, possible additional benefits of its formulation in phase space may lie in the definition of the target state. In the Wigner representation, the target state is a positional q and momentum p dependent distribution function which has the attraction of designing laser pulses which not only generates a product wavepacket on a desired location of the multi-dimensional PES, but also with a target momentum distribution.

6.1.1 The Density Operator

So far in this work each quantum system has been described by a state vector Ψ (or wavefunction), which contains a complete description of the quantum system - such a system is known as a *pure* state. However, when a complete description is unavailable, the system must be described by a statistical mixture of possible state vectors for the system - the system is then described as a *mixed* state.

Although mixed states can be treated as a statistical mixture of wave-

functions, it is more convenient to introduce a density operator [12]

$$\hat{\rho} = \sum_{\alpha} w_{\alpha} |\Psi_{\alpha}\rangle \langle \Psi_{\alpha}| \quad (6.2)$$

and deal with this directly. In Eq. (6.2) w_{α} are the ‘weights’ attributed to each pure state α , and $\sum_{\alpha} w_{\alpha} = 1$ for a normalised set of pure states $|\Psi\rangle$ ¹. $\hat{\rho}$ is an operator and may be used to describe both pure states and mixed states. A measure of the ‘purity’ of the system may be determined by taking the trace of the square of the density matrix, where $\text{Tr}(\rho^2) = 1$ for pure states and $\text{Tr}(\rho^2) < 1$ for mixed states [16]. The diagonal matrix elements of the density operator represent the probability of finding the quantum system in the pure state m , and are often referred to as the *populations*. The off-diagonal elements are known as the *coherences*, and are indicative of the synchronicity of the phases of the different states $|\Psi\rangle$. Energy relaxation between the system and environment in an open quantum system manifests itself in the density operator representation by variation of the *populations* towards an equilibrium distribution, and complete decoherence is observed when the *coherences* decay to zero.

Quantum Liouville Equation

The time dependence of the density operator is governed by the time dependence of its component state vectors $|\Psi_{\alpha}\rangle$, hence an equation of motion (EOM) for $\hat{\rho}$ may be derived from the Schrödinger equation. For a **total system** described by $\hat{\rho}$, the EOM is the quantum Liouville equation (QLE) (derived by von Neumann [4, 12]),

$$\begin{aligned} \frac{d\hat{\rho}}{dt} &= -\frac{i}{\hbar} \sum_{\alpha} w_{\alpha} \left[\hat{H} |\Psi_{\alpha}\rangle \langle \Psi_{\alpha}| - |\Psi_{\alpha}\rangle \langle \Psi_{\alpha}| \hat{H} \right] \\ &= -\frac{i}{\hbar} [\hat{H}, \hat{\rho}] = -\frac{i}{\hbar} \mathcal{L}\hat{\rho} \end{aligned} \quad (6.3)$$

¹ Ψ is a pure state wavefunction, but not necessarily an eigenfunction

where \mathcal{L} is known as the Liouville operator. The QLE determines the dynamics of a *closed* system, hence it suffers from the same limitations as the Schrödinger equation when a large number of DoF are considered. However, if the total system can be partitioned into a relevant system and an environment part then a reduced description of the system may be derived where the influence of the environment is subsumed into the dynamical evolution of the system. These will be discussed further in section 6.2.

6.1.2 Wigner Phase Space Distribution

In the previous chapters the dynamics of a quantum system focused on the coordinate representation $\Psi(x)$. Instantaneous snapshots of $|\Psi(x)|^2$ reveals the location distribution of the quantum system at a specific time, and visualising successive snapshots allows the direction of the particle's motion to be deduced. Further detail about the particle's motion may be obtained when its wavefunction is represented in the momentum representation $\Psi(p)$, which may be converted from the coordinate representation via a Fourier transform

$$\Psi(p) = \frac{1}{\sqrt{2\pi}} \int_{-\infty}^{\infty} \Psi(x) e^{-ipx} dx. \quad (6.4)$$

The variables p and q are conjugate variables in classical mechanics², and it is possible to observe the dynamics of a system in terms of both variables simultaneously when the system is represented in phase space. In classical mechanics the state of a system in phase space is characterised by a distribution function $f_C(p, q)$. It would also seem desirable to represent a quantum dynamical system in terms of a quantum phase space distribution, $f_Q(p, q)$, as a more detailed alternative to the coordinate representation. The Heisenberg uncertainty principle imposes a constraint on the correlation of the variables p and q for a quantum system, however it is satisfied for $f_Q(p, q)$

²where the position variable x has been replaced by q due to its conventional use as the conjugate variable of p

as long as the relation

$$\int_{-\infty}^{\infty} \int_{-\infty}^{\infty} f_Q^2(p, q) dp dq \leq \frac{1}{2\pi\hbar} \quad (6.5)$$

holds, and the root-mean-squared half widths of $f_Q(p)$ and $f_Q(q)$ are greater than $\frac{\hbar}{2}$.

Numerous phase space representations for quantum systems exist. For example, due to its smooth coarse-grained structure the positive-definite Husimi distribution function is popular for the quantum dynamical study of classically chaotic systems [13, 14]; in quantum optics the Glauber-Sudarshan distribution function is widely used due to its suitability for evaluating values of numerically-ordered operators. Wigner [15] was the first to develop a distribution function - the Wigner distribution (Eq. (6.6) below) - that incorporated quantum effects. He developed the distribution function to study quantum corrections for thermodynamic equilibrium and it has since proved invaluable for understanding dissipative processes. For pure states the Wigner function

$$W(p, q) = \frac{1}{2\pi\hbar} \int_{-\infty}^{\infty} e^{\frac{i}{\hbar}ps} \Psi\left(q - \frac{s}{2}\right) \Psi^*\left(q + \frac{s}{2}\right) ds. \quad (6.6)$$

is generated by taking the product of the wavefunctions $\Psi(q - \frac{s}{2})$ and $\Psi^*(q + \frac{s}{2})$ followed by a Fourier transform over the difference coordinate 's' [16]. When written in Dirac notation, i.e. where $\Psi(x) = \langle x | \Psi \rangle$, Eq. (6.6) is given by

$$\begin{aligned} W(p, q) &= \frac{1}{2\pi\hbar} \int_{-\infty}^{\infty} e^{\frac{i}{\hbar}ps} \left\langle q - \frac{s}{2} | \Psi \right\rangle \left\langle \Psi | q + \frac{s}{2} \right\rangle ds \\ &= \frac{1}{2\pi\hbar} \int_{-\infty}^{\infty} e^{\frac{i}{\hbar}ps} \left\langle q - \frac{s}{2} | \rho | q + \frac{s}{2} \right\rangle ds \end{aligned} \quad (6.7)$$

and it becomes apparent that the Wigner function is a convenient representation for the density operator defined in Eq. (6.2). The Wigner function can take on negative as well as positive values, hence it cannot be considered a true phase space *probability* distribution, rather a pseudo-probability distribution. However, the correct quantum probability distributions in co-

ordinate space and momentum space may be recovered by integrating over the p and q coordinates respectively

$$\int_{-\infty}^{\infty} W(p, q) dp = |\Psi(q)|^2, \quad (6.8)$$

$$\int_{-\infty}^{\infty} W(p, q) dq = |\Psi(p)|^2. \quad (6.9)$$

Dynamics of the Wigner Function

The EOM for $W(q, p, t)$ is obtained by taking the Wigner transform (applying prescription Eq. (6.7)) of the quantum Liouville equation, Eq. (6.3). For a single electronic state the Wigner-Moyal equation is given by

$$\frac{\partial}{\partial t} W(p, q; t) = -\frac{p}{m} \frac{\partial}{\partial q} W(p, q; t) + \sum_{n=1, \text{odd}}^{\infty} \frac{1}{n!} \left(-\frac{i\hbar}{2} \right)^{n-1} \frac{\partial^n V(q)}{\partial q^n} \frac{\partial^n}{\partial p^n} W(p, q; t) \quad (6.10)$$

where the first term is the kinetic part of the Hamiltonian and the summation accounts for the effect of the potential $V(q)$. Details of the derivation of the Wigner-Moyal equations for a single electronic state system and for a two state system are provided in Appendix C.

When the potential energy function may be expressed in a polynomial of the form $\sum_n^N a_n q^n$ the summation in Eq. (6.10) has a finite termination. For a harmonic oscillator (HO) of the form $a_2 q^2$ the summation has only a single term and the EOM coincides with the *classical* Liouville equation.

To develop an intuition of the dynamics of $W(q, p, t)$, Fig. 6.1 illustrates the characteristic elliptical orbit of the time evolution of $W(q, p, t)$ in a HO potential. Using the parameters $a_2 = 0.0075$ a.u. and $M_\mu = 20,000$ a.u., an initial Gaussian of the form

$$W(q, p, t_0) = \frac{1}{\pi\hbar} e^{-2\beta(q-q_0)^2 - \frac{p^2}{2\beta\hbar^2}} \quad (6.11)$$

using $\beta = 32.0$ a.u. and an initial displacement from equilibrium $q_0 = 0.3$ a.u. is left to evolve on the potential. For a non-dissipative system, the oscillations within a HO potential occurs with a regular period and a

consistent displacement from equilibrium at each turning point.

At $t = 0$ fs the Wigner function is distributed evenly about the initial displacement $q = 0.3$ a.u. with a net momentum of $p = 0.0$ a.u.. The displacement at $q_0 = 0.3$ induces a restoring force $-\frac{\partial V}{\partial q}$ which propagates $W(q, p, t)$ towards the centre of the HO. The distribution acquires a negative net momentum as illustrated in Fig. 6.1 which reaches a maximum negative value when the centre of $W(q, p, t)$ crosses q_0 . The influence of $\frac{\partial V}{\partial q}$ then reduces the magnitude of p until the centre of $W(q, p, t)$ reaches the turning point of $q = -0.3$ with a net momentum of $p = 0$ at $t=87$ fs. From here, $W(q, p, t)$ acquires positive momentum ($t=116.8$ fs) as it propagates back towards the equilibrium position of $q = 0.0$, where the restoring force again changes sign, $-\frac{\partial V}{\partial q}$, decelerating $W(q, p, t)$ as it approaches the initial turning point at $q = 0.3$. It is valuable to note the the correlated uncertainties between q and p throughout the time evolution: as the uncertainty in location increases to a maximum as the centre of W coincides with $q = 0$ the uncertainty of momentum is at a minimum, while at the turning points the converse is true. This behaviour is consistent with the Heisenberg uncertainty principle, and satisfies the prescription of Eq. (6.5).

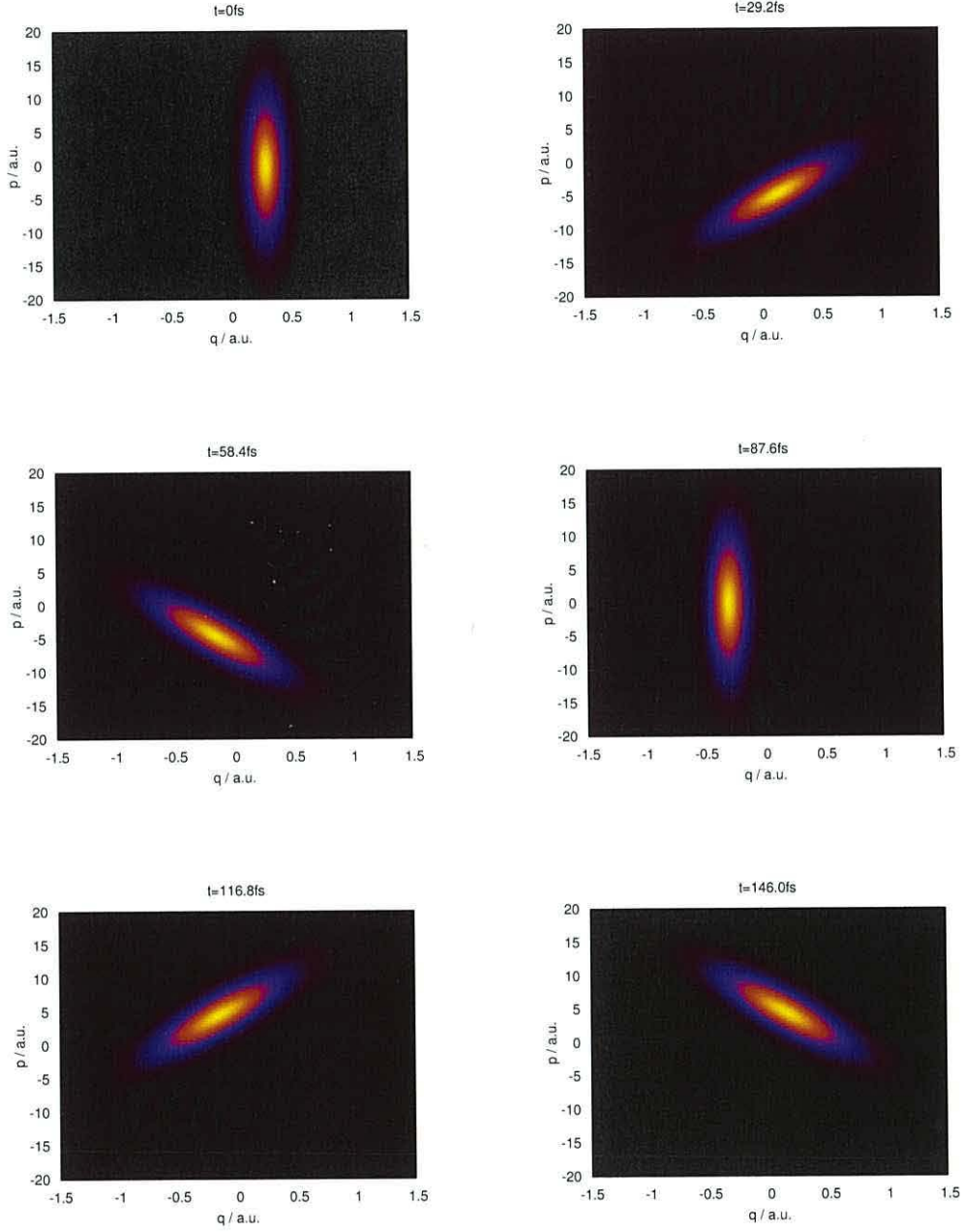


Figure 6.1: Instantaneous snapshots of a phase-space Wigner distribution representing a quantum particle oscillating in a harmonic oscillator potential.

6.2 Dissipative Dynamics

It was stated at the beginning of this chapter that a complete and explicit quantum dynamical description of a large **total system** is un-feasible, hence the starting point in a treatment of an open quantum system is the introduction of the reduced density operator, $\rho_S(t)$, which governs the dynamics of the sub-**system** of interest by tracing out the **environment** degrees of freedom

$$\rho_S(t) = \text{Tr}_E [\rho(t)] . \quad (6.12)$$

The dynamics of the reduced system may be expressed in the following form

$$\frac{\partial \rho_S(t)}{\partial t} = -\frac{i}{\hbar} \mathcal{L}_S \rho_S(t) + \int_0^t \mathcal{L}_D(\tau) \rho_S(\tau) d\tau + \mathcal{I}(t) \quad (6.13)$$

where $\mathcal{L}_S = [H_S, \bullet]$ and $\mathcal{I}(t)$ is an inhomogeneous term which vanishes for factorised initial conditions $\rho = \rho_s \otimes \rho_E$. The influence of the environment on the system is immersed into the dynamics of the system by integrating over the environment DoF where \mathcal{L}_D is the operator which characterises the influence of the environment on the reduced system. Despite the apparent simplicity of Eq. (6.13), the form of the second term is very complicated hence certain approximations are necessary for its solution. Two approximations that are often made are; (1) the Born approximation which assumes that the system is weakly coupled to the environment, where the environment is considered to contain a macroscopic number of DoF which consequently should not be affected by the few DoF of the system, hence the environment density operator ρ_E is considered time independent; and (2) the Markov approximation which assumes that the system dynamics is much slower than the environmental fluctuations. A key feature of the Markov approximation is that the reduced density operator loses all memory of its past, hence $\rho_S(\tau)$ in Eq. (6.13) becomes $\rho_S(t)$.

A fully satisfactory quantum master equation (QME) should adopt the following characteristics [2]: (1) $\rho_S(t)$ should remain positive semi-definite for all time i.e. no negative eigenvalues are permitted, (2) $\rho_S(t)$ should approach an equilibrium state at long times, and (3) $\rho_S(t)$ should satisfy the principal of

translational invariance i.e. the frictional force is required to be independent of the displacement coordinate q . Numerous methods have been proposed for the treatment of open quantum systems, and extensive reviews of these methods are provided in refs. [2, 18].

6.2.1 The Caldeira-Leggett Quantum Master Equation

The Markovian QME employed in this work is the Caldeira-Leggett (C-L) equation [19]. The derivation of the C-L QME may be found in the original path integral derivation by Caldeira and Leggett [20], or a detailed density matrix derivation may be found in Appendix D or in ref. [4]. Only a brief outline of the key features are presented here.

Several assumptions are made in the the derivation of the C-L equation:

- (1) Factorised initial conditions, i.e. system and environment are uncorrelated at $t = 0$.
- (2) Markovian approximation.
- (3) The Environment is characterised by a bath of harmonic oscillators.
- (4) Weak bilinear coupling between system-bath.
- (5) High temperature limit $k_B T \gtrsim \hbar \Omega$, where k_B , T , and Ω are the Boltzmann constant, temperature of the bath, and cut-off frequency for the bath respectively.

By defining the environment as a bath of harmonic oscillators the C-L Hamiltonian for the total system is given by

$$\hat{H}_T = \frac{P^2}{2M} + V(q) + \sum_n \left(\frac{p_n^2}{2m_n} + \frac{1}{2} m_n \omega_n^2 x_n^2 \right) - q \sum_n a_n x_n + q^2 \sum_n \frac{a_n^2}{2m_n \omega_n^2} \quad (6.14)$$

where the first two terms correspond to \hat{H}_S , and the third and fourth terms correspond to \hat{H}_E and \hat{H}_{SE} respectively. p , m , ω , and x are the momentum, mass, frequency and coordinates respectively of each harmonic environment DoF n . The final term in Eq. (6.14) is a counter term, \hat{H}_C , which serves to

neutralise the renormalisation of the system potential $V(q)$ generated by the system bath coupling \hat{H}_{SE} , this acts to preserve the principle of translational invariance.

Environment Correlation Function and Spectral Density

A key presumption in the derivation of many QMEs is that the system-environment coupling term may be expressed as a product of operators which act on the system sub-space and environment sub-space separately

$$\hat{H}_{SE} = K(q)F(x) \quad (6.15)$$

where K and F act on the system and environment variables respectively.

The *environment correlation function* defined as

$$C_{ij}(t, t') = \langle F_i(t) | F_j(t') \rangle, \quad (6.16)$$

contains all the information regarding the environment and is a measure of the correlation between expectation values of products of physical quantities taken at different times, i.e. the correlations that exists between interactions which occur at different times t and t' . It is the characterisation of this object within the Markov approximation which provides the cornerstone for the derivation of Markovian QMEs. Since the environment is assumed to be macroscopic in comparison to the system, it is rational to consider that the effect of the system on the environment will be buffered by its sheer scale. The time scale of this buffering is determined by a value, τ , which is a measure of the time for which some memory of the system-environment interaction remains³. For $t - t' = 0$ the correlation function $C_{ij}(t, t')$ has its maximum value, while at longer times, $t - t' > \tau$, $C_{ij}(t, t')$ becomes progressively less correlated until it reaches a value of zero for $t - t' \gg \tau$. Crucially, in the derivation of Markovian QMEs, the value τ is assumed to be much smaller than the time scale of the evolution of the system of interest.

³ τ is dependent on the type of environment under consideration, e.g. for a dilute gas τ may be determined by the mean time between two collisions [21].

In the C-L model the system's interaction with the environment of harmonic oscillators is defined by a weak bilinear coupling

$$\hat{H}_{SE} = K(q)F(x) = q \sum_j a_j x_j \quad (6.17)$$

where a_j and x_j are the coupling and coordinates associated with the j 'th DoF of the environment respectively. Specific details about the environment and its interaction with the system (e.g. coupling values) are encased in the *spectral density* of the system-environment coupling defined by

$$J(\omega) = \sum_j a_j^2 \frac{\hbar}{2m_j \omega_j} \delta(\omega - \omega_j). \quad (6.18)$$

The spectral density can be obtained from computational simulation [22], from ultra-fast spectroscopy experiments (e.g. from dynamical Stokes shift [23] or from photon echo experiments [24]), or from phenomenological models. A simple and widely used phenomenological form for $J(\omega)$ is an Ohmic form which is utilised in the C-L model

$$J(\omega) = \frac{2m\eta\hbar}{\pi} \omega \quad (6.19)$$

where η is the damping rate of the environment. The discrete representation of $J(\omega)$ in Eq. (6.18) has been replaced by a continuous function due to the assumption that the infinitely large environment will exhibit a continuous range of frequencies. A cut-off frequency, Ω , is introduced to circumvent the renormalisation which would be inflicted on the system potential $V(q)$ by the high frequency modes of the environment. Using a Lorentz-Drude cut-off the Ohmic spectral density may be expressed as

$$J(\omega) = \frac{2m\eta\hbar}{\pi} \omega \frac{\Omega^2}{\Omega^2 + \omega^2}. \quad (6.20)$$

The relation between the real and imaginary parts of the environment

correlation function and the spectral density are expressed as

$$C_R(\tau) = 2 \int_0^\infty J(\omega) \coth(\beta\hbar\omega/2) \cos(\omega\tau) d\omega \quad (6.21)$$

$$C_I(\tau) = 2 \int_0^\infty J(\omega) \sin(\omega\tau) d\omega. \quad (6.22)$$

C-L equation of motion

In terms of the real and imaginary correlation functions introduced above, the C-L equation is given by

$$\begin{aligned} \frac{\partial \rho_S(t)}{\partial t} = & \frac{i}{2\hbar^2} \int_0^\infty C_I(\tau) [q, [q, \rho_S(t)]_+] d\tau - \frac{i}{2m\hbar^2} \int_0^\infty C_I(\tau) [q, [p, \rho_S(t)]_+] \tau d\tau \\ & - \frac{1}{2\hbar^2} \int_0^\infty C_R(\tau) [q, [q, \rho_S(t)]] d\tau + \frac{1}{2m\hbar^2} \int_0^\infty C_R(\tau) [q, [p, \rho_S(t)]] \tau d\tau \end{aligned} \quad (6.23)$$

where $[a, b] = ab - ba$ and $[a, b]_+ = ab + ba$ are commutators and anticommutators respectively. The integrals in Eq. (6.23) are evaluated with the Ohmic model of the spectral density to yield the equation of motion for the reduced density operator in its final form

$$\frac{\partial \rho_S(t)}{\partial t} = -\frac{i}{\hbar} [H_S, \rho_S(t)] - \frac{i\eta}{\hbar} [q, [p, \rho_S(t)]_+] - \frac{2m\eta k_B T}{\hbar^2} [q, [q, \rho_S(t)]] \quad (6.24)$$

where the environmental effects of dissipation and decoherence on the system are contained in the second and third terms, and corresponds to the simplified form of \mathcal{L}_D in Eq. (6.13). A detailed derivation of Eq. (6.24) is provided in Appendix D.

C-L equation of motion for 2 electronic states

To characterise a model photoisomerisation reaction Eq. (6.24) must be extended to accommodate at least a two electronic state system. The total Hamiltonian for a two state system is expressed in a similar manner to the

time dependent Schrödinger equation in Chapter 3.3

$$H_S = \begin{bmatrix} H_g & -\mu\epsilon(t) \\ -\mu\epsilon^*(t) & H_e \end{bmatrix} \quad (6.25)$$

where μ and $\epsilon(t)$ are the transition dipole moment and external electric field respectively. The density matrix for a two state system partitions as follows

$$\rho_S = \begin{bmatrix} \rho_{11} & \rho_{12} \\ \rho_{21} & \rho_{22} \end{bmatrix}. \quad (6.26)$$

where ρ_{nn} are the electronic populations and $\rho_{n \neq m}$ are the electronic coherences. The Liouville-von Neumann EOM for an *isolated* two state system is then given by

$$\begin{aligned} \frac{\partial}{\partial t} \begin{bmatrix} \rho_{11} & \rho_{12} \\ \rho_{21} & \rho_{22} \end{bmatrix} &= -\frac{i}{\hbar} \left\{ \begin{bmatrix} H_g & -\mu\epsilon(t) \\ -\mu\epsilon^*(t) & H_e \end{bmatrix} \begin{bmatrix} \rho_{11} & \rho_{12} \\ \rho_{21} & \rho_{22} \end{bmatrix} \right. \\ &\quad \left. - \begin{bmatrix} \rho_{11} & \rho_{12} \\ \rho_{21} & \rho_{22} \end{bmatrix} \begin{bmatrix} H_g & -\mu\epsilon(t) \\ -\mu\epsilon^*(t) & H_e \end{bmatrix} \right\}. \end{aligned} \quad (6.27)$$

The equation of motion for each element of the two state density matrix is given by

$$\frac{\partial}{\partial t} \rho_{11} = -\frac{i}{\hbar} \{ [H_g, \rho_{11}] - \mu(\epsilon\rho_{21} - \rho_{12}\epsilon^*) \} + \mathcal{L}_D \rho_{11} \quad (6.28)$$

$$\frac{\partial}{\partial t} \rho_{22} = -\frac{i}{\hbar} \{ [H_e, \rho_{22}] + \mu(\rho_{21}\epsilon - \epsilon^*\rho_{12}) \} + \mathcal{L}_D \rho_{22} \quad (6.29)$$

$$\frac{\partial}{\partial t} \rho_{12} = -\frac{i}{\hbar} \{ H_g \rho_{12} - \rho_{12} H_e - \mu\epsilon(\rho_{22} - \rho_{11}) \} + \mathcal{L}_D \rho_{12} \quad (6.30)$$

$$\frac{\partial}{\partial t} \rho_{21} = \frac{\partial}{\partial t} \rho_{12}^*. \quad (6.31)$$

where $\mathcal{L}_{\mathcal{D}}$ representing the dissipative terms of the C-L equation have now been included.

C-L equations of motion for the Wigner function

By taking the Wigner transform of Eq. (6.24) C-L dissipation is incorporated in phase space as additional terms to the Wigner-Moyal equation Eq. (6.10), and for a single electronic state system is given by

$$\begin{aligned}\frac{\partial W}{\partial t} &= -\frac{i}{\hbar}\mathcal{L}_W W + \mathcal{L}_{\mathcal{D}W} W \\ -\frac{i}{\hbar}\mathcal{L}_W W &= -\frac{p}{m}\frac{\partial W}{\partial q} + \frac{\partial V}{\partial q}\frac{\partial W}{\partial p} + \sum_{n=0}^{\infty} \frac{1}{(2n+1)!} \left(\frac{-\hbar^2}{4}\right)^n \frac{\partial^{2n+1} V}{\partial q^{2n+1}} \frac{\partial^{2n+1} W}{\partial p^{2n+1}} \\ \mathcal{L}_{\mathcal{D}W} W &= \eta \frac{\partial p W}{\partial p} + \eta m k_B T \frac{\partial^2 W}{\partial p^2}.\end{aligned}\tag{6.32}$$

The Wigner function for a two state system may also be partitioned similarly to the density matrix

$$W_S = \begin{bmatrix} W_{11} & W_{12} \\ W_{21} & W_{22} \end{bmatrix}.\tag{6.33}$$

and taking the Wigner transform of the corresponding equation of motion for each component ρ_{nm} yields the equation of motion for each component

in Wigner phase space

$$\begin{aligned} \frac{\partial W_{11}}{\partial t} = & -\frac{p}{m} \frac{\partial W_{11}}{\partial q} + \frac{\partial V_g}{\partial q} \frac{\partial W_{11}}{\partial p} - \frac{\hbar^2}{24} \frac{\partial^3 V_g}{\partial q^3} \frac{\partial^3 W_{11}}{\partial p^3} \\ & - 2\frac{\mu}{\hbar} \Im[\epsilon W_{21}] + \mathcal{L}_{\mathcal{DW}} W_{11} \end{aligned} \quad (6.34)$$

$$\begin{aligned} \frac{\partial W_{22}}{\partial t} = & -\frac{p}{m} \frac{\partial W_{22}}{\partial q} + \frac{\partial V_e}{\partial q} \frac{\partial W_{22}}{\partial p} - \frac{\hbar^2}{24} \frac{\partial^3 V_e}{\partial q^3} \frac{\partial^3 W_{22}}{\partial p^3} \\ & + 2\frac{\mu}{\hbar} \Im[\epsilon W_{21}] + \mathcal{L}_{\mathcal{DW}} W_{22} \end{aligned} \quad (6.35)$$

$$\begin{aligned} \frac{\partial W_{21}}{\partial t} = & -\frac{p}{m} \frac{\partial W_{21}}{\partial q} - \frac{i}{\hbar} [V_e - V_g] W_{21} + \frac{1}{2} \left[\frac{\partial V_e}{\partial q} + \frac{\partial V_g}{\partial q} \right] \frac{\partial W_{21}}{\partial p} \\ & + \frac{i\hbar}{8} \left[\frac{\partial^2 V_e}{\partial q^2} - \frac{\partial^2 V_g}{\partial q^2} \right] \frac{\partial^2 W_{21}}{\partial p^2} - \frac{\hbar^2}{48} \left[\frac{\partial^3 V_e}{\partial q^3} + \frac{\partial^3 V_g}{\partial q^3} \right] \frac{\partial^3 W_{21}}{\partial p^3} \\ & - \frac{i}{\hbar} \mu \epsilon^* (W_{22} - W_{11}) + \mathcal{L}_{\mathcal{DW}} W_{12} \end{aligned} \quad (6.36)$$

where $W_{12}(q, p) = W_{21}^*(q, p)$ and the symbol \Im specifies the imaginary part. Note that transfer of population between W_{11} and W_{22} occurs only when the electric field is ‘switched on’. Details of the derivation of the above EOM are provided in Appendix C.

6.2.2 Optimal Control Theory for Wigner Phase Space Dynamics

The control scheme for the phase space dissipative system [26, 27] is formulated in an analogous manner to the wavefunction representation presented in Chapter 4.1.2. Since no derivation of an optimal control (OC) scheme for dissipative phase space system has been developed or published in the literature a detailed derivation will be presented here.

As developed for the wavefunction, the first step in the OC scheme is to define the objective functional to be maximised i.e. the overlap between the state of the system at time t_f and a specified target state. For the density operator the objective functional is defined in the same form as ref. [28]

$$J = \text{Tr} [T \rho(t_f)]. \quad (6.37)$$

Implementing the trace product rule [17] on Eq. (6.37) yields the objective functional for the Wigner phase space representation

$$J = (2\pi\hbar)^{-1} \text{Tr}[T\rho(t_f)] = \int_{-\infty}^{\infty} \int_{-\infty}^{\infty} W_T(q, p) W(q, p, t_f) dq dp \quad (6.38)$$

where W_T is the target phase space distribution function. Note that the above integral has a maximum value for a perfect overlap of $(2\pi\hbar)^{-1}$. By introducing a set of constraints J may be converted to a modified objective functional \bar{J} , whereby the calculation of the maximum of \bar{J} is permitted. In this formulation J is subject to the constraints that the optimised pulse will have a maximum energy value of $E = \int_{t_0}^{t_f} |\epsilon(t)|^2 dt$ and that the Wigner-Moyal equation is satisfied. The Lagrange functional is given by

$$\begin{aligned} J &= \int_{-\infty}^{\infty} \int_{-\infty}^{\infty} W_T(q, p) W(q, p, t_f) dq dp \\ &\quad - \int_0^{t_f} \int_{-\infty}^{\infty} \int_{-\infty}^{\infty} W_\beta \left(\frac{\partial}{\partial t} + \frac{i}{\hbar} \mathcal{L}_W \right) W dq dp dt - \lambda \int_0^{t_f} |\epsilon|^2 dt \\ &= \int_{-\infty}^{\infty} \int_{-\infty}^{\infty} W_T(q, p) W(q, p, t_f) dq dp - \int_0^{t_f} \int_{-\infty}^{\infty} \int_{-\infty}^{\infty} W_\beta \frac{\partial W}{\partial t} dq dp dt \\ &\quad - \int_0^{t_f} \int_{-\infty}^{\infty} \int_{-\infty}^{\infty} W_\beta \frac{i}{\hbar} \mathcal{L}_W W dq dp dt - \lambda \int_0^{t_f} |\epsilon|^2 dt \end{aligned} \quad (6.39)$$

where λ^4 is a scalar Lagrange multiplier and W_β is a phase space function Lagrange multiplier, analogous to χ of the wavefunction formulation in Chapter 4.1.2. The time derivative component of Eq. (6.39) is integrated by parts

⁴Note that $\lambda = 2\pi\hbar\lambda'$ to counteract the denominator arising from the trace product rule.

to yield

$$\begin{aligned}
-\int_0^{t_f} \int_{-\infty}^{\infty} \int_{-\infty}^{\infty} W_{\beta} \frac{\partial W}{\partial t} dq dp dt &= \int_{-\infty}^{\infty} \int_{-\infty}^{\infty} W_{\beta}(t_0) W(t_0) dq dp \\
&\quad - \int_{-\infty}^{\infty} \int_{-\infty}^{\infty} W_{\beta}(t_f) W(t_f) dq dp \\
&\quad + \int_0^{t_f} \int_{-\infty}^{\infty} \int_{-\infty}^{\infty} \frac{\partial W_{\beta}}{\partial t} W dq dp dt.
\end{aligned} \tag{6.40}$$

Inserting Eq. (6.40) into Eq. (6.39) and taking the variation with respect to W gives

$$\begin{aligned}
\frac{\delta \bar{J}}{\delta W} &= \int_{-\infty}^{\infty} \int_{-\infty}^{\infty} W_T(q, p) \delta W(q, p, t_f) dq dp + \\
&\quad - \int_{-\infty}^{\infty} \int_{-\infty}^{\infty} W_{\beta}(t_f) \delta W(t_f) dq dp \\
&\quad + \int_0^{t_f} \int_{-\infty}^{\infty} \int_{-\infty}^{\infty} \frac{\partial W_{\beta}}{\partial t} \delta W dq dp dt \\
&\quad - \int_0^{t_f} \int_{-\infty}^{\infty} \int_{-\infty}^{\infty} W_{\beta} \frac{i}{\hbar} \mathcal{L}_W \delta W dq dp dt \\
&= \int_{-\infty}^{\infty} \int_{-\infty}^{\infty} W_T(q, p) \delta W(q, p, t_f) dq dp + \\
&\quad - \int_{-\infty}^{\infty} \int_{-\infty}^{\infty} W_{\beta}(t_f) \delta W(t_f) dq dp \\
&\quad + \int_0^{t_f} \int_{-\infty}^{\infty} \int_{-\infty}^{\infty} \frac{\partial W_{\beta}}{\partial t} \delta W dq dp dt \\
&\quad - \int_0^{t_f} \int_{-\infty}^{\infty} \int_{-\infty}^{\infty} \frac{-i}{\hbar} (\mathcal{L}^{\dagger})_W W_{\beta} \delta W dq dp dt.
\end{aligned} \tag{6.41}$$

The initial Wigner distribution $W(q, p, t_0)$ is not subject to variation hence drops out of Eq. (6.41). Setting $\delta \bar{J} = 0$ leads to an equation of motion for W_{β}

$$\frac{\partial W_{\beta}}{\partial t} = -\frac{i}{\hbar} (\mathcal{L}^{\dagger})_W W_{\beta} \tag{6.42}$$

with the final condition that

$$W_\beta(q, p, t_f) = W_T(q, p). \quad (6.43)$$

Variation of W_β in Eq. (6.39) leads to the requirement

$$\frac{\partial W}{\partial t} + \frac{i}{\hbar} \mathcal{L}_W W = 0 \quad (6.44)$$

that the Wigner-Moyal equation be satisfied.

Variation of J with respect to the real and imaginary parts of the electric field gives

$$\frac{\delta \bar{J}}{\delta \Re \epsilon} = \int_0^{t_f} \delta \Re \epsilon \left(\int_{-\infty}^{\infty} \int_{-\infty}^{\infty} -\frac{i}{\hbar} W_\beta \frac{\partial \mathcal{L}_W}{\partial \Re \epsilon} W dq dp - 2\lambda \Re \epsilon \right) dt \quad (6.45)$$

and

$$\frac{\delta \bar{J}}{\delta \Im \epsilon} = \int_0^{t_f} \delta \Im \epsilon \left(\int_{-\infty}^{\infty} \int_{-\infty}^{\infty} -\frac{i}{\hbar} W_\beta \frac{\partial \mathcal{L}_W}{\partial \Im \epsilon} W dq dp - 2\lambda \Im \epsilon \right) dt. \quad (6.46)$$

Setting $\delta \bar{J} = 0$ for both real and imaginary parts leads to

$$2\lambda \Re \epsilon = -\frac{i}{\hbar} \int_{-\infty}^{\infty} \int_{-\infty}^{\infty} W_\beta \frac{\partial \mathcal{L}_W}{\partial \Re \epsilon} W dq dp \quad (6.47)$$

$$2\lambda \Im \epsilon = -\frac{i}{\hbar} \int_{-\infty}^{\infty} \int_{-\infty}^{\infty} W_\beta \frac{\partial \mathcal{L}_W}{\partial \Im \epsilon} W dq dp. \quad (6.48)$$

Combining these 2 equations and multiplying the imaginary part by i gives the following relation for the optimal electric field

$$\Re \epsilon + i \Im \epsilon = \epsilon = -\frac{i}{2\lambda \hbar} \int_{-\infty}^{\infty} \int_{-\infty}^{\infty} W_\beta \left(\frac{\partial \mathcal{L}_W}{\partial \Re \epsilon} + i \frac{\partial \mathcal{L}_W}{\partial \Im \epsilon} \right) W dq dp \quad (6.49)$$

with

$$\begin{aligned} \mathcal{L}_W &= H_W e^{i\hbar\Lambda/2} \bullet - \bullet e^{i\hbar\Lambda/2} H_W \\ &\simeq H_W \left(1 + \frac{i}{2} \hbar \Lambda + \dots \right) \bullet - \bullet \left(1 + \frac{i}{2} \hbar \Lambda + \dots \right) H_W. \end{aligned} \quad (6.50)$$

where $H_W = 0.5p^2/m + V(q)$ is the classical Hamiltonian and

$$\Lambda = \frac{\overleftarrow{\partial}}{\partial q} \frac{\overrightarrow{\partial}}{\partial p} - \frac{\overleftarrow{\partial}}{\partial p} \frac{\overrightarrow{\partial}}{\partial q} \quad (6.51)$$

where the arrows indicate the direction of derivative operation.

For transitions between different electronic states, and assuming the Condon approximation⁵ we have

$$\begin{aligned} \frac{\partial \mathcal{L}_W}{\partial \Re \epsilon} + i \frac{\partial \mathcal{L}_W}{\partial \Im \epsilon} &= \left(\frac{\partial H_W}{\partial \Re \epsilon} + i \frac{\partial H_W}{\partial \Im \epsilon} \right) \bullet - \bullet \left(\frac{\partial H_W}{\partial \Re \epsilon} + i \frac{\partial H_W}{\partial \Im \epsilon} \right) \\ &= \left(\begin{bmatrix} 0 & -\mu \\ -\mu & 0 \end{bmatrix} + i \begin{bmatrix} 0 & -i\mu \\ i\mu & 0 \end{bmatrix} \right) \bullet \\ &\quad - \bullet \left(\begin{bmatrix} 0 & -\mu \\ -\mu & 0 \end{bmatrix} + i \begin{bmatrix} 0 & -i\mu \\ i\mu & 0 \end{bmatrix} \right) \\ &= \begin{bmatrix} 0 & 0 \\ -2\mu & 0 \end{bmatrix} \bullet - \bullet \begin{bmatrix} 0 & 0 \\ -2\mu & 0 \end{bmatrix} \\ &= M. \end{aligned} \quad (6.52)$$

Inserting this dipole operator into the expression for the optimal electric field Eq. (6.49) gives

$$\epsilon = -\frac{i}{2\lambda\hbar} \int_{-\infty}^{\infty} \int_{-\infty}^{\infty} W_{\beta} M W dq dp. \quad (6.53)$$

Since μ is independent of both q and p then

$$\int_{-\infty}^{\infty} \int_{-\infty}^{\infty} W_{\beta} M W dq dp = \text{Tr}[\beta M \rho] \quad (6.54)$$

where the trace product rule has been applied.

By taking the trace of the density operator representation of the product $\beta M \rho$, followed by a Wigner transform of the result leads to the final form of

⁵i.e. the dipole moment μ is taken as independent of the spatial coordinate q , hence the terms containing the spatial derivatives embedded in Λ in Eq. (6.50) are zero.

the optimal electric field

$$\begin{aligned}
M\rho\beta &= \begin{bmatrix} 0 & 0 \\ -2\mu & 0 \end{bmatrix} \begin{bmatrix} \rho_{11} & \rho_{12} \\ \rho_{21} & \rho_{22} \end{bmatrix} \begin{bmatrix} \beta_{11} & \beta_{12} \\ \beta_{21} & \beta_{22} \end{bmatrix} \\
&- \begin{bmatrix} \rho_{11} & \rho_{12} \\ \rho_{21} & \rho_{22} \end{bmatrix} \begin{bmatrix} 0 & 0 \\ -2\mu & 0 \end{bmatrix} \begin{bmatrix} \beta_{11} & \beta_{12} \\ \beta_{21} & \beta_{22} \end{bmatrix} \\
&= -2 \begin{bmatrix} 0 & 0 \\ \mu(\rho_{11}\beta_{11} + \rho_{12}\beta_{21}) & \mu(\rho_{11}\beta_{12} + \rho_{12}\beta_{22}) \end{bmatrix} + 2 \begin{bmatrix} \rho_{12}\mu\beta_{11} & \rho_{12}\mu\beta_{12} \\ \rho_{22}\mu\beta_{11} & \rho_{22}\mu\beta_{12} \end{bmatrix} \\
&= 2 \begin{bmatrix} \rho_{12}\mu\beta_{11} & \rho_{12}\mu\beta_{12} \\ \rho_{22}\mu\beta_{11} - \mu(\rho_{11}\beta_{11} + \rho_{12}\beta_{21}) & \rho_{22}\mu\beta_{12} - \mu(\rho_{11}\beta_{12} + \rho_{12}\beta_{22}) \end{bmatrix} \quad (6.55)
\end{aligned}$$

and the trace is given by

$$\text{Tr}[M\rho\beta] = 2(\rho_{12}\mu\beta_{11} + \rho_{22}\mu\beta_{12} - \mu\rho_{11}\beta_{12} - \mu\rho_{12}\beta_{22}). \quad (6.56)$$

Finally, the improved pulse at each iteration $k+1$ is given by

$$\begin{aligned}
\delta\epsilon &= \frac{-i}{2\lambda\hbar} \int_{-\infty}^{\infty} \int_{-\infty}^{\infty} W_{\beta} MW dq dp \\
&= -\frac{i\mu}{\lambda\hbar} \int_{-\infty}^{\infty} \int_{-\infty}^{\infty} (W^{12}W_{\beta}^{11} \\
&\quad + W^{22}W_{\beta}^{12} - W^{11}W_{\beta}^{12} - W^{12}W_{\beta}^{22}) dq dp. \quad (6.57)
\end{aligned}$$

6.3 Optimal Control of a Model Isomerisation System with Dissipation in Phase Space

The phase space formulation of OCT introduced in the previous section has been applied on a model 2 state system to investigate the effects of environmental dissipation on a photoisomerisation type system. The ground electronic state is characterised by an asymmetric double well potential defined

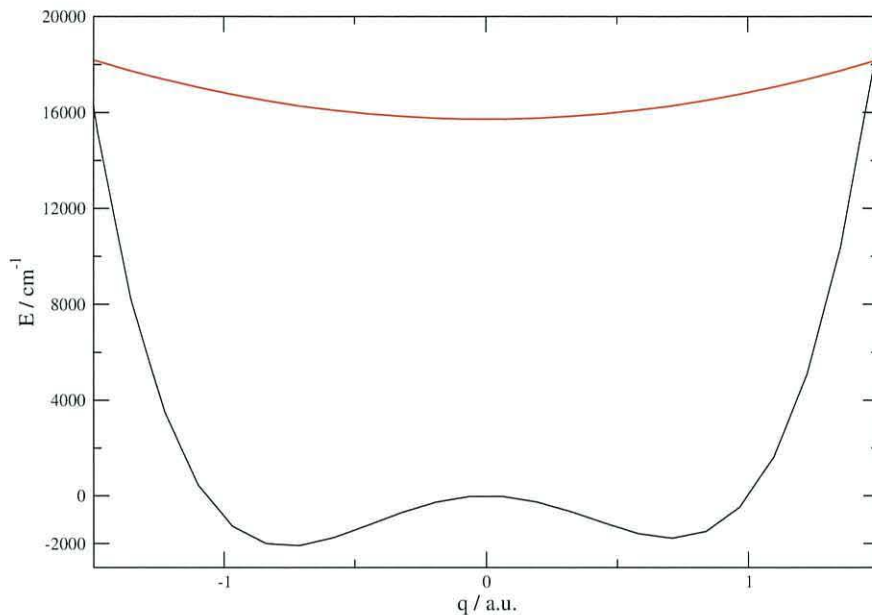


Figure 6.2: Ground (black) and excited (red) state potentials of the model system described in the text

by a fourth order polynomial of the type

$$V_g(q) = v_2 q^2 + v_3 q^3 + v_4 q^4 \quad (6.58)$$

where $v_2 = -7174 \text{ cm}^{-1}$, $v_3 = 439 \text{ cm}^{-1}$, and $v_4 = 6675 \text{ cm}^{-1}$. The excited electronic state, V_e , is characterised by a HO potential with a force constant of $v'_2 = 1097 \text{ cm}^{-1}$, and is positioned $v'_0 = 15732 \text{ cm}^{-1}$ higher in energy than the ground state.

A barrier height of 2110 cm^{-1} exists between the left hand well (LHW) and the right hand well (RHW) of the ground state potential (Fig. 6.2), and a barrier height of 1763 cm^{-1} opposes the back reaction. Model values of $M_\mu = 5090 \text{ a.u.}$ and $\mu = 1 \text{ a.u.}$ were assigned for the reduced moment of inertia and TDM of the system respectively. All calculations were carried out on a phase space grid with ranges of $-45.0 \text{ a.u.} \rightarrow +45.0 \text{ a.u.}$ in p , and $-2.0 \text{ a.u.} \rightarrow +2.0 \text{ a.u.}$ in q - with 32 grid points along q and 64 grid points along p .

6.3.1 Control in Non-dissipative Phase Space

The Krotov methodology of OCT (Chapter 4.1.2) is employed to find an optimised pulse shape for the transfer of population from the LHW to the RHW of the ground electronic state potential mediated by the excited electronic state. The Wigner transform of the ground vibrational eigenstate (which is located in the LHW), ν_0 , of the ground electronic state was chosen as the initial state of the system,

$$W(q, p, t_0) = \frac{1}{2\pi\hbar} \int_{-\infty}^{\infty} \langle q + \frac{s}{2} | \nu_0 \rangle \langle \nu_0 | q - \frac{s}{2} \rangle e^{-i\frac{sp}{\hbar}} ds \quad (6.59)$$

which has maximum amplitude at the LHW minimum $q_L = -0.76$ a.u.. The eigenstate ν_1 , located in the RHW at $q_R = 0.71$ a.u., was chosen as a suitable target state

$$W_T(q, p) = \frac{1}{2\pi\hbar} \int_{-\infty}^{\infty} \langle q + \frac{s}{2} | \nu_1 \rangle \langle \nu_1 | q - \frac{s}{2} \rangle e^{-i\frac{sp}{\hbar}} ds. \quad (6.60)$$

Fig. 6.3 illustrates the form of the initial guess field, ϵ^0 , and the corresponding time dependent populations of the ground electronic state W_{11} , excited state W_{22} , and electronic coherences $\Re[W_{21}]$. Two overlapping Gaussian envelopes

$$\epsilon^0(t) = A_1 e^{-\gamma_1(t-t_1)^2} \cos(\omega_1 t) + A_2 e^{-\gamma_2(t-t_2)^2} \cos(\omega_2 t) \quad (6.61)$$

were employed for the initial guess with parameters $A_1 = 1.0$ a.u., $A_2 = 1.15$ a.u., $t_1 = 29.03$ fs, $t_2 = 48.38$ fs, $\gamma_1 = 4.0 \times 10^6$ a.u., $\gamma_2 = 6.0 \times 10^6$ a.u., $\omega_1 = 0.08254$ hartree, and $\omega_2 = 0.07953$ hartree. The carrier frequencies, $\omega_{1/2}$, were chosen slightly off resonant with the energy separation, $V_e - V_g$, at q_L and q_R respectively. No manual refinement of the initial guess field was undertaken, as the aim of these calculations is to test the potency of the control scheme in Wigner phase space.

The first pulse excites a fraction of 0.84 of the ground state population, and 0.11 of this is subsequently returned to the ground state by the second pulse with a product yield of $\int_{-\infty}^{\infty} W_T^*(q, p) W(q, p, t_f) = 0.025$. During

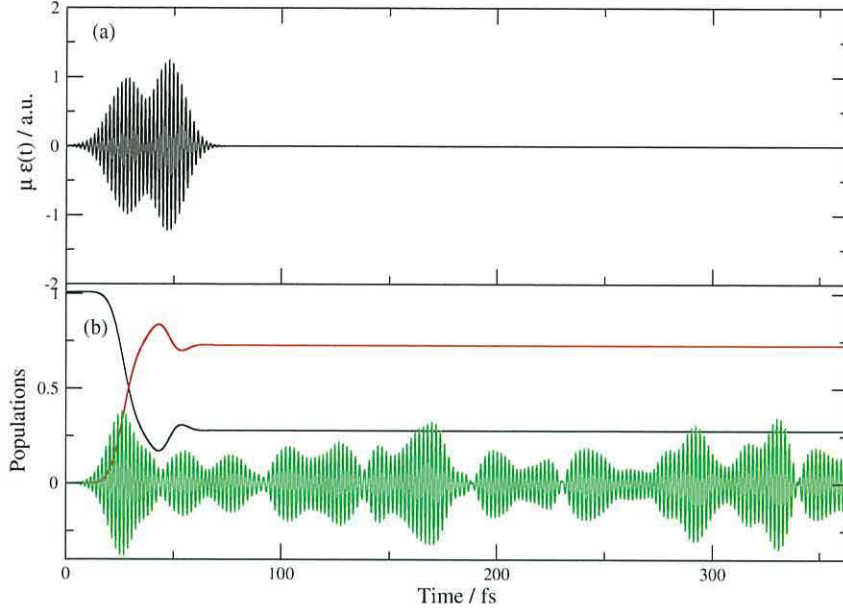


Figure 6.3: (a) Initial guess field. (b) Corresponding time dependent populations of W_{11} (black), W_{22} (red), and $\Re[W_{21}]$ (green) for the isolated (non-dissipative) system

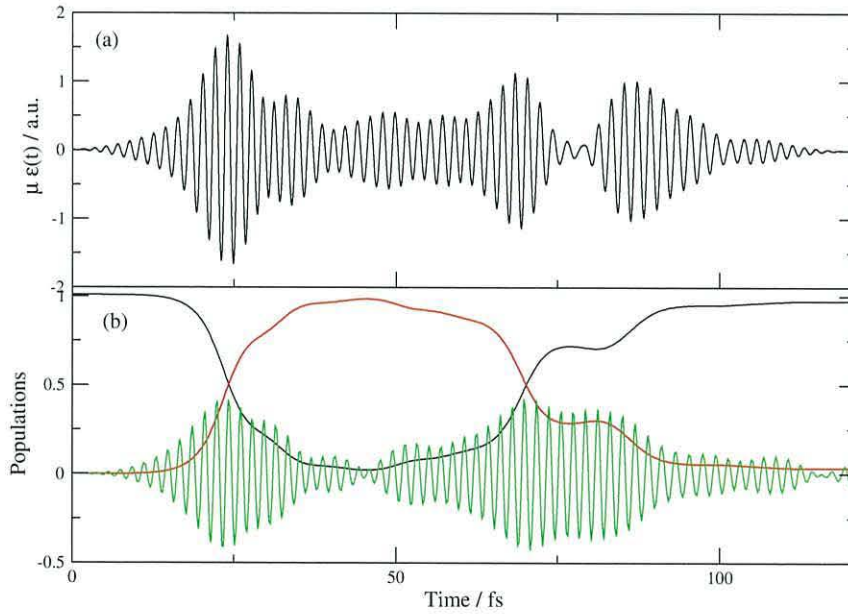


Figure 6.4: (a) Optimised field following 20 iterations of OCT, (b) Corresponding time dependent populations of W_{11} (black), W_{22} (red), and $\Re[W_{21}]$ (green) for the isolated system

the application of the external electric field the magnitude of the electronic coherence $\Re[W_{21}]$ increases from zero, reaching a maximum value approximately at t_1 , before exhibiting oscillatory behaviour when the external field is ‘turned off’.

A shape function $S(t) = \sin^2\left(\pi\frac{t}{T}\right)$ was imposed on the field at each iteration ‘ k ’ of the control scheme, for which a final time of $T = 121$ fs was chosen. Fig. 6.4 depicts the optimised electric field at $k = 20$, together with the corresponding time dependent populations. The optimised field is continuous throughout the propagation, however a clear pump-dump cycle is observed for the relative ground/excited state populations, while $S(t)$ ensures the smooth transition of the electric field ‘on’ and ‘off’. The time dependency of the electronic coherences in this instance seems to suggest a correlation between the relative populations and $\Re[W_{21}]$, where the latter appears to oscillate at the greatest magnitude when $W_{11} = W_{22}$.

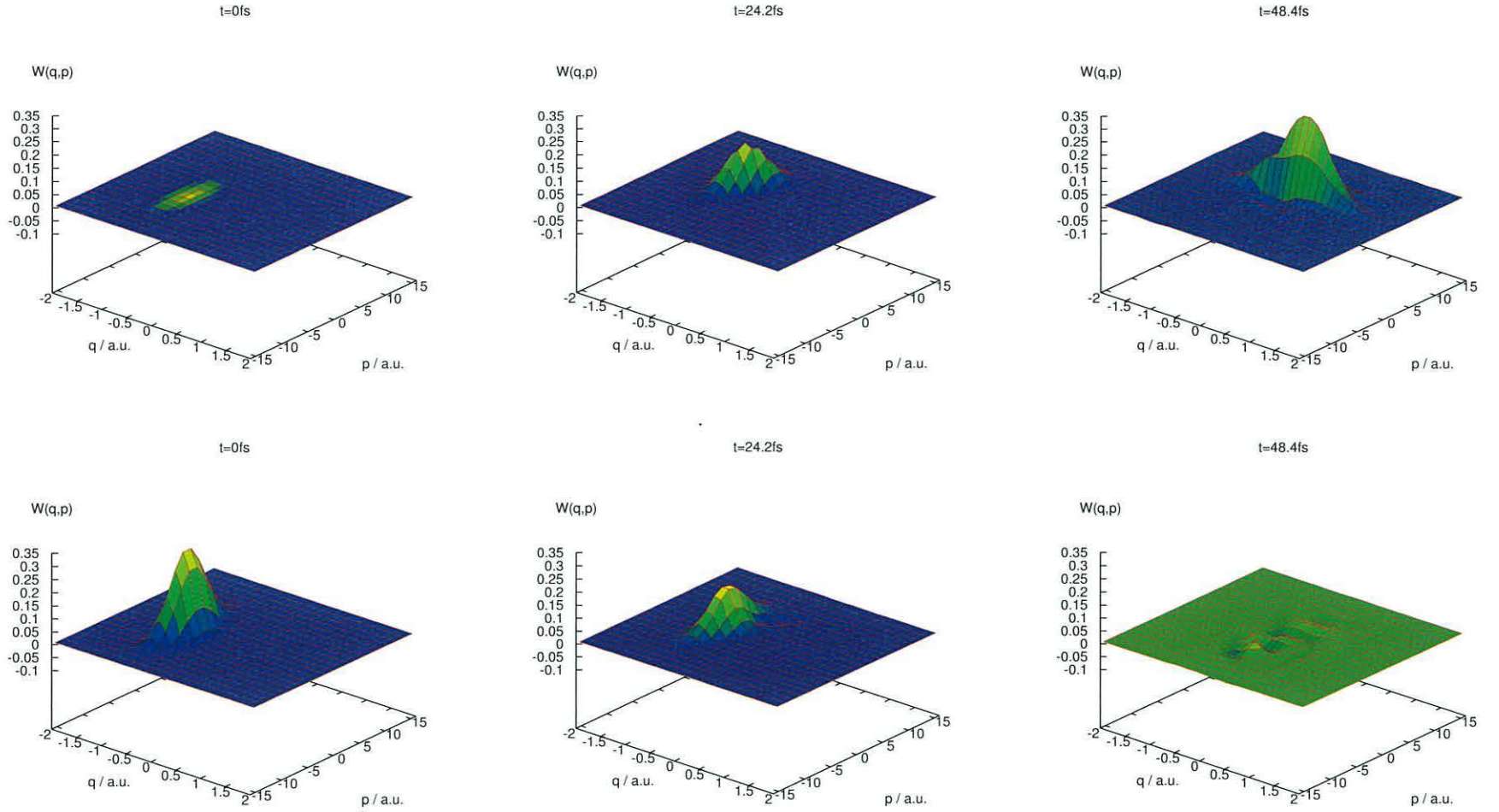


Figure 6.5: Top Row: Instantaneous snapshots of $W_{22}(q,p,t)$ for the isolated ($\eta = 0$) model system under the influence of the optimised field in Fig. 6.4; Bottom Row: Corresponding ground state snapshots $W_{11}(q,p,t)$

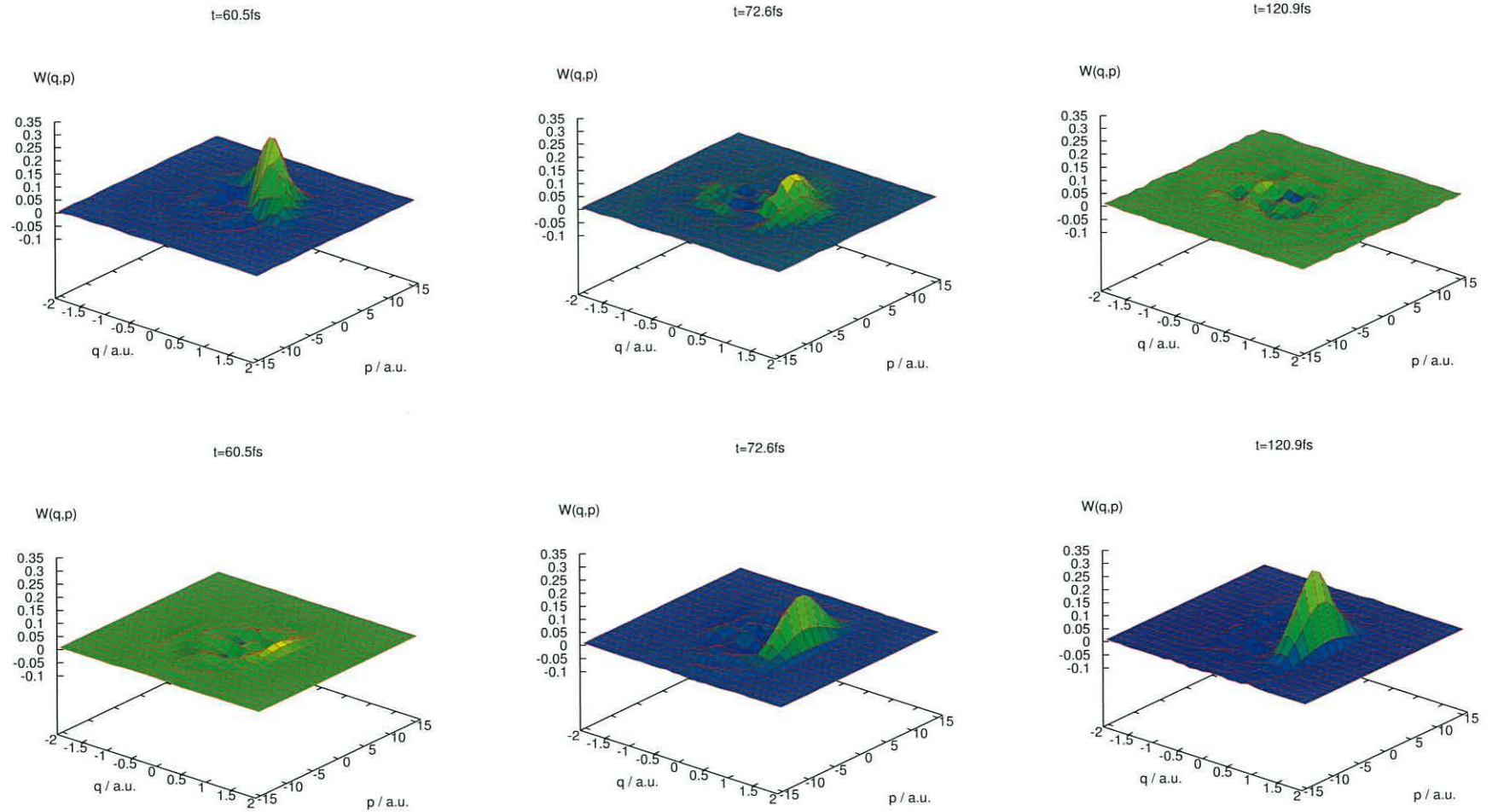


Figure 6.6: Top Row: Instantaneous snapshots of $W_{22}(q,p,t)$ for the isolated ($\eta = 0$) model system under the influence of the optimised field in Fig. 6.4; Bottom Row: Corresponding ground state snapshots $W_{11}(q,p,t)$

Figs. 6.5-6.6 illustrates the time evolution of the model system under the influence of the optimised field depicted by Fig. 6.4 through the perspective of instantaneous snapshots of $W_{11}(q, p, t)$ and $W_{22}(q, p, t)$. At $t = 0$ the system is in the ν_0 stationary state in the LHW of the ground state. A vertical transition is initiated by the external field generating population amplitude on $V_e(q)$ displaced from the HO minimum by q_L . At $t = 24$ fs the population is split evenly between the 2 states, and the excited state amplitude, displaced from equilibrium initially by q_L , acquires positive momentum under the restoring force $\frac{\partial V}{\partial q}$. Clockwise phase space motion, analogous to Fig. 6.1, propagates the Wigner function towards the opposite turning point acquiring a maximum net momentum at $q = 0$ when $t \approx 50$ fs. A gradual re-population of the ground state (Fig. 6.4) occurs from here onwards as different sections of $W_{22}(q, p, t)$ reaches the target destination centred at $q_R = 0.71$. At $t = T = 121$ fs a yield of 0.92 is observed.

6.3.2 Effect of C-L Dissipation on Control

In this section Caldeira-Leggett dissipation is included in the dynamical calculations. The additional dissipative terms, \mathcal{L}_D , in Eqs. (6.34-6.36) are activated by assigning a non-zero value for the system-environment friction coefficient η . A temperature of 600 K is assigned for the bath of harmonic oscillators which compose the environment. All other parameters such as the initial guess field remain the same as the previous section.

Fig. 6.7 illustrates the time dependent populations of the components W_{ij} under the influence of the initial guess field. For the friction coefficients utilised in these calculations the populations $W_{i=j}$ remain largely unchanged in comparison to the isolated system, however the off-diagonal elements undergo decoherence which occurs at a rate proportional to the magnitude of η .

Fig. 6.8 (a) depicts the progress of the OCT procedure at each iteration k for both the dissipative ($\eta = 5 \times 10^{-5}$) and isolated systems. A yield of 0.046 is observed for the dissipative system under the influence of the initial guess field, which is higher than for the isolated system (Fig. 6.3). How-

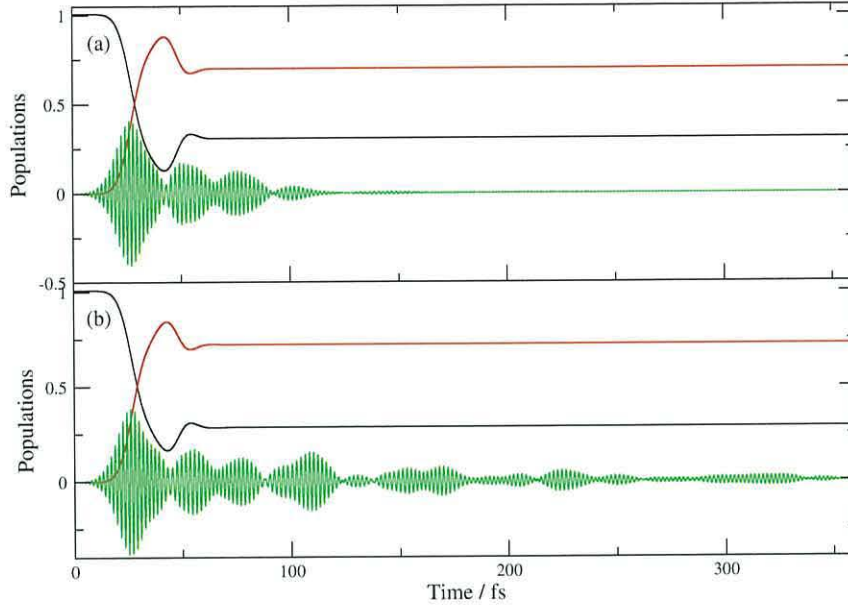


Figure 6.7: Time dependent populations of W_{11} (black), W_{22} (red), and $\Re[W_{21}]$ (green); (a) dissipative system with $T=600$ K and $\eta = 5 \times 10^{-4}$ a.u.; (b) dissipative system with $T=600$ K and $\eta = 5 \times 10^{-5}$ a.u.

ever, it is apparent that environmental dissipation has an adverse effect on the amount of control possible for this particular system, acquiring a yield of 0.78 after 20 iterations. The profile of the OCT progress plots are similar, a sharp increase in yield is observed for the first few iterations before reaching a plateau where little improvement is observed, with the dissipative progress consistently lagging behind the isolated system. Fig. 6.8 (b) illustrates the optimised pulse for the dissipative system after 20 iterations. It is very similar in form to the corresponding optimised pulse for the isolated system (Fig. 6.4), consequently a similar elongated pump-dump mechanism is observed.

6.3.3 Momentum Specific Target States

Optimal control in Wigner phase space naturally leads to the generation of product states with a pre-determined momentum distribution. In the previous sections the eigenstate ν_1 was utilised as the target state, which has

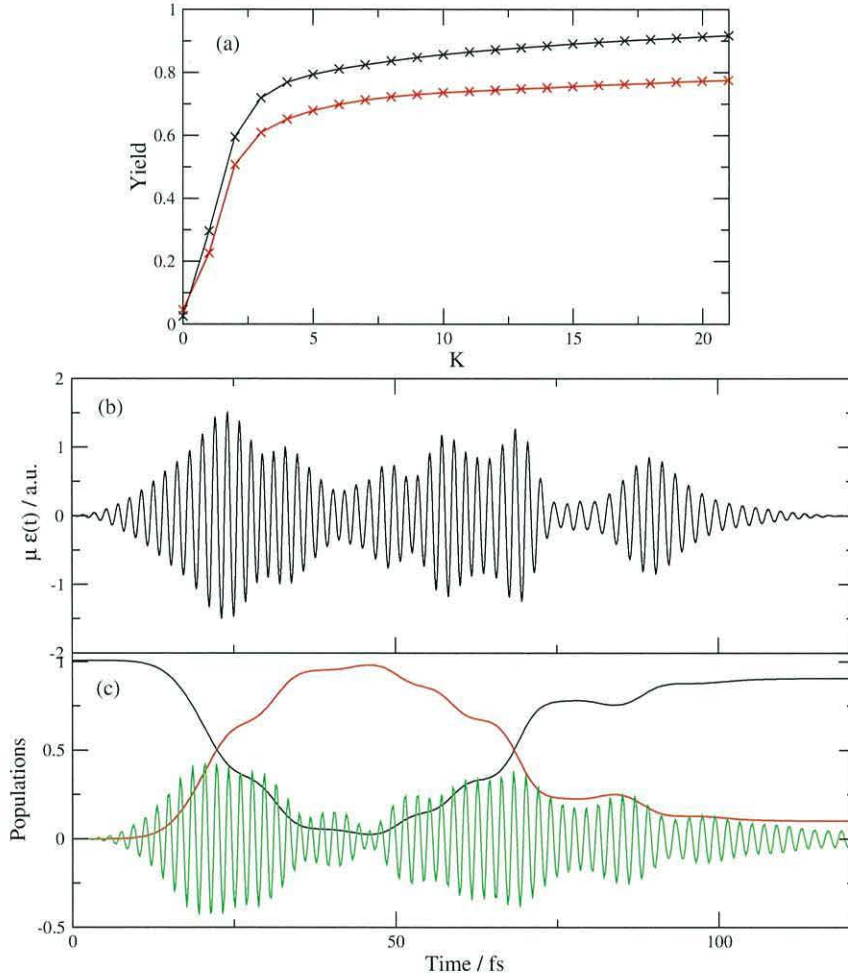


Figure 6.8: (a) Progress of yield against iteration of OCT for $\eta = 0$ (black) and $\eta = 5 \times 10^{-5}$ a.u. (red). (b) Optimised field following 20 iterations of OCT and (c) corresponding time dependent populations of W_{11} (black), W_{22} (red), and $\Re[W_{21}]$ (green) for the dissipative system with $T = 600$ K and $\eta = 5 \times 10^{-5}$.

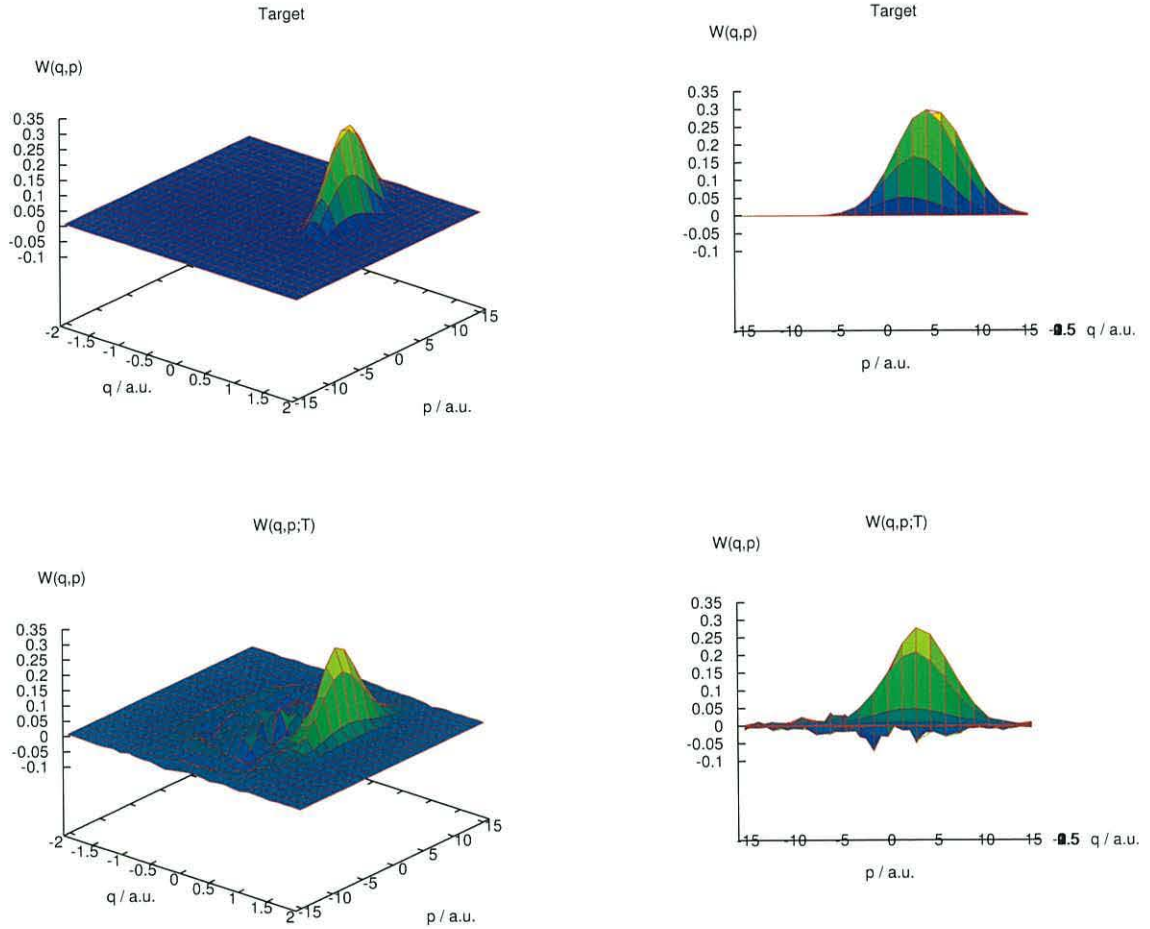


Figure 6.9: Top row: Moderate momentum target state (target A); Bottom row: Final distribution of $W(q,p;t_f)$ with the optimised electric field after 20 iterations

a momentum distribution around $p = 0$. Despite the specific nature of this target state, the optimal product yield compares favourably with the yields observed for the more general target states employed in previous chapters, albeit for a simple model system. In this section the ability of the control scheme to generate target states with significant net momenta is investigated. All other aspects of the system and control scheme are unchanged.

Fig. 6.9 illustrates a target state located in the RHW of the ground state

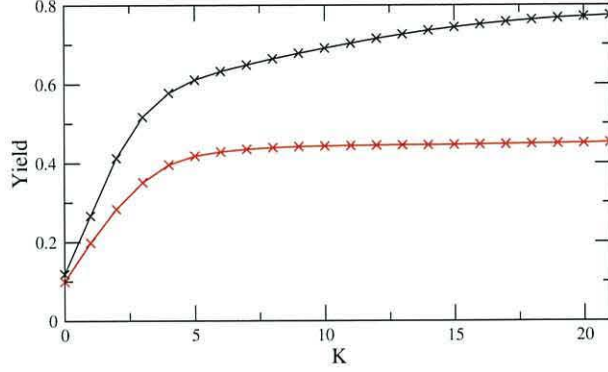


Figure 6.10: Progress of the optimal control procedure for the moderate momentum target state (target A) depicted in Fig. 6.9 for the isolated (black) and dissipative ($\eta = 5 \times 10^{-5}$) (red) systems.

potential with a momentum profile distributed around $p = 4.8$ a.u. (target A), and the product distribution yielded after 20 iterations of OCT. The progress of the optimal control procedure for this target state is illustrated in Fig. 6.10 where a yield of 0.77 is observed after 20 iterations. Fig. 6.11 illustrates an alternative target state with a narrower momentum distribution centred at $p = 13.0$ a.u. (target B). The yield after 20 iterations for this target state is even less at 0.33 (Fig. 6.12). These observations suggests that the possibility of finding a satisfactory optimised pulse diminishes when the net momentum of the target state is increased.

These results appear to be rational in the sense that a Wigner function with a large velocity would occupy a specific coordinate ' q ' distribution for only a small time frame, increasing the required precision of the optimised pulse. As a consequence, optimising the yield of a high velocity product would require a 'better' initial guess - the choice of final time t_f in particular is far more crucial than when a stationary target state is considered.

Upon closer inspection of Fig. 6.12 it becomes apparent that the initial guess field (which is identical to all previous examples) is less relevant for target state B. The progress in this instance is more lethargic, and more significant improvements are still observed for later iterations in comparison to the target states with smaller momentum. In addition, a large momentum target state would be composed of a superposition of high energy eigenstates,

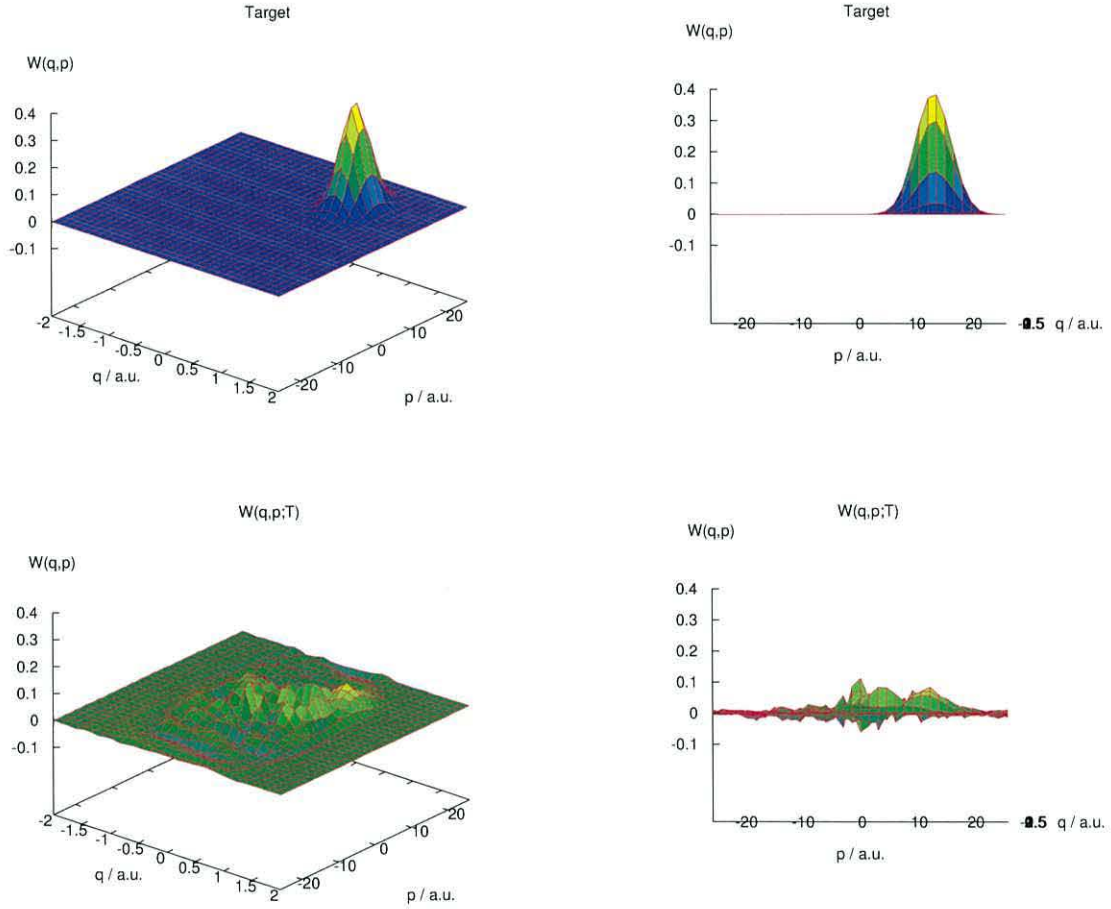


Figure 6.11: Top row: Large momentum target state (target B); Bottom row: Final distribution of $W(q,p;t_f)$ with the optimised electric field after 20 iterations

the generation of such ‘vibrationally hot’ products were achieved in Chapters 4-5 by dumping the state function on to a steep section of the ground state potential. The pulse sequence to achieve this will have characteristics very different to the initial guess employed here, including different carrier frequencies ω to initiate electronic transitions at coordinates q where $V_g(q)$ is large.

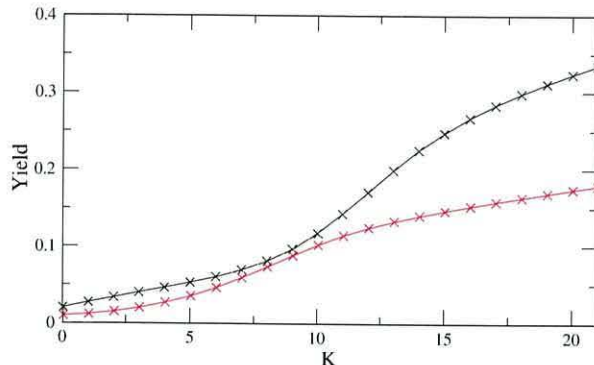


Figure 6.12: Progress of the optimal control procedure for the large momentum target state (target B) depicted in Fig. 6.11 for the isolated (black) and dissipative ($\eta = 5 \times 10^{-5}$) (red) systems.

Target states with rigid characteristics have the benefit of generating more rational product states than more loosely defined target states. Targets in the manner of those utilised in Chapters 4-5 are indiscriminate, and may allow products with arbitrarily high energy which in reality would continue to evolve to a different entity than the desired product. Of course, rigid target states may also be employed in the Schrödinger representation of OCT, for example a specific eigenstate ν_n may be used. While information about p in the wavefunction representation is implicitly contained within Ψ via its width and phase, the Wigner function provides an explicit representation of both p and q , hence momentum specific target states may be more conveniently defined in the Wigner representation.

6.4 Further Work

The focus of this chapter was the effect of the environment on a control scheme. A key assumption of the model was the Markov approximation which implies that the dynamics, or fluctuations, of the environment is much faster than the system dynamics. This approximation is valid for many physical phenomena, however the control schemes discussed in this thesis span the femto-picosecond timescale, and in such cases the Markov approximation is not always valid, and the more challenging non-Markovian approach should

be used.

Further work into the development of a control scheme for dissipative systems would focus on a non-Markovian approach. A promising approach based on the original work of Garg *et al* [29] involves coupling the system to an effective mode. The effective mode then Ohmically couples to the environment in the same manner discussed in the present chapter i.e. Markovian Caldeira-Leggett approach.

The system then experiences delayed (non-Markovian) dissipative dynamics. It was shown by Garg *et al* that a transformation from the system – effective mode – environment representation to a system directly coupled to a bath resulted in the transformation of $J(\omega)$ from Ohmic to a Lorentzian type $J'(\omega)$.

In an extension of the Garg approach we have developed an approach where the system is coupled to a chain of effective modes and the resulting transformed system-environment spectral density develops a more complicated multi-peaked form that could be related to the experimental $J(\omega)$ of large molecules obtained from e.g. 3-pulse photon echo experiments [24].

Bibliography

- [1] G. S. Evans, *The Development of a Quantum Mechanical Description of Intramolecular Energy Transfer*, Ph.D Thesis, University of Wales Bangor, (2005).
- [2] D. Kohen, C. C. Marston, D. J. Tannor, *J. Chem. Phys.*, (1997), **107**, 5236.
- [3] Y. Yan, R. Xu, *Ann. Rev. Phys. Chem.*, (2005), **56**, 187.
- [4] H. -P. Breuer and F. Petruccione, *The Theory of Open Quantum Systems*, Oxford University Press, (2002).
- [5] S. E. Sklarz, D. J. Tannor, *Phys. Rev. A*, (2004), **69**, 053408.
- [6] A. Bartana, R. Kosloff, D. J. Tannor, *J. Chem. Phys.*, (1993), **99**, 196.
- [7] A. Bartana, R. Kosloff, D. J. Tannor, *J. Chem. Phys.*, (1997), **106**, 1435.
- [8] P. Gross, S. D. Schwartz, *J. Chem. Phys.*, (1998), **109**, 5843.
- [9] Y. Ohtsuki, K. Nakagami, W. Zhu, H. Rabitz, *Chem. Phys.*, (2003), **287**, 197.
- [10] J. Cao, M. Messina, K. R. Wilson, *J. Phys. Chem.*, (1997), **106**, 5239.
- [11] D. Geppert, R. de Vivie-Riedle, *Chem. Phys. Lett.*, (2005), **404**, 289.
- [12] J. von Neumann, *Mathematical Foundations of Quantum Mechanics*, Princeton university press, (1983).
- [13] W. A. Lin and L. E. Ballentine, *Phys. Rev. Lett.*, (1990), **65**, 2927.
- [14] J. Y. Shin, H. W. Lee, *Phys. rev. E*, (1994), **50**, 902.

- [15] E. Wigner *Physica (Utrecht)*, (1940), **7**, 749.
- [16] D. J. Tannor, *Introduction to Quantum Mechanics: a Time-Dependent Perspective*, University Science Books, (2007).
- [17] W. P. Schleich, *Quantum Optics in Phase Space*, Wiley-VCH, (2001).
- [18] U. Weiss, *Quantum Dissipative Systems*, World Scientific Singapore, (1993).
- [19] A. O. Caldeira, A. J. Leggett, *Phys. Rev. Lett.*, (1981), **46**, 211.
- [20] A. O. Caldeira, A. J. Leggett, *Physica A*, (1983), **121**, 587.
- [21] R. L. Anderson, *Decoherence, Dephasing and Quantum Tunneling in Molecules with Large Amplitude Vibrations*, Ph.D Thesis, University of Wales Bangor, (2006).
- [22] A. Damjanovic, I. Kosztin, U. Kleinekathöfer, K. Schulten, *Phys. Rev. E*, (2002), **65**, 031919.
- [23] J. Gilmore, R. H. McKenzie, *J. Phys. Chem. A*, (2008), **112**, 2162.
- [24] Y. Nagasawa, J. Y. Yu, G. R. Fleming, *J. Chem. Phys.*, (1998), **109**, 6175.
- [25] C. Meier, D. J. Tannor, *J. Chem. Phys.*, (1999), **111**, 03365.
- [26] K. H. Hughes, M. Hywel, *Coherent Control of Molecules*, edited B. Lasorne, G. Worth (CCP6, Daresbury Laboratory, 2006).
- [27] K. H. Hughes, M. Hywel; (to be published).
- [28] S. A. Rice, M. Zhao, *Optimal Control of Molecular Dynamics*, Wiley, (2000).
- [29] A. Garg, J. N. Onuchic, V. Ambegaokar, *J. Chem. Phys.*, (1985), **83**, 4481.

Appendix A

Split-Operator Numerical Method on Two electronic states

In this section, the convention of Rice and Zhao¹ is used to expand the Split-Operator method into 2 electronic states.

The wavepacket is to be represented on two electronic states

$$\Psi(t) = \begin{pmatrix} \Psi_e(t) \\ \Psi_g(t) \end{pmatrix} \quad (\text{A.1})$$

where the subscript g refers to the ground electronic state, and the subscript e refers to an excited electronic state. As for the single state situation, the Hamiltonian \hat{H} within the evolution operator A is separated into its kinetic and potential components, with an additional component which describes the coupling between the two states resulting - in this case the external electromagnetic field. The 2×2 Hamiltonian can be partitioned to yield

$$\hat{H} = \hat{T} + \hat{V} + \hat{W} \quad (\text{A.2})$$

¹S. A. Rice, M. Zhao, *Optimal Control of Molecular Dynamics*, Wiley, (2000).

where \hat{T} and \hat{V} contain the diagonal components

$$\hat{H}_0 = \begin{pmatrix} T & 0 \\ 0 & T \end{pmatrix} \quad (\text{A.3})$$

$$\hat{V} = \begin{pmatrix} V_e & 0 \\ 0 & V_g \end{pmatrix} \quad (\text{A.4})$$

where V_e is the excited electronic state potential and V_g is the potential for the ground state. The operator \hat{W} contains the off-diagonal terms

$$\hat{W} = \begin{pmatrix} 0 & \mu\epsilon(t) \\ \mu\epsilon(t) & 0 \end{pmatrix} \quad (\text{A.5})$$

where $\mu(x)$ is the transition dipole moment and $\epsilon(t)$ is the time dependent electromagnetic field.

The split-operator approximation is applied to the short time propagator

$$e^{-(i/\hbar)\hat{H}\Delta t} = e^{-(i/2\hbar)\hat{H}_0\Delta t} e^{-(i/2\hbar)\hat{W}\Delta t} e^{-(i/\hbar)\hat{V}\Delta t} e^{-(i/2\hbar)\hat{W}\Delta t} e^{-(i/2\hbar)\hat{H}_0\Delta t} + 0(\Delta t)^3. \quad (\text{A.6})$$

The implementation of the matrix operators \hat{H}_0 and \hat{V} are straightforward when the wavepacket is represented in momentum space and coordinate space respectively. However, the matrix operator \hat{W} needs to be diagonalised before it can be implemented on the wavepacket in coordinate space. The unitary transform matrix, U , and its inverse, U^{-1} , have the form

$$U = \frac{\sqrt{2}}{2} \begin{pmatrix} 1 & -1 \\ 1 & 1 \end{pmatrix} \quad (\text{A.7})$$

$$U^{-1} = \frac{\sqrt{2}}{2} \begin{pmatrix} 1 & 1 \\ -1 & 1 \end{pmatrix} \quad (\text{A.8})$$

Applying the unitary transformation to the electromagnetic field part of

the short time propagator yields

$$U^{-1}e^{-(i/2\hbar)\hat{W}\Delta t}U = \begin{pmatrix} e^{-i[\mu\epsilon(t)\Delta t/2\hbar]} & 0 \\ 0 & e^{i[\mu\epsilon(t)\Delta t/2\hbar]} \end{pmatrix} \quad (\text{A.9})$$

For consistency, the same unitary transformation matrices needs to be applied to the potential part of the propagator as it is also implemented in coordinate space

$$U^{-1}e^{-(i/\hbar)\hat{V}\Delta t}U = \frac{1}{2} \begin{pmatrix} P_e + P_g & -P_e + P_g \\ -P_e + P_g & P_e + P_g \end{pmatrix} \quad (\text{A.10})$$

where

$$P_e = e^{-i(\hat{V}_e\Delta t/\hbar)} \quad (\text{A.11})$$

$$P_g = e^{-i(\hat{V}_g\Delta t/\hbar)} \quad (\text{A.12})$$

Inserting equations A.9 and A.10 into equation A.6 yields

$$\begin{aligned} e^{-(i/2\hbar)\hat{W}\Delta t}e^{-(i/\hbar)\hat{V}\Delta t}e^{-(i/2\hbar)\hat{W}\Delta t} &= \frac{1}{4} \begin{pmatrix} 1 & -1 \\ 1 & 1 \end{pmatrix} \begin{pmatrix} e^{-i[\mu\epsilon(t)\Delta t/2\hbar]} & 0 \\ 0 & e^{i[\mu\epsilon(t)\Delta t/2\hbar]} \end{pmatrix} \\ &\times \begin{pmatrix} P_e + P_g & -P_e + P_g \\ -P_e + P_g & P_e + P_g \end{pmatrix} \begin{pmatrix} e^{-i[\mu\epsilon(t)\Delta t/2\hbar]} & 0 \\ 0 & e^{i[\mu\epsilon(t)\Delta t/2\hbar]} \end{pmatrix} \begin{pmatrix} 1 & -1 \\ 1 & 1 \end{pmatrix} \end{aligned} \quad (\text{A.13})$$

Multiplying the matrices in equation A.13 followed by the application of the Euler formula, $e^{ix} = \cos x + i \sin x$, eventually yields

$$\frac{1}{2} \begin{pmatrix} (P_e + P_g) \cos A + (P_e - P_g) & -i(P_e + P_g) \sin A \\ -i(P_e + P_g) \sin A & (P_e + P_g) \cos A - (P_e - P_g) \end{pmatrix} \quad (\text{A.14})$$

where

$$A = \frac{\mu\epsilon(t)\Delta t}{\hbar}. \quad (\text{A.15})$$

A similar algorithm to the 1 electronic state split-operator may now be implemented on the 2 state system, where equation A.3 is applied to the wavepacket when it is represented in momentum space, $\Psi(k)$, and equation

A.14 is applied to the wavepacket when its represented in coordinate space, $\Psi(x)$.

Appendix B

Determination of Reduced Moment of Inertia

The reduced moment of inertia (or reduced mass) along a coordinate γ is given by

$$M_\mu = \sum_i m_i \left(\frac{\partial r_i}{\partial \gamma} \right) \left(\frac{\partial r_i}{\partial \gamma} \right) \quad (\text{B.1})$$

where m_i is the mass of the i 'th atom and r_i is its position vector in the centre of mass (CoM) axis frame¹. Fig. B.1 illustrates the CoM (x', y', z') axis frame and an arbitrary (x, y, z) axis frame for azomethane, including a vector σ which points from the CoM towards the origin of the arbitrary (x, y, z) axis frame.

The CoM position vectors r_i are related to their arbitrary axis frame counterparts d_i via the relation

$$r_i = d_i - \sigma \quad (\text{B.2})$$

where

$$\sigma = \frac{\sum_i m_i d_i}{M} \quad (\text{B.3})$$

where M is the total mass of the system. It therefore follows that the reduced moment of inertia may be determined from an arbitrary axis frame by the

¹not necessarily the principle axis frame

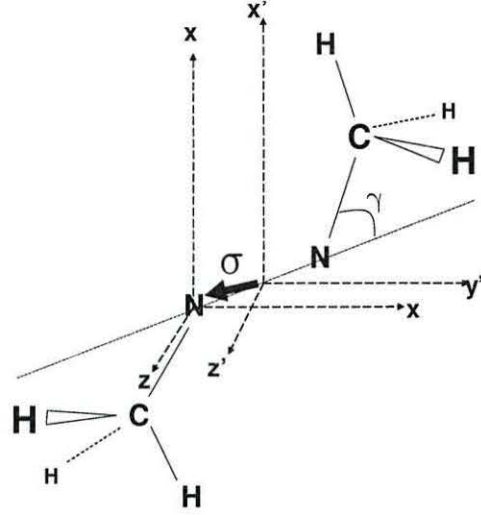


Figure B.1: The inversion isomerisation coordinate of azomethane. Labelled are both the arbitrary (x,y,z) and centre of mass (x',y',z') axis frames. Here σ is a vector pointing from the centre of mass to the the origin of the arbitrary (x,y,z) frame.

relation

$$M_{\mu} = \sum_i m_i \left(\left[\left(\frac{\partial d_i^x}{\partial \gamma} \right) - \left(\frac{\partial \sigma_x}{\partial \gamma} \right) \right]^2 + \left[\left(\frac{\partial d_i^y}{\partial \gamma} \right) - \left(\frac{\partial \sigma_y}{\partial \gamma} \right) \right]^2 + \left[\left(\frac{\partial d_i^z}{\partial \gamma} \right) - \left(\frac{\partial \sigma_z}{\partial \gamma} \right) \right]^2 \right). \quad (\text{B.4})$$

Appendix C

Derivation of the Wigner-Moyal equation

C.1 One Electronic State

Before proceeding we define the positional coordinates x and x' as the difference coordinates which are related to the diagonal coordinate q and the off-diagonal part of the coordinate r by $x = q + r/2$ and $x' = q - r/2$. Consequently, $q = 0.5(x + x')$ and $r = x - x'$. With these definitions the Wigner function $W(q, p)$ is related to the density matrix by

$$\begin{aligned} W(q, p) &= \frac{1}{2\pi\hbar} \int_{-\infty}^{\infty} \langle x|\rho|x' \rangle e^{-i\frac{rp}{\hbar}} dr \\ &= \frac{1}{2\pi\hbar} \int_{-\infty}^{\infty} \langle q + \frac{r}{2}|\rho|q - \frac{r}{2} \rangle e^{-i\frac{rp}{\hbar}} dr \end{aligned} \quad (C.1)$$

and

$$\langle x|\rho|x' \rangle = \rho(x, x') = \int_{-\infty}^{\infty} W(q, p) e^{i\frac{rp}{\hbar}} dr. \quad (C.2)$$

For a single electronic state system the quantum Liouville equation for the density matrix is given by

$$\frac{\partial}{\partial t} \rho(x, x') = -\frac{i}{\hbar} \left\{ -\frac{\hbar^2}{2m} \left(\frac{\partial^2}{\partial x^2} - \frac{\partial^2}{\partial x'^2} \right) + V(x) - V(x') \right\} \rho(x, x'). \quad (C.3)$$

The equation of motion for $W(q, p)$ is obtained by taking the Wigner transform of Eq. (C.3). Taking the Wigner transform of the LHS of Eq. (C.3) yields

$$\frac{1}{2\pi\hbar} \int_{-\infty}^{\infty} \frac{\partial}{\partial t} \rho(x, x') e^{-i\frac{rp}{\hbar}} dr = \frac{\partial}{\partial t} \frac{1}{2\pi\hbar} \int_{-\infty}^{\infty} \rho(x, x') e^{-i\frac{rp}{\hbar}} dr = \frac{\partial}{\partial t} W(q, p). \quad (\text{C.4})$$

Wigner transform of the kinetic energy part of the QLE

For the kinetic energy part in the RHS of Eq. (C.3) the following relations between the derivatives are used

$$\frac{\partial}{\partial x} = \frac{dq}{dx} \frac{\partial}{\partial q} + \frac{dr}{dx} \frac{\partial}{\partial r} = \frac{1}{2} \frac{\partial}{\partial q} + \frac{\partial}{\partial r} \quad (\text{C.5})$$

$$\begin{aligned} \frac{\partial^2}{\partial x^2} &= \frac{\partial}{\partial x} \left(\frac{dq}{dx} \frac{\partial}{\partial q} + \frac{dr}{dx} \frac{\partial}{\partial r} \right) \\ &= \left(\frac{1}{2} \frac{\partial}{\partial q} + \frac{\partial}{\partial r} \right) \left(\frac{1}{2} \frac{\partial}{\partial q} + \frac{\partial}{\partial r} \right) \\ &= \frac{1}{4} \frac{\partial^2}{\partial q^2} + \frac{\partial^2}{\partial r \partial q} + \frac{\partial^2}{\partial r^2} \end{aligned} \quad (\text{C.6})$$

$$\frac{\partial}{\partial x'} = \frac{dq}{dx'} \frac{\partial}{\partial q} + \frac{dr}{dx'} \frac{\partial}{\partial r} = \frac{1}{2} \frac{\partial}{\partial q} - \frac{\partial}{\partial r} \quad (\text{C.7})$$

$$\begin{aligned} \frac{\partial^2}{\partial x'^2} &= \frac{\partial}{\partial x'} \left(\frac{dq}{dx'} \frac{\partial}{\partial q} + \frac{dr}{dx'} \frac{\partial}{\partial r} \right) \\ &= \left(\frac{1}{2} \frac{\partial}{\partial q} - \frac{\partial}{\partial r} \right) \left(\frac{1}{2} \frac{\partial}{\partial q} - \frac{\partial}{\partial r} \right) \\ &= \frac{1}{4} \frac{\partial^2}{\partial q^2} - \frac{\partial^2}{\partial r \partial q} + \frac{\partial^2}{\partial r^2} \end{aligned} \quad (\text{C.8})$$

Consequently

$$\frac{\partial^2}{\partial x^2} - \frac{\partial^2}{\partial x'^2} = 2 \frac{\partial^2}{\partial r \partial q}. \quad (\text{C.9})$$

Substituting this expression for the derivatives into the kinetic part of Eq. (??) yields

$$i \frac{\hbar}{m} \frac{\partial^2}{\partial r \partial q} < q + \frac{r}{2} | \rho | q - \frac{r}{2} > . \quad (\text{C.10})$$

Taking the Wigner transform of Eq. (C.10) gives

$$\begin{aligned}
& \frac{1}{2\pi\hbar} \int_{-\infty}^{\infty} i \frac{\hbar}{m} \frac{\partial^2}{\partial r \partial q} \left(\left\langle q + \frac{r}{2} \left| \rho \right| q - \frac{r}{2} \right\rangle \right) e^{-i \frac{rp}{\hbar}} dr \\
&= \frac{i\hbar}{m2\pi\hbar} \frac{\partial}{\partial q} \int_{-\infty}^{\infty} \frac{\partial}{\partial r} \left\langle q + \frac{r}{2} \left| \rho \right| q - \frac{r}{2} \right\rangle e^{-i \frac{rp}{\hbar}} dr
\end{aligned} \tag{C.11}$$

Integrating by parts gives

$$\begin{aligned}
& \frac{i\hbar}{m2\pi\hbar} \frac{\partial}{\partial q} \left[\left\langle q + \frac{r}{2} \left| \rho \right| q - \frac{r}{2} \right\rangle e^{-i \frac{rp}{\hbar}} \right]_{-\infty}^{\infty} \\
& - \frac{i\hbar}{m2\pi\hbar} \frac{\partial}{\partial q} \int_{-\infty}^{\infty} \left\langle q + \frac{r}{2} \left| \rho \right| q - \frac{r}{2} \right\rangle \frac{\partial}{\partial r} e^{-i \frac{rp}{\hbar}} dr \\
&= 0 - \frac{i\hbar}{m2\pi\hbar} \frac{\partial}{\partial q} \int_{-\infty}^{\infty} \left\langle q + \frac{r}{2} \left| \rho \right| q - \frac{r}{2} \right\rangle \frac{-i}{\hbar} p e^{-i \frac{rp}{\hbar}} dr \\
&= -\frac{p}{m} \frac{\partial}{\partial q} \frac{1}{2\pi\hbar} \int_{-\infty}^{\infty} \left\langle q + \frac{r}{2} \left| \rho \right| q - \frac{r}{2} \right\rangle e^{-i \frac{rp}{\hbar}} dr \\
&= -\frac{p}{m} \frac{\partial}{\partial q} W(q, p).
\end{aligned} \tag{C.12}$$

In the first line of the above expression the term in square brackets is zero because of the boundary conditions that the density matrix tends to zero as $r \rightarrow \pm\infty$.

Wigner transform of the potential part of the QLE

For the potential energy part of the QLE it is assumed that V can be expanded in a Taylor series about q ,

$$\begin{aligned} V(x) &= V(q + r/2) \simeq \sum_{n=0}^{\infty} \frac{r^n}{n!2^n} \frac{\partial^n V}{\partial q^n} \\ &= V(q) + \frac{r}{2} \frac{\partial V}{\partial q} + \frac{r^2}{8} \frac{\partial^2 V}{\partial q^2} + \frac{r^3}{48} \frac{\partial^3 V}{\partial q^3} + \dots \end{aligned} \quad (\text{C.13})$$

$$\begin{aligned} V(x') &= V(q - r/2) \simeq \sum_{n=0}^{\infty} \frac{-r^n}{n!2^n} \frac{\partial^n V}{\partial q^n} \\ &= V(q) - \frac{r}{2} \frac{\partial V}{\partial q} + \frac{r^2}{8} \frac{\partial^2 V}{\partial q^2} - \frac{r^3}{48} \frac{\partial^3 V}{\partial q^3} + \dots \end{aligned} \quad (\text{C.14})$$

Taking $V(x) - V(x')$ removes the even powered terms¹. To 3rd order

$$V(x) - V(x') \simeq r \frac{\partial V}{\partial q} + \frac{r^3}{24} \frac{\partial^3 V}{\partial q^3} + \dots \quad (\text{C.15})$$

Substituting this representation of V into the Liouville equation and taking the Wigner transform gives

$$\begin{aligned} & -\frac{i}{\hbar} \frac{1}{2\pi\hbar} \int_{-\infty}^{\infty} \left\{ V(x) - V(x') \right\} \rho(x, x') e^{-i\frac{rp}{\hbar}} dr \\ & \simeq -\frac{i}{\hbar} \frac{1}{2\pi\hbar} \int_{-\infty}^{\infty} \left\{ r \frac{\partial V}{\partial q} + \frac{r^3}{24} \frac{\partial^3 V}{\partial q^3} \right\} < q + \frac{r}{2} | \rho | q - \frac{r}{2} > e^{-i\frac{rp}{\hbar}} dr \end{aligned} \quad (\text{C.16})$$

for the potential part. Inserting the relation

$$\left(\frac{-\hbar}{i} \right)^n \frac{\partial^n}{\partial p^n} e^{-i\frac{rp}{\hbar}} = r^n \quad (\text{C.17})$$

¹For the off-diagonal terms of a multi-state system the even powered terms do not cancel.

into Eq. (C.16) gives

$$\begin{aligned}
& -\frac{i}{\hbar} \frac{1}{2\pi\hbar} \int_{-\infty}^{\infty} \left\{ r \frac{\partial V}{\partial q} + \frac{r^3}{24} \frac{\partial^3 V}{\partial q^3} \right\} < q + \frac{r}{2} | \rho | q - \frac{r}{2} > e^{-i\frac{rp}{\hbar}} dr \\
& = -\frac{i}{\hbar} \frac{1}{2\pi\hbar} \int_{-\infty}^{\infty} \left\{ \frac{\partial V}{\partial q} - \frac{\hbar}{i} \frac{\partial}{\partial p} + \frac{1}{24} \frac{\partial^3 V}{\partial q^3} - \frac{\hbar^3}{-i} \frac{\partial^3}{\partial p^3} \right\} < q + \frac{r}{2} | \rho | q - \frac{r}{2} > e^{-i\frac{rp}{\hbar}} dr \\
& = \frac{\partial V}{\partial q} \frac{\partial}{\partial p} \frac{1}{2\pi\hbar} \int_{-\infty}^{\infty} < q + \frac{r}{2} | \rho | q - \frac{r}{2} > e^{-i\frac{rp}{\hbar}} dr \\
& - \frac{\hbar^2}{24} \frac{\partial^3 V}{\partial q^3} \frac{\partial^3}{\partial p^3} \frac{1}{2\pi\hbar} \int_{-\infty}^{\infty} < q + \frac{r}{2} | \rho | q - \frac{r}{2} > e^{-i\frac{rp}{\hbar}} dr \\
& = \frac{\partial V}{\partial q} \frac{\partial}{\partial p} W(q, p) - \frac{\hbar^2}{24} \frac{\partial^3 V}{\partial q^3} \frac{\partial^3}{\partial p^3} W(q, p). \tag{C.18}
\end{aligned}$$

Finally, the EOM for $W(q, p)$ for a single state system is given by

$$\frac{\partial W}{\partial t} = -\frac{p}{m} \frac{\partial W}{\partial q} + \frac{\partial V}{\partial q} \frac{\partial W}{\partial p} - \frac{\hbar^2}{24} \frac{\partial^3 V}{\partial q^3} \frac{\partial^3 W}{\partial p^3} \dots \tag{C.19}$$

C.2 Two Electronic State

The QLE for the density operator of a two state system is given by

$$\begin{aligned}
\frac{\partial}{\partial t} \begin{bmatrix} \rho_{11} & \rho_{12} \\ \rho_{21} & \rho_{22} \end{bmatrix} & = -\frac{i}{\hbar} \left\{ \begin{bmatrix} H_g & -\mu\varepsilon(t) \\ -\mu\varepsilon^*(t) & H_e \end{bmatrix} \begin{bmatrix} \rho_{11} & \rho_{12} \\ \rho_{21} & \rho_{22} \end{bmatrix} \right. \\
& \quad \left. - \begin{bmatrix} \rho_{11} & \rho_{12} \\ \rho_{21} & \rho_{22} \end{bmatrix} \begin{bmatrix} H_g & -\mu\varepsilon(t) \\ -\mu\varepsilon^*(t) & H_e \end{bmatrix} \right\} \tag{C.20}
\end{aligned}$$

where μ is the transition dipole moment, $\varepsilon(t)$ is the time dependent electric field and

$$H_{g/e} = -\frac{\hbar^2}{2m} \nabla^2 + V_{g/e} \tag{C.21}$$

where g/e represents the ground or excited state respectively.

The equations of motion for each element of the density matrix are

$$\begin{aligned}\frac{\partial}{\partial t}\rho_{11} &= -\frac{i}{\hbar}\{H_g\rho_{11} - \mu\varepsilon\rho_{21} - \rho_{11}H_g + \rho_{12}\mu\varepsilon^*\} \\ &= -\frac{i}{\hbar}\{[H_g, \rho_{11}] - \mu(\varepsilon\rho_{21} - \rho_{12}\varepsilon^*)\}\end{aligned}\quad (\text{C.22})$$

$$\begin{aligned}\frac{\partial}{\partial t}\rho_{22} &= -\frac{i}{\hbar}\{-\mu\varepsilon^*\rho_{12} + H_e\rho_{22} + \rho_{21}\mu\varepsilon - \rho_{22}H_e\} \\ &= -\frac{i}{\hbar}\{[H_e, \rho_{22}] + \mu(\varepsilon\rho_{21} - \varepsilon^*\rho_{12})\}\end{aligned}\quad (\text{C.23})$$

$$\begin{aligned}\frac{\partial}{\partial t}\rho_{12} &= -\frac{i}{\hbar}\{H_g\rho_{12} - \mu\varepsilon\rho_{22} + \rho_{11}\mu\varepsilon - \rho_{12}H_e\} \\ &= -\frac{i}{\hbar}\{H_g\rho_{12} - \rho_{12}H_e - \mu\varepsilon(\rho_{22} - \rho_{11})\}\end{aligned}\quad (\text{C.24})$$

$$\begin{aligned}\frac{\partial}{\partial t}\rho_{21} &= -\frac{i}{\hbar}\{-\mu\varepsilon^*\rho_{11} + H_e\rho_{21} - \rho_{21}H_g + \rho_{22}\mu\varepsilon^*\} \\ &= -\frac{i}{\hbar}\{H_e\rho_{21} - \rho_{21}H_g + \mu\varepsilon^*(\rho_{22} - \rho_{11})\} \\ &= \frac{i}{\hbar}\{\rho_{21}H_g - H_e\rho_{21} - \mu\varepsilon^*(\rho_{22} - \rho_{11})\} \\ &= \frac{i}{\hbar}\{H_g\rho_{12} - \rho_{12}H_e - \mu\varepsilon(\rho_{22} - \rho_{11})\}^* \\ &= \frac{\partial}{\partial t}\rho_{12}^*.\end{aligned}\quad (\text{C.25})$$

Note that the Hamiltonian to the left of the density matrix operates on the ket,

$$H_{g/e}\rho_{ij} = H_{g/e}|\Psi_i\rangle\langle\Psi_j| \quad (\text{C.26})$$

and the Hamiltonian to the right of the density matrix operates on the bra,

$$\rho_{ij}H_{g/e} = |\Psi_i\rangle\langle\Psi_j|H_{g/e} \quad (\text{C.27})$$

and that the operators are Hermitian. Consequently,

$$H_{g/e}\rho_{ij} = H_{g/e}|\Psi_i\rangle\langle\Psi_j| = (|\Psi_j\rangle\langle\Psi_i|H_{g/e})^* = \rho_{ji}^*H_{g/e}^* \quad (\text{C.28})$$

Operating in the position basis $\langle x | \bullet | x' \rangle$ gives

$$\begin{aligned}
\langle x | H_{g/e} \rho_{ij} | x' \rangle &= \langle x | H_{g/e} | \Psi_i \rangle \langle \Psi_j | x' \rangle \\
&= \langle x | -\frac{\hbar^2}{2m} \nabla^2 + V_{g/e} | \Psi_i \rangle \langle \Psi_j | x' \rangle \\
&= -\frac{\hbar^2}{2m} \frac{\partial^2}{\partial x^2} \Psi_i(x) \Psi_j^*(x') + V_{g/e}(x) \Psi_i(x) \Psi_j^*(x') \\
&= \left(-\frac{\hbar^2}{2m} \frac{\partial^2}{\partial x^2} + V_{g/e}(x) \right) \rho_{ij}(x, x') \quad (C.29)
\end{aligned}$$

$$\begin{aligned}
\langle x | \rho_{ij} H_{g/e} | x' \rangle &= \langle x | \Psi_i \rangle \langle \Psi_j | H_{g/e} | x' \rangle \\
&= \langle x | \Psi_i \rangle \langle \Psi_j | -\frac{\hbar^2}{2m} \nabla^2 + V_{g/e} | x' \rangle \\
&= -\frac{\hbar^2}{2m} \Psi_i(x) \frac{\partial^2}{\partial x'^2} \Psi_j^*(x') + V_{g/e}(x') \Psi_i(x) \Psi_j^*(x') \\
&= \left(-\frac{\hbar^2}{2m} \frac{\partial^2}{\partial x'^2} + V_{g/e}(x') \right) \rho_{ij}(x, x') \quad (C.30)
\end{aligned}$$

Also, the Hermitian property of the operators gives

$$\begin{aligned}
\langle x | \rho_{ij} H_{g/e} | x' \rangle &= \langle x | \Psi_i \rangle \langle \Psi_j | H_{g/e} | x' \rangle = (\langle x' | H_{g/e} \Psi_j \rangle \langle \Psi_i | x \rangle)^* \\
&= (\langle x' | H_{g/e} \rho_{ji} | x \rangle)^* \quad (C.31)
\end{aligned}$$

Applying this to Eqs. (C.22)-(C.25) gives

$$\begin{aligned}
\frac{\partial}{\partial t}\rho_{11}(x, x') &= -\frac{i}{\hbar}\left\{\left(-\frac{\hbar^2}{2m}\frac{\partial^2}{\partial x^2} + V_g(x)\right)\rho_{11}(x, x')\right. \\
&\quad \left.-\left(-\frac{\hbar^2}{2m}\frac{\partial^2}{\partial x'^2} + V_g(x')\right)\rho_{11}(x, x') - \mu(\varepsilon\rho_{21}(x, x') - \varepsilon^*\rho_{12}(x, x'))\right\} \\
&= -\frac{i}{\hbar}\left\{-\frac{\hbar^2}{2m}\left(\frac{\partial^2}{\partial x^2} - \frac{\partial^2}{\partial x'^2}\right) + V_g(x) - V_g(x')\right\}\rho_{11}(x, x') \\
&\quad + i\frac{\mu}{\hbar}[\varepsilon\rho_{21}(x, x') - \varepsilon^*\rho_{12}(x, x')] \tag{C.32}
\end{aligned}$$

$$\begin{aligned}
\frac{\partial}{\partial t}\rho_{22}(x, x') &= -\frac{i}{\hbar}\left\{\left(-\frac{\hbar^2}{2m}\frac{\partial^2}{\partial x^2} + V_e(x)\right)\rho_{22}(x, x')\right. \\
&\quad \left.-\left(-\frac{\hbar^2}{2m}\frac{\partial^2}{\partial x'^2} + V_e(x')\right)\rho_{22}(x, x') + \mu(\varepsilon\rho_{21}(x, x') - \varepsilon^*\rho_{12}(x, x'))\right\} \\
&= -\frac{i}{\hbar}\left\{-\frac{\hbar^2}{2m}\left(\frac{\partial^2}{\partial x^2} - \frac{\partial^2}{\partial x'^2}\right) + V_e(x) - V_e(x')\right\}\rho_{22}(x, x') \\
&\quad - i\frac{\mu}{\hbar}[\varepsilon\rho_{21}(x, x') - \varepsilon^*\rho_{12}(x, x')] \tag{C.33}
\end{aligned}$$

$$\begin{aligned}
\frac{\partial}{\partial t}\rho_{12}(x, x') &= -\frac{i}{\hbar}\left\{\left(-\frac{\hbar^2}{2m}\frac{\partial^2}{\partial x^2} + V_g(x)\right)\rho_{12}(x, x')\right. \\
&\quad \left.-\left(-\frac{\hbar^2}{2m}\frac{\partial^2}{\partial x'^2} + V_e(x')\right)\rho_{12}(x, x') - \mu\varepsilon(\rho_{22}(x, x') - \rho_{11}(x, x'))\right\} \\
&= -\frac{i}{\hbar}\left\{-\frac{\hbar^2}{2m}\left(\frac{\partial^2}{\partial x^2} - \frac{\partial^2}{\partial x'^2}\right) + V_g(x) - V_e(x')\right\}\rho_{12}(x, x') \\
&\quad + \frac{i}{\hbar}\mu\varepsilon[\rho_{22}(x, x') - \rho_{11}(x, x')] \tag{C.34}
\end{aligned}$$

$$\begin{aligned}
\frac{\partial}{\partial t}\rho_{21}(x, x') &= -\frac{i}{\hbar}\left\{\left(-\frac{\hbar^2}{2m}\frac{\partial^2}{\partial x^2} + V_e(x)\right)\rho_{21}(x, x')\right. \\
&\quad \left.-\left(-\frac{\hbar^2}{2m}\frac{\partial^2}{\partial x'^2} + V_g(x')\right)\rho_{21}(x, x') + \mu\varepsilon^*(\rho_{22}(x, x') - \rho_{11}(x, x'))\right\} \\
&= -\frac{i}{\hbar}\left\{-\frac{\hbar^2}{2m}\left(\frac{\partial^2}{\partial x^2} - \frac{\partial^2}{\partial x'^2}\right) + V_e(x) - V_g(x')\right\}\rho_{21}(x, x') \\
&\quad - \frac{i}{\hbar}\mu\varepsilon^*[\rho_{22}(x, x') - \rho_{11}(x, x')] \tag{C.35} \\
&= \frac{i}{\hbar}\left\{-\frac{\hbar^2}{2m}\left(\frac{\partial^2}{\partial x'^2} - \frac{\partial^2}{\partial x^2}\right) + V_g(x') - V_e(x)\right\}\rho_{21}(x, x') \\
&\quad - \frac{i}{\hbar}\mu\varepsilon^*[\rho_{22}(x, x') - \rho_{11}(x, x')] \\
&= \left(-\frac{i}{\hbar}\left\{-\frac{\hbar^2}{2m}\left(\frac{\partial^2}{\partial x^2} - \frac{\partial^2}{\partial x'^2}\right) + V_g(x) - V_e(x')\right\}\rho_{12}(x', x)\right. \\
&\quad \left.+ \frac{i}{\hbar}\mu\varepsilon[\rho_{22}(x', x) - \rho_{11}(x', x)]\right)^* \\
&= \frac{\partial}{\partial t}\rho_{12}^*(x', x). \tag{184}
\end{aligned}$$

Defining $W_{11}(q, p)$, $W_{12}(q, p)$, $W_{21}(q, p)$, $W_{22}(q, p)$ as the Wigner transforms of the corresponding density matrix elements $\rho_{ij}(x, x')$ - the equations of motion for $W_{ij}(q, p)$ are obtained by taking the Wigner transforms of Eqs. (C.32)-(C.35), in the same manner as the single state EOM was obtained. Taking the Wigner transform of Eq. (C.32) gives

$$\frac{\partial W_{11}}{\partial t} = -\frac{p}{m} \frac{\partial W_{11}}{\partial q} + \frac{\partial V_g}{\partial q} \frac{\partial W_{11}}{\partial p} - \frac{\hbar^2}{24} \frac{\partial^3 V_g}{\partial q^3} \frac{\partial^3 W_{11}}{\partial p^3} + i \frac{\mu}{\hbar} [\varepsilon W_{21}(q, p) - \varepsilon^* W_{12}(q, p)] \quad (\text{C.36})$$

Since $W_{12}(q, p) = W_{21}^*(q, p)$ we have

$$\frac{\partial W_{11}}{\partial t} = -\frac{p}{m} \frac{\partial W_{11}}{\partial q} + \frac{\partial V_g}{\partial q} \frac{\partial W_{11}}{\partial p} - \frac{\hbar^2}{24} \frac{\partial^3 V_g}{\partial q^3} \frac{\partial^3 W_{11}}{\partial p^3} - 2 \frac{\mu}{\hbar} \Im[\varepsilon W_{21}(q, p)]. \quad (\text{C.37})$$

An analogous equation may be written for $W_{22}(q, p)$

$$\begin{aligned} \frac{\partial W_{22}}{\partial t} &= -\frac{p}{m} \frac{\partial W_{22}}{\partial q} + \frac{\partial V_e}{\partial q} \frac{\partial W_{22}}{\partial p} - \frac{\hbar^2}{24} \frac{\partial^3 V_e}{\partial q^3} \frac{\partial^3 W_{22}}{\partial p^3} - i \frac{\mu}{\hbar} [\varepsilon W_{21}(q, p) - \varepsilon^* W_{12}(q, p)] \\ &= -\frac{p}{m} \frac{\partial W_{22}}{\partial q} + \frac{\partial V_e}{\partial q} \frac{\partial W_{22}}{\partial p} - \frac{\hbar^2}{24} \frac{\partial^3 V_e}{\partial q^3} \frac{\partial^3 W_{22}}{\partial p^3} + 2 \frac{\mu}{\hbar} \Im[\varepsilon W_{21}(q, p)] \end{aligned} \quad (\text{C.38})$$

For the off-diagonal terms W_{12} and W_{21} the kinetic energy components are the same for those of the diagonal terms. However, due to contributions from the ground and excited potential energy functions, the potential energy component of the equation of motion for the off-diagonal part of the Wigner function is different i.e. since Eq.(C.34) contains $V_g(x) - V_e(x')$ the even order differentials of the Taylor series remain in the final expression for W_{12} .

We proceed by expanding $V_g(x)$ and $V_e(x')$ in a Taylor series

$$\begin{aligned} V_g(x) &= V_g(q + r/2) \simeq \sum_{n=0}^{\infty} \frac{r^n}{n!2^n} \frac{\partial^n V_g}{\partial q^n} \\ &= V_g(q) + \frac{r}{2} \frac{\partial V_g}{\partial q} + \frac{r^2}{8} \frac{\partial^2 V_g}{\partial q^2} + \frac{r^3}{48} \frac{\partial^3 V_g}{\partial q^3} + \dots \end{aligned} \quad (\text{C.39})$$

$$\begin{aligned} V_e(x') &= V_e(q - r/2) \simeq \sum_{n=0}^{\infty} \frac{-r^n}{n!2^n} \frac{\partial^n V_e}{\partial q^n} \\ &= V_e(q) - \frac{r}{2} \frac{\partial V_e}{\partial q} + \frac{r^2}{8} \frac{\partial^2 V_e}{\partial q^2} - \frac{r^3}{48} \frac{\partial^3 V_e}{\partial q^3} + \dots \end{aligned} \quad (\text{C.40})$$

To 2nd order

$$\begin{aligned} V_g(x) - V_e(x') &\simeq [V_g(q) - V_e(q)] + \frac{r}{2} \left[\frac{\partial V_g(q)}{\partial q} + \frac{\partial V_e(q)}{\partial q} \right] \\ &\quad + \frac{r^2}{8} \left[\frac{\partial^2 V_g(q)}{\partial q^2} - \frac{\partial^2 V_e(q)}{\partial q^2} \right] \end{aligned} \quad (\text{C.41})$$

Inserting the relation

$$\left(\frac{-\hbar}{i} \right)^n \frac{\partial^n}{\partial p^n} e^{-i\frac{rp}{\hbar}} = r^n \quad (\text{C.42})$$

into the potential part of Eq. (C.34) gives

$$\begin{aligned}
& -\frac{i}{\hbar} \frac{1}{2\pi\hbar} \int_{-\infty}^{\infty} [V_g(x) - V_e(x')] < q + \frac{r}{2} |\rho_{12}| q - \frac{r}{2} > e^{-i\frac{rp}{\hbar}} dr \\
& = -\frac{i}{\hbar} \frac{1}{2\pi\hbar} \int_{-\infty}^{\infty} \left\{ [V_g(q) - V_e(q)] + \frac{r}{2} \left[\frac{\partial V_g(q)}{\partial q} + \frac{\partial V_e(q)}{\partial q} \right] \right. \\
& \quad \left. + \frac{r^2}{8} \left[\frac{\partial^2 V_g(q)}{\partial q^2} - \frac{\partial^2 V_e(q)}{\partial q^2} \right] \right\} < q + \frac{r}{2} |\rho_{12}| q - \frac{r}{2} > e^{-i\frac{rp}{\hbar}} dr \\
& = -\frac{i}{\hbar} \frac{1}{2\pi\hbar} \int_{-\infty}^{\infty} \left\{ [V_g(q) - V_e(q)] - \frac{\hbar}{2i} \left[\frac{\partial V_g(q)}{\partial q} + \frac{\partial V_e(q)}{\partial q} \right] \frac{\partial}{\partial p} \right. \\
& \quad \left. - \frac{\hbar^2}{8} \left[\frac{\partial^2 V_g(q)}{\partial q^2} - \frac{\partial^2 V_e(q)}{\partial q^2} \right] \frac{\partial^2}{\partial p^2} \right\} < q + \frac{r}{2} |\rho_{12}| q - \frac{r}{2} > e^{-i\frac{rp}{\hbar}} dr \\
& = -\frac{i}{\hbar} [V_g(q) - V_e(q)] \frac{1}{2\pi\hbar} \int_{-\infty}^{\infty} < q + r/2 |\rho_{12}| q - r/2 > e^{-i\frac{rp}{\hbar}} dr \\
& \quad + \frac{1}{2} \left[\frac{\partial V_g(q)}{\partial q} + \frac{\partial V_e(q)}{\partial q} \right] \frac{\partial}{\partial p} \frac{1}{2\pi\hbar} \int_{-\infty}^{\infty} < q + \frac{r}{2} |\rho_{12}| q - \frac{r}{2} > e^{-i\frac{rp}{\hbar}} dr \\
& \quad + \frac{i\hbar}{8} \left[\frac{\partial^2 V_g(q)}{\partial q^2} - \frac{\partial^2 V_e(q)}{\partial q^2} \right] \frac{\partial^2}{\partial p^2} \frac{1}{2\pi\hbar} \int_{-\infty}^{\infty} < q + r/2 |\rho_{12}| q - r/2 > e^{-i\frac{rp}{\hbar}} dr \\
& = -\frac{i}{\hbar} [V_g(q) - V_e(q)] W_{12}(q, p) + \frac{1}{2} \left[\frac{\partial V_g(q)}{\partial q} + \frac{\partial V_e(q)}{\partial q} \right] \frac{\partial}{\partial p} W_{12}(q, p) \\
& \quad + \frac{i\hbar}{8} \left[\frac{\partial^2 V_g(q)}{\partial q^2} - \frac{\partial^2 V_e(q)}{\partial q^2} \right] \frac{\partial^2}{\partial p^2} W_{12}(q, p) \tag{C.43}
\end{aligned}$$

The equation of motion for W_{12} is then

$$\begin{aligned}
\frac{\partial W_{12}}{\partial t} &= -\frac{p}{m} \frac{\partial W_{12}}{\partial q} - \frac{i}{\hbar} [V_g - V_e] W_{12} + \frac{1}{2} \left[\frac{\partial V_g}{\partial q} + \frac{\partial V_e}{\partial q} \right] \frac{\partial W_{12}}{\partial p} \\
&\quad + \frac{i\hbar}{8} \left[\frac{\partial^2 V_g}{\partial q^2} - \frac{\partial^2 V_e}{\partial q^2} \right] \frac{\partial^2 W_{12}}{\partial p^2} + \frac{i}{\hbar} \mu \varepsilon (W_{22} - W_{11}) \tag{C.44}
\end{aligned}$$

For $W_{21}(q, p)$ we use the same approach but for a potential difference

$$\begin{aligned}
V_e(x) - V_g(x') &\simeq [V_e(q) - V_g(q)] + \frac{r}{2} \left[\frac{\partial V_e(q)}{\partial q} + \frac{\partial V_g(q)}{\partial q} \right] \\
&\quad + \frac{r^2}{8} \left[\frac{\partial^2 V_e(q)}{\partial q^2} - \frac{\partial^2 V_g(q)}{\partial q^2} \right] \tag{C.45}
\end{aligned}$$

to obtain the equation of motion

$$\begin{aligned}
\frac{\partial W_{21}}{\partial t} = & -\frac{p}{m} \frac{\partial W_{21}}{\partial q} - \frac{i}{\hbar} [V_e - V_g] W_{21} + \frac{1}{2} \left[\frac{\partial V_e}{\partial q} + \frac{\partial V_g}{\partial q} \right] \frac{\partial W_{21}}{\partial p} \\
& + \frac{i\hbar}{8} \left[\frac{\partial^2 V_e}{\partial q^2} - \frac{\partial^2 V_g}{\partial q^2} \right] \frac{\partial^2 W_{21}}{\partial p^2} - \frac{i}{\hbar} \mu \varepsilon^* (W_{22} - W_{11}). \quad (\text{C.46})
\end{aligned}$$

Appendix D

Derivation of the Caldeira-Leggett equation

The Caldeira-Leggett model describes the Brownian motion of a particle in a potential $V(x)$. The assumptions of this model are

- Factorised initial conditions.
- Markovian dynamics
- Environment - bath of harmonic oscillators.
- Weak bilinear coupling.
- Applies to the high temperature limit, $k_B T \gtrsim \hbar \Omega$ where Ω is the cut-off frequency for the spectral density.

The Hamiltonian for the environment H_E is then given by

$$H_E = \sum_n \left(\frac{p_n^2}{2m_n} + \frac{1}{2} m_n \omega_n^2 x_n^2 \right) \quad (\text{D.1})$$

where the m_n and ω_n are the masses and frequencies of the environment harmonic oscillators. The weak bilinear coupling part, H_I is expressed as

$$H_I = -x \sum_n a_n x_n = -xB \quad (\text{D.2})$$

The system-bath coupling also acts as potential term and leads to a renormalisation of the system potential $V(x)$. To counterbalance this renormalisation of $V(x)$ a counter term H_c of the form

$$H_c = x^2 \sum_n \frac{a_n^2}{2m_n \omega_n^2} \quad (\text{D.3})$$

is included in the total Hamiltonian Starting from the second order Born-Markov approximation of the master equation

$$\begin{aligned} \frac{\partial \rho_S(t)}{\partial t} &= -\frac{1}{\hbar^2} \int_0^\infty \text{Tr}_E \{ [H_I(t), [H_I(\tau) \rho_S(t) \otimes \rho_E]] \} d\tau \\ &= -\frac{1}{\hbar^2} \int_0^\infty \text{Tr}_E \{ [H_I(t), [H_I(-\tau) \rho_S(t) \otimes \rho_E]] \} d\tau \end{aligned} \quad (\text{D.4})$$

Substituting the explicit form of H_I defined in Eq. (D.2) and expanding the Lie bracket gives

$$\begin{aligned}
\frac{\partial \rho_S(t)}{\partial t} &= -\frac{1}{\hbar^2} \int_0^\infty \text{Tr}_E \{ [xB, [x(-\tau)B(-\tau)\rho_S(t) \otimes \rho_E]] \} d\tau \\
&= -\frac{1}{\hbar^2} \int_0^\infty \left(\text{Tr}_E \{ xBx(-\tau)B(-\tau)\rho_S(t) \otimes \rho_E \} \right. \\
&\quad - \text{Tr}_E \{ xB\rho_S(t) \otimes \rho_E x(-\tau)B(-\tau) \} \\
&\quad - \text{Tr}_E \{ x(-\tau)B(-\tau)\rho_S(t) \otimes \rho_E xB \} \\
&\quad \left. + \text{Tr}_E \{ \rho_S(t) \otimes \rho_E x(-\tau)B(-\tau)xB \} \right) d\tau \\
&= -\frac{1}{\hbar^2} \int_0^\infty \left(\text{Tr}_E \{ BB(-\tau)\rho_E \} xx(-\tau)\rho_S(t) \right. \\
&\quad - \text{Tr}_E \{ B\rho_E B(-\tau) \} x\rho_S(t)x(-\tau) \\
&\quad - \text{Tr}_E \{ B(-\tau)\rho_E B \} x(-\tau)\rho_S(t)x \\
&\quad \left. + \text{Tr}_E \{ \rho_E B(-\tau)B \} \rho_S(t)x(-\tau)x \right) d\tau \\
&= -\frac{1}{\hbar^2} \int_0^\infty \left(\text{Tr}_E \{ BB(-\tau)\rho_E \} xx(-\tau)\rho_S(t) \right. \\
&\quad - \text{Tr}_E \{ B(-\tau)B\rho_E \} x\rho_S(t)x(-\tau) \\
&\quad - \text{Tr}_E \{ BB(-\tau)\rho_E \} x(-\tau)\rho_S(t)x \\
&\quad \left. + \text{Tr}_E \{ B(-\tau)B\rho_E \} \rho_S(t)x(-\tau)x \right) d\tau \\
&= -\frac{1}{\hbar^2} \int_0^\infty \left(\text{Tr}_E \{ BB(-\tau)\rho_E \} [xx(-\tau)\rho_S(t) - x(-\tau)\rho_S(t)x] \right. \\
&\quad \left. + \text{Tr}_E \{ B(-\tau)B\rho_E \} [\rho_S(t)x(-\tau)x - x\rho_S(t)x(-\tau)] \right) d\tau \\
&= -\frac{1}{\hbar^2} \int_0^\infty \left(\langle BB(-\tau) \rangle [xx(-\tau)\rho_S(t) - x(-\tau)\rho_S(t)x] \right. \\
&\quad \left. + \langle B(-\tau)B \rangle [\rho_S(t)x(-\tau)x - x\rho_S(t)x(-\tau)] \right) d\tau \\
&= -\frac{1}{\hbar^2} \int_0^\infty \left(C(-\tau) [xx(-\tau)\rho_S(t) - x(-\tau)\rho_S(t)x] \right. \\
&\quad \left. + C^\dagger(-\tau) [\rho_S(t)x(-\tau)x - x\rho_S(t)x(-\tau)] \right) d\tau \tag{D.5}
\end{aligned}$$

Introducing the real and imaginary correlation functions

$$C_R(\tau) = C(-\tau) + C^\dagger(-\tau) = \langle [B, B(-\tau)]_+ \rangle \quad (D.6)$$

$$C_I(\tau) = i[C(-\tau) - C^\dagger(-\tau)] = i \langle [B, B(-\tau)] \rangle \quad (D.7)$$

and noting that

$$\begin{aligned} & [x, [x(-\tau), \rho_S(t)]_+] + [x, [x(-\tau), \rho_S(t)]] \\ &= xx(-\tau)\rho_S(t) + x\rho_S(t)x(-\tau) - x(-\tau)\rho_S(t)x - \rho_S(t)x(-\tau)x \\ &+ xx(-\tau)\rho_S(t) - x\rho_S(t)x(-\tau) - x(-\tau)\rho_S(t)x + \rho_S(t)x(-\tau)x \\ &= 2[xx(-\tau)\rho_S(t) - x(-\tau)\rho_S(t)x] \end{aligned} \quad (D.8)$$

and

$$\begin{aligned} & [x, [x(-\tau), \rho_S(t)]_+] - [x, [x(-\tau), \rho_S(t)]] \\ &= xx(-\tau)\rho_S(t) + x\rho_S(t)x(-\tau) - x(-\tau)\rho_S(t)x - \rho_S(t)x(-\tau)x \\ &- xx(-\tau)\rho_S(t) + x\rho_S(t)x(-\tau) + x(-\tau)\rho_S(t)x - \rho_S(t)x(-\tau)x \\ &= -2[\rho_S(t)x(-\tau)x - x\rho_S(t)x(-\tau)] \end{aligned} \quad (D.9)$$

we can re-express Eq. (D.5) as

$$\begin{aligned} \frac{\partial \rho_S(t)}{\partial t} &= \frac{1}{\hbar^2} \int_0^\infty \left(\frac{i}{2} C_I(\tau) [x, [x(-\tau), \rho_S(t)]_+] \right. \\ &\quad \left. - \frac{1}{2} C_R(\tau) [x, [x(-\tau), \rho_S(t)]] \right) d\tau \quad (D.10) \\ \text{Proof} &= \frac{1}{2\hbar^2} \int_0^\infty \left([C^\dagger(\tau) - C(\tau)] [x, [x(-\tau), \rho_S(t)]_+] \right. \\ &\quad \left. - [C(\tau) + C^\dagger(\tau)] [x, [x(-\tau), \rho_S(t)]] \right) d\tau \\ &= -\frac{1}{\hbar^2} \int_0^\infty \left(C(\tau) [xx(-\tau)\rho_S(t) - x(-\tau)\rho_S(t)x] \right. \\ &\quad \left. + C^\dagger(\tau) [\rho_S(t)x(-\tau)x - x\rho_S(t)x(-\tau)] \right) d\tau \end{aligned}$$

Defining the spectral density as

$$J(\omega) = \sum_j a_j^2 \frac{\hbar}{2m_j \omega_j} \delta(\omega - \omega_j) \quad (\text{D.11})$$

the correlation functions can be expressed as

$$C_R(\tau) = 2 \int_0^\infty J(\omega) \coth(\beta \hbar \omega / 2) \cos(\omega \tau) d\omega \quad (\text{D.12})$$

$$C_I(\tau) = 2 \int_0^\infty J(\omega) \sin(\omega \tau) d\omega \quad (\text{D.13})$$

Since the bath is assumed to be infinitely large it will have such a large range of frequencies that the discrete representation of $J(\omega)$ may be replaced by a smooth continuous version. In the Caldeira-Leggett model an Ohmic spectral density is used where the spectral density is proportional to the frequency and

$$J(\omega) = \frac{2m\eta\hbar}{\pi} \omega \quad (\text{D.14})$$

depends on the frequency independent damping of rate η . However, expressed in this form the high frequency modes of the environment leads to a renormalisation of the system potential $V(x)$, and to circumvent this, a cut-off frequency Ω is introduced into $J(\omega)$

$$J(\omega) = \frac{2m\eta\hbar}{\pi} \omega f(\omega/\Omega) \quad (\text{D.15})$$

Typical choices of $f(\omega/\Omega)$ include an exponential $\exp(-\omega/\Omega)$ and the example we shall use here - the Lorentz-Drude cut-off function - which leads to a spectral density given by

$$J(\omega) = \frac{2m\eta\hbar}{\pi} \omega \frac{\Omega^2}{\Omega^2 + \omega^2} \quad (\text{D.16})$$

When this form of $J(\omega)$ is then inserted into the correlation functions of Eq. (D.12) and (D.13) we get

$$C_R(\tau) = \frac{4m\eta\hbar}{\pi}\Omega^2 \int_0^\infty \frac{\omega}{\Omega^2 + \omega^2} \coth(\beta\hbar\omega/2) \cos(\omega\tau) d\omega \quad (D.17)$$

$$C_I(\tau) = \frac{4m\eta\hbar}{\pi}\Omega^2 \int_0^\infty \frac{\omega}{\Omega^2 + \omega^2} \sin(\omega\tau) d\omega \quad (D.18)$$

These integrals are evaluated in Appendix D.1 to give

$$C_R(\tau) = \frac{4m\eta\Omega^2}{\beta} \sum_{n=-\infty}^{n=\infty} \frac{\Omega e^{-\Omega\tau} - |\nu_n| e^{-|\nu_n|\tau}}{(\Omega^2 - \nu_n^2)} \quad (D.19)$$

$$C_I(\tau) = 2m\eta\hbar\Omega^2 e^{-\Omega\tau} \quad (D.20)$$

The cut-off frequency Ω and the Matsubara frequencies ν_n contained in the bath correlation functions give rise to correlation times of Ω^{-1} and ν_n^{-1} for $n \neq 0$. The largest correlation time is therefore the largest of the 2 terms $\tau_B = \text{Max}\{\Omega^{-1}, \hbar/(2\pi k_B T)\}$. For the Born-Markov approximation to hold the following condition must hold $\hbar\eta \ll \text{Min}\{\hbar\Omega, 2\pi k_B T\}$, which implies that the bath correlation time τ_B is much smaller than the relaxation time $\tau_B \ll \tau_R$. If we denote $\omega_0 = \tau_S^{-1}$ as the typical frequency of the system evolution we also require that $\hbar\omega_0 \ll \text{Min}\{\hbar\Omega, 2\pi k_B T\}$. Because ω_0 is assumed to be so small then for $e^{-\frac{i}{\hbar}H_S\tau} \rightarrow e^{-\frac{i}{\hbar}\omega_0\tau}$ we can approximate $x(-\tau) = \exp(\mathcal{L}_S\tau)x$ by a low order truncation of an expansion of the exponential (see Appendix D.3)

$$\begin{aligned} x(-\tau) &= e^{\mathcal{L}_S\tau}x = e^{-\frac{i}{\hbar}H_S\tau}x e^{\frac{i}{\hbar}H_S\tau} \\ &\approx x - \frac{i}{\hbar}[H_S, x]\tau = x + \left(\frac{i\hbar}{m} \frac{\partial}{\partial x}\right)\tau = x - \frac{p}{m}\tau \end{aligned} \quad (D.21)$$

Substitution into Eq. (D.10) gives

$$\begin{aligned}
\frac{\partial \rho_S(t)}{\partial t} &= \frac{1}{\hbar^2} \int_0^\infty \frac{i}{2} C_I(\tau) [x, [x(-\tau), \rho_S(t)]_+] \\
&\quad - \frac{1}{2} C_R(\tau) [x, [x(-\tau), \rho_S(t)]] d\tau \\
&= \frac{i}{2\hbar^2} \int_0^\infty C_I(\tau) [x, [x, \rho_S(t)]_+] d\tau - \frac{i}{2m\hbar^2} \int_0^\infty C_I(\tau) [x, [p, \rho_S(t)]_+] \tau d\tau \\
&\quad - \frac{1}{2\hbar^2} \int_0^\infty C_R(\tau) [x, [x, \rho_S(t)]] d\tau + \frac{1}{2m\hbar^2} \int_0^\infty C_R(\tau) [x, [p, \rho_S(t)]] \tau d\tau
\end{aligned} \tag{D.22}$$

To solve some of the 4 integrals on the right-hand side of the above equation we make use of the following relation

$$\begin{aligned}
\int_0^\infty e^{i\omega\tau} d\tau &= \lim_{\varepsilon \rightarrow 0} \int_0^\infty e^{-\varepsilon\tau + i\omega\tau} d\tau \lim_{\varepsilon \rightarrow 0} \frac{e^{-\varepsilon\tau + i\omega\tau}}{-\varepsilon + i\omega} \Big|_0^\infty = \lim_{\varepsilon \rightarrow 0} \frac{1}{\varepsilon - i\omega} \\
&= \lim_{\varepsilon \rightarrow 0} \frac{i}{i\varepsilon + \omega} = i \frac{\mathcal{P}}{\omega} + \pi\delta(\omega)
\end{aligned} \tag{D.23}$$

The last line is the integral kernel of Plemelj's identity (see Appendix D.2). Taking the real and imaginary parts of Plemelj's identity and the integral of the exponential gives

$$\int_0^\infty \cos(\omega\tau) d\tau = \pi\delta(\omega) \tag{D.24}$$

$$\int_0^\infty \sin(\omega\tau) d\tau = \frac{\mathcal{P}}{\omega} \tag{D.25}$$

Coming back to Eq. (D.22): for the first term on the right hand side of this equation, the only time dependency (τ dependency) is in the correlation function $C_I(\tau)$. Hence, applying the relation Eq. (D.25) to Eq. (D.13) gives¹

$$\int_0^\infty C_I(\tau) d\tau = 2 \int_0^\infty \frac{J(\omega)}{\omega} d\omega \tag{D.26}$$

¹Note that $\int_0^\infty f(x)\delta(x-a)dx = f(a)$ if $0 < a < \infty$. If $a = 0$ then the integral gives $f(a)/2$ because the delta function is located at $x = 0$. i.e. half of δ function lies to the left of $x = 0$ and half to the right of $x = 0$. (even though the δ function is meant to be infinitely narrow)

Making use of the discrete representation of $J(\omega)$ as defined in Eq. (D.11) gives

$$\begin{aligned} 2 \int_0^\infty \frac{J(\omega)}{\omega} d\omega &= 2 \int_0^\infty \frac{1}{\omega} \sum_j a_j^2 \frac{\hbar}{2m_j \omega_j} \delta(\omega - \omega_j) d\omega \\ &= 2 \sum_j a_j^2 \frac{\hbar}{2m_j \omega_j^2} \end{aligned} \quad (\text{D.27})$$

Substitution into the first integral of Eq. (D.22) gives

$$\begin{aligned} \frac{i}{2\hbar^2} \int_0^\infty C_I(\tau) [x, [x, \rho_S(t)]_+] d\tau &= \frac{i}{\hbar} \sum_j a_j^2 \frac{\hbar}{2m_j \omega_j^2} [x, [x, \rho_S(t)]_+] \\ &= \frac{i}{\hbar} \sum_j a_j^2 \frac{\hbar}{2m_j \omega_j^2} [x^2 \rho_S(t) + x \rho_S(t) x \\ &\quad - x \rho_S(t) x - \rho_S(t) x^2] \\ &= \frac{i}{\hbar} \sum_j a_j^2 \frac{\hbar}{2m_j \omega_j^2} [x^2 \rho_S(t) - \rho_S(t) x^2] \\ &= \frac{i}{\hbar} \sum_j a_j^2 \frac{\hbar}{2m_j \omega_j^2} [x^2, \rho_S(t)] \\ &= \frac{i}{\hbar} [H_c, \rho_S(t)] \end{aligned} \quad (\text{D.28})$$

This is the term compensated for in the counter Hamiltonian part H_c defined earlier in Eq. (D.3). The effect of the bath induced term of Eq. (D.28) that affects H_S is then cancelled by H_c of Eq. (D.3).

For the second term on the right hand side of Eq. (D.22) the only time (τ) dependency in the integral is

$$\begin{aligned}
\int_0^\infty \tau C_I(\tau) d\tau &= 2 \int_0^\infty \int_0^\infty J(\omega) \tau \sin(\omega\tau) d\tau d\omega \\
&= 2 \int_0^\infty J(\omega) \frac{-\partial}{\partial \omega} \int_0^\infty \cos(\omega\tau) d\tau d\omega \\
&= -2 \int_0^\infty J(\omega) \frac{\partial}{\partial \omega} \delta(\omega) \pi d\omega \\
&= 2\pi \int_0^\infty \delta(\omega) \frac{\partial}{\partial \omega} J(\omega) d\omega \\
&= 2\pi \int_0^\infty \delta(\omega) \frac{\partial}{\partial \omega} \frac{2m\eta\hbar\omega}{\pi} d\omega \\
&= 4\hbar m\eta \int_0^\infty \delta(\omega) d\omega \\
&= 2\hbar m\eta
\end{aligned} \tag{D.29}$$

Here, use has been made of the following relation for the δ function

$$\int f(x) \delta^n(x) dx = - \int \frac{\partial f}{\partial x} \delta^{n-1}(x) dx \tag{D.30}$$

where $\delta^n(x)$ is the n^{th} derivative of the delta function. Also note that the lower bound of the integral cuts through the δ function at $x = 0$ giving a value of 1/2 for the integral (see the footnote associated with Eq. (D.26))

Inserting the result of Eq. (D.29) into the second term of Eq. (D.22) gives

$$\begin{aligned}
-\frac{i}{2m\hbar^2} \int_0^\infty C_I(\tau) [x, [p, \rho_S(t)]_+] \tau d\tau &= -\frac{i}{2m\hbar^2} [x, [p, \rho_S(t)]_+] 2\hbar m\eta \\
&= -\frac{i\eta}{\hbar} [x, [p, \rho_S(t)]_+]
\end{aligned} \tag{D.31}$$

For the time-dependency part of the third term on the right hand side of Eq. (D.22) we have

$$\begin{aligned}\int_0^\infty C_R(\tau) d\tau &= 2 \int_0^\infty \int_0^\infty J(\omega) \coth(\beta\hbar\omega/2) \cos(\omega\tau) d\tau d\omega \\ &= 2\pi \int_0^\infty J(\omega) \coth(\beta\hbar\omega/2) \delta(\omega) d\omega\end{aligned}\quad (\text{D.32})$$

Using the following series expansion of the coth term

$$\coth x = \frac{1}{x} + \frac{x}{3} - \frac{x^2}{45} + \dots \quad (\text{D.33})$$

and the Ohmic form of $J(\omega)$, and then taking the limit $\omega \rightarrow 0$ gives

$$\begin{aligned}&2\pi \int_0^\infty \frac{2m\eta\hbar}{\pi} \omega \coth(\beta\hbar\omega/2) \delta(\omega) d\omega = \\ &4 \int_0^\infty m\eta\hbar\omega \left(\frac{2}{\beta\hbar\omega} + \frac{\beta\hbar\omega}{6} - \frac{(\beta\hbar\omega)^2}{180} + \dots \right) \delta(\omega) d\omega = \\ &4 \int_0^\infty m\eta\hbar \left(\frac{2}{\beta\hbar} + \frac{\beta\hbar\omega^2}{6} - \frac{\omega(\beta\hbar\omega)^2}{180} + \dots \right) \delta(\omega) d\omega = \\ &4m\eta\hbar \frac{2}{\beta\hbar} \frac{1}{2} = 4 \frac{m\eta}{\beta} \\ &= 4m\eta k_B T\end{aligned}\quad (\text{D.34})$$

The third term on the right-hand side of Eq. (D.22) is then given by

$$-\frac{1}{2\hbar^2} \int_0^\infty C_R(\tau) [x, [x, \rho_S(t)]] d\tau = -\frac{2m\eta k_B T}{\hbar^2} [x, [x, \rho_S(t)]] \quad (\text{D.35})$$

For the 4th term on the right hand side of Eq. (D.22) we use the spectral density with the Drude cut-off frequency as expressed in Eq. (D.17)

$$\begin{aligned}
& \frac{1}{2m\hbar^2} \int_0^\infty C_R(\tau)[x, [p, \rho_S(t)]] \tau d\tau = \frac{1}{2m\hbar^2} \int_0^\infty \frac{4m\eta\hbar}{\pi} \Omega^2 \\
& \int_0^\infty \frac{\omega}{\Omega^2 + \omega^2} \coth(\beta\hbar\omega/2) \cos(\omega t) d\omega [x, [p, \rho_S(t)]] \tau d\tau \\
& = \frac{2\eta\Omega^2}{\pi\hbar} \int_0^\infty \int_0^\infty \frac{\omega}{\Omega^2 + \omega^2} \coth(\beta\hbar\omega/2) \cos(\omega t) d\omega \tau d\tau [x, [p, \rho_S(t)]]
\end{aligned} \tag{D.36}$$

Inserting the expansion the hyperbolic cotangent function as defined in Eq. (D.33) into Eq. (D.36)

$$\begin{aligned}
& \frac{2\eta\Omega^2}{\pi\hbar} \int_0^\infty \int_0^\infty \frac{\omega}{\Omega^2 + \omega^2} \coth(\beta\hbar\omega/2) \cos(\omega t) d\omega \tau d\tau [x, [p, \rho_S(t)]] \\
& = \frac{2\eta\Omega^2}{\pi\hbar} \int_0^\infty \int_0^\infty \frac{\omega}{\Omega^2 + \omega^2} \left[\frac{2k_B T}{\hbar\omega} + \frac{1}{3} \frac{\hbar\omega}{2k_B T} - \frac{1}{45} \left(\frac{\hbar\omega}{2k_B T} \right)^3 + \dots \right] \\
& \cos(\omega t) d\omega \tau d\tau [x, [p, \rho_S(t)]] \\
& = \frac{2\eta\Omega^2}{\pi\hbar} \int_0^\infty \int_0^\infty \frac{1}{\Omega^2 + \omega^2} \left[\frac{2k_B T}{\hbar} + \frac{1}{3} \frac{\hbar\omega^2}{2k_B T} - \frac{\omega}{45} \left(\frac{\hbar\omega}{2k_B T} \right)^3 + \dots \right] \\
& \cos(\omega t) d\omega \tau d\tau [x, [p, \rho_S(t)]]
\end{aligned} \tag{D.37}$$

and taking the high temperature limit such that $\hbar\Omega \gtrsim k_B T$ gives

$$\begin{aligned}
& \frac{2\eta\Omega^2}{\pi\hbar} \int_0^\infty \int_0^\infty \frac{1}{\Omega^2 + \omega^2} \left[\frac{2k_B T}{\hbar} + \frac{1}{3} \frac{\hbar\omega^2}{2k_B T} - \frac{\omega}{45} \left(\frac{\hbar\omega}{2k_B T} \right)^3 + \dots \right] \\
& \cos(\omega t) d\omega \tau d\tau [x, [p, \rho_S(t)]] \\
& \simeq \frac{2\eta\Omega^2}{\pi\hbar} \int_0^\infty \int_0^\infty \frac{1}{\Omega^2 + \omega^2} \frac{2k_B T}{\hbar} \cos(\omega t) d\omega \tau d\tau [x, [p, \rho_S(t)]] \\
& = \frac{4\eta k_B T \Omega^2}{\pi\hbar^2} \int_0^\infty \frac{1}{\Omega^2 + \omega^2} \int_0^\infty \cos(\omega t) \tau d\tau d\omega [x, [p, \rho_S(t)]] \\
& = \frac{4\eta k_B T \Omega^2}{\pi\hbar^2} \int_0^\infty \frac{1}{\Omega^2 + \omega^2} \int_0^\infty \frac{\partial}{\partial \omega} \sin(\omega t) d\tau d\omega [x, [p, \rho_S(t)]] \\
& = \frac{4\eta k_B T \Omega^2}{\pi\hbar^2} \int_0^\infty \frac{1}{\Omega^2 + \omega^2} \frac{\partial}{\partial \omega} \frac{\mathcal{P}}{\omega} d\omega [x, [p, \rho_S(t)]] \\
& = \frac{4\eta k_B T \Omega^2}{\pi\hbar^2} [x, [p, \rho_S(t)]] \int_0^\infty \frac{1}{\Omega^2 + \omega^2} \frac{-1}{\omega^2} d\omega \\
& = -\frac{4\eta k_B T \Omega^2}{\pi\hbar^2} [x, [p, \rho_S(t)]] \int_0^\infty \frac{d\omega}{(\Omega^2 + \omega^2)\omega^2} \tag{D.38}
\end{aligned}$$

where \mathcal{P} is Cauchy's principal value. Contour integration can be used to calculate the integral as follows. Extend $\omega \rightarrow z$ the complex plane²

$$\begin{aligned}
\int_0^\infty \frac{d\omega}{(\Omega^2 + \omega^2)\omega^2} &= \frac{1}{2} \int_{-\infty}^\infty \frac{d\omega}{(\Omega^2 + \omega^2)\omega^2} \rightarrow \frac{1}{2} \oint_C \frac{dz}{(\Omega^2 + z^2)z^2} = i\pi \text{Res}(i\Omega) \\
&= -\frac{\pi}{2\Omega^3} \tag{D.39}
\end{aligned}$$

where

$$\text{Res}(i\Omega) = \lim_{z \rightarrow i\Omega} (z - i\Omega) \frac{1}{z^2(z - i\Omega)(z + i\Omega)} = -\frac{1}{2i\Omega^3} \tag{D.40}$$

Substituting Eq. (D.39) back into Eq. (D.38) gives

$$\begin{aligned}
\frac{1}{2m\hbar^2} \int_0^\infty C_R(\tau) [x, [p, \rho_S(t)]] \tau d\tau &= -\frac{4\eta k_B T \Omega^2}{\pi\hbar^2} [x, [p, \rho_S(t)]] \frac{-\pi}{2\Omega^3} \\
&= \frac{2\eta k_B T}{\hbar^2 \Omega} [x, [p, \rho_S(t)]] \tag{D.41}
\end{aligned}$$

²and noting that since the integrand is an even function the integral from $0 \rightarrow \infty$ is half the integral between $\pm\infty$.

To realise the relative importance of this term, Eq. (D.41), when compared to Eq. (D.35) we approximate the momentum term by

$$p \sim m \frac{d}{dt} x(t=0) = m \frac{d}{dt} x \cos(\omega_0 t = 0) = -m x \omega_0 \quad (\text{D.42})$$

where ω_0 is a typical frequency of the system. If we replace the momentum term of Eq. (D.41) by $-m x \omega_0$ it is observed that the equation differs from Eq. (D.35) only by the factor ω_0/Ω . Since Ω is the large cut-off frequency, the term ω_0/Ω is very small and consequently this fourth term, Eq. (D.41), can be neglected from the Master equation.

Since the first term, Eq. (D.28), is cancelled by the counter Hamiltonian, only the second and third integrals of Eq. (D.22) survive. Finally, the Caldeira-Leggett equation is given by

$$\frac{\partial \rho_S(t)}{\partial t} = -\frac{i}{\hbar} [H_S, \rho_S(t)] - \frac{i\eta}{\hbar} [x, [p, \rho_S(t)]_+] - \frac{2m\eta k_B T}{\hbar^2} [x, [x, \rho_S(t)]] \quad (\text{D.43})$$

D.1 Contour integration of C_R and C_I

D.1.1 C_I

These integrals may be solved by the theorem of residues of contour integration. For $C_I(\tau)$ we proceed as follows. We extend the integral to the complex plane and take the imaginary part of the final answer

$$\int_0^\infty \frac{\omega}{\Omega^2 + \omega^2} \sin(\omega t) d\omega \rightarrow \oint_C \frac{z}{\Omega^2 + z^2} e^{iz\tau} dz \quad (D.44)$$

where C is a closed semi-circle in the upper half of the complex plane. The integrand has a residue at

$$\begin{aligned} R(i\Omega) &= \lim_{z \rightarrow i\Omega} (z - i\Omega) \frac{ze^{iz\tau}}{(z - i\Omega)(z + i\Omega)} \\ &= \frac{i\Omega e^{-\Omega\tau}}{i2\Omega} = \frac{e^{-\Omega\tau}}{2} \end{aligned} \quad (D.45)$$

where $R(i\Omega)$ is the residue at the singular point $i\Omega$. From the theorem of residues, which is

$$\oint_C f(z) dz = 2\pi i * \text{sum of the residues of } f(z) \text{ at the singular points inside } (D.46)$$

the value of the contour integral of Eq. (D.45) is

$$\oint_C \frac{z}{\Omega^2 + z^2} e^{iz\tau} dz = 2\pi i \frac{e^{-\Omega\tau}}{2} = i\pi e^{-\Omega\tau} \quad (D.47)$$

Next, we express z in polar form $z = re^{i\theta}$. With $dz = ire^{i\theta} d\theta$ we get

$$\oint_C \frac{z}{\Omega^2 + z^2} e^{iz\tau} dz = \int_{-r}^r \frac{\omega}{\Omega^2 + \omega^2} e^{i\omega\tau} d\omega + \int_0^\pi \frac{z}{\Omega^2 + z^2} e^{iz\tau} dz \quad (D.48)$$

Here the integral has been partitioned to the line from $-r \rightarrow r$ along the real axis and another part associated with the semicircle in the upper half where $z = re^{i\theta}$. The integral along the semicircle $\rightarrow 0$ as $r \rightarrow \infty$. This is always

the case if we have an integral along the semi-circle of the form

$$\int \frac{P(z)}{Q(z)} e^{imz} dz \quad (D.49)$$

where $m > 0$, $P(z)$ and $Q(z)$ are polynomials where $Q(z)$ has no real zeros and is of at least 1 degree greater than $P(z)$. For the exponential part we can see that $|e^{iz\tau}| \leq 1$ as $r \rightarrow \infty$:

$$|e^{iz\tau}| = |e^{i\omega\tau - \epsilon\tau}| = |e^{i\omega\tau}| \cdot |e^{-\epsilon\tau}| = |e^{-\epsilon\tau}| \leq 1 \quad (D.50)$$

On the right hand side we recognise that the periodic function $|e^{i\omega\tau}|$ can never exceed 1. Since we are considering the upper plane (ϵ is the vertical axis) $\epsilon \geq 0$ and $\tau \geq 0$ then $|e^{iz\tau}| \leq 1$. For the rational term - because $Q(z) \rightarrow \infty$ more rapidly than $P(z) \rightarrow \infty$ as $r \rightarrow \infty$ the rational term tends to zero. For proofs see books on complex analysis.

Anyway, back to Eq. (D.48). As $r \rightarrow \infty$

$$r \rightarrow \infty \quad \oint_C \frac{z}{\Omega^2 + z^2} e^{iz\tau} dz = \int_{-\infty}^{\infty} \frac{\omega}{\Omega^2 + \omega^2} e^{i\omega\tau} d\omega = i\pi e^{-\Omega\tau} \quad (D.51)$$

Taking the imaginary part of the integrand gives

$$i \int_{-\infty}^{\infty} \frac{\omega}{\Omega^2 + \omega^2} \sin(\omega\tau) d\omega = i\pi e^{-\Omega\tau} \quad (D.52)$$

and so

$$\int_{-\infty}^{\infty} \frac{\omega}{\Omega^2 + \omega^2} \sin(\omega\tau) d\omega = \pi e^{-\Omega\tau} \quad (D.53)$$

Since the integrand is an even function the integral from $0 \rightarrow \infty$ is half the integral from $-\infty \rightarrow \infty$. Hence

$$\int_0^{\infty} \frac{\omega}{\Omega^2 + \omega^2} \sin(\omega\tau) d\omega = \frac{\pi}{2} e^{-\Omega\tau} \quad (D.54)$$

Inserting this into Eq. (D.18) gives

$$\begin{aligned}
C_I(\tau) &= \frac{4m\eta\hbar}{\pi}\Omega^2 \int_0^\infty \frac{\omega}{\Omega^2 + \omega^2} \sin(\omega\tau) d\omega \\
&= \frac{4m\eta\hbar}{\pi}\Omega^2 \frac{\pi}{2} e^{-\Omega\tau} \\
&= 2m\eta\hbar\Omega^2 e^{-\Omega\tau}
\end{aligned} \tag{D.55}$$

D.1.2 C_R

For the real part of the correlation function $C_R(\tau)$ the theorem of residues is also used. To proceed, we start by expanding the hyperbolic cotangent term in the following series,

$$\coth(\beta\hbar\omega/2) = \frac{2}{\beta\hbar} \sum_{n=-\infty}^{n=\infty} \frac{\omega}{\omega^2 + \nu_n^2} \tag{D.56}$$

where $\nu_n = 2\pi n/(\beta\hbar)$ are known as the **Matsubara frequencies**. Substituting Eq. (D.56) into C_R in Eq. (D.17) gives the following integral to solve

$$\begin{aligned}
\int_0^\infty \frac{\omega \coth(\beta\hbar\omega/2)}{\Omega^2 + \omega^2} \cos(\omega\tau) d\omega &= \int_0^\infty \frac{\omega}{\Omega^2 + \omega^2} \frac{2}{\beta\hbar} \sum_{n=-\infty}^{n=\infty} \frac{\omega}{\omega^2 + \nu_n^2} \cos(\omega\tau) d\omega \\
&= \frac{2}{\beta\hbar} \sum_{n=-\infty}^{n=\infty} \int_0^\infty \frac{\omega^2 \cos(\omega\tau)}{(\Omega^2 + \omega^2)(\nu_n^2 + \omega^2)} d\omega
\end{aligned} \tag{D.57}$$

Since the summation index n only affects the constant ν_n there is only one integral that needs to be solved. Continuing in the same manner as the previous section for C_I we express the integral in the complex plane

$$\int_0^\infty \frac{\omega^2 \cos(\omega\tau)}{(\Omega^2 + \omega^2)(\nu_n^2 + \omega^2)} d\omega \rightarrow \oint_C \frac{z^2 e^{iz\tau}}{(\Omega^2 + z^2)(\nu_n^2 + z^2)} dz \tag{D.58}$$

where again C is a closed semi-circle in the upper half of the complex plane. The integrand has a residues at

$$\begin{aligned} R(i\Omega) &= \lim_{z \rightarrow i\Omega} (z - i\Omega) \frac{z^2 e^{iz\tau}}{(z - i\Omega)(z + i\Omega)(\nu_n^2 - \Omega^2)} \\ &= \frac{-\Omega^2 e^{-\Omega\tau}}{i2\Omega(\nu_n^2 - \Omega^2)} = \frac{-\Omega e^{-\Omega\tau}}{i2(\nu_n^2 - \Omega^2)} = \frac{\Omega e^{-\Omega\tau}}{i2(\Omega^2 - \nu_n^2)} \end{aligned} \quad (D.59)$$

and another one at

$$\begin{aligned} R(i\nu_n) &= \lim_{z \rightarrow i|\nu_n|} (z - i|\nu_n|) \frac{z^2 e^{iz\tau}}{(z^2 + \Omega^2)(z - i|\nu_n|)(z + i|\nu_n|)} \\ &= \frac{-\nu_n^2 e^{-|\nu_n|\tau}}{i2|\nu_n|(-\nu_n^2 + \Omega^2)} = \frac{-|\nu_n| e^{-|\nu_n|\tau}}{i2(\Omega^2 - \nu_n^2)} \end{aligned} \quad (D.60)$$

(To emphasise that ν_n are positive and real we use $|\nu_n|$.) Therefore

$$\begin{aligned} \oint_C \frac{z^2 e^{iz\tau}}{(\Omega^2 + z^2)(\nu_n^2 + z^2)} dz &= 2\pi i * \text{sum of the residue of } f(z) \\ &\quad \text{at the singular points inside } C \\ &= 2\pi i [R(i\Omega) + R(i|\nu_n|)] \\ &= 2\pi i \left(\frac{\Omega e^{-\Omega\tau}}{i2(\Omega^2 - \nu_n^2)} - \frac{|\nu_n| e^{-|\nu_n|\tau}}{i2(\Omega^2 - \nu_n^2)} \right) \\ &= \pi \frac{\Omega e^{-\Omega\tau} - |\nu_n| e^{-|\nu_n|\tau}}{(\Omega^2 - \nu_n^2)} \end{aligned} \quad (D.61)$$

where τ and $|\nu_n|$ are positive real numbers. As in the previous section for C_I , if we express z in polar form, partition the integral into a component along the purely real axis $\pm r$ and another component associated with the semi-circle, and extend $r \rightarrow \infty$; we find that the integral along the semi-circle is zero for the same reasons given previously. Consequently,

$$\begin{aligned} \oint_C \frac{z^2 e^{iz\tau}}{(\Omega^2 + z^2)(\nu_n^2 + z^2)} dz &= \int_{-\infty}^{\infty} \frac{\omega^2 e^{i\omega\tau}}{(\Omega^2 + \omega^2)(\nu_n^2 + \omega^2)} d\omega \\ &= \pi \frac{\Omega e^{-\Omega\tau} - |\nu_n| e^{-|\nu_n|\tau}}{(\Omega^2 - \nu_n^2)} \end{aligned} \quad (D.62)$$

Taking the real part gives

$$\int_{-\infty}^{\infty} \frac{\omega^2 \cos(\omega\tau)}{(\Omega^2 + \omega^2)(\nu_n^2 + \omega^2)} d\omega = \pi \frac{\Omega e^{-\Omega\tau} - |\nu_n| e^{-|\nu_n|\tau}}{(\Omega^2 - \nu_n^2)} \quad (\text{D.63})$$

Since the integrand is an even function the integral from $0 \rightarrow \infty$ is half the integral from $-\infty \rightarrow \infty$. Hence

$$\int_0^{\infty} \frac{\omega^2 \cos(\omega\tau)}{(\Omega^2 + \omega^2)(\nu_n^2 + \omega^2)} d\omega = \frac{\pi}{2} \frac{\Omega e^{-\Omega\tau} - |\nu_n| e^{-|\nu_n|\tau}}{(\Omega^2 - \nu_n^2)} \quad (\text{D.64})$$

Inserting this into Eq. (D.17) gives

$$\begin{aligned} C_R(\tau) &= \frac{4m\eta\hbar}{\pi} \Omega^2 \int_0^{\infty} \frac{\omega}{\Omega^2 + \omega^2} \coth(\beta\hbar\omega/2) \cos(\omega\tau) d\omega \\ &= \frac{4m\eta\hbar}{\pi} \Omega^2 \frac{2}{\beta\hbar} \sum_{n=-\infty}^{n=\infty} \int_0^{\infty} \frac{\omega^2 \cos(\omega\tau)}{(\Omega^2 + \omega^2)(\nu_n^2 + \omega^2)} d\omega \\ &= \frac{4m\eta}{\pi} \Omega^2 \frac{2}{\beta} \sum_{n=-\infty}^{n=\infty} \frac{\pi}{2} \frac{\Omega e^{-\Omega\tau} - |\nu_n| e^{-|\nu_n|\tau}}{(\Omega^2 - \nu_n^2)} \\ &= \frac{4m\eta\Omega^2}{\beta} \sum_{n=-\infty}^{n=\infty} \frac{\Omega e^{-\Omega\tau} - |\nu_n| e^{-|\nu_n|\tau}}{(\Omega^2 - \nu_n^2)} \end{aligned} \quad (\text{D.65})$$

D.2 Plemelj Identity

This is an identity for breaking up of the integral of an analytical function around a closed semi-circle. i.e.

$$\begin{aligned} \oint_{\Omega} \frac{f(z)}{z - u} dz &= \int_{S_{\infty}} \frac{f(z)}{z - u} dz + \int_{u+r}^{\infty} \frac{f(\omega)}{\omega - u} d\omega \\ &\quad + \int_{-\infty}^{u-r} \frac{f(\omega)}{\omega - u} d\omega + \int_{\pi}^0 \frac{f(u + re^{i\phi})}{u + re^{i\phi} - u} i r e^{i\phi} d\phi \\ &= \mathcal{P} \int_{-\infty}^{\infty} \frac{f(\omega)}{\omega - u} d\omega + i\pi f(u) \end{aligned} \quad (\text{D.66})$$

D.3 Hamilton commutator

$$\begin{aligned}
[H_s, x] &= [T + V, x] = [T, x] \\
&= -\frac{\hbar^2}{2m} \frac{\partial^2}{\partial x^2} x \bullet + x \frac{\hbar^2}{2m} \frac{\partial \bullet}{\partial x^2} \\
&= -\frac{\hbar^2}{2m} \frac{\partial}{\partial x} \frac{\partial x}{\partial x} \bullet - \frac{\hbar^2}{2m} \frac{\partial}{\partial x} \frac{\partial \bullet}{\partial x} x + x \frac{\hbar^2}{2m} \frac{\partial \bullet}{\partial x^2} \\
&= -\frac{\hbar^2}{2m} \frac{\partial \bullet}{\partial x} - x \frac{\hbar^2}{2m} \frac{\partial^2 \bullet}{\partial x^2} - \frac{\hbar^2}{2m} \frac{\partial \bullet}{\partial x} + x \frac{\hbar^2}{2m} \frac{\partial \bullet}{\partial x^2} \\
&= -\frac{\hbar^2}{m} \frac{\partial \bullet}{\partial x}
\end{aligned}
\tag{D.67}$$

With $p = -i\hbar\partial/\partial x$

$$-\frac{i}{\hbar} [H_s, x] = \frac{i\hbar}{m} \frac{\partial}{\partial x} = -\frac{p}{m}
\tag{D.68}$$